Doctorate of National Interest
in
Space Science and Technology

Constraining physics beyond ΛCDM through the cosmic microwave background and the large scale structure of the Universe

Salvatore Samuele Sirletti

Supervisor
Prof. Mario Ballardini
Università degli Studi di Ferrara

Co-Supervisors
Dr. Alessandro Gruppuso
INAF – OAS Bologna

Prof. Paolo Natoli
Università degli Studi di Ferrara

To Filomena,
my light in this dark Universe.

To Massimiliano,
my guide into science and music.

To Carmela,
who taught me how to dream.

To Benedetto Leone,
whose mind I wish I had.

Contents

Abstract

This thesis investigates physics beyond the standard cosmological model (ΛCDM) through three interconnected topics: third-order corrections to primordial perturbations from inflation, signals of Cosmic Birefringence in the Cosmic Microwave Background (CMB) polarization, and photon–axion interactions in galactic magnetic fields. Using a combination of cosmological observations and theoretical modeling, these studies aim to improve our understanding of early-universe processes and possible new physics breaking fundamental symmetries.

Cosmic inflation amplifies quantum fluctuations that seeded the observed anisotropies in the CMB and large-scale structure. Comparing theoretical predictions with observational data requires precision matching the improvements in measurement sensitivity. An analytical solution at third order in slow-roll parameters has been derived for scalar and tensor primordial perturbations by solving the Mukhanov–Sasaki equation, using an approach distinct from previous literature. Comparisons with numerical solutions identify the scales and observational regimes where third-order corrections become relevant, including large-scale structure surveys, CMB spectral distortions, 21 cm experiments, and primordial black hole limits. Constraints on slow-roll parameters have been obtained, and forecasts for upcoming experiments such as LiteBIRD and the Simons Observatory assess the potential observational impact of higher-order corrections.

Physics beyond the Standard Model can violate parity symmetry, inducing a rotation of the CMB polarization plane by an angle β, an effect known as Cosmic Birefringence. *Planck* data indicate a 5σ detection of an EB signal, whose origin remains uncertain: it could arise from pseudoscalar particles (axions or axion-like particles, ALPs) coupled to the electromagnetic field via the Chern–Simons interaction, or result from systematic calibration uncertainties in the polarimeters. A comprehensive analysis of *Planck* PR3 data has been performed, including pipeline validation and consistency checks across different component-separation methods (`Commander`, `NILC`, `SEVEM`, and `SMICA`), confirming the signal of $\beta \simeq 0.30 \pm 0.05$ degrees (68% CL), consistent with previous literature but excluding possible systematic errors. The key focus is the investigation of the scale dependence of $\beta(\ell)$ through harmonic-space estimators applied to different multipole subsets, independently of the signal's physical origin. Two complementary methods—a parametric power-law fit and a non-parametric Bayesian reconstruction—have been used to test whether *Planck* data are consistent with scale independence. Such tests constrain the birefringence spectrum and narrow the viable axion/ALP mass range to ultra-light regimes. Forecasts suggest that LiteBIRD, Simons Observatory, and CMB-S4 will significantly improve constraints on both the birefringence amplitude and its scale dependence.

CMB photons passing through galactic halos can convert into axions via the Chern–Simons interaction, producing spectral distortions in the CMB. These distortions may be detectable by future CMB experiments such as the Simons Observatory when combined with galaxy surveys from the Vera Rubin Observatory Legacy Survey of Space and Time (LSST), Dark Energy Spectroscopic Instrument (DESI), and Euclid. The photon–axion conversion probability, modeled by a two-level Schrödinger equation, is often estimated using the Landau–Zener approximation, which assumes linear halo profiles. However, the validity of this approximation under realistic conditions—characterized by non-linear profiles, multiple resonances, and stochastic noise—remains uncertain. Here, the Schrödinger equation has been solved numerically using the Wentzel–Kramers–Brillouin (WKB) approximation, enabling a systematic exploration of the applicability of the Landau–Zener approximation and determining the scenarios where a full numerical approach is essential for accurate cosmological predictions.

List of Publications

Author's papers representing the original work of this thesis:

- [1] M. Ballardini, A. Davoli, and **S. S. Sirletti**. Third-order corrections to the slow-roll expansion: Calculation and constraints with Planck, ACT, SPT, and BICEP/Keck. *Phys. Dark Univ.*, 47:101813, 2025. doi: 10.1016/j.dark.2025.101813.

- [2] The CosmoVerse White Paper: Addressing observational tensions in cosmology with systematics and fundamental physics. *Phys. Dark Univ.*, 49:101965, 2025. doi: 10.1016/j.dark.2025.101965.

- [3] M. Ballardini, A. Gruppuso, S. Paradiso, **S. S. Sirletti** [Corresponding author], and P. Natoli. Planck constraints on the scale dependence of isotropic cosmic birefringence. *JCAP*, 09:075, 2025. doi: 10.1088/1475-7516/2025/09/075.

- [4] **S. S. Sirletti**, S. Goldstein, J. C. Hill, J. Huang, M. Johnson, and C. Mondino. Multi-resonance photon-axion conversion in galaxy halos: A WKB approach. (2025) [In preparation]

Other author's papers not reported in this thesis:

- [5] **S. S. Sirletti**, M. De Laurentis, and P. Nicolini. Exotic Compact Objects from Quantum Gravity. Preprint: *https://arxiv.org/abs/2512.01711*.

- [6] O.H.E. Philcox, K. Zhong, and **S. S. Sirletti**. Separating the Inseparable: Constraining Arbitrary Primordial Bispectra with Cosmic Microwave Background Data. Preprint: *https://arxiv.org/abs/2511.19179*

Acknowledgments

The author acknowledges that this this thesis and the publications listed above were produced while attending the PhD program in Space Science and Technology at the University of Trento, Cycle XXXVIII, with the support of a scholarship co-financed by the Ministerial Decree no. 351 of 9th April 2022, based on the NRRP - funded by the European Union - NextGenerationEU - Mission 4 "Education and Research", Component 2 "From Research to Business", Investment 3.3.

Chapter 1

Introduction to Cosmology

Modern Cosmology, understood as a science in its own right, is a relatively young field that began in 1917 when Einstein applied the laws of General Relativity to create the first mathematical model of the Universe [7].

The foundation of all standard cosmological theories is the **cosmological principle**: when viewed on large scales, called **cosmological scales** (beyond 100 Mpc[1]), the Universe appears both homogeneous and isotropic, meaning that the density can be considered spatially constant and without any preferred direction at any given time [8].

The fundamental challenge of cosmology is determining the correct matter-energy density, which governs why and how the Universe evolves based on its content. Following the cosmological principle, matter is generally described through the energy-momentum tensor $T_{\mu\nu}$ of a perfect fluid:

$$T_{\mu\nu} = (\varepsilon + p)u_\mu u_\nu - g_{\mu\nu}p. \tag{1.1}$$

Here, ε is the energy density in the rest frame, p is the fluid's pressure in the rest frame, u_μ represents the fluid's four-velocity, and $g_{\mu\nu}$ is the metric tensor defining the metric $\mathrm{d}s^2 = g_{\mu\nu}\mathrm{d}x^\mu \mathrm{d}x^\nu$ that describes spacetime structure.

The field equations of General Relativity are [9]

$$R_{\mu\nu} - \frac{1}{2}g_{\mu\nu}R = \frac{8\pi G}{c^4}T_{\mu\nu}. \tag{1.2}$$

Here, $R_{\mu\nu}$ is the Ricci tensor, R is the Ricci curvature scalar, G is the universal gravitational constant, and c is the speed of light.

Sometimes the field equations are written in a compact form defining the left hand side as the Einstein tensor $G_{\mu\nu}$ and the constant $8\pi G/c^4$ as χ:

$$G_{\mu\nu} = \chi T_{\mu\nu}. \tag{1.3}$$

Taking the covariant derivative of both sides with respect to x^μ, denoted by $(\cdot)^{;\mu} \equiv \nabla^\mu$ and using the contracted Bianchi identity

$$G^{\mu\nu}{}_{;\nu} = 0, \tag{1.4}$$

one automatically obtains the conservation equation:

$$T^{\mu\nu}{}_{;\nu} = 0. \tag{1.5}$$

Throughout this work, the Einstein summation convention is adopted: repeated indices imply summation over all four spacetime coordinates. The latter is not an independent equation but rather a consistency requirement: the Einstein tensor has vanishing covariant derivative by

[1]Recall that $1\,\mathrm{pc} \sim 3.26\,\mathrm{ly}$.

construction (Bianchi identity), which forces the stress-energy tensor to be covariantly conserved (Liouville equation).

Einstein himself developed the first mathematical model of the Universe using General Relativity. He strongly believed in a static, stationary Universe, and since the field equations are inherently dynamical[2] and would inevitably cause the Universe to contract under gravitational attraction, Einstein introduced a quantity Λ, the **cosmological constant**, to stabilize his equations and obtain a consistent static model. While this model is completely incorrect—empirical evidence shows the Universe is expanding—and mathematically unstable, understanding how Einstein introduced the constant Λ remains historically important. More significantly, if Λ satisfies certain conditions, it can drive the expansion of the Universe rather than stabilize it. The introduction of the cosmological constant was mathematically justified: indeed, adding a term proportional to the metric tensor, $\Lambda g_{\mu\nu}$, preserves the Liouville equation since by definition of covariant derivative ${g_{\mu\nu}}^{;\nu} = 0$.

According to Einstein, Λ represents a perfect fluid with a non-standard equation of state (as will be shown later) permeating the entire Universe that controls expansion or contraction. The effect of Λ becomes significant only on cosmological scales, where it counterbalances gravitational contraction to keep the Universe static.

Later, when compelling evidence emerged that the Universe is undergoing a dynamic of expansion, Einstein famously called Λ *"the greatest mistake of my life."*

Although the static view of the Universe has been completely abandoned in light of overwhelming evidence that our Universe is not only expanding but accelerating in its expansion, the cosmological constant Λ has experienced a renaissance in recent decades. The Λ term now describes a component that mathematically produces accelerated expansion consistent with observational evidence. The field equations including the Λ term are often called **Einstein's equations in complete form**. Since Λ was introduced ad hoc, it can be placed on either side of the equation; its physical interpretation can vary depending on its placement in different cosmological theories, though the interpretation already presented is adopted here.

The complete field equations become

$$\begin{cases} R_{\mu\nu} - \frac{1}{2} g_{\mu\nu} R - \Lambda g_{\mu\nu} = \frac{8\pi G}{c^4} T_{\mu\nu} \\ {T_{\mu\nu}}^{;\nu} = 0, \end{cases} \tag{1.6}$$

where, in contemporary physical cosmology, Λ represents the mathematical term for the component driving the Universe's accelerated expansion—namely, a model of dark energy.

In General Relativity, the equation of motion of a point follows the **geodesic equation**, which corresponds to $\mathbf{F} = m\mathbf{a}$ in classical non-relativistic mechanics:

$$\frac{\mathrm{d}^2 x^\lambda}{\mathrm{d}s^2} + \Gamma^\lambda_{\mu\nu} \frac{\mathrm{d}x^\mu}{\mathrm{d}s} \frac{\mathrm{d}x^\nu}{\mathrm{d}s} = 0, \tag{1.7}$$

where $\Gamma^\lambda_{\mu\nu}$ are the affine connections, known as Christoffel symbols of the second kind, representing the geometric forces on the manifold and defined as

$$\Gamma^\alpha_{\mu\nu} = \frac{1}{2} g^{\alpha\lambda} \left(\frac{\partial g_{\lambda\mu}}{\partial x^\nu} + \frac{\partial g_{\nu\lambda}}{\partial x^\mu} - \frac{\partial g_{\mu\nu}}{\partial x^\lambda} \right). \tag{1.8}$$

1.1 Hubble's Law

In the 1920s, the conception of the Universe changed radically with Edwin Hubble's discoveries. Until then, it was believed that the entire Universe was confined around our galaxy and was static. Other galaxies that were observed, generally called **nebulae**—a name still used today

[2]The field equations are dynamic because they contain second derivatives of the metric (appearing in the Ricci tensor), with the metric components acting as gravitational potentials.

for historical reasons—were considered systems internal to the Milky Way, partly because they appear as simple "little clouds" through telescopes. Hubble discovered that these clusters are actually external to the Milky Way and are comparable in size to it, if not larger. This expanded our conception of the Universe, revealing the existence of billions upon billions of other galaxies beyond our own. This demonstration came from observations of **Cepheids**, stars with time-variable luminosity that follows very regular patterns, allowing the definition of periods of different brightness. By knowing a Cepheid's luminosity period, its **absolute luminosity** can be determined, and from this, by measuring the **luminous flux**, a formula that gives the star's distance can be derived [10]:

$$d = \sqrt{\frac{\mathcal{L}}{4\pi\Phi}} \quad \text{with} \quad \mathcal{L} \propto T^{\alpha}, \tag{1.9}$$

where Φ is the flux measured in $\mathrm{W} \cdot \mathrm{m}^{-2}$, $\mathcal{L}$ is the absolute luminosity measured in W, 4π is the total solid angle in steradians, T is the period measured in days, and $\alpha = 1$ for classical Cepheids.

Hubble measured that the distance to nebula M33 (the Triangulum Galaxy), which contains Cepheids, was much greater than the estimated size of the Milky Way, thus proving that M33 was indeed another galaxy.

Subsequently, Hubble arrived at another startling result: performing spectroscopic measurements on luminous stars in external galaxies, he noticed an absorption of HI lines proportional to distance. The more distant a galaxy, the greater the redshift of its spectrum. Interpreting this as a Doppler effect, Hubble showed that galaxies are receding from us (after removing all other motions from the calculation). The law was constructed by comparing spectroscopic measurements (v) with photometric measurements (d). From the electromagnetic Doppler effect, it is known that for a source receding from the observer ($v > 0$), a parameter z, the **redshift**, can be defined:

$$z = \frac{v}{c} = \frac{\Delta\lambda}{\lambda} = \frac{\Delta\nu}{\nu}, \tag{1.10}$$

which can be measured through the displacement of spectral lines in the object's spectrum, particularly absorption lines. The law that Hubble found, the famous **Hubble's law**, is [10]

$$v = H_0 d \quad \Longleftrightarrow \quad z = \frac{H_0}{c} d, \tag{1.11}$$

where H_0 is a particular constant called the **Hubble constant**, whose physical meaning will be clarified below. It is trivial to see that the Hubble constant has units of inverse time:

$$[H_0] = \mathrm{time}^{-1}, \tag{1.12}$$

and another constant, this time temporal, called the **Hubble time** can thus be defined:

$$t_0 = H_0^{-1}. \tag{1.13}$$

A natural question arises: why is this effect necessarily attributed to the expansion of the Universe rather than to the objects' proper motions? Hubble noticed an extremely peculiar fact: even when all proper motions of bodies are subtracted (approach motions due to gravity, galactic rotation motions, etc.), which generate Doppler redshift, there is always a non-zero redshift implying recession, and this is present for any object observed. Since peculiar motions such as galactic rotation have been eliminated from the calculation, it follows that there is a recession motion that can only be justified in two ways:

1. Earth is located at a special observation point in the Universe from which all galaxies recede from us;

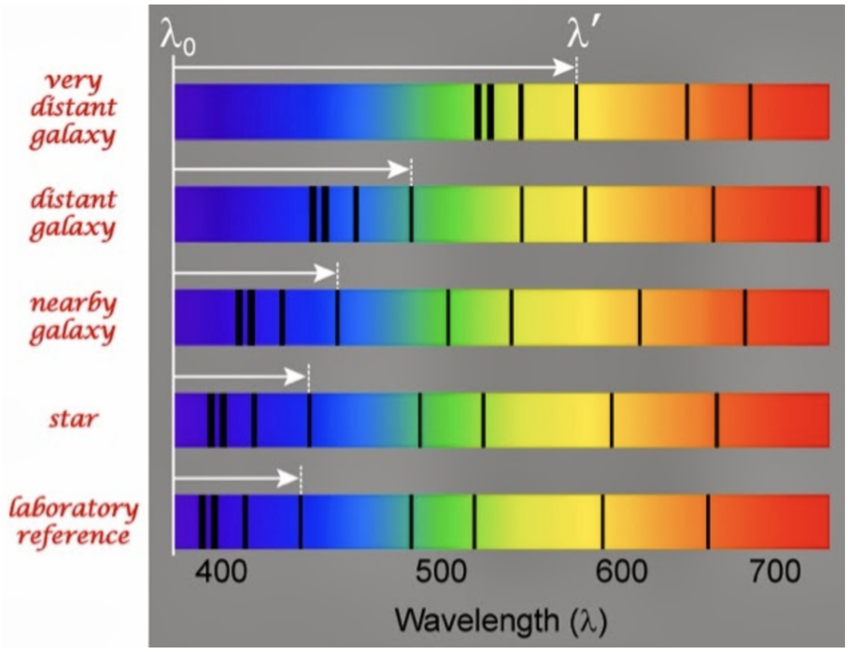

Figure 1.1: Cosmological redshift as a function of distance: the farther a galaxy is, the greater its recession from us and therefore the higher the redshift measured compared to what is expected in the laboratory.

2. The Universe is a four-dimensional manifold in expansion, and galaxies are at rest on this manifold that gradually expands; the recession effect is therefore caused by the expansion of the space in which they lie; light emitted by a galaxy, if the Universe is expanding, will travel through regions of space that are expanding and will undergo redshift, as shown in fig. 1.1.

It is clear that the first hypothesis is so restrictive, unnatural, and highly fine-tuned as to be completely disregarded, making the second interpretation the correct one. It should be specified that this type of redshift is not caused by any gravitational field variation (gravitational redshift phenomenon); in this case, it is the expansion of space that causes redshift, and this is a **cosmological redshift**. This therefore led to a renewed and drastic revision of the human conception of the Universe, obviously causing the collapse of all paradigms according to which the Universe was something that had always existed and was a stationary system. These paradigms already failed to provide exhaustive explanations for what is observed, foremost being the so-called **Olbers' paradox**, which poses the following question, considering the cosmological principle valid: how is it possible that the night sky is dark if the Universe is static, stationary, and has always existed? Indeed, if the Universe had always existed and were finite—the belief held before Hubble's discoveries—then light from outside Earth would have had time to isotropize all of space, such that at night a celestial vault uniformly and isotropically illuminated should be seen. Olbers' paradox is obviously resolved once this new conception of our Universe is adopted: that it is much larger than expected since the Milky Way is just one of billions and billions of galaxies within it, and because the Universe is continuously expanding. Simply put, there are regions of space where light departing from these regions has not even had time to reach Earth; space is so large and continuously expanding that luminous isotropization has not been possible. Obviously, this new vision led to the rejection of physically consistent theories of the Universe that assumed it to be stationary.

A standard cosmological theory must therefore predict:

1. A Universe ruled on large scales by the cosmological principle;

2. A Universe that is not static but expanding, i.e., a *dynamic* expanding system;

3. A Universe that originated at some time (**Big Bang theory** of G. Lemaître).

The metric underlying all cosmological theories is the Friedmann-Lemaître-Robertson-Walker (FLRW) metric [11, 12, 13], constructed to satisfy point 1 (the Cosmological Principle) by design. When this metric is substituted into Einstein's field equations, the resulting solutions describe an evolving Universe with a definite beginning, naturally incorporating points 2 and 3.

1.2 Construction of the FLRW Metric

Having presented Hubble's law, it is essential to understand how the cosmological principle and expansion are connected and how these affect the construction of a metric on which to build a cosmological model consistent with observations.

From the cosmological principle, it is deduced that, given the conditions of homogeneity and isotropy on large scales, the Universe manifold must expand through a **homothety**, a transformation that by definition preserves geometric shape. Furthermore, at a given instant, changing reference frame on this manifold must not affect the metric since, on large scales, every observer sees the Universe in the same way. Thus, at a given instant, the metric must be preserved under changes of reference frame, and therefore the acceptable transformations must inevitably be **isometries**.

Mathematically, a spacetime[3] is said to be spatially homogeneous and isotropic if it can be foliated into a one-parameter family of three-dimensional spacelike hypersurfaces such that, for each fixed t, given two reference systems x and $\tilde{x}$ belonging to the hypersurface, there exists an isometry in space that takes x to $\tilde{x}$. This means that the Universe manifold is viewed as a four-dimensional manifold $\mathcal{M}^4$ decomposed into an infinite series of three-dimensional manifolds that evolve according to a parameter t defined as time. The evolution from manifold to manifold as the parameter t varies therefore represents the expansion of the Universe over time. Since the Universe expands through homotheties, the **global curvature** of the manifold $\mathcal{M}^3$ is conserved and always the same. From what has been said, denoting the direct product with $\times$:

$$\mathcal{M}^4 = \mathcal{M}^3 \times \mathbb{R}. \tag{1.14}$$

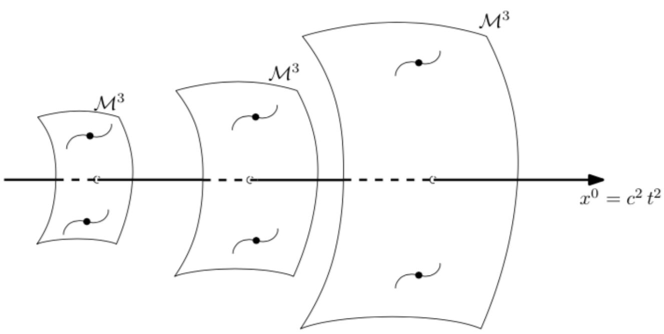

Figure 1.2: Foliation of spacetime. The spatial submanifold $\mathcal{M}^3$ evolves according to a homothety, maintaining constant global curvature. Time is viewed as a parameter that at each "instant" (value) returns a specific 3-manifold $\mathcal{M}^3$.

[3]It should be noted that what is about to be stated is a mathematical theorem valid for any space of any dimension; as always, the discussion refers for convenience to four-dimensional spacetime.

An **isometry** is a transformation that preserves the form of the metric and therefore also distances. Given two reference systems x^α and $\tilde{x}^\alpha$ with respectively $g_{\mu\nu}(x^\alpha)$ and $\tilde{g}_{\mu\nu}(\tilde{x}^\alpha)$, the transformation between the two reference systems is an isometry if and only if the equality holds:

$$\tilde{g}_{\mu\nu}(\tilde{x}^\alpha) = g_{\mu\nu}(\tilde{x}^\alpha). \tag{1.15}$$

The equation that governs and intrinsically defines isometries is called the **Killing equation**:

$$\xi_{\nu;\mu} + \xi_{\mu;\nu} = 0, \tag{1.16}$$

where ξ^μ is the connection vector between two very close reference systems:

$$\tilde{x}^\alpha = x^\alpha + \varepsilon \xi^\alpha(x), \tag{1.17}$$

with $\varepsilon << 1$.

Therefore, in conclusion, the form of the connection vector ξ, also called the **Killing vector**, together with the Killing equation, determines the isometries of the metric by imposing additional constraints on the form of $g_{\mu\nu}$. More precisely, when any isometry is assumed for the metric, the corresponding Killing vector and its equation must be considered, which impose additional conditions on how the metric should be constructed—namely, the isometry conditions.

In appendix A.1, all calculations leading to eq. (1.16) starting from imposing an isometry (1.15) between two reference systems connected through (1.17) are presented.

The manifold $\mathcal{M}^3$ therefore undergoes expansion, a homothety, as the parameter varies. At a fixed instant, due to the cosmological principle and because the Universe is observed as a whole, the metric is preserved at every point of the manifold: the transformation from one point to another of the manifold $\mathcal{M}^3$ is an isometry. Mathematically, all this is called **foliation** of spacetime. A representation of the foliation is shown in fig. 1.2.

It is therefore necessary to find the metric, or rather the class of metrics, that is consistent with observations—one that agrees with Hubble's law on expansion and respects the isometries connected to the cosmological principle.

The reference system usually adopted is the system of **comoving coordinates** where the matter of the Universe (and therefore each observer) is stationary with respect to these coordinates, even though there is expansion. As the Universe expands, it causes two observers to move apart, but the comoving coordinate system moves with the expansion, so in these coordinates stationarity is maintained[4]. Figure 1.3 shows how the geographical coordinates of meridians and parallels, being the same if the sphere expands, are coomoving cordinates. Imposing the comoving coordinate system simplifies calculations: two observers in these coordinates are spatially at rest and move only along time. This ensures that all observers on the manifold are equivalent, and therefore no privileged observation points of the Universe exist; isotropy is respected. It should be noted that comoving coordinates are nothing other than the usual Lagrangian fluid dynamics coordinates. Since the relative position in the comoving coordinate system between two galaxies (two observers) does not change, and at the same time the expansion of the Universe will cause the distance between them to increase anyway, the comoving coordinate system ensures that expansion appears not as a change in relative position between the two observers, but as a change in the spatial part of the metric.

[4] An example is the Earth with a coordinate system of meridians and parallels: supposing the Earth expands by homothety (the radius gradually increases), the distance between two points changes, but the meridian+parallel coordinate system expands with the Earth, so two points, even though they will be at a greater distance after expansion, will always remain at the same coordinates as before. In practice, an observer at Greenwich and an

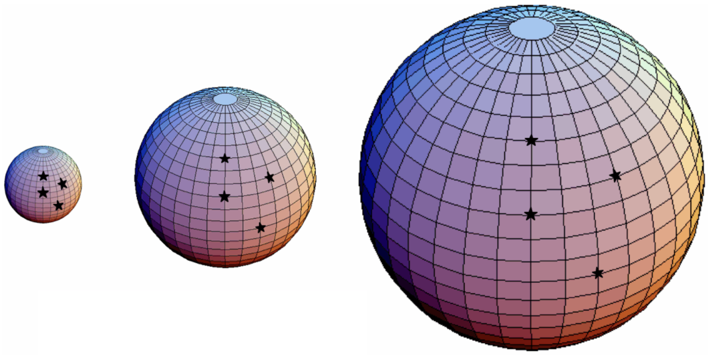

Figure 1.3: Example of comoving coordinates on a sphere; expansion does not change the coordinates of points.

From these considerations, the form of the metric can be constructed, which in Cartesian coordinates is:

$$\mathrm{d}s^2 = g_{\mu\nu}\mathrm{d}x^\mu \mathrm{d}x^\nu = c^2\mathrm{d}t^2 - A(r,t)[\mathrm{d}x^2 + \mathrm{d}y^2 + \mathrm{d}z^2]. \tag{1.18}$$

Isotropy ensures the complete diagonality of the metric, while homogeneity ensures the equality $g_{11} = g_{22} = g_{33}$. The factor $A(r,t)$ depends on time because, as already discussed, it must contain information regarding the expansion of the Universe, and this must be attributed solely to a variation of the spatial part through a multiplicative factor. Homogeneity and isotropy automatically impose, since $g_{0k} = 0\,\forall\, k$, the synchronization of clocks in coordinate time. Furthermore, since spacetime is the same for every observer, g_{00} will be equal at every point and for every observer. This allows one to state that physical time flows equally in all reference frames, i.e., all observers are synchronized with each other, measuring the flow of time in the same way. Moreover, since g_{00} is constant, it can be set equal to 1 for simplicity, as was done. These properties indeed allow the identification of a **cosmological time scale** that is the same for every observer in the Universe, and it is understood that the coordinate system adopted is a synchronous reference frame. The foliation of spacetime also allows the factorization of $A(r,t)$ into a part depending only on time, called the **scale factor** $a(t)$, and one depending only on space, called the **form factor** $F(r)$:

$$A(r,t) = a^2(t)F(r); \tag{1.19}$$

the evolution of the scale factor $a(t)$ contains information about the temporal evolution of the Universe, i.e., about expansion; the factor $F(r)$ determines the topology at fixed time—a topology that cannot change due to homothetic expansion.

It is thus derived that the form of the FLRW metric is given by:

$$\mathrm{d}s^2 = c^2\mathrm{d}t^2 - a^2(t)F(r)[\mathrm{d}x^2 + \mathrm{d}y^2 + \mathrm{d}z^2], \tag{1.20}$$

or equivalently in spherical coordinates:

$$\mathrm{d}s^2 = c^2\mathrm{d}t^2 - a^2(t)F(r)[\mathrm{d}r^2 + r^2\mathrm{d}\Omega^2] = c^2\mathrm{d}t^2 - a^2(t)F(r)[\mathrm{d}r^2 + r^2\mathrm{d}\vartheta^2 + r^2\sin^2\vartheta\mathrm{d}\varphi^2]. \tag{1.21}$$

Since every transformation at fixed time must be an isometry, the Killing equation of isometries (1.16) will return the factor $F(r)$: the isometries, by imposing strong restrictions on the metric, provide the geometry at fixed times. The expansion dictated by $a(t)$ is due to dynamics, and therefore the equations that determine the temporal evolution of the scale factor will be Einstein's field equations.

observer in Rome will respectively always be at the first meridian (0° E) and the second meridian (15° E).

Starting from the Killing eq. (1.16), as shown in appendix A.2, it is possible to obtain:

$$F(r) = \frac{1}{\left(1 + \frac{k}{4}r^2\right)^2} \quad \text{with} \quad k = -1, 0, 1. \tag{1.22}$$

The **Friedmann-Lemaître-Robertson-Walker FLRW metric** [11, 12, 13] is thus obtained:

$$\mathrm{d}s^2 = c^2\mathrm{d}t^2 - \frac{a^2(t)}{\left(1 + \frac{k}{4}r^2\right)^2}[\mathrm{d}r^2 + r^2\mathrm{d}\vartheta^2 + r^2\sin^2\vartheta\mathrm{d}\varphi^2]. \tag{1.23}$$

With a coordinate change of the form:

$$\bar{t} = t\,, \quad \bar{r} = \frac{r}{1 + \frac{k}{4}r^2}\,, \quad \bar{\vartheta} = \vartheta \quad \text{and} \quad \bar{\varphi} = \varphi, \tag{1.24}$$

which further rescales r, calculating

$$\mathrm{d}\bar{r} = \frac{1 - \frac{k}{4}r^2}{\left(1 + \frac{k}{4}r^2\right)^2}\mathrm{d}r$$

and showing that

$$\frac{\mathrm{d}\bar{r}^2}{1 - k\bar{r}^2} = \frac{\mathrm{d}r^2}{\left(1 + \frac{k}{4}r^2\right)^2},$$

the FLRW metric can be rewritten in a much more convenient form, called the **standard form of the FLRW metric**:

$$\mathrm{d}s^2 = c^2\mathrm{d}t^2 - a^2(t)\left[\frac{\mathrm{d}r^2}{1 - kr^2} + r^2\mathrm{d}\Omega^2\right]. \tag{1.25}$$

It should be noted that the metric found, in agreement with Killing, does not represent a single metric, but rather *a class of metrics* as $a(t)$ and k vary.

It can be shown that k represents the **topology of the Universe** spatially, i.e., the spatial **global curvature**:

- If $k = 1 \Rightarrow$ spatially spherical Universe ($\mathcal{M}^3$ is a sphere);
- If $k = 0 \Rightarrow$ spatially flat Universe ($\mathcal{M}^3$ is flat);
- If $k = -1 \Rightarrow$ spatially hyperbolic Universe ($\mathcal{M}^3$ is hyperbolic);

note the use of the term *spatially*: this means that it is the spatial part of the manifold that is topologically flat, spherical, or hyperbolic, precisely as specified in parentheses, and not the entire four-dimensional spacetime manifold. In fig. 1.4 the three kinds of curvature of the Universe are shown.

It is therefore established that $a(t)$ gives the dynamics (connected with geometry) of the Universe, and will be given by solving the gravitational field equations imposing this metric; k instead is connected with the amount of matter because it is connected with curvature.

1.3 The Cosmological Equations

The dynamics of the Universe is governed by Einstein's equation eq. (1.6) and parametrized through the scale factor $a(t)$. From its evolution in time, it will be seen that a different evolution of $a(t)$ represents a different temporal evolution of the Universe. Moreover, the scales are so large that the Universe is considered to have constant density at every point due to homogeneity and isotropy. The method for solving the field equations is almost identical to that developed

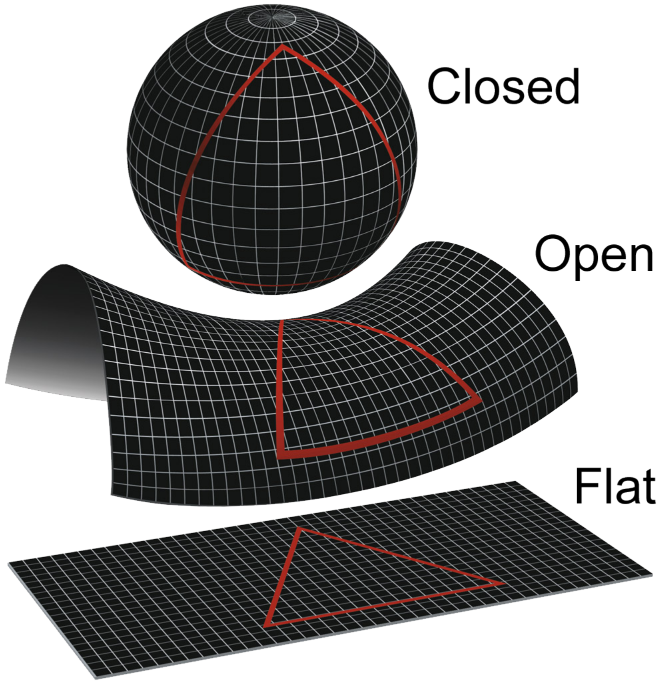

Figure 1.4: The different shapes of the Universe according to k.

by Schwarzschild [14]: knowing the form of the metric, one works on the l.h.s. of Einstein's equations by calculating the Ricci tensor and Ricci scalar, and the r.h.s. by calculating the form of $T_{\mu\nu}$. The components of $R_{\mu\nu}$ are obtained by computing the Christoffel symbols, and these can be found by writing the point Lagrangian, computing the Euler-Lagrange equations and comparing them with the geodesic equations since they must necessarily be equal (Maupertuis' principle).

Since the equations and everything else are valid even for very small r and should not depend on it (as the expansional dynamics is not characterized by where the observer is located), for simplicity the observer is placed in a neighborhood of $r = 0$, i.e., for $r \to 0$. In this limit we have

$$\text{For} \quad r \to 0 \quad \Longrightarrow \quad \frac{1}{\left(1 + \frac{k}{4}r^2\right)^2} \simeq \left(1 - \frac{k}{2}r^2\right) + O(r^4), \tag{1.26}$$

which implies that very close to the origin the metric is well approximated by

$$\text{For} \quad r \to 0 \quad \Longrightarrow \quad \mathrm{d}s^2 = c^2\mathrm{d}t^2 - a^2(t)\left(1 - \frac{k}{2}r^2\right)[\mathrm{d}x^2 + \mathrm{d}y^2 + \mathrm{d}z^2]. \tag{1.27}$$

Starting from the $g_{\mu\nu}$ components and working with the definition eq. (1.8), it is possible to derive all the Christoffel symbols. Subsequently, using the definition of the Ricci tensor written in terms of these and their derivatives, $R_{\mu\nu}$ can be found and then, by contraction, R. In this way the left-hand side of the field equations is determined.

The calculation of the Christoffel symbols and the components of the Ricci tensor, and the Ricci scalar are presented in appendix B. The results are:

$$R_{00} = -\frac{3}{c^2}\frac{\ddot{a}}{a}, \tag{1.28}$$

$$R_{11} = R_{22} = R_{33} = \frac{a^2}{c^2}\left[\frac{\ddot{a}}{a} + \frac{2\dot{a}^2}{a^2} + \frac{2kc^2}{a^2}\right], \tag{1.29}$$

and consequently the Ricci scalar

$$R = -\frac{6}{c^2}\left[\frac{\ddot{a}}{a} + \left(\frac{\dot{a}}{a}\right)^2 + \frac{kc^2}{a^2}\right]. \tag{1.30}$$

Having now found the left-hand side of Einstein's equations, the energy-momentum tensor that describes the matter fluid must be found. The fluid is considered perfect and therefore the energy-momentum tensor will be in the form eq. (1.1). Since the reference system is comoving with the expansion of the Universe and it by definition moves with the expansion, then in this reference system the matter fluid (representing galaxies, observers and everything) is stationary. Since the fluid is comoving with the expansion and therefore stationary, i.e., at rest with respect to the spatial coordinates, the components of the 3-velocity are zero, while in time obviously u^0 is generally non-zero:

$$\begin{cases} u^0 \neq 0 \\ u^k = 0 \quad \forall \quad k = 1, 2, 3. \end{cases} \tag{1.31}$$

It is known that $u_\alpha u^\alpha = 1$ (normalization condition for the four-velocity of massive particles) and from it $g_{\alpha\beta}u^\alpha u^\beta = 1$ which transforms, since $u^k = 0$, into $g_{00}u^0 u^0$ and therefore implies

$$u^0 = \frac{1}{\sqrt{g_{00}}}. \tag{1.32}$$

In the FLRW metric the chronology is imposed such that $\mathrm{d}\tau = \mathrm{d}t$ and therefore such that $g_{00} = 1$, so that the result obtained is $u^0 = 1$ and thus in complete form

$$u^\alpha = (1, 0, 0, 0) = u_\alpha. \tag{1.33}$$

It is then trivial to calculate the various components of the energy-momentum tensor in this case: from the form of the metric and the components of the four-velocity, it is immediately clear that the energy-momentum tensor has a diagonal matrix representation.

Immediately we have

$$T^{00} = (\varepsilon + p)u^0 u^0 - pg^{00} = \varepsilon + p - p = \varepsilon; \tag{1.34}$$

then

$$T^{11} = T^{22} = T^{33} = (\varepsilon + p)u^1 u^1 - pg^{11} = -pg^{11} = p\frac{\left(1 + \frac{k}{4}r^2\right)^2}{a^2}$$

having remembered that $g^{11} = 1/g_{11}$. From here

$$T^1{}_1 = T^2{}_2 = T^3{}_3 = g_{11}T^{11} = -p, \tag{1.35}$$

and therefore

$$T^\alpha{}_\beta = \mathrm{diag}(\varepsilon, -p, -p, -p). \tag{1.36}$$

The trace is clearly

$$T = \varepsilon - 3p. \tag{1.37}$$

We are now ready to develop the field eq. (1.6). Knowing T, the calculation is very simple if the mixed form of the equations is used:

$$R^\alpha{}_\beta - \Lambda\delta^\alpha_\beta = \chi\left(T^\alpha{}_\beta - \frac{1}{2}\delta^\alpha_\beta T\right). \tag{1.38}$$

It should be recalled that the only two equations that matter are for $R^0{}_0$ and $R^1{}_1$.

- The first equation, for ${R^0}_0$, is

$$ {R^0}_0 - \Lambda = \chi\left({T^0}_0 - \frac{1}{2}T\right). \tag{1.39} $$

Substituting all the expressions found previously:

$$ -\frac{3}{c^2}\frac{\ddot{a}}{a} - \Lambda = \frac{8\pi G}{c^4}\left(\varepsilon - \frac{\varepsilon}{2} + \frac{3p}{2}\right) $$

$$ \Downarrow $$

$$ \frac{\ddot{a}}{a} = -\frac{4\pi G}{3c^2}(\varepsilon + 3p) + \frac{\Lambda c^2}{3}. \tag{1.40} $$

- The second equation, for ${R^1}_1$, is instead

$$ {R^1}_1 - \Lambda = \chi\left({T^1}_1 - \frac{1}{2}T\right). \tag{1.41} $$

Substituting all the expressions found:

$$ -\frac{1}{c^2}\left[\frac{\ddot{a}}{a} + 2\frac{\dot{a}^2}{a^2} + \frac{2kc^2}{a^2}\right] - \Lambda = \chi\left(-p - \frac{1}{2}\varepsilon + \frac{3}{2}p\right), $$

and also substituting the equation found in the previous point, with some algebraic steps we have

$$ \left(\frac{\dot{a}}{a}\right)^2 + \frac{kc^2}{a^2} - \frac{\Lambda c^2}{3} = \frac{8\pi G}{3c^2}\varepsilon. \tag{1.42} $$

Finally, it is recalled that Einstein's system of equations has as a gauge constraint that the covariant derivative of the energy-momentum tensor must vanish, eq. (1.6). Thanks to the contracted Bianchi's identity eq. (1.4) the gauge constraint can be written as

$$ {T_\alpha}^\beta{}_{;\beta} = 0, \tag{1.43} $$

given also that both the energy-momentum tensor and the metric in this case are symmetric and therefore

$$ {T^\alpha}_\beta = {T_\alpha}^\beta = {T^\beta}_\alpha. \tag{1.44} $$

In this case it is possible to use a formula for the covariant derivative that is very convenient for calculations:

$$ {T_\alpha}^\beta{}_{;\beta} = \frac{1}{\sqrt{-g}}\frac{\partial}{\partial x^\sigma}(\sqrt{-g}{T^\sigma}_\beta) - \frac{1}{2}g_{\mu\nu,\alpha}T^{\mu\nu}; \tag{1.45} $$

Given the cosmological principle that imposes uniformity, it is clear that ε and p can only depend on time and therefore the only non-trivial component of ${T_\alpha}^\beta{}_{;\beta}$ is ${T_0}^0{}_{;0}$:

$$ {T_0}^0{}_{;0} = \frac{1}{\sqrt{-g}}\frac{\partial}{\partial x^0}(\sqrt{-g}{T^0}_0) - \frac{1}{2}g_{\mu\nu,0}T^{\mu\nu}, \tag{1.46} $$

where the sum over σ has also been reduced to only the term ${T^0}_0$ since all the others are zero. The only gauge equation is then

$$ {T_0}^0{}_{;0} = 0 \tag{1.47} $$

which corresponds to energy conservation since the 00 component of the tensor is the energy component.

The first and second terms of this equation are developed in order: the first term, substituting all the values found previously, is

$$\frac{1}{\sqrt{-g}}\frac{\partial}{\partial x^0}(\sqrt{-g}T^0_{\ 0}) = \frac{\left(1+\frac{k}{4}r^2\right)^3}{a^3}\frac{1}{c}\frac{\partial}{\partial t}\left[\frac{a^3}{\left(1+\frac{k}{4}r^2\right)^3}\varepsilon\right];$$

the second term instead is

$$g_{\mu\nu,0}T^{\mu\nu} = g_{00,0}T^{00} + g_{11,0}T^{11} + g_{22,0}T^{22} + g_{33,0}T^{33},$$

and, since $g_{00,0} = 0$ because $g_{00} = 1$, $g_{11} = g_{22} = g_{33}$ and $T^{11} = T^{22} = T^{33}$, it reduces to

$$g_{\mu\nu,0}T^{\mu\nu} = 3g_{11,0}T^{11} = \frac{3}{c}\frac{\partial}{\partial t}\left[-\frac{a^2}{\left(1+\frac{k}{4}r^2\right)^2}\right]p\frac{\left(1+\frac{k}{4}r^2\right)^2}{a^2}.$$

Placing ourselves also in the neighborhood of the origin, i.e., for $r \to 0$, the equation becomes

$$r \to 0 \quad \Rightarrow \quad T_0{}^0{}_{;0} = \frac{1}{a^3}\frac{\partial}{\partial t}[a^3\varepsilon] + \frac{3}{2}p\frac{1}{a^2}\frac{\partial(a^2)}{\partial t} = 0, \tag{1.48}$$

and, differentiating and performing trivial algebraic steps, the energy conservation equation is found:

$$\dot{\varepsilon} + 3\left(\frac{\dot{a}}{a}\right)(p+\varepsilon) = 0. \tag{1.49}$$

This equation is the energy conservation equation that derives from the gauge condition (1.6) and is therefore one of the cosmological equations. It is necessary to point out that this equation is not independent with respect to the others, being the conservation equation a consistency requirement arising from the field equations, as demonstrated in eq. (1.5).

Ultimately, Einstein's complete field equation system (1.6) reduces to the following system when considering the FLRW metric:

$$\begin{cases} \left(\frac{\dot{a}}{a}\right)^2 + \frac{kc^2}{a^2} = \frac{8\pi G}{3c^2}\varepsilon + \frac{\Lambda c^2}{3} \\ \frac{\ddot{a}}{a} = -\frac{4\pi G}{3c^2}(\varepsilon + 3p) + \frac{\Lambda c^2}{3} \\ \dot{\varepsilon} + 3\left(\frac{\dot{a}}{a}\right)[p+\varepsilon] = 0 \end{cases} \tag{1.50}$$

This system, often called the **Friedmann equation system**, characterizes the **standard cosmological model** and its equations are called **cosmological equations**. The system provides precisely the expansional dynamics of the Universe as it returns a, its acceleration $\ddot{a}$ and its velocity $\dot{a}$.

In order to solve the cosmological equations system, a last equation connecting the pressure and the energy-density, a **equation of state (EoS)**, must be *added by hand*:

$$p = w\varepsilon \tag{1.51}$$

Its inclusion is necessary to make the system solvable: without it, there would be two independent equations for three unknown parameters (a, ε, p), and the system would be underdetermined. In other words, to obtain a solution one must provide physical knowledge, in this case the relation between pressure and energy density. Generally, the EoS is an expression which relates p with ε and its derivative with respect to the time $\dot{\varepsilon}$, i.e., $p = p(\varepsilon, \dot{\varepsilon})$. The simplest choice is a linear dependence between p and ε. The constant w is known as the **equation-of-state parameter** (or **adiabatic index**). For standard matter, w lies in the **Zeldovich interval** $[0, 1]$ [15], which arises from the causality requirement that the speed of sound in a medium c_s cannot exceed the speed of light. The relation between w and the sound speed is given by

$$c_s^2 = c^2 \frac{\mathrm{d}p}{\mathrm{d}\varepsilon}, \tag{1.52}$$

which implies

$$w = \left(\frac{c_s}{c}\right)^2. \tag{1.53}$$

Since causality requires $c_s \leq c$, we obtain $w \leq 1$. For non-standard forms of matter such as dark energy, w can extend to negative values, with the physically motivated range being

$$w \leq 1. \tag{1.54}$$

As lower bound it is possible to set $w = -1$ corresponding to a cosmological constant. Lower values, $w < -1$, would describe phantom energy, leading to a catastrophic "Big Rip" scenario where the universe's accelerated expansion eventually tears apart all matter and spacetime [16].

Representative values for different matter types are:

- dust (non-relativistic matter): $w = 0$,
- radiation: $w = \frac{1}{3}$,
- stiff matter: $w = 1$,
- cosmological constant (dark energy): $w = -1$.

Historically the system assumes $\Lambda = 0$ but today, as already discussed at the beginning of the chapter, $\Lambda \neq 0$ is considered because a Universe in accelerated expansion is observed and therefore there is something that accelerates it [17]. Λ represents the correction due to this energy whose nature is not yet known, generally called **dark energy**. It should be noted that if $p > 0$ also $\varepsilon > 0$ and this implies that $\ddot{a} < 0$ if $\Lambda = 0$, while the opposite is found and therefore the insertion of the cosmological constant is necessary.

The vast majority of cosmological models, although very advanced, can be traced back, once the equations are rewritten in the appropriate form, to the standard cosmological model. The standard cosmological model can vary fundamentally by changing the fluid and equation of state, but otherwise the model equations are in agreement with observations.

1.4 Friedmann Models

From the system of cosmological equations eq. (1.50), the last equation can first be taken and substituted into the third, obtaining

$$\dot{\varepsilon} + 3\left(\frac{\dot{a}}{a}\right)[1+w]\varepsilon = 0, \tag{1.55}$$

which, dividing both members by ε, becomes

$$\frac{\dot{\varepsilon}}{\varepsilon} + 3\left(\frac{\dot{a}}{a}\right)[1+w] = 0. \tag{1.56}$$

This equation is clearly a separable variables equation:

$$\frac{\mathrm{d}\varepsilon}{\varepsilon \mathrm{d}t} = -3(1+w)\frac{\mathrm{d}a}{a\mathrm{d}t} \quad \Rightarrow \quad \ln\frac{\varepsilon}{\varepsilon_0} = -3(1+w)\ln\frac{a}{a_0}$$

and therefore

$$\frac{\varepsilon}{\varepsilon_0} = \left(\frac{a}{a_0}\right)^{-3(1+w)} \implies \varepsilon = \frac{\varepsilon_0 a_0^{3(1+w)}}{a^{3(1+w)}}, \tag{1.57}$$

which can be written much more conveniently as

$$\varepsilon \sim \frac{1}{a^{3(1+w)}}; \tag{1.58}$$

this equation indicates that $a(t)$, and thus the evolution of the Universe, is determined by w and ε, i.e., precisely by the type of fluid being considered. From this, it is understood that the evolution of the Universe can be studied through different epochs, where in each of them a different type of matter/fluid is dominant over the others and governs the evolution. Since $\varepsilon = \rho c^2$, one can write

$$\frac{\varepsilon}{\varepsilon_0} = \frac{\rho}{\rho_0}, \tag{1.59}$$

leading to a rewrite of the equation:

$$\rho \sim \frac{1}{a^{3(1+w)}}, \tag{1.60}$$

which further indicates that the scale factor evolves like energy and mass.

Now the second equation of the system is taken and rewritten in terms of ρ:

$$\left(\frac{\dot{a}}{a}\right)^2 = \frac{8\pi G}{3}\rho, \tag{1.61}$$

and into it the form of ρ written in terms of ρ_0 and a_0 can be substituted:

$$\left(\frac{\dot{a}}{a}\right)^2 = \frac{8\pi G \rho_0}{3}\left(\frac{a_0}{a}\right)^{3(1+w)}; \tag{1.62}$$

for convenience, everything is grouped into a constant:

$$\left(\frac{\dot{a}}{a}\right)^2 = \frac{c_0}{a^{3(1+w)}} \quad \text{with} \quad c_0 = \frac{8\pi G \rho_0}{3} a_0^{3(1+w)}. \tag{1.63}$$

From the equation just written it is derived that

$$(\dot{a})^2 = \frac{c_0}{a^{3w+1}}, \tag{1.64}$$

the square root is taken, also defining $\tilde{c}_0 = \sqrt{c_0}$, and obviously the positive solution is taken because an expansion of the Universe is desired, not a contraction:

$$\dot{a} = \frac{\tilde{c}_0}{a^{\frac{3w+1}{2}}}; \tag{1.65}$$

solving the equation

$$\dot{a} a^{\frac{3w+1}{2}} = \tilde{c}_0 \quad \Rightarrow \quad a^{\frac{3w+1}{2}} \mathrm{d}a = \tilde{c}_0 \mathrm{d}t,$$

and integrating immediately

$$a^{\frac{3}{2}(w+1)} = \tilde{c}_0 t + b,$$

where in b all the integration constants are grouped and $\tilde{c}_0$ has been redefined; for $\tilde{c}_0$, as will be seen shortly, only the unit of measurement will matter and therefore this definition, since w is dimensionless, will not affect the calculations. Assuming the Big Bang theory to be valid, at $t = 0$ the scale factor was $a(t) = 0$, which implies that $b = 0$, so that then

$$a^{\frac{3}{2}(w+1)} = \tilde{c}_0 t. \tag{1.66}$$

Taking up c_0 again for a moment, its part $\frac{8\pi G\rho}{3}$ has units

$$\frac{\mathrm{N}\cdot\mathrm{m}^2}{\mathrm{kg}^2}\frac{\mathrm{kg}}{\mathrm{m}^3}=\frac{\mathrm{N}}{\mathrm{m}\cdot\mathrm{kg}}=\frac{\mathrm{m}\cdot\mathrm{kg}}{\mathrm{m}\cdot\mathrm{s}^2\cdot\mathrm{kg}}=\frac{1}{\mathrm{s}^2},$$

so the units of c_0 are

$$[c_0]=\frac{1}{\mathrm{time}^2}[a_0^{3(1+w)}]\quad\Rightarrow\quad[\tilde{c}_0]=\frac{1}{\mathrm{time}}[a_0^{\frac{3(1+w)}{2}}];$$

from these considerations another very important one can be drawn: the factor $\tilde{c}_0$ can be seen as

$$\tilde{c}_0=\frac{a_0^{\frac{3}{2}(w+1)}}{t_0}\tag{1.67}$$

and this therefore allows rewriting

$$a^{\frac{3}{2}(w+1)}=\frac{a_0^{\frac{3}{2}(w+1)}}{t_0}t\quad\Longrightarrow\quad\frac{a}{a_0}=\left(\frac{t}{t_0}\right)^{\frac{2}{3(w+1)}},\tag{1.68}$$

which further implies

$$a(t)=\tilde{a}_0 t^{\frac{2}{3(w+1)}}\quad\text{with}\quad\tilde{a}_0=\frac{a_0}{t_0^{2/3(w+1)}};\tag{1.69}$$

t_0, as will be seen, is interpreted as the **present time**, or rather it is the cosmological time elapsed since physical measurements in the Universe could begin.

The function

$$H(t)=\frac{\dot{a}}{a},\tag{1.70}$$

is defined, which is therefore the growth rate that varies with time. Calling this parameter H is not accidental since physically it represents the expansion and is therefore connected with Hubble's constant H_0. H is called the **Hubble function**. It will be shown later that H_0 is nothing other than the Hubble function calculated at the present time. The second equation of the system is therefore rewritten, in the simple case where $k=0$ and $\Lambda=0$, as

$$H^2=\frac{8\pi G}{3c^2}\varepsilon.\tag{1.71}$$

From the solutions found, since

$$a\propto t^{\frac{2}{3(1+w)}}\quad\Longrightarrow\quad\dot{a}\propto\frac{2}{3(w+1)}t^{-\frac{1+3w}{3(1+w)}},\tag{1.72}$$

then with a simple ratio it is found that

$$H=\frac{2}{3(1+w)t}.\tag{1.73}$$

H therefore has units s^{-1} and the only physical observable that has the same units is Hubble's constant; it is therefore established that

$$H_0=\frac{2}{3(1+w)t_0},\tag{1.74}$$

where t_0, from Hubble's law, is precisely the time since the galaxies were all at the same position and began to recede: that is, what is called the **age of the observable Universe**. Thanks to the fact that H_0 is a measurable observable and

$$t_0=\frac{2}{3(1+w)H_0};\tag{1.75}$$

with current available data, it is measured that

$$t_0 \sim 13.8\,\mathrm{Gyr}; \tag{1.76}$$

this time is called the **age of the observable Universe**; obviously the reported value is measured with appropriate corrections to the standard cosmological model.

Returning to the discussion, taking up the second equation of the system written as a function of ρ, the behavior of matter density as a function of time can also be derived:

$$\left(\frac{\dot{a}}{a}\right)^2 = \frac{8\pi G}{3}\rho \quad \Rightarrow \quad \rho = \frac{3}{8\pi G}H^2, \tag{1.77}$$

and, substituting $H(t)$, it is found that

$$\rho = \frac{3}{8\pi G}\left[\frac{4}{9(1+w)^2 t^2}\right] = \frac{1}{6\pi G(1+w)^2}\frac{1}{t^2}, \tag{1.78}$$

showing how density decreases with time, whatever the type of perfect matter being considered.

In summary, in the simple case where $k = 0$ and $\Lambda = 0$ (**Friedmann models**) the cosmological equations become

$$\begin{cases} \frac{a}{a_0} = \left(\frac{t}{t_0}\right)^{\frac{2}{3(w+1)}} \\ \frac{\rho}{\rho_0} = \left(\frac{a_0}{a}\right)^{3(1+w)} \\ H = \frac{2}{3(1+w)t} \\ \rho = \frac{1}{6\pi G(1+w)^2 t^2} \end{cases} . \tag{1.79}$$

Given the various values of w, the various epochs of evolution are distinguished, where a given epoch is characterized by a specific matter fluid predominant over the others. The simplest cases, as already mentioned, are:

- **Matter-dominated epoch:** Universe dominated by incoherent dust without interaction and with zero pressure, i.e., baryonic matter that is now observed. Since $p = 0$ then obviously

  $$w = 0. \tag{1.80}$$

  Substituting into the results found gives:

  $$\begin{cases} a \sim t^{2/3} \\ \rho \sim a^{-3} \\ H \sim \frac{2}{3t} \\ \rho = \frac{1}{6\pi G t^2} \end{cases} . \tag{1.81}$$

  Note however that $a \sim t^{2/3}$ implies, since $\frac{2}{3} < 1$, that $\ddot{a} < 0$, in sharp contrast with what is observed. Therefore, such an epoch is not current. There is thus a need to introduce Λ in order to obtain an epoch where dark energy is predominant and accelerates the expansion of the Universe, $\ddot{a} > 0$.

- **Radiation-dominated epoch**: case where the Universe is dominated by a relativistic fluid (photons and neutrinos). From the laws of thermodynamics, particularly Stefan-Boltzmann's law for black body radiation, it can be found that

  $$w = \frac{1}{3}. \tag{1.82}$$

In this condition therefore

$$\begin{cases} a \sim t^{1/2} \\ \rho \sim a^{-4} \\ H \sim \frac{1}{2t} \\ \rho = \frac{1}{32\pi G t^2} \end{cases} . \tag{1.83}$$

- **Stiff matter-dominated Universe**: the Universe is dominated by a rigid relativistic fluid; this occurred in primordial epochs, for example when matter was all in the form of quarks. In this case it is found that

$$w = 1. \tag{1.84}$$

In this condition therefore

$$\begin{cases} a \sim t^{1/3} \\ \rho \sim a^{-6} \\ H \sim \frac{1}{3t} \\ \rho = \frac{1}{24\pi G t^2} \end{cases} . \tag{1.85}$$

1.5 Cosmological Redshift

Since the Universe is a dynamic system in expansion, and light has finite velocity, it is very difficult to introduce a chronology for its evolution, just as at large distances, i.e., cosmological ones, the very concept of distance becomes very ambiguous. It therefore becomes necessary from a practical point of view to search for a parameter that is convenient for uniquely defining cosmological epochs. The redshift parameter, which is defined empirically from Hubble's law, or mathematically from the FLRW metric, is precisely that parameter that can be used for this purpose. Indeed, taking into account that objects at the same redshift are at the same distance and at the same cosmological epoch, the problem of measurements is solved precisely thanks to this parameter. Furthermore, its introduction also allows the introduction of a chronology. Figure 1.5 shows how the expansion generates a redshift.

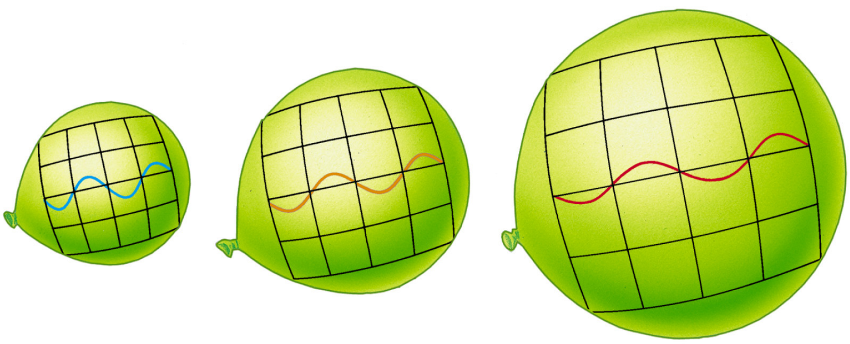

Figure 1.5: Cosmological redshift viewed through comoving coordinates and expansion.

Let us then consider the FLRW metric in its general form of eq. (1.25) and consider that the celestial body emits a ray of light. The spacetime path of light is $\mathrm{d}s^2 = 0$ and from homogeneity and isotropy, since the light ray is observed from Earth without any angular displacement, it can be written that

$$\mathrm{d}s^2 = c^2\mathrm{d}t^2 - a^2(t)F(r)\mathrm{d}r^2 = 0. \tag{1.86}$$

Introducing the cosmological redshift parameter z as the relative difference between the wavelength at emission and reception, or also as the same difference in frequency,

$$z = \frac{\lambda_0 - \lambda_1}{\lambda_1} = \frac{\nu_1 - \nu_0}{\nu_0}, \tag{1.87}$$

if eq. (1.86) is solved, it is possible to connect this redshift parameter to the evolution of the Universe, in particular $z+1$ will represent the ratio of the scale factor at the two different times of emission and reception:

$$z + 1 = \frac{a(t_0)}{a(t_1)} \quad \Rightarrow \quad z = \frac{a(t_0)}{a(t_1)} - 1. \tag{1.88}$$

Therefore, looking at objects at a certain redshift, one is looking at different cosmic epochs when the Universe was smaller. Using redshift, there are no problems with time measurements since this is a quantity that can be measured experimentally and directly, unlike time which cannot be measured directly. So, as anticipated, cosmological redshift is an excellent parameter that can be substituted for time in observations. If, for example, an object is observed at $z = 2$, it means that at t_1 the volume of the Universe was 3 times smaller than the current one.

Furthermore, it is customary to normalize to one the value of $a(t_0)$ so that

$$a(t_0) = 1 \quad \Rightarrow \quad \frac{1}{a(t)} = z + 1 \quad \Leftrightarrow \quad a(t) = \frac{1}{z+1}. \tag{1.89}$$

The FLRW metric (1.25) and the related cosmological equations (1.50) allow one to obtain, consistently with what is observed, Hubble's law in parametric form with respect to time. The redshift parameter then allows the definition of the ratio $a(t_0)/a(t_1)$ in connection with H_0 that emerges from Hubble's law, creating the already mentioned correlation between H_0 and the definition of $H(t)$ (1.70).

1.5.1 The Hubble Tension

The Hubble constant H_0 is the value of a time-dependent parameter $H(t)$. One of the main problems of modern cosmology concerns precisely the determination of H_0. Different measurements of the Hubble constant exist, obtained through fundamentally different approaches.

On one hand, experiments such as *Planck*, ACT (Atacama Cosmology Telescope), and SPT (South Pole Telescope) [18, 19, 20, 21] measure H_0 through dynamical calculations within the framework of the ΛCDM cosmological model, using data from observations of the last scattering surface (the CMB). On the other hand, Riess and collaborators employ the cosmic distance ladder [17]: this method uses Cepheid variables to calibrate nearby distances using eq. (1.9), Type Ia supernovae as secondary standard candles, and other techniques to build a chain of distance measurements extending to cosmological scales.

Both approaches yield highly precise measurements, representing some of the most accurate determinations in the history of science. However, they are statistically inconsistent with each other: the discrepancy between the two methods reaches approximately 5σ significance. This problem is known as the **Hubble tension** and represents one of the major challenges in modern cosmology, potentially indicating either systematic errors in one or both methods, or new physics beyond the standard ΛCDM model.

An updated and extensive review on this subject can be found in [2], to which the author of this thesis contributed as part of the collaboration, specifically writing the section on inflation.

1.6 The ΛCDM model

Considering the different species that compose the Universe, one has

$$\varepsilon = \sum_{i=1}^{n} \varepsilon_i, \tag{1.90}$$

where, in the current observational situation of the Universe, the main observed species are

$$\varepsilon = \varepsilon_{\text{rad}} + \varepsilon_{\text{b}} + \varepsilon_{\Lambda} + \varepsilon_{\text{DM}}. \tag{1.91}$$

- ε_{rad} represents radiation, i.e., matter in relativistic form such as photons and neutrinos.
- ε_{b} represents the standard baryonic matter component that is in a dust state ($w = 0$).
- ε_{Λ} represents the dark energy component that causes the accelerated expansion of the universe, as discussed in the previous sections.
- Finally, ε_{DM} represents another matter component in a dust state that is not directly observed but without which galaxies and all other structures observed in the universe could not form. Also in this case, as in that of dark energy, the nature of this matter is not yet understood, which is therefore called **dark matter**.

Now consider the second equation of the standard cosmological model, in the general case. This equation is written at the time of observation, i.e., in the present epoch with t_0 and H_0:

$$H_0^2 = \left(\frac{\dot{a}}{a}\right)^2_{t=t_0} = \frac{8\pi G}{3c^2}\varepsilon - \frac{kc^2}{a^2(t_0)} + \frac{\Lambda c^2}{3}; \tag{1.92}$$

both members are divided by H_0^2 and $\varepsilon = \sum_i \varepsilon_i = \rho c^2 = \sum_i \rho_i c^2$ is written:

$$1 = \frac{8\pi G}{3H_0^2}\rho - \frac{kc^2}{a_0^2 H_0^2} + \frac{\Lambda c^2}{3H_0^2}. \tag{1.93}$$

It is now noticed that the reciprocal of the first term represents a density, indeed the unit of H_0^2 is s^{-2} and the constant G has units $\text{m}^2/(\text{s}^2 \cdot \text{kg})$, and therefore one has kg/m^3. This density is called the **critical density** ρ_c:

$$\rho_c = \frac{3H_0^2}{8\pi G}. \tag{1.94}$$

Having introduced the critical density, the equation therefore becomes

$$1 = \frac{\rho}{\rho_c} - \frac{kc^2}{a_0^2 H_0^2} + \frac{\Lambda c^2}{3H_0^2} \tag{1.95}$$

The parameter ρ/ρ_c is usually indicated with Ω and is called the **density parameter**. Since the total density ρ is a sum over all species, $\rho = \sum_i \rho_i$, then also for Ω itself one has

$$\Omega = \sum_i \Omega_i = \Omega_{\text{b}} + \Omega_{\text{rad}} + \Omega_{\text{DM}}. \tag{1.96}$$

The second term of eq. (1.95) can also be seen as a density parameter, in this case a **geometric density parameter**:

$$-\frac{kc^2}{a_0^2 H_0^2} = \Omega_k, \tag{1.97}$$

just as the third term of the previous equation can be seen as

$$\frac{\Lambda c^2}{3H_0^2} = \frac{\rho_\Lambda}{\rho_c} = \Omega_\Lambda. \tag{1.98}$$

The relation therefore becomes

$$\Omega + \Omega_k + \Omega_\Lambda = \Omega_{\rm b} + \Omega_{\rm rad} + \Omega_{\rm DM} + \Omega_k + \Omega_\Lambda = 1, \tag{1.99}$$

so it is possible to see in a completely direct way that the density of matter and energy of the Universe determines its shape, i.e., the geometry:

$$\text{If } k = 0 \quad \Leftrightarrow \quad \Omega_k = 0 \quad \Rightarrow \quad \Omega + \Omega_\Lambda = 1 \quad \rho = \rho_c; \tag{1.100}$$

$$\text{If } k = 1 \quad \Leftrightarrow \quad \Omega_k < 0 \quad \Rightarrow \quad \Omega + \Omega_\Lambda > 1 \quad \rho > \rho_c; \tag{1.101}$$

$$\text{If } k = -1 \quad \Leftrightarrow \quad \Omega_k > 0 \quad \Rightarrow \quad \Omega + \Omega_\Lambda < 1 \quad \rho < \rho_c; \tag{1.102}$$

this is the reason why ρ_c is called critical density: if $\rho = \rho_c$ the Universe is flat, not globally curved, but as soon as the density decreases or increases the Universe curves positively or negatively, globally assuming hyperbolic or spherical geometry.

Obviously the equation represents a natural constraint on the fluids of the Universe, valid at any epoch t or, analogously, at any redshift z; more precisely indeed

$$\Omega(t) + \Omega_k(t) + \Omega_\Lambda(t) = 1 \quad \forall\, t, \tag{1.103}$$

or

$$\Omega(z) + \Omega_k(z) + \Omega_\Lambda(z) = 1 \quad \forall\, z. \tag{1.104}$$

Currently the following quantities are measured from Planck 2018 [22]:

$$\begin{gathered}
\Omega_{\rm b} = 0.0493 \pm 0.0010 \\
\Omega_{\rm c} = 0.265 \pm 0.007 \\
\Omega_{\rm m} = 0.315 \pm 0.007 \\
\Omega_{\rm rad} \sim 9 \times 10^{-5} \\
\Omega_\Lambda = 0.685 \pm 0.007 \\
\Omega_k \sim 0,
\end{gathered} \tag{1.105}$$

$\Omega_{\rm b}$ represents the ordinary barionic matter, $\Omega_{\rm c}$ is the dark matter contribution, and $\Omega_{\rm m} = \Omega_{\rm b} + \Omega_{\rm c}$.

These values are primarily derived from a combination of CMB observations (particularly from the *Planck* satellite [22]), large-scale structure surveys such as baryon acoustic oscillations (BAO) measurements [23, 24, 25], and Type Ia supernovae data [17]. The baryon density $\Omega_{\rm b}$ is tightly constrained by CMB acoustic peaks and Big Bang nucleosynthesis, while $\Omega_{\rm DM}$ is determined from gravitational effects on large-scale structure and galaxy rotation curves. The cosmological constant Ω_Λ is inferred from the observed accelerated expansion and the overall flatness constraint $\Omega_k \sim 0$.

It is therefore found that the universe is observed to be globally flat, $k = 0$, and that standard relativistic and non-relativistic matter represents at most only about 5% of the content of our universe, while instead $\sim$ 95% of the Universe's content is divided between a type of non-relativistic (cold) matter that is not observed directly and is not present in the standard model of elementary particles but is necessary to obtain the formation of the structures currently observed (galaxies and galaxy clusters), and another type of energy that causes the accelerated expansion of the universe.

Since the standard cosmological model is dominated by dark energy and dark matter, it is called ΛCDM, where Λ represents the cosmological constant, while the acronym CDM stands for Cold Dark Matter.

Even though from an observational point of view the nature of dark energy and matter still cannot be understood, the standard cosmological model is among the most elegant and consistent models obtained in the history of science.

1.7 The Cosmic Microwave Background Radiation

The **observable Universe** is defined by the cosmological horizon, determined by the integral relation derived from eq. (1.86):

$$\int_{t_1}^{t_0} \frac{c\mathrm{d}t}{a(t)} = \int_{r_0}^{0} \sqrt{F(r)}\mathrm{d}r.$$

This defines the physical observable redshift z, which in principle allows observation of the entire causal Universe. However, the **observed Universe**—what can actually be detected and observed—is limited by the availability of observable messengers and their properties.

The primary messenger for cosmological observations is electromagnetic radiation (light). However, there exists a fundamental barrier: the **last scattering surface**, which marks the most distant light-emitting event observable. This surface formed during the **recombination epoch** at redshift $z_{\mathrm{rec}} \sim 1100$, when the Universe's temperature dropped to approximately 3000 K. At this point, electrons combined with protons to form neutral hydrogen atoms, rendering the Universe transparent to photons for the first time. Prior to recombination, photons were continuously scattered by the ionized plasma, preventing free propagation. Therefore, electromagnetic observations cannot probe epochs before the last scattering surface. The time of recombination t_{rec} from the Big Bang is

$$t_{\mathrm{rec}} \sim 380{,}000\,\text{years}. \tag{1.106}$$

In principle, other messengers could probe earlier epochs. Neutrinos decoupled from the primordial plasma at higher temperatures than photons, creating a **cosmic neutrino background** that would contain information from earlier times. Similarly, **primordial gravitational waves** generated during the inflationary epoch (discussed later) could provide a window into the very early Universe. However, current technology does not allow detection of these messengers: measurements of the cosmic neutrino background and the stochastic background of primordial gravitational waves remain beyond present observational capabilities. Thus, the last scattering surface represents the practical limit of direct observations of the early Universe.

The radiation emitted at the last scattering surface was composed of very energetic photons (gamma rays and X-rays), but due to cosmological redshift, it reaches Earth at a frequency around $\nu \sim 160$ GHz and at a temperature $T \sim 2.725$ K, thus presenting itself in the microwave spectrum. Being a radiation that permeates space in every direction due to homogeneity and isotropy, this is said to be **Cosmic Microwave Background Radiation, CMBR** or more commonly **CMB**.

Although the CMB appears highly isotropic across the entire sky, it presents tiny temperature fluctuations of the order of $\Delta T/T \sim 10^{-5}$, known as **CMB anisotropies**. These temperature variations, equal to about 10 μK compared to the average temperature of 2.725 K, represent primarily the primordial density fluctuations in the universe that formed at the Big Bang. Other secondary effects such as the Integrated Sachs-Wolfe (ISW) and the Sunyaev–Zel'dovich (SZ) effects, or the gravitational lensing, contribute to these anisotropies [26, 27, 28]. The anisotropies are of fundamental importance since they constitute the seeds from which all the cosmic structures observed today formed: galaxies, galaxy clusters and the large-scale structure of the universe. Indeed, the anisotropies in density of the galaxies (Large Scale Structure) are identical to those in temperature:

$$\frac{\Delta\rho_{\mathrm{LSS}}}{\rho_{\mathrm{LSS}}} = \frac{\Delta T_{\mathrm{CMB}}}{T_{\mathrm{CMB}}} \sim 10^{-5}. \tag{1.107}$$

Without these small initial inhomogeneities, the universe would have remained perfectly uniform and the complex structures that characterize the modern cosmos could never have formed. The detailed analysis of the anisotropy pattern also provides valuable information on fundamental cosmological parameters, allowing the determination with high precision of the geometry of the universe, its composition in ordinary matter, dark matter and dark energy. Being the anisotropies traces of fluctuations formed in the first instants after the Big Bang, they also allow testing theoretical models of the primordial universe, as well as models of quantum gravity and string theory.

The existence of the CMB was predicted theoretically in 1948 by Alpher and Herman [29], while in 1964 Doroshkevich and Novikov calculated for the first time that this primordial radiation should be mainly in the microwave spectrum [30, 31]. The first discovery from an experimental point of view was made in 1965 completely accidentally by Penzias and Wilson while working on radio wave detection from Echo satellites at Bell Telephone Laboratories [32]. This discovery earned them the Nobel Prize in 1978.

In subsequent years there were numerous experiments confirming the black body spectrum of the CMB. The first experiment specifically dedicated to the observation and study of the CMB was the **Cosmic Background Explorer (COBE)**, operating in the years 1989-1993 [33]. This experiment led to the definitive confirmation of a perfect black body spectrum and, in 1992, to the discovery of the first CMB anisotropies on large scales, a result that earned the 2006 Nobel Prize to Smoot and Mather [34].

Subsequently, in the first decade of the 2000s, the **Wilkinson Microwave Anisotropy Probe (WMAP)** satellite measured for the first time precisely the CMB anisotropies with an angular resolution of $\sim 0.2°$ [35]. Thanks to these measurements, precise determinations of cosmological parameters were made for the first time, confirming the ΛCDM model as the standard cosmological paradigm.

In the second decade of the 2000s, the ***Planck*** satellite succeeded in making very high precision measurements of the anisotropies, with angular resolutions up to ~ 7 arcmin and sensitivity up to μK in temperature [18, 36, 37]. For the first time, *Planck* also precisely measured the polarization of the CMB signal, in particular the E-modes. The *Planck* experiment succeeded in determining cosmological parameters with unprecedented precision, to the point that still today, after a decade and numerous other precision experiments, its data and maps are still actively used in scientific research. As mentioned in previous sections, it was precisely with the precise measurements of *Planck* that the Hubble tension clearly emerged.

In fig. 1.6 the temperature anisotropies of CMB as seen by COBE, WMAP, and *Planck* are shown.

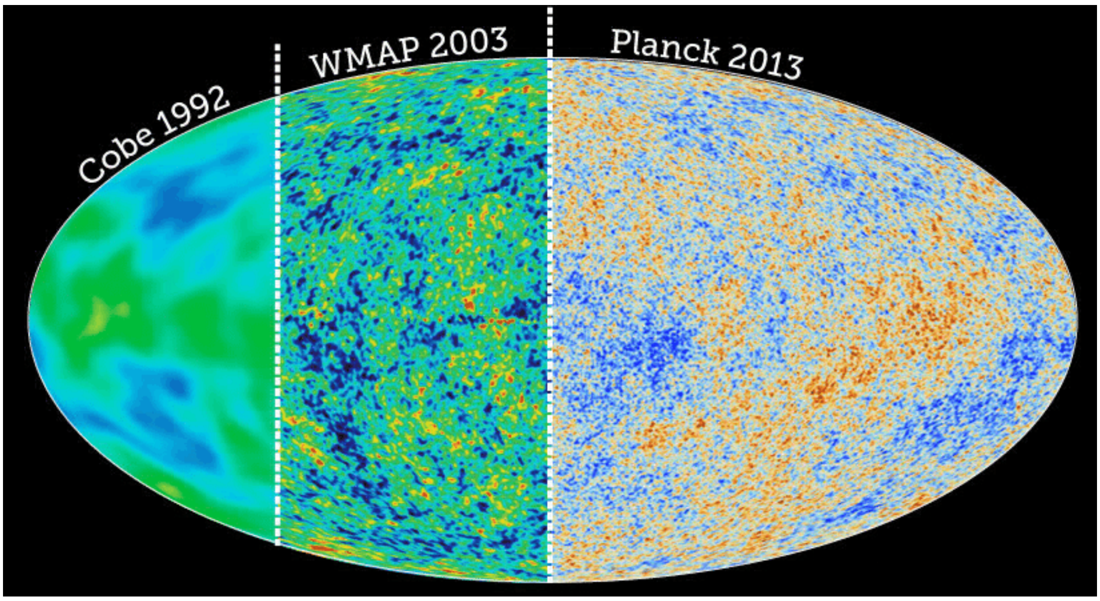

Figure 1.6: Temperature anisotropies of the CMB seen by COBE, WMAP and *Planck* at different resolutions. Image from [38].

Currently the CMB still plays a key role in theoretical and observational cosmology, continuing to represent one of the most important elements for the study of the universe. For this reason, despite the very precise measurements of *Planck*, there are today many experiments in progress and in preparation, both ground-based (ACT, SPT, BICEP/Keck Array) [20, 19, 39, 40] and space-based (LiteBIRD, scheduled for launch in 2032, and Simons Observatory) [41, 42, 43]. Currently the main purpose of these experiments is focused on observing the polarization of radiation, in particular the B-modes, since the E-modes have already been observed by *Planck* and at very small scales by ACT. The detection of primordial B-modes would represent direct proof of cosmic inflation and the energy scales at which it occurred, as well as the primordial gravitational waves signal.

1.8 Inflation Theory

The standard cosmological model, as presented so far, exhibits inconsistencies with observations, in addition to problems related to the actual nature of dark matter and dark energy. All these inconsistencies were resolved in the 1980s with the introduction of **inflationary theory** by Alan Guth and Alexei Starobinsky [44, 45]. In brief, inflationary theory proposes that, in the moments immediately following the Big Bang, the Universe underwent rapid exponential expansion, called inflation. Let us first give a brief overview of these problems and then present the basic concepts of inflation theory.

- **The horizon problem (or homogeneity and isotropy problem)**:

  In relativity, given the finite speed of light, only events within the light cone can be causally connected since these are correlated by a cause-and-effect relationship.

  Now consider the last scattering surface where the cosmic microwave background radiation was emitted. The CMB extends across the entire sky, such that no causal connection is possible between all its points: some regions are so distant that, from the Big Bang until the formation of the CMB, not even light could have traveled such distances. In physical terms, the CMB is so extended that the light cones of all its points could never have overlapped in the past if a standard scenario of universe expansion is assumed. For this reason, before observing it, one would expect a surface that was homogeneous and presented identical physical parameters only within certain angular scales, corresponding to regions that could have been somehow causally connected in the past. The mapping of the CMB, together with the measurements that could be made on it, shows instead the exact opposite: the surface appears homogeneous over 4π steradians, presenting the same identical physical parameters at every point, such as the average temperature. Furthermore, even the CMB anisotropies themselves are identical at any scale and in any direction they are measured. This would be possible if and only if every region of the surface in the past had been causally connected with all the others. Such a scenario could not have occurred with a standard evolution from the Big Bang to the CMB predicted by the equations of the standard cosmological model (1.50), as shown in fig. 1.7.

  If instead it is hypothesized that the Universe underwent inflationary expansion, the problem is resolved, as also shown in fig. 1.8: the Universe, before undergoing inflation, was small enough that all points were causally correlated. Then, undergoing inflationary expansion, each light cone expanded exponentially with spacetime (indeed the light cone expands as a function of $a(t)$); thus effectively in the past all regions of the last scattering surface were causally correlated.

- **Flatness problem**:

  As seen previously, observations predict that the Universe should be spatially flat, i.e., have $k = 0$. At the same time it has been seen, eq. (1.94), that for $k = 0$ the matter density

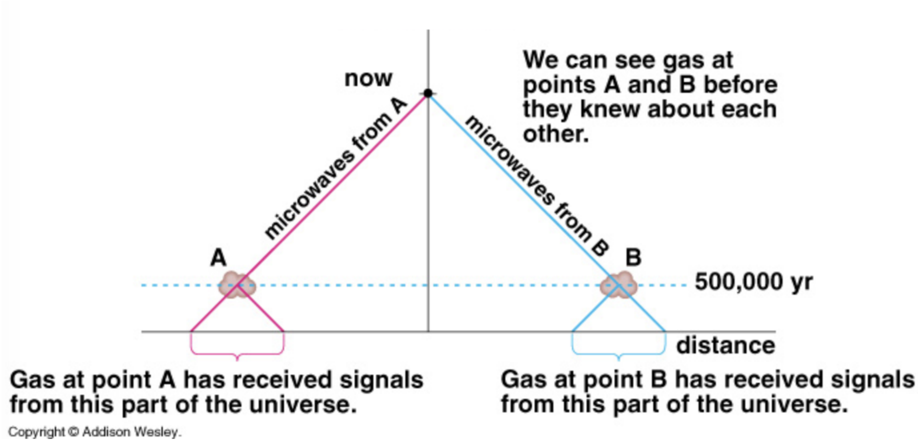

Figure 1.7: The problem of non-correlation of all CMB regions explained with gaseous regions at A and B. Credits: Addinson Wesley.

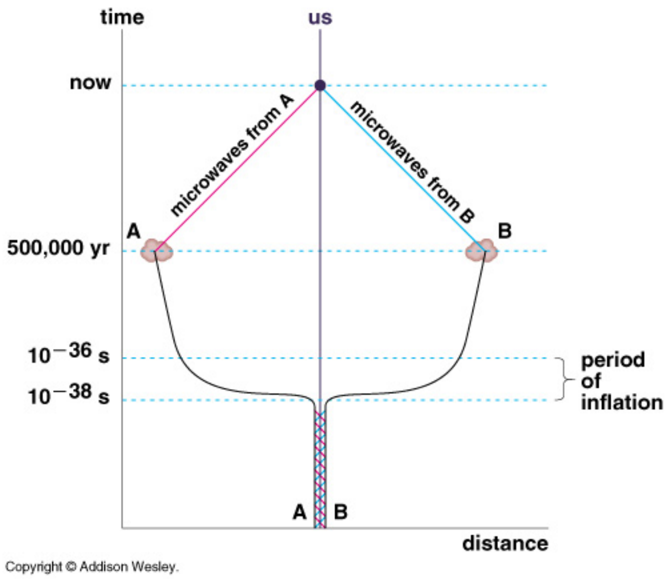

Figure 1.8: How inflation theory manages to solve the problem of overlapping all light cones. Credits: Addinson Wesley.

is critical, i.e., $\rho = \rho_c$. It is therefore noted that $\rho = \rho_c$ is a highly unstable equilibrium point: an infinitesimal density fluctuation would be enough to change the geometry of the Universe by curving it. Why then is this value observed which, as can be understood, is highly improbable?

- **Magnetic monopole problem**:

  In the first moments of the Universe's birth, all fundamental forces are theorized to be grouped under a single force, after which **spontaneous symmetry breaking** occurred that led the forces to differentiate. This theory, however, predicts the existence of magnetic monopoles, objects which as is well known have never been observed. To be honest, this is primarily a problem of the standard model, but it is thought that the answer might reside in an explanation of cosmological nature.

Beyond these standard cosmological problems resolved by inflation, there exists a more fundamental issue related to the limits of the FLRW model itself: the initial singularity problem. The Universe emerged, according to the standard cosmological model, from an initial point since

$a(t) \to 0$ for $t \to 0$; but at that point, since $\rho \sim a^{-n}$, we have $\rho \to \infty$. Physically this has no meaning, and General Relativity is not capable of describing the physics of such singularities.

The branch of physics that attempts to address this problem is **quantum gravity** and, associated with it, **quantum cosmology**. While not a standard prediction of inflationary theory, inflation offers a framework to approach this problem [45, 46]: the initial singularity could potentially be resolved by assuming that the Universe emerged through quantum tunneling through a potential barrier, with the fluctuations that led to the creation of the Universe being false vacuum fluctuations typical of quantum field theory. Alternative approaches include **pre-Big Bang models** and other extensions of standard cosmology that attempt to avoid or explain the initial singularity.

1.8.1 Mathematical Description of Inflation

In the very early universe, assuming $\Lambda = 0$ appears to be a very good approximation, since the energy densities were much higher than those associated with the Λ responsible for the currently observed accelerated expansion of the Universe.

In the standard cosmological model, regardless of the type of matter considered, to achieve accelerated expansion $\ddot{a} > 0$ in the case where $\Lambda = 0$, it is required that

$$\varepsilon + 3p < 0 \quad \Longrightarrow \quad p < -\frac{\varepsilon}{3}, \tag{1.108}$$

which follows immediately from the first equation of the cosmological system (1.50). Assuming $k = 0$ and $\Lambda = 0$, the second cosmological equation becomes, assuming the presence of an inflationary component:

$$\frac{\dot{a}}{a} = \sqrt{\frac{8\pi G}{3c^2}\varepsilon_{\text{inf}}} = \sqrt{\frac{8\pi G}{3}\rho_{\text{inf}}}. \tag{1.109}$$

If ρ_{inf} is assumed to be a constant energy density over time, integration immediately yields a **de Sitter solution**, characterized by exponential expansion:

$$a(t) = a_0 e^{\sqrt{\frac{8\pi}{3}\rho_{\text{inf}}}\,t} = a_0 e^{Ht}. \tag{1.110}$$

A natural way to model the inflationary component is to introduce a scalar field $\phi = \phi(x^\mu)$ with self-interaction potential $V = V(\phi)$. The Lagrangian density is

$$\mathscr{L} = \frac{1}{2}\partial_\mu\phi\partial^\mu\phi - V(\phi), \tag{1.111}$$

and from the variational principle

$$\delta\mathscr{S} = \delta\int\mathscr{L}\sqrt{-g}\,\mathrm{d}\Omega, \tag{1.112}$$

the associated energy and pressure are obtained:

$$\rho(t) = \frac{1}{2}\dot{\phi}^2 + V(\phi), \qquad p(t) = \frac{1}{2}\dot{\phi}^2 - V(\phi). \tag{1.113}$$

At some initial time t_{in}, one can have $\phi(t_{\text{in}}) = \text{constant}$ (for example $\phi = 0$) with $\dot{\phi}(t_{\text{in}}) = 0$ and $V(\phi, T) > 0$. In this case

$$\rho(t_{\text{in}}) = V(\phi), \qquad p(t_{\text{in}}) = -V(\phi), \tag{1.114}$$

which implies

$$p = -\rho, \tag{1.115}$$

a condition that guarantees accelerated expansion in accordance with eq. (1.108).

Considering the first Friedmann equation and substituting ρ and p, one obtains:

$$\frac{\ddot{a}}{a} = -\kappa\left(\dot{\phi}^2 - 2V\right), \tag{1.116}$$

where κ is a positive constant.

In some historical models ("old inflation"), it was assumed that for $T \gg T_c$ the potential was symmetric and temperature-dependent, and that upon cooling below T_c, spontaneous symmetry breaking would occur, causing the field to remain temporarily trapped near $\phi = 0$. In this configuration, the energy is dominated by $V(\phi, T)$ and the expansion is quasi-de Sitter:

$$\frac{\ddot{a}}{a} \simeq +\kappa V \quad \Rightarrow \quad a(t) \propto e^{Ht}. \tag{1.117}$$

In **slow-roll inflation** models, which are more widely used today, there is no need to invoke a true thermal phase transition. In these models, the potential $V(\phi)$ is sufficiently flat to allow the field to evolve slowly, with $V \gg \dot{\phi}^2/2$. Inflation ends when the slow-roll parameter

$$\epsilon \equiv -\frac{\dot{H}}{H^2} \simeq \frac{\dot{\phi}^2}{2V} \approx 1, \tag{1.118}$$

that is, when the kinetic energy becomes comparable to the potential energy. At this point, ϕ begins to oscillate around the minimum of V, transferring its energy to Standard Model fields in the reheating process, as shown in fig. 1.9.

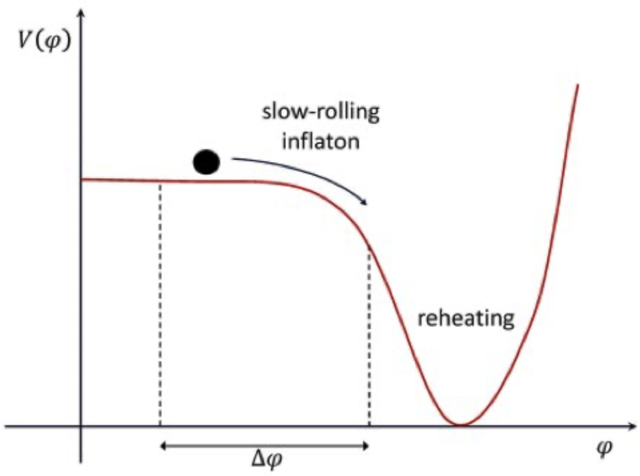

Figure 1.9: Slow-roll inflation model.

For inflation to resolve the cosmological problems described, it is necessary that this phase lasts long enough to produce exponential expansion of at least **50–60 e-folds**, where one e-fold corresponds to an increase in the scale factor $a(t)$ by a factor of e. More precisely, the number N of e-folds is defined as

$$N = \int_{t_{\text{start}}}^{t_{\text{end}}} H \, \mathrm{d}t. \tag{1.119}$$

The slow-roll phase is introduced to achieve this duration. This duration ensures that the primordial Universe is sufficiently dilated to make current cosmological observables coherent, such as the isotropy of the CMB and the near-flatness of the Universe's geometry.

This single scalar field model represents the simplest form of inflation; many others exist, based either on different potentials or on more complex mechanisms (for example, quantum tunneling or multifield inflation).

The scalar field that drives inflation is called the **inflaton**. Depending on the model, it can be identified with different fields, such as:

1. **Dilaton:** A field arising from string theories;
2. **Higgs boson:** In scenarios where the Higgs field acts as the inflaton;
3. **Scalaron:** An inflaton emerging from modified gravity theories of the $f(R)$ type.

The theory of inflation, despite various possible implementations, represents today the most solid and coherent mechanism for explaining cosmological observations, and has become part of the standard ΛCDM model.

1.8.2 Primordial Power Spectra

Analogous to the CMB power spectra, which represent the fundamental mathematical tools for studying CMB physics, the **primordial power spectra (PPS)** constitute the most relevant quantities associated with cosmic inflation. Inflationary expansion generates quantum fluctuations that are stretched to cosmological scales, producing both scalar and tensor perturbations of the metric. The scalar perturbations, characterized by the scalar PPS, source density fluctuations that leave observable imprints in CMB temperature anisotropies and in the matter distribution of the large-scale structure. The tensor perturbations, described by the tensor PPS, represent primordial gravitational waves and contribute primarily to CMB polarization through the generation of B-modes.

The primordial power spectra are typically characterized by the scalar spectral index n_s and the tensor-to-scalar ratio r, which serve as parameters for comparing theoretical predictions with CMB observational data. Phenomenologically, the PPS can be parametrized as scale-dependent power-laws with characteristic amplitudes, conventionally written as

$$\mathscr{P}_\zeta(k) = A_s \left(\frac{k}{k_*}\right)^{n_s - 1} \quad \text{and} \quad \mathscr{P}_t(k) = A_t \left(\frac{k}{k_*}\right)^{n_t}, \tag{1.120}$$

where A_s and A_t represent the scalar and tensor amplitudes respectively, n_s and n_t denote the scalar and tensor spectral indices, and the tensor-to-scalar ratio is defined as

$$r = \frac{A_t}{A_s}. \tag{1.121}$$

The reference scale k_*, typically set to $0.05\,\mathrm{Mpc}^{-1}$, represents the pivot scale at which observations are normalized. This parametrization is motivated by the requirement that inflation generates primordial scale-invariant or nearly scale-invariant power spectra. The *Planck* collaboration confirmed the nearly scale-invariant nature of the scalar PPS, measuring $n_s = 0.9649 \pm 0.0042$ at 68% confidence level, while constraining the tensor-to-scalar ratio to $r < 0.036$ at 95% confidence level [18, 47]. This approximate scale-invariance enables further parametrization through higher-order terms that describe the scale-dependent evolution of spectral indices and their runnings, i.e., the derivatives with respect to the logarithm of the scale.

Beyond this phenomenological description, a rigorous theoretical framework for computing the PPS analytically can be developed within the slow-roll inflationary paradigm. In the slow-roll scenario, the primordial power spectra can be expressed in terms of the Hubble parameter and the hierarchy of its time derivatives, known as the **Hubble flow functions (HFFs)**:

$$\epsilon_1(N) = -\frac{\mathrm{d}\ln H}{\mathrm{d}N}, \qquad \epsilon_{i+1}(N) = \frac{\mathrm{d}\ln|\epsilon_i|}{\mathrm{d}N} \qquad \forall\, i \geq 1, \tag{1.122}$$

where $\mathrm{d}N \equiv \mathrm{d}\ln a$ is the number of e-folds. This formulation provides a model-independent parametrization of inflationary dynamics that connects directly to observable quantities. The analytical calculation of the PPS using the HFF formalism, including higher-order corrections in the slow-roll expansion, is developed in detail in chapter 3, where third-order corrections to inflationary predictions are systematically derived and compared with observational constraints.

Chapter 2

CMB Physics and Cosmic Birefringence

In the previous chapter, the Cosmic Microwave Background radiation and its anisotropies were introduced, which are fundamental for testing cosmological models.

In this chapter, the physics of the Cosmic Microwave Background radiation is developed and the cosmic birefringence effect, which affects the polarization plane of the CMB, is introduced.

2.1 CMB Anisotropies and Power Spectra

The CMB radiation is among the most nearly perfect black-body sources observable in nature. At a specific epoch, the primordial cosmological plasma began emitting all available radiation, which subsequently propagated freely through space. For this reason, the fundamental physics describing the CMB is governed by black-body radiation laws.

A **black body** is an idealized object that absorbs all incident electromagnetic radiation regardless of frequency or angle of incidence. To maintain thermal equilibrium, the black body re-emits this absorbed radiation; this emission is called black-body radiation. The spectrum emitted by a black body follows **Planck's law**:

$$B_\nu(T) = \frac{2h\nu^3}{c^2} \frac{1}{e^{\frac{h\nu}{k_B T}} - 1}, \tag{2.1}$$

where $B_\nu(T)$ is the **spectral radiance** (power per unit area per unit solid angle per unit frequency), h is Planck's constant, and k_B is Boltzmann's constant. The shape of B_ν as a function of ν depends only on the temperature of the body, not on the material composition. Similarly, the peak intensity frequency depends only on temperature (**Wien displacement law**).

The total radiation energy density emitted by a black body is proportional to the fourth power of temperature:

$$\rho_{\text{tot}}^{\text{EM}} = \frac{8\pi^5 k_B^4}{15c^3h^3} T^4 = \sigma T^4, \tag{2.2}$$

where σ is the Stefan-Boltzmann constant, and this relation is known as the **Stefan-Boltzmann law**.

An important cosmological consequence of this law is that, since radiation energy density scales as $\rho_r \propto a^{-4}$, the temperature of radiation necessarily evolves as $T \propto a^{-1}$. A second consequence is that the shape of the black-body spectrum remains unchanged during cosmic expansion—only the temperature and frequencies shift due to redshift. This preservation is crucial because it ensures that the CMB black-body spectrum remains unaltered throughout its $\simeq 13.8\,\text{Gyr}$ history. When the COBE collaboration first observed the CMB spectrum, it was confirmed to be an almost perfect black-body radiation. COBE also detected CMB anisotropies, which were previously unknown [33, 34].

In CMB physics, the spectral radiance B_ν is typically called **intensity** and denoted as I. The COBE satellite revealed that this intensity is not spatially constant (purely homogeneous) but depends on the observation direction: $I = I(\hat{n})$, where $\hat{n}$ represents the observation direction. Therefore, I exhibits intrinsic fluctuations across the sky rather than being constant on the celestial sphere.

Since these fluctuations δI are small, an expansion to linear order in temperature can be performed:

$$\delta I = \left.\frac{\mathrm{d}I}{\mathrm{d}T}\right|_{T_0} \delta T(\hat{n}) + \text{higher order terms}, \tag{2.3}$$

where T_0 is the mean (background) CMB temperature

$$T_0 = \frac{1}{4\pi}\int_\Omega \mathrm{d}\Omega\, T(\hat{n}). \tag{2.4}$$

As discussed previously, $T_0 = 2.7255\,\text{K}$ while the temperature fluctuations δT are of order μK.

From eq. (2.1) one obtains

$$\left.\frac{\mathrm{d}I}{\mathrm{d}T}\right|_{T_0} = \frac{2\pi h}{c^2}\frac{h\nu^4}{k_B}\frac{e^{\frac{h\nu}{k_B T_0}}}{(e^{\frac{h\nu}{k_B T_0}}-1)^2}\frac{1}{T_0^2} \equiv K(\nu, T_0) \tag{2.5}$$

and therefore one can write:

$$I(\hat{n}) = K(\nu, T_0)\delta T(\hat{n}) + \text{higher order terms} \tag{2.6}$$

It is thus understood that fluctuations in electromagnetic intensity are directly related to temperature anisotropies:

$$\delta I(\hat{n}) \propto \delta T(\hat{n}). \tag{2.7}$$

From an *observational perspective*, inverting this relation yields what are known as **CMB anisotropy maps**:

$$\delta T(\hat{n}) = \frac{\delta I(\hat{n})}{K(\nu, T_0)}. \tag{2.8}$$

Anisotropies are not merely observational phenomena; they can also be predicted theoretically when perturbation theory effects are incorporated into the description of matter-radiation decoupling in an expanding universe. The temperature fluctuations can be decomposed as:

$$\delta T(\hat{n}) = \delta T_{\text{SW}} + \delta T_{\text{ISW}}, \tag{2.9}$$

where

- δT_{SW} depends on physics at the last scattering surface (LSS), called the **ordinary Sachs-Wolfe effect** [26]. This arises from gravitational redshift and blueshift of photons climbing out of or falling into gravitational potential wells present at the time of recombination. It dominates the CMB power spectrum on large angular scales.

- δT_{ISW} depends on the evolution of gravitational potentials, called the **integrated Sachs-Wolfe effect** [26]. This occurs when gravitational potentials evolve along the photon path from the last scattering surface to the observer, particularly during the transition to dark energy domination. It contributes to the large-scale power and provides a probe of cosmic acceleration.

These contributions are given by:

$$\delta T(\hat{n}) = \left[\frac{1}{2}\delta_\gamma + \Psi + \hat{n}\cdot\mathbf{v}_e\right]_{\mathrm{LSS}} + \int_{\eta_{\mathrm{LSS}}}^{\eta_{\mathrm{now}}} \mathrm{d}\eta\,[\Psi' + \Phi'], \tag{2.10}$$

where the terms represent:

- $\frac{1}{2}\delta_\gamma$: fluctuations in radiation energy density,
- Ψ: the Bardeen gravitational potential,
- $\hat{n}\cdot\mathbf{v}_e$: Doppler effect due to electron motion during photon scattering,
- The integrated Sachs-Wolfe term: evolution of gravitational perturbation potentials Ψ and Φ in conformal time η.

The conformal time η is defined to be

$$\mathrm{d}\eta = \frac{\mathrm{d}t}{a} = \frac{\mathrm{d}a}{a^2 H} \tag{2.11}$$

The detailed physics of these effects is not delved into here, but they are mentioned to illustrate the physical origin of temperature anisotropies: they arise from gravitational effects, gravitational perturbations, Doppler shifts from γe^- scattering, and intrinsic radiation density fluctuations.

The quantity $\delta T(\hat{n})$ can also be expressed by treating it as a stochastic variable dependent on observation direction:

$$\delta T(\hat{n}) = T(\hat{n}) - T_0, \tag{2.12}$$

where $T(\hat{n})$ is the **CMB temperature measured along the line of sight** $\hat{n}$ and T_0 is the background temperature.

Since $T(\hat{n})$ is a scalar function defined on the sphere, it can be expanded using spherical harmonics as a basis:

$$T(\hat{n}) = \sum_{\ell=0}^{+\infty}\sum_{m=-\ell}^{\ell} a_{\ell m} Y_{\ell m}(\hat{n}), \tag{2.13}$$

where the information contained in T is encoded in the $a_{\ell m}$ coefficients.

Multiplying both sides by $Y^*_{\ell' m'}(\hat{n})$ and integrating over the sphere:

$$\int_{4\pi} \mathrm{d}\Omega\, T(\hat{n}) Y^*_{\ell' m'}(\hat{n}) = \sum_{\ell=0}^{+\infty}\sum_{m=-\ell}^{\ell} a_{\ell m} \underbrace{\int_{4\pi} \mathrm{d}\Omega\, Y_{\ell m}(\hat{n}) Y^*_{\ell' m'}(\hat{n})}_{\delta_{\ell\ell'}\delta_{mm'}}, \tag{2.14}$$

Using the orthogonality relation of spherical harmonics, the sums collapse and one obtains:

$$a_{\ell' m'} = \int_{4\pi} \mathrm{d}\Omega\, T(\hat{n}) Y^*_{\ell' m'}(\hat{n}). \tag{2.15}$$

For $\ell = 0$, one has $m = 0$, corresponding to the **monopole term**:

$$\begin{aligned} a_{00} &= \int_{4\pi} \mathrm{d}\Omega\, T(\hat{n}) Y_{00}(\hat{n}) \\ &= \int_{4\pi} \mathrm{d}\Omega\, T(\hat{n}) \frac{1}{\sqrt{4\pi}} \\ &= \frac{T_0}{\sqrt{4\pi}}\sqrt{4\pi} = T_0\sqrt{4\pi} \end{aligned} \tag{2.16}$$

Therefore:

$$\begin{aligned} T(\hat{n}) &= a_{00}Y_{00} + \sum_{\ell=1}^{\infty}\sum_{m=-\ell}^{\ell} a_{\ell m}Y_{\ell m}(\hat{n}) \\ &= T_0\sqrt{4\pi}\frac{1}{\sqrt{4\pi}} + \sum_{\ell=1}^{\infty}\sum_{m=-\ell}^{\ell} a_{\ell m}Y_{\ell m}(\hat{n}) \\ &= T_0 + \sum_{\ell=1}^{\infty}\sum_{m=-\ell}^{\ell} a_{\ell m}Y_{\ell m}(\hat{n}), \end{aligned} \tag{2.17}$$

and thus:

$$\delta T(\hat{n}) = T(\hat{n}) - T_0 = \sum_{\ell=1}^{\infty}\sum_{m=-\ell}^{\ell} a_{\ell m}Y_{\ell m}(\hat{n}). \tag{2.18}$$

The $\ell = 1$ term is the **dipole** and is typically excluded from analysis because it is not cosmologically fundamental—it arises from the motion of the observer relative to the CMB rest frame. In our case, this is the motion of the Milky Way galaxy relative to the CMB frame. Therefore, observational studies focus on:

$$\underbrace{\delta T(\hat{n})}_{\text{map space}} = \underbrace{\sum_{\ell=2}^{\infty}\sum_{m=-\ell}^{\ell} a_{\ell m}Y_{\ell m}(\hat{n})}_{\text{harmonic space}}. \tag{2.19}$$

Theoretical predictions are typically formulated in harmonic space. The $a_{\ell m}$ coefficients are predicted to be *Gaussian random variables* with

$$\begin{cases} \langle a_{\ell m}\rangle = 0 \\ \langle a_{\ell m}a^*_{\ell' m'}\rangle = C_\ell \delta_{\ell\ell'}\delta_{mm'} \end{cases} \tag{2.20}$$

where:

- C_ℓ is the **angular power spectrum**; these quantities (parameterized by ℓ) characterize the $a_{\ell m}$ coefficients and are typically functions of cosmological parameters:

  $$C_\ell = C_\ell(\{\Omega_i\}), \tag{2.21}$$

  meaning they vary with changes in cosmological parameters.

- The Kronecker deltas $\delta_{\ell\ell'}\delta_{mm'}$ enforce the Gaussian assumption: the $a_{\ell m}$ are uncorrelated Gaussian variables, so different ℓ and m modes are statistically independent. The C_ℓ values thus measure the variance of the $a_{\ell m}$ coefficients.

If the $a_{\ell m}$ are Gaussian variables, any linear combination of them is also Gaussian, meaning δT is Gaussian. In general, characterizing a stochastic variable requires computing all possible correlation functions:

$$C_1 = \langle \delta T(\hat{n}_1)\delta T^*(\hat{n}_2)\rangle \qquad \text{(2-point correlation function)} \tag{2.22}$$

$$C_2 = \langle \delta T(\hat{n}_1)\delta T^*(\hat{n}_2)\delta T(\hat{n}_3)\rangle \qquad \text{(3-point correlation function)} \tag{2.23}$$

$$\vdots$$

However, for Gaussian δT, all *odd* correlation functions vanish:

$$C_{2n+1} = 0 \quad \forall\, n \in \mathbb{N}, \tag{2.24}$$

while *even* correlation functions are determined by the 2-point function:

$$C_{2n} = F_n(C_2) \quad \forall n \in \mathbb{N}. \tag{2.25}$$

In other words, all information is contained in the 2-point correlation function for Gaussian variables. Working under the Gaussian assumption, the 2-point correlation function is computed:

$$\begin{aligned} C_2 &= C_2(\hat{n}_1, \hat{n}_2) = \langle \delta T(\hat{n}_1) \delta T^*(\hat{n}_2) \rangle \\ &= \sum_{\ell m} \sum_{\ell' m'} \underbrace{\langle a_{\ell m} a^*_{\ell' m'} \rangle}_{C_\ell \delta_{\ell\ell'} \delta_{mm'}} Y_{\ell m}(\hat{n}_1) Y^*_{\ell' m'}(\hat{n}_2) \\ &= \sum_{\ell m} C_\ell Y_{\ell m}(\hat{n}_1) Y^*_{\ell m}(\hat{n}_2) = \sum_\ell C_\ell \sum_m Y_{\ell m}(\hat{n}_1) Y^*_{\ell m}(\hat{n}_2). \end{aligned} \tag{2.26}$$

Using the **addition theorem for spherical harmonics**:

$$\sum_{m=-\ell}^{\ell} Y_{\ell m}(\hat{n}_1) Y^*_{\ell m}(\hat{n}_2) = \frac{2\ell+1}{4\pi} P_\ell(\hat{n}_1 \cdot \hat{n}_2) = \frac{2\ell+1}{4\pi} P_\ell(\cos\theta), \tag{2.27}$$

the **2-point correlation function** is found:

$$C_2 = C(\hat{n}_1, \hat{n}_2) = \sum_\ell C_\ell \frac{2\ell+1}{4\pi} P_\ell(\hat{n}_1 \cdot \hat{n}_2). \tag{2.28}$$

This yields two key results:

1. The 2-point correlation function depends only on the angle $\cos\theta = \hat{n}_1 \cdot \hat{n}_2$ between observation directions, not on $\hat{n}_1$ and $\hat{n}_2$ individually. This demonstrates that the correlation function is *rotationally invariant.*

2. The set $\{C_\ell\}$ contains *all statistical information* about δT.

These results explain why C_ℓ is considered the fundamental quantity in CMB physics and analysis. This is also why the 2-point correlation function and power spectrum are sometimes used interchangeably.

Since C_ℓ represents the fundamental observable in CMB analysis, developing robust *estimators* for these quantities at each multipole ℓ is essential. In appendix C, the construction of the estimators $\hat{C}_\ell$ is presented, starting from the ideal case and progressively including realistic effects such as incomplete sky coverage, instrumental noise, and finite angular resolution.

2.2 CMB Polarization

The **linear polarization** of the observed CMB radiation arises from Thomson scattering during the epoch of recombination. While the decoupling of photons from matter is not instantaneous, photons undergo their final scatterings with free electrons in an anisotropic radiation field. This anisotropy, caused by temperature fluctuations and velocity fields, imparts a net linear polarization to the CMB. In contrast to a perfectly homogeneous and isotropic blackbody distribution (which produces unpolarized radiation), the presence of temperature fluctuations and quadrupole anisotropies generates preferential polarization directions [48].

Polarization measurements provide extensive information about the primordial universe and its evolution, particularly regarding the physics of recombination and potential signatures of primordial gravitational waves.

The **Stokes parameters** Q and U, commonly used in optics to characterize linear polarization, can describe CMB polarization as well.

For an electric field $\mathbf{E}$, the parameter Q is defined as:

$$Q = \langle E_x^2 \rangle - \langle E_y^2 \rangle, \tag{2.29}$$

and the parameter U corresponds to a 45° rotation:

$$U = \langle E_{x'}^2 \rangle - \langle E_{y'}^2 \rangle, \tag{2.30}$$

where the $x'y'$ plane is rotated 45° with respect to the xy plane.

The intensity I, cfr. eq. (2.3), is sometimes considered as a Stokes parameter as well:

$$I = \langle E_x^2 \rangle + \langle E_y^2 \rangle. \tag{2.31}$$

Unpolarized radiation (natural light) is characterized by $Q = U = 0$.

CMB polarization could also exhibit circular polarization, which is not produced by Thomson scattering under standard conditions. The description of this component, requiring a third Stokes parameter V, is omitted here, as it is important in some other theoretical models but not central to this discussion.

Since polarization arises from products of electric field components, it transforms as a rank-2 tensor. The **polarization tensor** $\underline{P}$ can be defined as:

$$\underline{P} = Q\sigma_3 + U\sigma_1 = \begin{pmatrix} Q & U \\ U & -Q \end{pmatrix}, \tag{2.32}$$

where σ_1 and σ_3 are two out of the three Pauli matrices

$$\sigma_1 = \begin{pmatrix} 0 & 1 \\ 1 & 0 \end{pmatrix}, \quad \sigma_2 = \begin{pmatrix} 0 & -i \\ i & 0 \end{pmatrix}, \quad \sigma_3 = \begin{pmatrix} 1 & 0 \\ 0 & -1 \end{pmatrix}. \tag{2.33}$$

This expression reveals the **spin-2 nature** of $\underline{P}$. The matrices $\underline{M}_{\pm}$ can be defined as:

$$\underline{M}_{\pm} = \frac{1}{2}(\sigma_3 \pm i\sigma_1) = \frac{1}{2}\begin{pmatrix} 1 & \pm i \\ \pm i & -1 \end{pmatrix} \tag{2.34}$$

allowing $\underline{P}$ to be expressed in terms of the rotationally invariant quantities $Q \pm iU$, as will be shown later:

$$\underline{P} = (Q + iU)\underline{M}_{+} + (Q - iU)\underline{M}_{-}. \tag{2.35}$$

The polarization tensor $\underline{P}$ can also be characterized by:

$$\text{Amplitude:} \quad \sqrt{Q^2 + U^2} \tag{2.36}$$

$$\text{Polarization direction:} \quad 2\phi = \arctan\left(\frac{U}{Q}\right) \tag{2.37}$$

These quantities are rotationally invariant: the polarization direction and amplitude remain unchanged under coordinate rotations of Q and U.

In order to construct a deeper mathematical description of what has just been discussed, the discussion can be started by considering that when describing polarized light from the sky, Stokes parameters are defined with respect to a fixed coordinate system. However, defining a rotationally invariant orthogonal basis on a sphere is impossible. While the coordinate system is well-defined over small patches, it becomes ambiguous when considering the full sky. Therefore, it becomes essential for cosmological predictions to employ two rotationally invariant quantities derived from U and Q: the electric-type and magnetic-type components E and B.

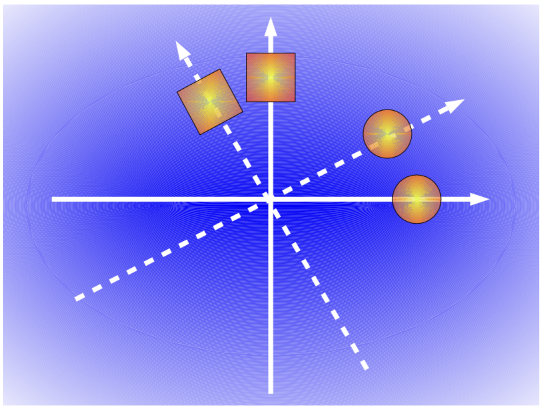

Figure 2.1: Different rotation properties of scalar and tensor functions. For scalars (represented as spheres), rotation affects only the argument. Components of higher-rank tensors (represented as squares) must account for both argument rotation and shape transformation.

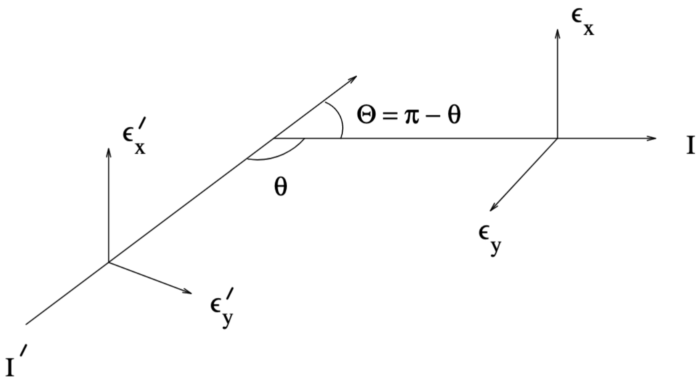

Figure 2.2: Reference frames describing light propagation during Thomson scattering. The incident unpolarized light propagates along the $\hat{e}'_z = \hat{n}'$ direction. The outgoing polarized light propagates along $\hat{e}_z = \hat{n}$, at an angle θ relative to the incident direction. Figure from [48]

For computational convenience, the polarization can be redefined with a rank-2 tensor I_{ij} (where $I_{ij} \equiv 2P_{ij}$, so $\underline{I} = 2\underline{P}$). The Stokes parameters relate to this tensor as:

$$\begin{cases} Q = \frac{I_{11}-I_{22}}{4} \\ U = \frac{I_{12}}{2} \end{cases} \Rightarrow \quad I_{ij} = 2P_{ij} = \begin{pmatrix} 2Q & 2U \\ 2U & -2Q \end{pmatrix}. \tag{2.38}$$

As illustrated in fig. 2.1, scalar quantities such as temperature remain invariant under rotations of angle ϕ around $\hat{n}$, while higher-rank tensors transform accordingly. Under rotation by angle ϕ, vectors transform as:

$$\hat{e}'_i = R_{ij}\hat{e}^j \quad \text{with} \quad R_{ij} = \begin{pmatrix} \cos\phi & \sin\phi \\ -\sin\phi & \cos\phi \end{pmatrix}, \tag{2.39}$$

so that the basis vectors transform as:

$$\begin{cases} \hat{e}'_1 = \hat{e}_1\cos\phi + \hat{e}_2\sin\phi \\ \hat{e}'_2 = -\hat{e}_1\sin\phi + \hat{e}_2\cos\phi \end{cases}. \tag{2.40}$$

Under rotation by angle ϕ, the Stokes parameters transform as:

$$\begin{cases} Q' = Q\cos(2\phi) + U\sin(2\phi) \\ U' = -Q\sin(2\phi) + U\cos(2\phi) \end{cases}. \tag{2.41}$$

Starting from the definitions in eq. (2.55), it is possible to derive that quadrupole anisotropies generate polarization. Consider Thomson scattering with incoming unpolarized light characterized by Stokes parameters (I', Q', U') and outgoing light with Stokes parameters (I, Q, U), as illustrated in fig. 2.2.

The Thomson scattering differential cross-section is given by

$$\frac{\mathrm{d}\sigma}{\mathrm{d}\Omega} = \frac{3\sigma_T}{8\pi}|\hat{\varepsilon}' \cdot \hat{\varepsilon}|^2, \tag{2.42}$$

where $\hat{\varepsilon}'$ is the polarization direction of the incident light, $\hat{\varepsilon}$ is the polarization direction of the scattered light, and σ_T is the total Thomson cross section. For this process, it is convenient to work with

$$I_x = \frac{I+Q}{2} \quad \text{and} \quad I_y = \frac{I-Q}{2}. \tag{2.43}$$

Imposing that the incoming light from a single direction is unpolarized, $I'_x = I'_y = I'/2$, one can determine I_x and I_y along a single outgoing direction by noting that $\mathrm{d}\sigma/\mathrm{d}\Omega$ provides the weights of the contributions to that direction:

$$I_x = \frac{3\sigma_T}{8\pi}\left[I'_x(\hat{\varepsilon}'_x \cdot \hat{\varepsilon}_x)^2 + I'_y(\hat{\varepsilon}'_y \cdot \hat{\varepsilon}_x)^2\right] = \frac{3\sigma_T}{16\pi}I', \tag{2.44}$$

$$I_y = \frac{3\sigma_T}{8\pi}\left[I'_x(\hat{\varepsilon}'_x \cdot \hat{\varepsilon}_y)^2 + I'_y(\hat{\varepsilon}'_y \cdot \hat{\varepsilon}_y)^2\right] = \frac{3\sigma_T}{16\pi}I'\cos^2\theta, \tag{2.45}$$

and consequently

$$I = I_x + I_y = \frac{3\sigma_T}{16\pi}I'(1+\cos^2\theta), \tag{2.46}$$

$$Q = I_x - I_y = \frac{3\sigma_T}{16\pi}I'\sin^2\theta. \tag{2.47}$$

To obtain the total scattered intensity I, one must sum over all possible contributions by integrating over all incident directions:

$$I = \frac{3\sigma_T}{16\pi}\int \mathrm{d}\Omega\, I'(\theta,\phi)(1+\cos^2\theta), \tag{2.48}$$

$$Q = \frac{3\sigma_T}{16\pi}\int \mathrm{d}\Omega\, I'(\theta,\phi)\sin^2\theta\cos(2\phi), \tag{2.49}$$

$$U = -\frac{3\sigma_T}{16\pi}\int \mathrm{d}\Omega\, I'(\theta,\phi)\sin^2\theta\sin(2\phi), \tag{2.50}$$

where Q and U have been obtained through eq. (2.41). By expanding $I'(\theta,\phi)$ in spherical harmonics (cf. eq. (2.13)), the integration yields

$$I = \frac{3\sigma_T}{16\pi}\left[\frac{8}{3}\sqrt{\pi}a_{00} + \frac{4}{3}\sqrt{\frac{\pi}{5}}a_{20}\right], \tag{2.51}$$

$$Q = \frac{3\sigma_T}{4\pi}\sqrt{\frac{2\pi}{15}}\Re[a_{22}], \tag{2.52}$$

$$U = -\frac{3\sigma_T}{4\pi}\sqrt{\frac{2\pi}{15}}\Im[a_{22}], \tag{2.53}$$

demonstrating that Q and U are determined by the quadrupole term a_{22}.

This transformation can be derived by expressing the electric field components more rigorously. With amplitudes a_i and phases θ_i:

$$E_x = a_x(t)\cos[\omega_0 t - \theta_x(t)], \quad E_y = a_y(t)\cos[\omega_0 t - \theta_y(t)], \tag{2.54}$$

the Stokes parameters become:

$$I = \langle a_x^2\rangle + \langle a_y^2\rangle, \tag{2.55}$$

$$Q = \langle a_x^2\rangle - \langle a_y^2\rangle, \tag{2.56}$$

$$U = \langle 2a_x a_y \cos(\theta_x - \theta_y)\rangle. \tag{2.57}$$

Transforming $\mathbf{E}$ under rotation eq. (2.40) yields E'_x and E'_y, from which a'_x, a'_y, and subsequently Q' and U' can be derived.

From the rotation properties described in eq. (2.41), two rotationally invariant parameters (up to a phase) can be constructed: $Q \pm iU$. Indeed:

$$Q' \pm iU' = Q\cos(2\phi) + U\sin(2\phi) \pm i(-Q\sin(2\phi) + U\cos(2\phi)) \tag{2.58}$$

$$= Q(\cos(2\phi) \mp i\sin(2\phi)) + iU(\cos(2\phi) \pm i\sin(2\phi)) \tag{2.59}$$

yielding:

$$Q' \pm iU' = (Q \pm iU)e^{\mp i2\phi}, \tag{2.60}$$

demonstrating that $Q \pm iU$ are **spin-2 quantities**, i.e. they transform with a phase factor of 2ϕ under a rotation of the reference frame by an angle ϕ. These are functions of the observation direction $\hat{n} = (\sin\theta\cos\phi, \sin\theta\sin\phi, \cos\theta)$: $(Q \pm iU) = (Q \pm iU)(\hat{n})$.

For full-sky analysis, expansion in spherical harmonics is employed, analogous to the temperature decomposition discussed previously. While the temperature field is scalar and expands using ordinary spherical harmonics, polarization quantities require expansion of $Q \pm iU$ using **spin-2 spherical harmonics** ${}_{\pm 2}Y_{\ell m}$ due to their spin-2 nature:

$$(Q \pm iU)(\hat{n}) = \sum_{\ell=0}^{\infty} \sum_{m=-\ell}^{\ell} a_{\pm 2,\ell m}\, {}_{\pm 2}Y_{\ell m}(\hat{n}), \tag{2.61}$$

with inverse relations:

$$a_{2,\ell m} = \int \mathrm{d}\Omega\, {}_{+2}Y^*_{\ell m}(\hat{n})(Q + iU)(\hat{n}), \tag{2.62}$$

$$a_{-2,\ell m} = \int \mathrm{d}\Omega\, {}_{-2}Y^*_{\ell m}(\hat{n})(Q - iU)(\hat{n}). \tag{2.63}$$

Linear combinations of these quantities define the **E- and B-mode harmonic coefficients**:

$$\begin{cases} E_{\ell m} = a_{E,\ell m} = -\frac{1}{2}(a_{2,\ell m} + a_{-2,\ell m}) \\ B_{\ell m} = a_{B,\ell m} = -\frac{1}{2i}(a_{2,\ell m} - a_{-2,\ell m}) \end{cases} \tag{2.64}$$

Under parity transformation $\hat{n} \to -\hat{n}$, E-mode coefficients remain unchanged while B-mode coefficients change sign. Indeed, using the parity property of spin-weighted harmonics

$${}_sY_{\ell m}(-\hat{n}) = (-1)^\ell\, {}_{-s}Y_{\ell m}(\hat{n}), \tag{2.65}$$

under parity transformations the harmonic coefficients transform as

$$a'_{s,\ell m} = \int d\Omega\, (Q \pm iU)(-\hat{n})\, {}_sY^*_{\ell m}(\hat{n}) = \int d\Omega\, (Q \pm iU)(\hat{n})\, {}_sY^*_{\ell m}(-\hat{n})$$

$$= (-1)^\ell \int d\Omega\, (Q \pm iU)(\hat{n})\, {}_{-s}Y^*_{\ell m}(\hat{n}) = (-1)^\ell a_{-s,\ell m}. \tag{2.66}$$

Therefore, using the definitions in eq. (2.64), one obtains

$$E'_{\ell m} = -\tfrac{1}{2}\left(a'_{2,\ell m} + a'_{-2,\ell m}\right) = -\tfrac{1}{2}(-1)^{\ell}\left(a_{-2,\ell m} + a_{2,\ell m}\right) = (-1)^{\ell} E_{\ell m}, \tag{2.67}$$

$$B'_{\ell m} = -\tfrac{1}{2i}\left(a'_{2,\ell m} - a'_{-2,\ell m}\right) = -\tfrac{1}{2i}(-1)^{\ell}\left(a_{-2,\ell m} - a_{2,\ell m}\right) = (-1)^{\ell+1} B_{\ell m}. \tag{2.68}$$

This demonstrates that E and B modes are eigenstates of parity transformation:

$$\hat{n} \xrightarrow{\mathcal{P}} -\hat{n} \quad \Rightarrow \quad \begin{cases} E \xrightarrow{\mathcal{P}} (-1)^{\ell} E & \text{(even parity)} \\ B \xrightarrow{\mathcal{P}} (-1)^{\ell+1} B & \text{(odd parity)} \end{cases} \tag{2.69}$$

E modes behave like vectors (electric field), while B modes behave like pseudovectors (magnetic field). Hence the terminology: **electric-type modes** and **magnetic-type modes**.

E and B modes allow the representation:

$$(Q \pm iU) = \sum_{\ell=0}^{\infty} \sum_{m=-\ell}^{\ell} (E_{\ell m} \pm iB_{\ell m})\, {}_{\pm 2}Y_{\ell m}(\hat{n}) = \sum_{\ell=0}^{\infty} \sum_{m=-\ell}^{\ell} (a_{E,\ell m} \pm i a_{B,\ell m})\, {}_{\pm 2}Y_{\ell m}(\hat{n}). \tag{2.70}$$

The polarization tensor $\underline{P}$ can be expressed following eq. (2.35). Defining:

$$Y^{E}_{\ell m} \underline{M}_E = \frac{1}{2}\left({}_2Y_{\ell m}\underline{M}_+ + {}_{-2}\, Y_{\ell m}\underline{M}_-\right), \tag{2.71}$$

$$Y^{B}_{\ell m} \underline{M}_B = \frac{1}{2i}\left({}_2Y_{\ell m}\underline{M}_+ - {}_{-2}\, Y_{\ell m}\underline{M}_-\right), \tag{2.72}$$

the polarization tensor becomes:

$$\underline{P} = \sum_{\ell=0}^{\infty} \sum_{m=-\ell}^{\ell} \left[E_{\ell m} Y^{E}_{\ell m}\underline{M}_E + B_{\ell m} Y^{B}_{\ell m}\underline{M}_B\right]. \tag{2.73}$$

The polarization has thus been decomposed into modes with patterns analogous to electromagnetic fields. E-mode polarization exhibits vectors that are radial around cold spots and tangential around hot spots, while B-mode polarization displays curl-like patterns with vectors exhibiting vorticity around any given point, regardless of temperature, as shown in fig. 2.3.

The **E-mode and B-mode scalar fields** are defined as:

$$E(\hat{n}) = \sum_{\ell=0}^{\infty} \sum_{m=-\ell}^{\ell} E_{\ell m} Y_{\ell m}(\hat{n}), \tag{2.74}$$

$$B(\hat{n}) = \sum_{\ell=0}^{\infty} \sum_{m=-\ell}^{\ell} B_{\ell m} Y_{\ell m}(\hat{n}). \tag{2.75}$$

These scalar fields are the primary quantities used in CMB polarization analysis.

The E and B decomposition is fundamental for several reasons and it is crucial in cosmology because it relates perturbations to polarization observables. While Q and U are the direct observables, the E and B geometric decomposition of $\underline{P}$ is more convenient in data analysis and physical descriptions: it separates polarization tensor components excited by scalar-type perturbations (E modes) from those excited by tensor-type perturbations (B modes), providing a direct link to the underlying physics of structure formation and primordial gravitational waves.

2.3 CMB Power Spectra

In section 2.1, the power spectrum C_ℓ was introduced as the two-point correlation function between temperature anisotropies. By describing the CMB signal with polarization modes E

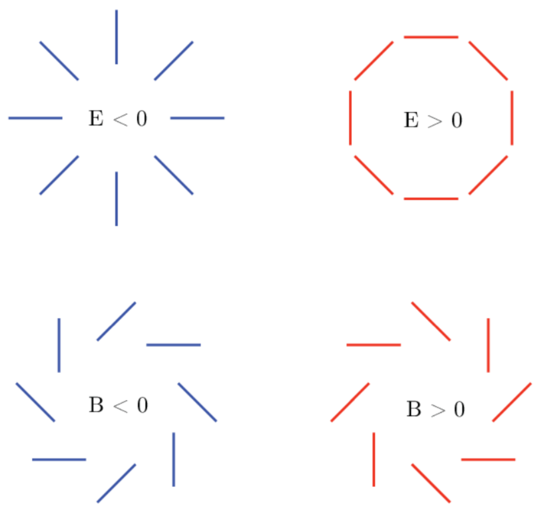

Figure 2.3: Polarization vectors around regions with different E and B mode signatures. E modes are parity-even (unchanged under mirror reflection), while B modes are parity-odd (sign-reversed under reflection).

and B, additional power spectra are introduced. Together with the temperature power spectrum C_ℓ (henceforth denoted C_ℓ^{TT}), which correlates temperature-temperature (TT) signals, other pure power spectra exist: C_ℓ^{EE} and C_ℓ^{BB}, correlating E-mode with E-mode and B-mode with B-mode signals, respectively. Moreover, cross-correlation spectra can be studied, such as C_ℓ^{EB}, C_ℓ^{TB}, and C_ℓ^{TE}.

The general formula for the power spectrum at a given multipole ℓ correlating quantities X and Y is

$$C_\ell^{XY} = \frac{1}{2\ell+1} \sum_{m=-\ell}^{\ell} \langle a_{X,\ell m}\, a^*_{Y,\ell m} \rangle, \tag{2.76}$$

where statistical isotropy implies that the expectation value $\langle a_{X,\ell m}\, a^*_{Y,\ell' m'} \rangle$ is diagonal in (ℓ, m) and independent of m. Indeed, assuming all coefficients follow Gaussian statistics:

$$\langle a_{X,\ell m} a^*_{Y,\ell' m'} \rangle = C_\ell^{XY} \delta_{\ell\ell'} \delta_{mm'}, \tag{2.77}$$

where Gaussian statistics implies no correlation between different ℓ and ℓ' or different m and m'. The averaging is performed over the entire sky.[1] The averaging over m at fixed ℓ stems from the underlying assumption of isotropy. As stated by [49]: *"assuming that the Universe is statistically isotropic with no preferred direction, one averages the squared coefficients over m to obtain the power spectra."*

C_ℓ^{XY} is actually an ensemble-averaged power spectrum, where the ensemble average is performed over a set of possible realizations of the CMB sky. Indeed, these formulas derive from the desire to characterize the *statistics* of how these quantities are distributed across the sky. The observed power spectrum of a single realization is instead an estimator of the true one,

$$\hat{C}_\ell^{XY} = \frac{1}{2\ell+1} \sum_{m=-\ell}^{\ell} a_{X,\ell m}\, a^*_{Y,\ell m}. \tag{2.78}$$

[1]These formulas follow from the orthogonality relation of spherical harmonics (forming a complete basis on the sphere):

$$\int_\Omega Y_{\ell m} Y^*_{\ell' m'} \mathrm{d}\Omega = 4\pi \delta_{\ell\ell'} \delta_{mm'}.$$

In appendix C, a more detailed analysis of the estimator $\hat{C}_\ell$ is presented.
The six CMB power spectra are:

$$C_\ell^{TT} = \frac{1}{2\ell+1}\sum_{m=-\ell}^{\ell}\langle a_{T,\ell m}a^*_{T,\ell m}\rangle, \tag{2.79}$$

$$C_\ell^{EE} = \frac{1}{2\ell+1}\sum_{m=-\ell}^{\ell}\langle a_{E,\ell m}a^*_{E,\ell m}\rangle = \frac{1}{2\ell+1}\sum_{m=-\ell}^{\ell}\langle E_{\ell m}E^*_{\ell m}\rangle, \tag{2.80}$$

$$C_\ell^{BB} = \frac{1}{2\ell+1}\sum_{m=-\ell}^{\ell}\langle a_{B,\ell m}a^*_{B,\ell m}\rangle = \frac{1}{2\ell+1}\sum_{m=-\ell}^{\ell}\langle B_{\ell m}B^*_{\ell m}\rangle, \tag{2.81}$$

$$C_\ell^{EB} = \frac{1}{2\ell+1}\sum_{m=-\ell}^{\ell}\langle a_{B,\ell m}a^*_{E,\ell m}\rangle = \frac{1}{2\ell+1}\sum_{m=-\ell}^{\ell}\langle E_{\ell m}B^*_{\ell m}\rangle, \tag{2.82}$$

$$C_\ell^{TE} = \frac{1}{2\ell+1}\sum_{m=-\ell}^{\ell}\langle a_{T,\ell m}a^*_{E,\ell m}\rangle, \tag{2.83}$$

$$C_\ell^{TB} = \frac{1}{2\ell+1}\sum_{m=-\ell}^{\ell}\langle a_{T,\ell m}a^*_{B,\ell m}\rangle. \tag{2.84}$$

On average, no cross-correlation exists between certain mode combinations:

$$C_\ell^{TB} = 0 \quad \text{and} \quad C_\ell^{EB} = 0, \tag{2.85}$$

provided parity is conserved in the processes that generate the CMB. This result can be understood by considering parity transformations: under parity, $T \to T$ and $B \to -B$, so the correlation $TB \to -TB$. Averaging over the entire celestial sphere causes these anti-symmetric contributions to cancel.

If physics beyond the Standard Model violates parity symmetry, then non-zero values should be observed:

$$C_\ell^{TB} \neq 0 \quad \text{and} \quad C_\ell^{EB} \neq 0. \tag{2.86}$$

These parity-violating correlations serve as sensitive probes of new physics, including axion-like particles, modified gravity theories, and other extensions to the Standard Model. The search for such signatures represents an active frontier in CMB cosmology, with current and future experiments designed to detect these subtle but potentially revolutionary signals.

2.4 Cosmic Birefringence

As demonstrated, CMB polarization is sensitive to physics beyond the Standard Model that violates parity symmetry under spatial coordinate inversion. If dark energy or dark matter (individually or collectively) exhibit parity-violating properties, polarized CMB light can provide insights into their nature and help address fundamental questions about these components. When parity symmetry is broken by new physics beyond the Standard Model, TB and EB correlations arise, generating non-zero C_ℓ^{TB} and C_ℓ^{EB} power spectra.

Among the various mechanisms that can generate parity violation and/or TB and EB correlations, one is particularly compelling because it involves the **axion** field a—currently one of the most promising dark matter or dark energy (depending on the mass) candidates.

If parity violation occurs through a coupling between an axion-like scalar field a and the electromagnetic field $F^{\mu\nu}$, the Universe filled with a acts as a birefringent medium, affecting CMB polarization.

The axion field a was introduced to solve the **strong CP problem**—the puzzle of why CP symmetry is not significantly violated by strong interactions despite theoretical expectations.

The QCD Lagrangian contains a CP-violating topological term:

$$\mathcal{L}_{\mathrm{CP}} = \bar{\vartheta}\frac{\alpha_s}{8\pi}G_a^{\mu\nu}\tilde{G}_{a\mu\nu}, \tag{2.87}$$

where $\bar{\vartheta} = \vartheta + \arg(\det(M_q))$ combines the QCD θ-parameter with phases from the quark mass matrix M_q. This term arises from the non-trivial vacuum structure of non-Abelian gauge theories.

The topological term induces a neutron electric dipole moment $d_n \simeq 10^{-16}\bar{\vartheta}\, e\,\mathrm{cm}$. Experimental measurements constrain $d_n^{\mathrm{exp}} \leq 1.8 \times 10^{-26}\, e\,\mathrm{cm}$, requiring $\bar{\vartheta} \leq 10^{-10}$. This represents the strong CP problem: two unrelated physical quantities must cancel with extraordinary precision to yield $\bar{\vartheta} \simeq 0$.

The Peccei-Quinn mechanism resolves this fine-tuning by introducing the axion field a:

$$\mathcal{L}_{\mathrm{PQ}} = \frac{a}{f_a}\frac{\alpha_s}{8\pi}G_a^{\mu\nu}\tilde{G}_{a\mu\nu}, \tag{2.88}$$

where f_a is the axion decay constant. This allows $\bar{\vartheta}$ to dynamically relax to zero, naturally solving the CP problem.

The axion couples to electromagnetic fields through a similar **Chern-Simons interaction**:

$$\mathcal{L}_{\mathrm{CS}} = -\frac{g_{a\gamma\gamma}}{4}aF_{\mu\nu}\tilde{F}^{\mu\nu}, \tag{2.89}$$

where $g_{a\gamma\gamma} \propto 1/f_a$ is the axion-photon coupling and by definition:

$$F_{\mu\nu} = \partial_\mu A_\nu - \partial_\nu A_\mu \quad \text{and} \quad \tilde{F}_{\mu\nu} = \frac{1}{2}\varepsilon_{\mu\nu\alpha\beta}F^{\alpha\beta}, \tag{2.90}$$

where

$$A_\mu = (\phi, \mathbf{A}) \tag{2.91}$$

is the quadripotential which collects the scalar electric potential ϕ and the vector potential $\mathbf{A}$.

In the convention adopted throughout this work, $F_{\mu\nu}$ is written with respect to the electric and magnetic fields components as

$$F_{\mu\nu} = \begin{pmatrix} 0 & -E_x/c & -E_y/c & -E_z/c \\ E_x/c & 0 & -B_z & B_y \\ E_y/c & B_z & 0 & -B_x \\ E_z/c & -B_y & B_x & 0 \end{pmatrix}. \tag{2.92}$$

More generally, **axion-like particles (ALPs)** describe light pseudoscalar fields with similar physics but not necessarily tied to solving the strong CP problem.

A parity-violating coupling between an axion-like field[2] a and the electromagnetic field was first proposed by [50] in 1989.

The invariant product $F\tilde{F}$ can be expressed as:

$$F_{\mu\nu}\tilde{F}^{\mu\nu} = -4\mathbf{E}\cdot\mathbf{B}, \tag{2.93}$$

[2]The axion field is denoted by a in this chapter and throughout the work. However, to prevent notational conflicts with the cosmological scale factor (also denoted by a in earlier chapters), the symbol χ will be adopted for the axion field in contexts where both quantities are simultaneously discussed.

which changes sign under parity transformation. Assuming a is a pseudoscalar, the Lagrangian remains invariant while parity violation occurs through the field dynamics.

Analysis of the electromagnetic field equations with axion coupling reveals a helicity-dependent dispersion relation, yielding different phase velocities for the two circular polarization states [49]:

$$\frac{\omega_\pm}{k} \simeq 1 \pm \frac{g_{a\gamma\gamma} a'}{2}, \tag{2.94}$$

where $a' = \mathrm{d}a/\mathrm{d}\eta$ is the time derivative of the axion field with respect to conformal time.

This difference in phase velocities leads to rotation of the polarization plane. Even when the second term is extremely small, the cumulative effect may become significant during photon propagation from the last scattering surface to observation. The two helicity states evolve as $E_\pm \propto e^{-i\int \mathrm{d}\eta\, \omega_\pm}$, causing the Stokes parameters to rotate by an angle β:

$$\beta(\eta_0) = -\frac{1}{2}\int_{\eta_{\rm LSS}}^{\eta_0} \mathrm{d}\eta\, (\omega_+ - \omega_-) = \frac{g_{a\gamma\gamma}}{2}[a(\eta_{\rm LSS}) - a(\eta_0)], \tag{2.95}$$

where $\eta_{\rm LSS}$ is the conformal time at the last scattering surface and η_0 is the present conformal time.

The observed Stokes parameters are then related to the primordial values through:

$$Q^{\rm obs} \pm iU^{\rm obs} = (Q^{\rm prim} \pm iU^{\rm prim})e^{\pm 2i\beta}, \tag{2.96}$$

where the superscript "prim" denotes primordial values at the last scattering surface (it will be dropped off in the next), and "obs" indicates the values observed today.

This rotation mechanism, known as **cosmic birefringence**, provides a direct probe of axion-like dark matter or dark energy and other parity-violating physics. The effect can manifest as either isotropic rotation (uniform across the sky) and/or anisotropic rotation (direction-dependent), each carrying different information about the underlying axion field dynamics and cosmological evolution. In particular, an anisotropic birefringence field $\beta(\hat{n})$ may exist even if its sky-averaged (isotropic) component vanishes, i.e. $\langle\beta(\hat{n})\rangle = 0$. In this case, the ensemble-averaged parity-violating correlations vanish, $\langle C_\ell^{EB}\rangle = \langle C_\ell^{TB}\rangle = 0$, although local anisotropies in $\beta(\hat{n})$ still induce measurable mode couplings between E and B modes. Such a scenario represents a pure anisotropic birefringence case, where parity violation is present but averages out globally.

2.4.1 How Isotropic Cosmic Birefringence Changes the Power Spectra

Taking the decomposition of the linear polarization $Q(\hat{n}) \pm iU(\hat{n})$ in terms of E and B modes, the expansion can be written as:

$$Q(\hat{n}) \pm iU(\hat{n}) = \sum_{\ell=0}^{\infty}\sum_{m=-\ell}^{\ell} (E_{\ell m} \pm iB_{\ell m})\, {}_{\pm 2}Y_{\ell m}(\hat{n}). \tag{2.97}$$

If the Universe is filled with an axion-like scalar field a that generates cosmic birefringence, a rotation of the polarization plane by angle β occurs. In presence of **Isotropic Cosmic Birefringence (ICB)** β is constant. The linear polarization rotates by angle β, so the observed quantities become the primordial quantities rotated according to the spin-2 nature of the Stokes parameters:

$$Q^{\rm obs} \pm iU^{\rm obs} = (Q^{\rm prim} \pm iU^{\rm prim})e^{\pm 2i\beta}, \tag{2.98}$$

where the left-hand side represents observed quantities and the right-hand side represents primordial quantities at the last scattering surface.

From eqs. (2.97) and (2.98):

$$E_{\ell m}^{\rm obs} \pm iB_{\ell m}^{\rm obs} = (E_{\ell m} \pm iB_{\ell m})e^{\pm 2i\beta}. \tag{2.99}$$

Expanding the exponential:

$$E_{\ell m}^{\rm obs} \pm iB_{\ell m}^{\rm obs} = (E_{\ell m} \pm iB_{\ell m})[\cos(\pm 2\beta) + i\sin(\pm 2\beta)] \tag{2.100}$$
$$= (E_{\ell m} \pm iB_{\ell m})[\cos(2\beta) \pm i\sin(2\beta)]. \tag{2.101}$$

Performing the multiplication:

$$E_{\ell m}^{\rm obs} \pm iB_{\ell m}^{\rm obs} = E_{\ell m}\cos(2\beta) \pm iE_{\ell m}\sin(2\beta) \pm iB_{\ell m}\cos(2\beta) - B_{\ell m}\sin(2\beta) \tag{2.102}$$
$$= E_{\ell m}\cos(2\beta) - B_{\ell m}\sin(2\beta) \pm i\left(E_{\ell m}\sin(2\beta) + B_{\ell m}\cos(2\beta)\right), \tag{2.103}$$

yielding:

$$\begin{cases} E_{\ell m}^{\rm obs} = E_{\ell m}\cos(2\beta) - B_{\ell m}\sin(2\beta) \\ B_{\ell m}^{\rm obs} = E_{\ell m}\sin(2\beta) + B_{\ell m}\cos(2\beta) \end{cases}. \tag{2.104}$$

From eq. (2.104), the observed power spectra can be computed as functions of the primordial power spectra (those at the last scattering surface). These differ from the primordial spectra due to birefringence effects.

- $C_\ell^{EE,\rm obs}$: From the definition:

$$C_\ell^{EE,\rm obs} = \frac{1}{2\ell+1}\sum_{m=-\ell}^{\ell}\langle E_{\ell m}^{\rm obs}E_{\ell m}^{\rm obs*}\rangle. \tag{2.105}$$

Substituting eq. (2.104):

$$\begin{aligned} C_\ell^{EE,\rm obs} &= \frac{1}{2\ell+1}\sum_{m=-\ell}^{\ell}\langle(E_{\ell m}\cos(2\beta) - B_{\ell m}\sin(2\beta))(E_{\ell m}^*\cos(2\beta) - B_{\ell m}^*\sin(2\beta))\rangle \\ &= \frac{1}{2\ell+1}\sum_{m=-\ell}^{\ell}\langle E_{\ell m}E_{\ell m}^*\rangle\cos^2(2\beta) - \langle E_{\ell m}B_{\ell m}^*\rangle\cos(2\beta)\sin(2\beta) \\ &\quad - \langle B_{\ell m}E_{\ell m}^*\rangle\sin(2\beta)\cos(2\beta) + \langle B_{\ell m}B_{\ell m}^*\rangle\sin^2(2\beta) \\ &= C_\ell^{EE}\cos^2(2\beta) + C_\ell^{BB}\sin^2(2\beta) - \frac{\sin(2\beta)\cos(2\beta)}{2\ell+1}\sum_{m=-\ell}^{\ell}\langle E_{\ell m}B_{\ell m}^* + E_{\ell m}^*B_{\ell m}\rangle. \end{aligned}$$

Using the identity:

$$\frac{\langle E_{\ell m}B_{\ell m}^*\rangle + \langle E_{\ell m}^*B_{\ell m}\rangle}{2} = \Re[\langle E_{\ell m}B_{\ell m}^*\rangle] \quad\Leftrightarrow\quad \langle E_{\ell m}B_{\ell m}^*\rangle + \langle E_{\ell m}^*B_{\ell m}\rangle = 2\Re[\langle E_{\ell m}B_{\ell m}^*\rangle] \tag{2.106}$$

and the definition of C_ℓ^{EB}:

$$\boxed{C_\ell^{EE,\rm obs} = C_\ell^{EE}\cos^2(2\beta) + C_\ell^{BB}\sin^2(2\beta) - C_\ell^{EB}\sin(4\beta)} \tag{2.107}$$

- $C_\ell^{BB,\rm obs}$: From the definition:

$$C_\ell^{BB,\rm obs} = \frac{1}{2\ell+1}\sum_{m=-\ell}^{\ell}\langle B_{\ell m}^{\rm obs}B_{\ell m}^{\rm obs*}\rangle. \tag{2.108}$$

Substituting eq. (2.104):

$$
\begin{aligned}
C_\ell^{BB,\mathrm{obs}} &= \frac{1}{2\ell+1}\sum_{m=-\ell}^{\ell}\langle (E_{\ell m}\sin(2\beta)+B_{\ell m}\cos(2\beta))(E^*_{\ell m}\sin(2\beta)+B^*_{\ell m}\cos(2\beta))\rangle \\
&= \frac{1}{2\ell+1}\sum_{m=-\ell}^{\ell}\langle E_{\ell m}E^*_{\ell m}\rangle \sin^2(2\beta)+\langle E_{\ell m}B^*_{\ell m}\rangle \sin(2\beta)\cos(2\beta) \\
&\quad + \langle B_{\ell m}E^*_{\ell m}\rangle \cos(2\beta)\sin(2\beta)+\langle B_{\ell m}B^*_{\ell m}\rangle \cos^2(2\beta) \\
&= C_\ell^{EE}\sin^2(2\beta)+C_\ell^{BB}\cos^2(2\beta)+\frac{\sin(2\beta)\cos(2\beta)}{2\ell+1}\sum_{m=-\ell}^{\ell}\langle E_{\ell m}B^*_{\ell m}+E^*_{\ell m}B_{\ell m}\rangle,
\end{aligned}
$$

yielding:

$$
\boxed{C_\ell^{BB,\mathrm{obs}} = C_\ell^{EE}\sin^2(2\beta)+C_\ell^{BB}\cos^2(2\beta)+C_\ell^{EB}\sin(4\beta)} \tag{2.109}
$$

- $C_\ell^{EB,\mathrm{obs}}$: From the definition:

$$
C_\ell^{EB,\mathrm{obs}} = \frac{1}{2\ell+1}\sum_{m=-\ell}^{\ell}\langle E^{\mathrm{obs}}_{\ell m}B^{\mathrm{obs}*}_{\ell m}\rangle = \frac{1}{2\ell+1}\sum_{m=-\ell}^{\ell}\frac{\langle E^{\mathrm{obs}}_{\ell m}B^{\mathrm{obs}*}_{\ell m}\rangle+\langle E^{\mathrm{obs}*}_{\ell m}B^{\mathrm{obs}}_{\ell m}\rangle}{2}. \tag{2.110}
$$

Substituting eq. (2.104) and expanding:

$$
\begin{aligned}
C_\ell^{EB,\mathrm{obs}} &= \frac{1}{2\ell+1}\frac{1}{2}\sum_{m=-\ell}^{\ell}\langle E_{\ell m}E^*_{\ell m}\rangle\sin(4\beta)+\langle E_{\ell m}B^*_{\ell m}\rangle\cos(4\beta) \\
&\quad +\langle E^*_{\ell m}B_{\ell m}\rangle\cos(4\beta)-\langle B_{\ell m}B^*_{\ell m}\rangle\sin(4\beta) \\
&= \frac{\sin(4\beta)}{2}C_\ell^{EE}+\cos(4\beta)C_\ell^{EB}-\frac{\sin(4\beta)}{2}C_\ell^{BB},
\end{aligned}
$$

yielding:

$$
\boxed{C_\ell^{EB,\mathrm{obs}} = \frac{1}{2}\sin(4\beta)\left(C_\ell^{EE}-C_\ell^{BB}\right)+\cos(4\beta)C_\ell^{EB}} \tag{2.111}
$$

- $C_\ell^{TT,\mathrm{obs}}$:

The rotation angle β does not affect the temperature T, which is a scalar invariant under rotation:

$$
T \xrightarrow{R} T \quad \Rightarrow \quad T_{\ell m} \xrightarrow{R} T_{\ell m}, \tag{2.112}
$$

where $T = \sum_{\ell=0}^{\infty}\sum_{m=-\ell}^{\ell} T_{\ell m}Y_{\ell m}$.

The observed coefficients $T^{\mathrm{obs}}_{\ell m}$ are identical to the primordial ones:

$$
T^{\mathrm{obs}}_{\ell m} = T_{\ell m}, \tag{2.113}
$$

therefore:

$$
C_\ell^{TT,\mathrm{obs}} = \frac{1}{2\ell+1}\sum_{m=-\ell}^{\ell}\langle T^{\mathrm{obs}}_{\ell m}T^{\mathrm{obs}*}_{\ell m}\rangle = \frac{1}{2\ell+1}\sum_{m=-\ell}^{\ell}\langle T_{\ell m}T^*_{\ell m}\rangle = C_\ell^{TT} \tag{2.114}
$$

$$
\boxed{C_\ell^{TT,\mathrm{obs}} = C_\ell^{TT}} \tag{2.115}
$$

- $C_\ell^{TE,\mathrm{obs}}$: From the definition:

$$C_\ell^{TE,\mathrm{obs}} = \frac{1}{2\ell+1}\sum_{m=-\ell}^{\ell}\langle T_{\ell m}^{\mathrm{obs}} E_{\ell m}^{\mathrm{obs}*}\rangle = \frac{1}{2\ell+1}\sum_{m=-\ell}^{\ell}\frac{\langle T_{\ell m}^{\mathrm{obs}} E_{\ell m}^{\mathrm{obs}*}\rangle + \langle T_{\ell m}^{\mathrm{obs}*} E_{\ell m}^{\mathrm{obs}}\rangle}{2}. \tag{2.116}$$

Substituting eq. (2.104):

$$\begin{aligned} C_\ell^{TE,\mathrm{obs}} &= \frac{1}{2\ell+1}\frac{1}{2}\sum_{m=-\ell}^{\ell}\langle T_{\ell m}E_{\ell m}^*\rangle\cos(2\beta) - \langle T_{\ell m}B_{\ell m}^*\rangle\sin(2\beta) \\ &\quad + \langle T_{\ell m}^* E_{\ell m}\rangle\cos(2\beta) - \langle T_{\ell m}^* B_{\ell m}\rangle\sin(2\beta) \\ &= \frac{1}{2\ell+1}\sum_{m=-\ell}^{\ell}\frac{\langle T_{\ell m}E_{\ell m}^*\rangle + \langle T_{\ell m}^* E_{\ell m}\rangle}{2}\cos(2\beta) \\ &\quad - \frac{1}{2\ell+1}\sum_{m=-\ell}^{\ell}\frac{\langle T_{\ell m}B_{\ell m}^*\rangle + \langle T_{\ell m}^* B_{\ell m}\rangle}{2}\sin(2\beta) \end{aligned}$$

$$\boxed{C_\ell^{TE,\mathrm{obs}} = C_\ell^{TE}\cos(2\beta) - C_\ell^{TB}\sin(2\beta)} \tag{2.117}$$

- $C_\ell^{TB,\mathrm{obs}}$: From the definition:

$$C_\ell^{TB,\mathrm{obs}} = \frac{1}{2\ell+1}\sum_{m=-\ell}^{\ell}\langle T_{\ell m}^{\mathrm{obs}} B_{\ell m}^{\mathrm{obs}*}\rangle = \frac{1}{2\ell+1}\sum_{m=-\ell}^{\ell}\frac{\langle T_{\ell m}^{\mathrm{obs}} B_{\ell m}^{\mathrm{obs}*}\rangle + \langle T_{\ell m}^{\mathrm{obs}*} B_{\ell m}^{\mathrm{obs}}\rangle}{2}. \tag{2.118}$$

By analogous calculation:

$$C_\ell^{TB,\mathrm{obs}} = \frac{1}{2\ell+1}\frac{1}{2}\sum_{m=-\ell}^{\ell}\langle T_{\ell m}E_{\ell m}^*\rangle\sin(2\beta) + \langle T_{\ell m}B_{\ell m}^*\rangle\cos(2\beta) + \langle T_{\ell m}^* E_{\ell m}\rangle\sin(2\beta) + \langle T_{\ell m}^* B_{\ell m}\rangle\cos(2\beta) \tag{2.119}$$

$$\boxed{C_\ell^{TB,\mathrm{obs}} = C_\ell^{TE}\sin(2\beta) + C_\ell^{TB}\cos(2\beta)} \tag{2.120}$$

In summary, due to birefringence which rotates the Stokes parameters and linear polarization, the observed power spectra differ from the primordial ones according to:

$$C_\ell^{EE,\mathrm{obs}} = C_\ell^{EE}\cos^2(2\beta) + C_\ell^{BB}\sin^2(2\beta) - C_\ell^{EB}\sin(4\beta), \tag{2.121}$$

$$C_\ell^{BB,\mathrm{obs}} = C_\ell^{EE}\sin^2(2\beta) + C_\ell^{BB}\cos^2(2\beta) + C_\ell^{EB}\sin(4\beta), \tag{2.122}$$

$$C_\ell^{EB,\mathrm{obs}} = \frac{1}{2}\sin(4\beta)\left(C_\ell^{EE} - C_\ell^{BB}\right) + \cos(4\beta)\,C_\ell^{EB}, \tag{2.123}$$

$$C_\ell^{TT,\mathrm{obs}} = C_\ell^{TT}, \tag{2.124}$$

$$C_\ell^{TE,\mathrm{obs}} = C_\ell^{TE}\cos(2\beta) - C_\ell^{TB}\sin(2\beta), \tag{2.125}$$

$$C_\ell^{TB,\mathrm{obs}} = C_\ell^{TE}\sin(2\beta) + C_\ell^{TB}\cos(2\beta). \tag{2.126}$$

If there is no birefringence effect, $\beta = 0$ and the observed power spectra are identical to those generated at the last scattering surface. Note that in the computation above, primordial EB and TB power spectra have been included to maintain generality, allowing for other effects that might generate such correlations. In the case of the ΛCDM model, these power spectra are null ($C_\ell^{EB} = C_\ell^{TB} = 0$) and the system reduces to:

$$C_\ell^{EE,\mathrm{obs}} = C_\ell^{EE} \cos^2(2\beta) + C_\ell^{BB} \sin^2(2\beta), \tag{2.127}$$

$$C_\ell^{BB,\mathrm{obs}} = C_\ell^{EE} \sin^2(2\beta) + C_\ell^{BB} \cos^2(2\beta), \tag{2.128}$$

$$C_\ell^{EB,\mathrm{obs}} = \frac{1}{2} \sin(4\beta) \left(C_\ell^{EE} - C_\ell^{BB} \right), \tag{2.129}$$

$$C_\ell^{TT,\mathrm{obs}} = C_\ell^{TT}, \tag{2.130}$$

$$C_\ell^{TE,\mathrm{obs}} = C_\ell^{TE} \cos(2\beta), \tag{2.131}$$

$$C_\ell^{TB,\mathrm{obs}} = C_\ell^{TE} \sin(2\beta). \tag{2.132}$$

Chapter 3

Third order corrections to Slow-Roll Inflationary Predictions

As introduced in section 1.8, cosmic inflation represents the most successful mechanism for explaining a wide range of cosmological observations, particularly the anisotropies of the Cosmic Microwave Background (CMB). The theory provides a compelling framework for understanding the initial conditions of the Universe, where spacetime inhomogeneities amplified during the inflationary expansion serve as the seeds necessary for the formation of the large-scale structure (LSS) observed today. During this epoch, quantum fluctuations of the inflaton field—a scalar field that drives inflation—are stretched to macroscopic scales through exponential expansion. These fluctuations constitute the origin of density perturbations and gravitational waves, eventually manifesting as the temperature and polarization anisotropies observed in the CMB and the inhomogeneous distribution of galaxies throughout the Universe.

Since the introduction of inflationary theory, a vast class of models has been developed to explain the underlying mechanism, as collected and reviewed in the Encyclopædia Inflationaris [51]. These models stem from the extensive variety of possible inflaton potentials $V(\phi)$, which can be motivated by diverse theoretical frameworks spanning quantum gravity, string theory, and supergravity. Consequently, it becomes essential to distinguish and constrain inflationary models through precise cosmological observations. Furthermore, developing accurate theoretical predictions is crucial for establishing robust parametrizations of inflationary observables and conducting meaningful comparisons with observational data.

As discussed in section 1.8.2, the primordial power spectra (PPS) of scalar and tensor perturbations represent the fundamental theoretical quantities connecting inflationary dynamics to observable CMB anisotropies and LSS. While the phenomenological parametrization introduced in eq. (1.120) provides a useful framework for comparing observations with theoretical predictions, the nearly scale-invariant nature of the PPS—confirmed by *Planck* observations—enables a more rigorous analytical treatment through higher-order corrections in the slow-roll expansion. These corrections systematically account for the scale-dependent evolution of spectral indices and their runnings, thereby refining theoretical predictions beyond the simple power-law approximation.

Observational consistency requires contemporary inflationary scenarios to satisfy the slow-roll conditions, which ensure that the inflaton field remains dominated by potential energy while evolving gradually down its potential, with negligible kinetic energy and acceleration. This slow-roll regime ensures that the inflationary epoch persists for a sufficient duration and generates observables consistent with current measurements. Fortunately, within this framework, it becomes possible to develop a robust and model-independent theoretical description of inflaton dynamics through the Hubble Flow Functions (HFFs) introduced in eq. (1.122), thereby establishing a rigorous mathematical foundation for the PPS beyond the phenomenological parametrization.

The dynamics of both scalar and tensor perturbations $\delta\phi$ in the inflaton field ϕ are governed by the Mukhanov-Sasaki equation [52, 53]. Under the slow-roll approximation, this equation can be solved perturbatively using the HFFs that characterize the inflationary dynamics. Once solutions are obtained to a given order in the slow-roll expansion, the corresponding perturbative form of the PPS can be extracted to that same order of approximation, providing increasingly precise theoretical predictions for comparison with observations.

The perturbative solutions to the primordial power spectra are systematically classified according to their order in the slow-roll expansion:

- **Leading Order (LO)**: The zeroth-order solution, corresponding to the pure power-law parametrization.
- **Next-to-Leading Order (NLO)**: First-order corrections in slow-roll parameters.
- **Next-to-Next-to-Leading Order (NNLO or N2LO)**: Second-order corrections [54, 55, 56].
- **Next-to-Next-to-Next-to-Leading Order (N3LO)**: Third-order corrections [57, 58].

This analytical approach enables precise connections between expansion parameters and the physical parameters of single-field slow-roll inflationary models, facilitating robust parameter inference and model testing. The accuracy of these analytical predictions has become increasingly crucial in light of forthcoming cosmological surveys such as LiteBIRD [59] and Simons Observatory [42] for CMB observations, and Euclid [60, 61, 62, 63] for LSS measurements, which all promise significant improvements in the precision of cosmological measurements across multiple observational channels. As observational precision continues to advance, theoretical predictions must achieve correspondingly higher levels of accuracy to fully exploit the constraining power of next-generation experiments.

The work presented in [1] encompasses one of the research projects pursued in this thesis, where scalar and tensor perturbations are calculated up to third-order corrections in the slow-roll expansion. While initial computations of these results were presented by [57], this work obtains them through a different analytical approach to the integral evaluations. Furthermore, the final results are systematically compared with those obtained in [57] and validated against numerical solutions of the Mukhanov-Sasaki and tensor perturbation equations to assess the effectiveness and importance of third-order PPS solutions.

The numerical code `PyPPSinflation`, developed specifically for this research, computes numerical PPS from the Mukhanov-Sasaki equation solutions and compares them with analytical approximations at first, second, and third order. This code has been made publicly available[1]. Given the sensitivity of current CMB surveys, including *Planck* [64], ACT [65], SPT [19], and BICEP/Keck [39], constraints on slow-roll parameters are derived in [1] by comparing different truncation orders of the PPS expansion. The analysis investigates implications for spectral indices, their runnings, and higher-order running parameters. Additionally, forecasts for future cosmic-variance limited CMB space missions are presented.

The subsequent sections of this chapter are based on the work [1].

3.1 Mukhanov-Sasaki Equation and the Green Function Method

The first work that proposed the N2LO solution was by Stewart and Gong [54], who constructed a general analytical approach using the Green function method applied to the Mukhanov-Sasaki equation. This pioneering work established the theoretical foundation for systematic perturbative calculations of primordial power spectra beyond the leading-order approximation.

For more than two decades, the Stewart-Gong framework remained the state-of-the-art approach for higher-order slow-roll calculations. It was not until the work of Auclair and

[1] https://github.com/SirlettiSS/PyPPSinflation

Ringeval [57], published more than 20 years after the original Stewart-Gong analysis, that the N3LO solution was proposed for the first time, extending the perturbative expansion to third order in slow-roll parameters and opening new possibilities for precision cosmology.

The Mukhanov-Sasaki equation governs the evolution of gauge-invariant scalar perturbations during inflation and serves as the fundamental starting point for all analytical calculations of primordial power spectra. For a scalar field ϕ with potential $V(\phi)$, the equation describes the dynamics of the comoving curvature perturbation ζ in Fourier space.

To derive this equation, it is necessary to start from the most general form of scalar linear perturbations on the homogeneous and isotropic background metric, which can be written in the Bardeen's gauge as [66]

$$\mathrm{d}s^2 = a^2(\eta)\left\{(1+2A)\mathrm{d}\eta^2 - 2\partial_i B\mathrm{d}x^i\mathrm{d}\eta - [(1+2\mathcal{R})\delta_{ij} + 2\partial_i\partial_j H_T]\mathrm{d}x^i\mathrm{d}x^j\right\}, \tag{3.1}$$

where the homogeneous and isotropic background is perturbed by four scalar functions: A represents the lapse function perturbation, B describes the shift vector potential, while $\mathcal{R}$ and H_T characterize the trace and traceless components of the spatial metric perturbations, respectively. These quantities are gauge-dependent.

The gauge-invariant comoving curvature perturbation ζ is then constructed as

$$\zeta = \mathcal{R} - \frac{H}{\dot\phi}\delta\phi, \tag{3.2}$$

which relates the spatial curvature perturbation $\mathcal{R}$ to the inflaton field perturbation $\delta\phi$ in a gauge-invariant combination.

The power spectrum of the curvature perturbation, given by the 2-point correlation function $\langle\zeta(\mathbf{x},\eta)\zeta(\mathbf{y},\eta)\rangle$, is

$$\mathcal{P}_\zeta(k) = \left(\frac{H}{2\pi}\right)^2\left(\frac{H}{\dot\phi}\right)^2\Big|_{k=aH} = \frac{H^4}{4\pi^2\dot\phi^2} = \frac{H^2}{8\pi^2\epsilon_1}. \tag{3.3}$$

This represents only the leading order of the scalar PPS, denoted as $\mathcal{P}_{\zeta,0}$. Higher-order corrections can be systematically included through a perturbative approach.

To determine $\mathcal{P}_\zeta(k)$ analytically, a systematic approach to scalar-field perturbations is required. The starting point is the action for the scalar field ϕ minimally coupled with gravity and including a self-interaction potential $V(\phi)$, which describes the effective action during inflation:

$$\mathscr{S} = \int \mathrm{d}^4x\sqrt{-g}\left[-\frac{1}{2}R + \frac{1}{2}(\partial_\mu\phi)^2 - V(\phi)\right]. \tag{3.4}$$

Two key quantities can be defined:

$$z = \frac{a\dot\phi}{H} \tag{3.5}$$

and

$$\varphi = a\left(\delta\phi - \dot\phi\frac{\mathcal{R}}{H}\right) = -z\zeta, \tag{3.6}$$

where φ represents the perturbations of the scalar field in comoving coordinates, i.e., $\varphi \equiv (\delta\phi)_c$. From the definition of the perturbations φ, the effective action related to the perturbations is written as

$$\mathscr{S} = \int \mathrm{d}^3x\mathrm{d}\eta\ \mathcal{L} = \int \mathrm{d}^3x\mathrm{d}\eta\ \frac{1}{2}\left[\left(\frac{\partial\varphi}{\partial\eta}\right)^2 - (\nabla\varphi)^2 + \left(\frac{1}{z}\frac{\mathrm{d}^2z}{\mathrm{d}\eta^2}\right)\varphi^2\right], \tag{3.7}$$

where η is the conformal time eq. (2.11).

The Lagrangian density $\mathcal{L}$ corresponds to a Klein-Gordon Lagrangian for a massless field with effective potential

$$V(\varphi) = \frac{1}{2}\frac{1}{z}\frac{\mathrm{d}^2z}{\mathrm{d}\eta^2}\varphi^2. \tag{3.8}$$

The corresponding equation of motion for the perturbation φ is therefore the Klein-Gordon equation:

$$\Box\varphi + \frac{\partial V}{\partial \varphi} = 0. \tag{3.9}$$

Since

$$\frac{\partial V}{\partial \varphi} = \frac{1}{z}\frac{\mathrm{d}^2 z}{\mathrm{d}\eta^2}\varphi, \tag{3.10}$$

and switching to Fourier modes where

$$\Box\varphi \;\longrightarrow\; \left(\frac{\partial^2}{\partial\eta^2} + k^2\right)\varphi_k, \tag{3.11}$$

the equation of motion for the perturbations φ of the scalar field ϕ in Fourier space becomes:

$$\frac{\mathrm{d}^2\varphi_k}{\mathrm{d}\eta^2} + \left(k^2 - \frac{1}{z}\frac{\mathrm{d}^2 z}{\mathrm{d}\eta^2}\right)\varphi_k = 0. \tag{3.12}$$

This equation, describing the dynamics of scalar field perturbations, is known as the **Mukhanov-Sasaki equation**.

The boundary conditions are:

$$\varphi_k \;\longrightarrow\; \begin{cases} \frac{1}{\sqrt{2k}}e^{-ik\eta} & \text{for} \quad -k\eta \to +\infty \\ A_k z & \text{for} \quad -k\eta \to 0 \end{cases}. \tag{3.13}$$

The first condition is the **Bunch-Davies initial condition**: at $\eta \to -\infty$ (early times), spacetime is approximately flat and the solution reduces to a free plane wave. At super-horizon scales (large scales), $\eta \to 0$, the solution φ becomes proportional to z by a factor A_k, ensuring that perturbations freeze upon crossing the horizon.

The analytical primordial power spectrum, considering both scalar and tensor modes, is given by

$$\mathcal{P}(k) = \frac{k^3}{2\pi^2}\lim_{-k\eta\to 0}\left|\frac{\varphi_k}{z}\right|^2 = \frac{k^3}{2\pi^2}|A_k|^2. \tag{3.14}$$

Analytically, the goal is to determine A_k by solving the Mukhanov-Sasaki equation with the boundary conditions from eq. (3.13). A general form for the solution can be found, and by introducing the slow-roll expansion, this general form can be treated perturbatively to obtain solutions at different orders.

To seek the general form of the solution, it is convenient to set

$$y = \sqrt{2k}\varphi_k \tag{3.15}$$

and

$$x = -k\eta = -k\int\frac{\mathrm{d}t}{a} = -k\int\frac{\mathrm{d}a}{a^2 H}, \tag{3.16}$$

where the last equalities follow from the definition (2.11).

Expressing the quantities in terms of y and x, the Mukhanov-Sasaki equation from eq. (3.12) becomes

$$\frac{\mathrm{d}^2 y}{\mathrm{d}x^2} + \left(1 - \frac{1}{z}\frac{\mathrm{d}^2 z}{\mathrm{d}x^2}\right)y = 0. \tag{3.17}$$

The boundary conditions from eq. (3.13) are correspondingly transformed as

$$y \;\longrightarrow\; \begin{cases} e^{-ix} & \text{for} \quad x \to +\infty \\ \sqrt{2k}A_k z & \text{for} \quad x \to 0 \end{cases}. \tag{3.18}$$

Green's Function Method

Let L_x be a generic n-dimensional differential operator. For coordinates $x \equiv (x_1, x_2, \ldots, x_n)$, a general differential equation can be written as

$$L_x u(x) = f(x). \tag{3.19}$$

For example, with $n = 3$, one can define $L_x = \nabla \cdot$, $u(x) = \mathbf{B}(x)$, and $f(x) = 0$ to obtain Maxwell's equation $\nabla \cdot \mathbf{B} = 0$.

The Green's function $G(x, x')$ is generally defined as the distribution satisfying

$$L_x G(x, x') = \delta(x - x'). \tag{3.20}$$

From the fundamental properties of the Dirac delta function, it follows immediately that $f(x)$ in the differential equation under study can be written in terms of $G(x, x')$:

$$f(x) = \int f(x')\delta(x - x')\mathrm{d}x' = \int f(x')L_x G(x, x')\mathrm{d}x' \tag{3.21}$$

$$= L_x \int f(x')G(x, x')\mathrm{d}x'. \tag{3.22}$$

Since $f(x) = L_x u(x)$, the particular solution is

$$u(x) = \int f(x')G(x, x')\mathrm{d}x', \tag{3.23}$$

and the general solution becomes

$$u(x) = q(x) + \int f(x')G(x, x')\mathrm{d}x', \tag{3.24}$$

where $y(x)$ is the solution of the associated homogeneous equation

$$L_x y(x) = 0. \tag{3.25}$$

The Green's function can be constructed using two linearly independent solutions $y_1(x)$ and $y_2(x)$ of the homogeneous equation. The general formula is

$$G(x, u) = \frac{y_1(u)y_2(x) - y_1(x)y_2(u)}{W(u)}, \tag{3.26}$$

where $W(u)$ is the Wronskian of the two solutions, defined as

$$W(u) = y_1(u)y_2'(u) - y_1'(u)y_2(u). \tag{3.27}$$

The solution proceeds by setting the following ansatz *in the scalar case*:

$$z = \frac{1}{x} f^{(\mathrm{s})}(\ln x). \tag{3.28}$$

We will avoid the superscript (s) for the rest of this section, referring always to the scalar case.

Therefore:

$$\frac{\mathrm{d}z}{\mathrm{d}x} = \frac{f'(\ln x)/x - f(\ln x)}{x^2} = \frac{f' - f}{x^2}, \tag{3.29}$$

$$\frac{\mathrm{d}^2 z}{\mathrm{d}x^2} = \frac{(f''/x - f'/x)x^2 - 2x(f' - f)}{x^4} \tag{3.30}$$

$$= \frac{f'' - f'}{x^3} - \frac{2(f' - f)}{x^3} = \frac{f'' - 3f' + 2f}{x^3}, \tag{3.31}$$

where primes denote derivatives with respect to $\ln x$. Defining

$$g(\ln x) = \frac{-3f'(\ln x) + f''(\ln x)}{f(\ln x)}, \tag{3.32}$$

it is possible to obtain

$$\frac{1}{z}\frac{\mathrm{d}^2 z}{\mathrm{d}x^2} = \frac{2}{x^2} + \frac{1}{x^2} g(\ln x). \tag{3.33}$$

With the ansatz from eq. (3.28), equation from eq. (3.17) can be written as

$$\frac{\mathrm{d}^2 y}{\mathrm{d}x^2} + \left(1 - \frac{2}{x^2}\right) y = \frac{1}{x^2} g(\ln x) y. \tag{3.34}$$

First, the homogeneous solution y_0 of the homogeneous equation

$$\frac{\mathrm{d}^2 y_0}{\mathrm{d}x^2} + \left(1 - \frac{2}{x^2}\right) y_0 = 0, \tag{3.35}$$

is found to be

$$y_0(x) = \left(1 + \frac{i}{x}\right) e^{ix}. \tag{3.36}$$

The general solution must be found using the Green's function method, where the Green's function of the operator

$$L_x = \frac{\mathrm{d}^2}{\mathrm{d}x^2} + \left(1 - \frac{2}{x^2}\right) \tag{3.37}$$

can be verified to be

$$G(x, u) = \frac{i}{2} \left[y_0^*(u) y_0(x) - y_0^*(x) y_0(u) \right], \tag{3.38}$$

where

$$y_0^*(x) = \left(1 - \frac{i}{x}\right) e^{-ix}. \tag{3.39}$$

The complete solution of the Mukhanov-Sasaki equation from eq. (3.34) is therefore

$$y(x) = y_0(x) + \int_x^{+\infty} \mathrm{d}u\; G(x, u) \frac{g(\ln u)}{u^2} y(u), \tag{3.40}$$

or explicitly:

$$y(x) = y_0(x) + \frac{i}{2} \int_x^{+\infty} \mathrm{d}u\; \frac{g(\ln u)}{u^2} y(u) \left[y_0^*(u) y_0(x) - y_0^*(x) y_0(u) \right]. \tag{3.41}$$

This represents the general form of the solution, which must now be expanded perturbatively in the slow-roll parameters.

To apply the slow-roll approximation, the following **slow-roll parameters** are defined at $k_* = a_* H_*$, the horizon crossing:

$$\delta_1 = \frac{\ddot{\phi}}{H\dot{\phi}}, \qquad \delta_{n+1} = \frac{1}{H^n \dot{\phi}} \frac{\mathrm{d}^{n+1}\phi}{\mathrm{d}t^{n+1}} \qquad \forall\; n \geq 1, \tag{3.42}$$

$$\epsilon_1 = \frac{1}{2} \left(\frac{\dot{\phi}}{H} \right)^2. \tag{3.43}$$

Note that the quantities δ_n can be related with the HFFs ϵ_n from eq. (1.122). Indeed, it is sufficient to exploit the definition $\mathrm{d}N = H\mathrm{d}t$ to write the derivatives of H with respect to time as functions of the derivatives of the scalar field ϕ and connect the HFFs with the slow-roll parameters. For instance, by repeated derivation it is possible to find

$$\delta_1 = -\epsilon_1 + \frac{\epsilon_2}{2}, \tag{3.44}$$

$$\delta_2 = 2\epsilon_1^2 + \frac{\epsilon_2^2}{4} + \frac{1}{2}\epsilon_2\epsilon_3 - \frac{5}{2}\epsilon_1\epsilon_3. \tag{3.45}$$

From the slow-roll parameters (or HFFs), it is possible to start from $f(\ln x) = xz$ from eq. (3.28) and, by perturbative expansion, determine $g(\ln x)$ up to a certain order, which appears in the solution. This means that the steps to follow are:

- Write f and its derivatives as series of terms expressed with ϵ_i and δ_i;
- Write g as series of terms expressed with ϵ_i and δ_i.

The function f can be expanded as

$$f(\ln x) = \sum_{n=0}^{+\infty} \frac{f_n}{n!}(\ln x)^n = xz. \tag{3.46}$$

From eq. (3.16) it is possible to express x in terms of ϵ_1 and δ_1, in order to write f with these terms.

By repeated integration by parts of x and using the definitions from eqs. (3.42) and (3.43), it is possible to find at first order

$$x \simeq \frac{k}{aH}(1 + \epsilon_1 + 3\epsilon_1^2 + 3\epsilon_1\delta_1). \tag{3.47}$$

Being

$$f_n = \left.\frac{\mathrm{d}^n f}{(\mathrm{d}\ln x)^n}\right|_{\substack{k=aH\\x=1}} = \left.\frac{\mathrm{d}^n(xz)}{(\mathrm{d}\ln x)^n}\right|_{k=aH}, \tag{3.48}$$

from **??** it is possible to find

$$f_0 = f(\ln x)\Big|_{\substack{k=aH\\x=1}} = z \simeq \frac{k\dot{\phi}}{H^2}(1 + \epsilon_1 + 5\epsilon_1^2 + 3\epsilon_1\delta_1)\Big|_{k=aH}, \tag{3.49}$$

$$f_1 = \left.\frac{\mathrm{d}(xz)}{\mathrm{d}\ln x}\right|_{\substack{k=aH\\x=1}} = \frac{k\dot{\phi}}{H^2}(-2\epsilon_1 - \delta_1 - 6\epsilon_1^2 - 4\epsilon_1\delta_1)\Big|_{k=aH}, \tag{3.50}$$

$$f_2 = \left.\frac{\mathrm{d}^2(xz)}{(\mathrm{d}\ln x)^2}\right|_{\substack{k=aH\\x=1}} = \frac{k\dot{\phi}}{H^2}(8\epsilon_1^2 + 9\epsilon_1\delta_1 + \delta_2)\Big|_{k=aH}. \tag{3.51}$$

As for $f(\ln x)$, it is possible to expand $g(\ln x)$ in series obtaining

$$g(\ln x) = \sum_{n=0}^{+\infty} \frac{g_{n+1}}{n!}(\ln x)^n. \tag{3.52}$$

The subscript comes from the definition of $g(\ln x)$: by expanding in series, the 0th term will be

$$g(\ln x_0) = \frac{-3f'(\ln x_0) + f''(\ln x_0)}{f(\ln x_0)}; \tag{3.53}$$

the series for f' starts from $n = 1$

$$f'(\ln x) = \sum_{n=1}^{+\infty} \frac{f_n}{n!} n(\ln x)^{n-1}, \tag{3.54}$$

and then

$$g(\ln x_0) = g_1, \tag{3.55}$$

containing the term for $n = 1$.

The computation of g_1 and g_2 considering eq. (3.46): at first order $f' \sim f_1$ and $f'' \sim f_2$, then

$$g_1 \simeq \frac{-3f_1 + f_2}{f_0}. \tag{3.56}$$

For the second coefficient:

$$g_2 = \frac{\mathrm{d}g}{\mathrm{d}\ln x} = \frac{(-3f'' + f''')f - (-3f' + f'')f'}{f^2}, \tag{3.57}$$

cancelling higher-order terms such as those $\sim f'''f$ and $\sim f''f'$,

$$g_2 \simeq -3\frac{f_2}{f_0} + 3\frac{f_1^2}{f_0^2}. \tag{3.58}$$

From $g(\ln x)$ it is possible to solve $y(x)$ perturbatively by expanding:

$$y(x) = y_0(x) + \sum_{n=1}^{\infty} y_n(x). \tag{3.59}$$

By expanding both the sides of the integral equation eq. (3.41):

$$\begin{aligned} y_0(x) + \sum_{n=1}^{+\infty} y_n(x) = y_0(x) + \frac{i}{2}\int_x^{+\infty} \mathrm{d}u \, \frac{1}{u^2} \left[\sum_{n=1}^{+\infty} \frac{g_n}{(n-1)!} (\ln u)^{n-1} \right] \\ \times \left[y_0(u) + \sum_{n=1}^{\infty} y_n(u) \right] \left[y_0^*(u) y_0(x) - y_0^*(x) y_0(u) \right]. \end{aligned} \tag{3.60}$$

It is important to recall that $y_0(x)$ is known a priori, being the solution of the homogeneous equation.

Stopping e.g. at $n = 1$:

$$\begin{aligned} y_1(x) = \frac{i}{2}\int_x^{+\infty} \frac{\mathrm{d}u}{u^2} \left[g_1 + g_2 \ln u \right] \left[y_0(u) + y_1(u) \right] \\ \times \left[y_0^*(u) y_0(x) - y_0^*(x) y_0(u) \right]. \end{aligned} \tag{3.61}$$

The different contributions are:

- $g_1 y_0$ gives the first-order term;
- $g_1 y_1$ gives a second-order term contributing to y_2 as y_{21};
- $g_2 y_0$ gives a second-order term contributing to y_2 as y_{22};
- $g_2 y_1$, $g_1 y_2$, and $g_2 y_1$ give all third-order terms contributing to y_3.

The first-order term is:

$$y_1(x) = \frac{i}{2}\int_x^{+\infty} \frac{\mathrm{d}u}{u^2} g_1 y_0(u) \left[y_0^*(u)y_0(x) - y_0^*(x)y_0(u)\right], \tag{3.62}$$

while the second-order term is

$$y_2(x) = y_{21}(x) + y_{22}(x), \tag{3.63}$$

with

$$y_{21}(x) = \frac{i}{2}\int_x^{+\infty} \frac{\mathrm{d}u}{u^2} g_1 y_1(u) \left[y_0^*(u)y_0(x) - y_0^*(x)y_0(u)\right], \tag{3.64}$$

$$y_{22}(x) = \frac{i}{2}\int_x^{+\infty} \frac{\mathrm{d}u}{u^2} g_2 y_0(u) \ln u \left[y_0^*(u)y_0(x) - y_0^*(x)y_0(u)\right]. \tag{3.65}$$

Once $y(x)$ is determined up to a certain order, the limit for $x \to 0$ is evaluated in order to recover $\sqrt{2k}A_k z$ in eq. (3.18) and therefore the PPS from eq. (3.14).

The same identical procedure is applied in the case of the tensor PPS. Here the definition of $f(\ln x)$ changes with respect to eq. (3.28):

$$a = \frac{1}{x} f^{(\mathrm{t})}(\ln x). \tag{3.66}$$

3.2 Third-Order Expansion of the Primordial Power Spectra

In this section, the computation of the third-order expansion developed in [1] is presented.

Following the same procedure explained in the previous section, it is possible to compute the g_n coefficients for both scalar and tensor perturbations up to third order as

$$g_1 \simeq -3\frac{f_1}{f_0} + \frac{f_2}{f_0}, \tag{3.67a}$$

$$g_2 \simeq 3\frac{f_1^2}{f_0^2} - 3\frac{f_2}{f_0} - \frac{f_1 f_2}{f_0^2} + \frac{f_3}{f_0}, \tag{3.67b}$$

$$g_3 \simeq -3\frac{f_1^3}{f_0^3} + \frac{9}{2}\frac{f_1 f_2}{f_0^2} - \frac{3}{2}\frac{f_3}{f_0}. \tag{3.67c}$$

At the same time, x can be expressed in terms of the slow-roll parameters up to third order as

$$x = -k\int \frac{\mathrm{d}t}{a} \simeq \frac{k}{aH}\left[1 + \epsilon_1 + \epsilon_1^2 + \epsilon_1^3 + \epsilon_1\epsilon_2 + 3\epsilon_1^2\epsilon_2 + \epsilon_1\epsilon_2^2 + \epsilon_1\epsilon_2\epsilon_3 + \mathcal{O}(\epsilon^4)\right]. \tag{3.68}$$

Taylor expanding around $x = 1$ using eq. (3.68) at third order leads to different coefficients compared to the expansion performed in [54] around horizon crossing $aH = k$, as explained in [67]. Keeping terms up to third order in the slow-roll parameters and expressing everything with respect to the HFFs, the scalar coefficients are:

$$f_0^{(\mathrm{s})} \simeq \left.\frac{a\dot{\phi}}{H}\right|_{x=1}, \tag{3.69a}$$

$$f_1^{(\mathrm{s})} \simeq \frac{a\dot{\phi}}{H}\left[1-\frac{aH}{k}\left(1+\frac{\epsilon_2}{2}\right)\right]_{x=1}, \tag{3.69b}$$

$$f_2^{(\mathrm{s})} \simeq \frac{a\dot{\phi}}{H}\left[1-3\frac{aH}{k}\left(1+\frac{\epsilon_2}{2}\right)+\left(\frac{aH}{k}\right)^2\left(2-\epsilon_1+\frac{3\epsilon_2}{2}-\frac{\epsilon_1\epsilon_2}{2}+\frac{\epsilon_2\epsilon_3}{2}+\frac{\epsilon_2^2}{4}\right)\right]_{x=1}, \tag{3.69c}$$

$$\begin{aligned} f_3^{(\mathrm{s})} \simeq \frac{a\dot{\phi}}{H}\Bigg[&1-7\frac{aH}{k}\left(1+\frac{\epsilon_2}{2}\right)+\left(\frac{aH}{k}\right)^2\left(12-6\epsilon_1+9\epsilon_2-3\epsilon_1\epsilon_2+\frac{3\epsilon_2^2}{2}+3\epsilon_2\epsilon_3\right) \\ &-\left(\frac{aH}{k}\right)^3\left(6-7\epsilon_1+\frac{11\epsilon_2}{2}+2\epsilon_1^2+\frac{3\epsilon_2^2}{2}+3\epsilon_2\epsilon_3-6\epsilon_1\epsilon_2\right. \\ &\left.+\epsilon_1^2\epsilon_2-\frac{5\epsilon_1\epsilon_2^2}{4}-\frac{3\epsilon_1\epsilon_2\epsilon_3}{2}+\frac{3\epsilon_2^2\epsilon_3}{4}+\frac{\epsilon_2^3}{8}+\frac{\epsilon_2\epsilon_3^2}{2}+\frac{\epsilon_2\epsilon_3\epsilon_4}{2}\right)\Bigg]_{x=1} \end{aligned} \tag{3.69d}$$

and using eq. (3.67), the coefficients for the primordial scalar perturbations are:

$$g_1^{(\mathrm{s})} \simeq 3\epsilon_1+\frac{3}{2}\epsilon_2+4\epsilon_1^2+\frac{13}{2}\epsilon_1\epsilon_2+\frac{1}{4}\epsilon_2^2+5\epsilon_1^3+\frac{35}{2}\epsilon_1^2\epsilon_2+\frac{15}{2}\epsilon_1\epsilon_2^2+\frac{1}{2}\epsilon_2\epsilon_3+5\epsilon_1\epsilon_2\epsilon_3\,, \tag{3.70a}$$

$$g_2^{(\mathrm{s})} \simeq -3\epsilon_1\epsilon_2-11\epsilon_1^2\epsilon_2-\frac{13}{2}\epsilon_1\epsilon_2^2-\frac{3}{2}\epsilon_2\epsilon_3-8\epsilon_1\epsilon_2\epsilon_3-\frac{1}{2}\epsilon_2^2\epsilon_3-\frac{1}{2}\epsilon_2\epsilon_3^2-\frac{1}{2}\epsilon_2\epsilon_3\epsilon_4\,, \tag{3.70b}$$

$$g_3^{(\mathrm{s})} \simeq \frac{3}{2}\epsilon_1\epsilon_2^2+\frac{3}{2}\epsilon_1\epsilon_2\epsilon_3+\frac{3}{4}\epsilon_2\epsilon_3^2+\frac{3}{4}\epsilon_2\epsilon_3\epsilon_4\,. \tag{3.70c}$$

The same computations can be performed for tensor perturbations. The f and g coefficients up to third order correspond to:

$$f_0^{(\mathrm{t})} \simeq a|_{x=1}\,, \tag{3.71a}$$

$$f_1^{(\mathrm{t})} \simeq a\left(1-\frac{aH}{k}\right)_{x=1}, \tag{3.71b}$$

$$f_2^{(\mathrm{t})} \simeq a\left[1-3\frac{aH}{k}+\left(\frac{aH}{k}\right)^2(2-\epsilon_1)\right]_{x=1}, \tag{3.71c}$$

$$f_3^{(\mathrm{t})} \simeq a\left[1-7\frac{aH}{k}+\left(\frac{aH}{k}\right)^2(12-6\epsilon_1)-\left(\frac{aH}{k}\right)^3\left(6-7\epsilon_1+2\epsilon_1^2-\epsilon_1\epsilon_2\right)\right]_{x=1} \tag{3.71d}$$

and

$$g_1^{(\mathrm{t})} \simeq 3\epsilon_1+4\epsilon_1^2+4\epsilon_1\epsilon_2+5\epsilon_1^3+14\epsilon_1^2\epsilon_2+4\epsilon_1\epsilon_2^2+4\epsilon_1\epsilon_2\epsilon_3\,, \tag{3.72a}$$

$$g_2^{(\mathrm{t})} \simeq -3\epsilon_1\epsilon_2-11\epsilon_1^2\epsilon_2-4\epsilon_1\epsilon_2^2-4\epsilon_1\epsilon_2\epsilon_3\,, \tag{3.72b}$$

$$g_3^{(\mathrm{t})} \simeq \frac{3}{2}\epsilon_1\epsilon_2^2+\frac{3}{2}\epsilon_1\epsilon_2\epsilon_3\,. \tag{3.72c}$$

3.2.1 The Primordial Power Spectra Including Third-Order Corrections

Once the g_n coefficients have been established for both scalar and tensor perturbations through third order in slow-roll parameters, the subsequent task requires computing the recursive solutions from eq. (3.41) incorporating third-order corrections, expressed as:

$$y(x) \simeq y_0(x)+y_1(x)+y_2(x)+y_3(x)\,. \tag{3.73}$$

The expressions for y_0, y_1, y_2, and y_3 exhibit universality, as the slow-roll parameter dependencies that differentiates scalar from tensor perturbations resides entirely within the g_n functions.

Since the right-hand side of eq. (3.34) incorporates terms of at least first order in the slow-roll expansion, the zeroth-order solution reduces to the homogeneous solution $y_0(x)$, from eq. (3.36).

The first-order correction to eq. (3.36) is obtained by substituting $g = g_1$ and $y = y_0$ into the right-hand side of eq. (3.41), resulting in:

$$\begin{aligned} y_1(x) &= \frac{ig_1}{2} \int_x^\infty \frac{\mathrm{d}u}{u^2}\, y_0(u)\,[y_0^*(u)y_0(x) - y_0^*(x)y_0(u)] \\ &= \frac{i\,g_1}{3}\left[\frac{2}{x}e^{ix} + i\,y_0^*(x)\int_x^\infty \frac{\mathrm{d}u}{u}\, e^{2iu}\right]. \end{aligned} \tag{3.74}$$

At second order, the correction incorporates two separate contributions:

$$y_2(x) = y_{21}(x) + y_{22}(x)\,, \tag{3.75}$$

arising from the substitution $g = g_1 + g_2 \ln x$ and $y = y_0 + y_1$ into eq. (3.41), which produces:

$$\begin{aligned} y_{21}(x) &= \frac{ig_1}{2}\int_x^\infty \frac{\mathrm{d}u}{u^2}\, y_1(u)\,[y_0^*(u)y_0(x) - y_0^*(x)y_0(u)] \\ &= -\frac{ig_1^2}{9}\left[\frac{2}{3x}e^{ix} - \left(\frac{5}{3x} - \frac{i}{3}\right)e^{-ix}\int_x^\infty \frac{\mathrm{d}u}{u}\, e^{2iu} + i\,y_0(x)\int_x^\infty \frac{\mathrm{d}u}{u}\, e^{-2iu}\int_u^\infty \frac{\mathrm{d}t}{t}\, e^{2it}\right] \end{aligned} \tag{3.76a}$$

$$\begin{aligned} y_{22}(x) &= \frac{ig_2}{2}\int_x^\infty \frac{\mathrm{d}u}{u^2}\, y_0(u)\ln u\,[y_0^*(u)y_0(x) - y_0^*(x)y_0(u)] \\ &= \frac{ig_2}{3}\left[\frac{8}{3x}e^{ix} + \frac{2}{x}\ln x\; e^{ix} + \frac{7i}{3}\,y_0^*(x)\int_x^\infty \frac{\mathrm{d}u}{u}\, e^{2iu} + i\,y_0^*(x)\int_x^\infty \frac{\mathrm{d}u}{u}\, e^{2iu}\ln u\right]. \end{aligned} \tag{3.76b}$$

The third-order correction encompasses three distinct components:

$$y_3(x) = y_{31}(x) + y_{32}(x) + y_{33}(x)\,. \tag{3.77}$$

These contributions emerge from the substitution $g = g_1 + g_2 \ln x + g_3 \ln^2 x$ and $y = y_0 + y_1 + y_2$ into eq. (3.41):

$$y_{31}(x) \equiv \frac{ig_1}{2}\int_x^\infty \frac{\mathrm{d}u}{u^2}\, y_2(u)\,[y_0^*(u)y_0(x) - y_0^*(x)y_0(u)]\,, \tag{3.78a}$$

$$y_{32}(x) \equiv \frac{ig_2}{2}\int_x^\infty \frac{\mathrm{d}u}{u^2}\, y_1(u)\ln u\,[y_0^*(u)y_0(x) - y_0^*(x)y_0(u)]\,, \tag{3.78b}$$

$$y_{33}(x) \equiv \frac{ig_3}{4}\int_x^\infty \frac{\mathrm{d}u}{u^2}\, y_0(u)\ln^2 u\,[y_0^*(u)y_0(x) - y_0^*(x)y_0(u)]\,. \tag{3.78c}$$

The computational complexity arising from the multitude of terms necessitates individual treatment of these three contributions. The first third-order component can be decomposed by incorporating expressions from eqs. (3.76a) and (3.76b):

$$\begin{aligned} y_{31}(x) = \frac{g_1^3}{18}\int_x^\infty \frac{\mathrm{d}u}{u^2} & \left[\frac{2e^{iu}}{3u} - \left(\frac{5}{3u} - \frac{i}{3}\right)e^{-iu}\int_u^\infty \frac{\mathrm{d}t}{t}\, e^{2it} + iy_0(u)\int_u^\infty \frac{\mathrm{d}t}{t}\, e^{-2it}\int_t^\infty \frac{\mathrm{d}s}{s}\, e^{2is}\right] \\ & [y_0^*(u)y_0(x) - y_0^*(x)y_0(u)] \\ - \frac{g_1 g_2}{6}\int_x^\infty \frac{\mathrm{d}u}{u^2} & \left[\frac{8e^{iu}}{3u} + \frac{2e^{iu}\ln u}{u} + \frac{7i}{3}\,y_0^*(u)\int_u^\infty \frac{\mathrm{d}t}{t}\, e^{2it} + i\,y_0^*(u)\int_u^\infty \frac{\mathrm{d}t}{t}\, e^{2it}\ln t\right] \\ & [y_0^*(u)y_0(x) - y_0^*(x)y_0(u)] \\ \equiv y_{311} + y_{312}\,. & \end{aligned} \tag{3.79a}$$

Following integration, these components yield:

$$\begin{aligned}y_{311} =&\frac{g_1^3}{27}\left[\frac{4ie^{ix}}{9x}-\left(\frac{2}{9}+\frac{10i}{9x}\right)e^{-ix}\int_x^\infty\frac{\mathrm{d}u}{u}\,e^{2iu}+\frac{2}{3}\left(-1+\frac{2i}{x}\right)e^{ix}\int_x^\infty\frac{\mathrm{d}u}{u}\,e^{-2iu}\int_u^\infty\frac{\mathrm{d}t}{t}\,e^{2it}\right.\\&\left.-\left(1-\frac{i}{x}\right)e^{-ix}\int_x^\infty\frac{\mathrm{d}u}{u}\,e^{2iu}\int_u^\infty\frac{\mathrm{d}t}{t}\,e^{-2it}\int_t^\infty\frac{\mathrm{d}s}{s}\,e^{2is}\right]\end{aligned}\tag{3.80a}$$

and

$$\begin{aligned}y_{312} =&\frac{i\,g_1g_2}{9}\left[-\left(\frac{28}{9x}+\frac{2\ln x}{3x}\right)e^{ix}-\left(\frac{26i}{9}-\frac{16}{9x}\right)e^{-ix}\int_x^\infty\frac{\mathrm{d}u}{u}\,e^{2iu}\right.\\&+\left(\frac{5}{3x}-\frac{i}{3}\right)e^{-ix}\int_x^\infty\frac{\mathrm{d}u}{u}\,e^{2iu}\ln u+\frac{7}{3}\left(\frac{1}{x}-i\right)e^{ix}\int_x^\infty\frac{\mathrm{d}u}{u}\,e^{-2iu}\int_u^\infty\frac{\mathrm{d}t}{t}\,e^{2it}\\&\left.+\left(\frac{1}{x}-i\right)e^{ix}\int_x^\infty\frac{\mathrm{d}u}{u}\,e^{-2iu}\int_u^\infty\frac{\mathrm{d}t}{t}\,e^{2it}\ln t\right].\end{aligned}\tag{3.80b}$$

A beneficial integral identity for simplifying the final expression is:

$$\int_x^\infty\frac{\mathrm{d}u}{u}\,e^{-2iu}\int_u^\infty\frac{\mathrm{d}t}{t}\,e^{2it}\ln t=\int_x^\infty\frac{\mathrm{d}u}{u}\,e^{-2iu}\int_x^\infty\frac{\mathrm{d}t}{t}\,e^{2it}\ln t-\int_x^\infty\frac{\mathrm{d}u}{u}\,e^{2iu}\ln u\int_u^\infty\frac{\mathrm{d}t}{t}\,e^{-2it}.\tag{3.81}$$

The second third-order contribution, employing eq. (3.74), assumes the form:

$$y_{32}(x)=-\frac{g_1g_2}{6}\int_x^\infty\frac{\mathrm{d}u}{u^2}\left[\frac{2e^{iu}}{u}+i\,y_0^*(u)\int_u^\infty\frac{\mathrm{d}t}{t}\,e^{2it}\right]\ln u\left[y_0^*(u)y_0(x)-y_0^*(x)y_0(u)\right].\tag{3.82}$$

After evaluation, this produces:

$$\begin{aligned}y_{32}(x) =&\frac{ig_1g_2}{9}\left[-\left(\frac{28}{9x}+\frac{2\ln x}{3x}\right)e^{ix}-\left(\frac{26i}{9}+\frac{2}{9x}-\frac{2\ln x}{x}\right)e^{-ix}\int_x^\infty\frac{\mathrm{d}u}{u}\,e^{2iu}\right.\\&-\frac{1}{3}\left(\frac{1}{x}+i\right)e^{-ix}\int_x^\infty\frac{\mathrm{d}u}{u}\,e^{2iu}\ln u+\frac{7}{3}\left(\frac{1}{x}-i\right)e^{ix}\int_x^\infty\frac{\mathrm{d}u}{u}\,e^{-2iu}\int_u^\infty\frac{\mathrm{d}t}{t}\,e^{2it}\\&\left.+\left(\frac{1}{x}-i\right)e^{ix}\int_x^\infty\frac{\mathrm{d}u}{u}\,e^{-2iu}\ln u\int_u^\infty\frac{\mathrm{d}t}{t}\,e^{2it}\right].\end{aligned}\tag{3.83}$$

The third component of the third-order correction, utilizing eq. (3.36), is expressed as:

$$y_{33}(x)=\frac{i\,g_3}{4}\int_x^\infty\frac{\mathrm{d}u}{u^2}\left(1+\frac{i}{u}\right)e^{iu}\ln^2 u\left[y_0^*(u)y_0(x)-y_0^*(x)y_0(u)\right].\tag{3.84}$$

Following integration, this results in:

$$\begin{aligned}y_{33}(x) =&\frac{ig_3}{6}\left[\left(\frac{52}{9x}+\frac{16\ln x}{3x}+\frac{2\ln^2 x}{x}\right)e^{ix}+\frac{50}{9}\left(\frac{1}{x}+i\right)e^{-ix}\int_x^\infty\frac{\mathrm{d}u}{u}e^{2iu}\right.\\&\left.+\frac{14}{3}\left(\frac{1}{x}+i\right)e^{-ix}\int_x^\infty\frac{\mathrm{d}u}{u}\,e^{2iu}\ln u+\left(\frac{1}{x}+i\right)e^{-ix}\int_x^\infty\frac{\mathrm{d}u}{u}\,e^{2iu}\ln^2 u\right].\end{aligned}\tag{3.85}$$

The comprehensive integral manipulations and integration-by-parts procedures employed to obtain these results are documented in appendix D.

To extract the primordial power spectra, the asymptotic behavior of $y(x)$ in the super-Hubble regime ($x\to 0$) must be determined. Within this limit, the asymptotic forms for $y_0(x)$, $y_1(x)$,

$y_{21}(x)$, $y_{22}(x)$, $y_{31}(x)$, $y_{32}(x)$, and $y_{33}(x)$ are:

$$y_0(x) \rightarrow ix^{-1} \tag{3.86a}$$

$$y_1(x) \rightarrow \frac{ig_1}{3}\left[\left(\alpha + \frac{i\pi}{2}\right)x^{-1} - \frac{\ln x}{x}\right] \tag{3.86b}$$

$$y_{21}(x) \rightarrow \frac{ig_1^2}{18}\left[\left(i\pi\alpha - \frac{i\pi}{3} + \frac{\pi^2}{4} + \alpha^2 - \frac{2}{3}\alpha - 4\right)x^{-1} - 2\left(\alpha - \frac{1}{3} + \frac{i\pi}{2}\right)\frac{\ln x}{x} + \frac{\ln^2 x}{x}\right] \tag{3.86c}$$

$$y_{22}(x) \rightarrow \frac{ig_2}{6}\left[\left(\frac{i\pi}{3} - \frac{\pi^2}{12} + \frac{2\alpha}{3} + i\pi\alpha + \alpha^2\right)x^{-1} - \frac{2\ln x}{3x} - \frac{\ln^2 x}{x}\right] \tag{3.86d}$$

$$\begin{aligned} y_{31}(x) \rightarrow & \frac{ig_1^3}{27}\left[\left(\frac{\alpha^3}{6} - \frac{\alpha^2}{3} + \frac{i\pi\alpha^2}{4} + \frac{\pi^2\alpha}{8} - \frac{16\alpha}{9} - \frac{i\pi\alpha}{3} - \mathcal{Z} + 4 - \frac{\pi^2}{12} + \frac{5i\pi^3}{48} - \frac{8i\pi}{9}\right)x^{-1}\right. \\ & + \left(-\frac{\alpha^2}{2} - \frac{i\pi\alpha}{2} + \frac{2\alpha}{3} + \frac{i\pi}{3} - \frac{\pi^2}{8} + \frac{16}{9}\right)\frac{\ln x}{x} \\ & \left. + \left(\frac{\alpha}{2} - \frac{1}{3} + \frac{i\pi}{4}\right)\frac{\ln^2 x}{x} - \frac{\ln^3 x}{6x}\right] \\ & + \frac{ig_1g_2}{6}\left[\left(\frac{\alpha^3}{3} - \frac{2\alpha^2}{3} + \frac{i\pi\alpha^2}{6} + \frac{5\pi^2\alpha}{36} + \frac{4i\alpha}{3} - \frac{4\alpha}{27} + \frac{2i\pi\alpha}{3} + \frac{4i}{3} - \frac{16}{9}\right.\right. \\ & \left. - \frac{7\pi^2}{54} + \frac{i\pi^3}{72} - \frac{38i\pi}{27} + \frac{2\pi}{3}\right)x^{-1} - \left(\frac{\alpha^2}{3} + \frac{2\alpha}{9} + \frac{i\pi\alpha}{3} - \frac{\pi^2}{36} - \frac{4}{27} + \frac{i\pi}{9}\right)\frac{\ln x}{x} \\ & \left. + \frac{2\ln^2 x}{9x} + \frac{\ln^3 x}{9x}\right] \end{aligned} \tag{3.86e}$$

$$\begin{aligned} y_{32}(x) \rightarrow & \frac{ig_1g_2}{6}\left[\left(\frac{2\alpha^2}{3} + \frac{4i\alpha}{3} - \frac{76\alpha}{27} + \frac{2i\pi\alpha}{3} + \frac{4i}{3} + \frac{8}{9} - \frac{38i\pi}{27} - \frac{2\pi}{3} + \frac{11\pi^2}{54}\right)x^{-1}\right. \\ & \left. - \left(\frac{2\alpha}{9} + \frac{i\pi}{9} - \frac{4}{27}\right)\frac{\ln x}{x} - \left(\frac{\alpha}{3} + \frac{i\pi}{6} - \frac{2}{9}\right)\frac{\ln^2 x}{x} + \frac{2}{9}\frac{\ln^3 x}{x}\right] \end{aligned} \tag{3.86f}$$

$$\begin{aligned} y_{33}(x) \rightarrow & \frac{ig_3}{6}\left[\left(\frac{\alpha^3}{3} + \frac{\alpha^2}{3} + \frac{i\pi\alpha^2}{2} + \frac{2\alpha}{9} + \frac{i\pi\alpha}{3} - \frac{\pi^2\alpha}{12} - \frac{2\zeta(3)}{3}\right.\right. \\ & \left. \left. + \frac{i\pi}{9} + \frac{4}{3} + \frac{i\pi^3}{24} - \frac{\pi^2}{36}\right)x^{-1} - \frac{2\ln x}{9x} - \frac{\ln^2 x}{3x} - \frac{\ln^3 x}{3x}\right] \end{aligned} \tag{3.86g}$$

where $\alpha \equiv 2 - \ln 2 - \gamma$ with $\gamma \simeq 0.5772$ representing the Euler-Mascheroni constant and $\zeta(3) \simeq 1.2020$ known as the Apéry constant, which is the Reimann's zeta function computed in 3. The term $\mathcal{Z}$ encodes differences arising from the approximation scheme employed to calculate the triple integral in eq. (3.79), as detailed in appendix E. The approach for determining the super-Hubble asymptotic solutions of the required integrals is detailed in appendix E.

The Primordial Power Spectrum of Scalar Perturbations

For scalar curvature perturbations, the dimensionless PPS of the comoving curvature perturbation ζ_k is specified as

$$\mathcal{P}_\zeta(k) = \frac{k^2}{4\pi^2}\lim_{x\to 0}\left|\frac{y^{(\mathrm{s})}}{z}\right|^2. \tag{3.87}$$

The primary objective is to evaluate the PPS at horizon crossing. Although the g_n coefficients have been expanded around $x = 1$, a corresponding expansion must be performed for the squared modulus of $1/(xz)$ appearing in eq. (3.87) when expressing explicitly $y^{(\mathrm{s})}$, yielding:

$$\begin{aligned}\left|\frac{1}{xz}\right|^2 \simeq \left(\frac{H^2}{k\dot{\phi}}\right)^2 & \left[1 - 2\epsilon_1 - 2\epsilon_1\epsilon_2 + \epsilon_1^2 - 2\epsilon_1\epsilon_2^2 - 2\epsilon_1\epsilon_2\epsilon_3\right. \\ & + \left(2\epsilon_1 + \epsilon_2 + \epsilon_1\epsilon_2 - 2\epsilon_1^2 - 2\epsilon_1^2\epsilon_2 + \epsilon_1\epsilon_2^2 + 2\epsilon_1\epsilon_2\epsilon_3\right)\ln x \\ & + \left(2\epsilon_1^2 + \epsilon_1\epsilon_2 + \frac{\epsilon_2^2}{2} - \frac{\epsilon_2\epsilon_3}{2} + 3\epsilon_1^2\epsilon_2 + \frac{\epsilon_1\epsilon_2^2}{2} - \epsilon_1\epsilon_2\epsilon_3\right)\ln^2 x \\ & \left. + \left(\frac{4\epsilon_1^3}{3} + \frac{\epsilon_1\epsilon_2^2}{3} + \frac{\epsilon_2^3}{6} - \frac{2\epsilon_1\epsilon_2\epsilon_3}{3} - \frac{\epsilon_2^2\epsilon_3}{2} + \frac{\epsilon_2\epsilon_3^2}{6} + \frac{\epsilon_2\epsilon_3\epsilon_4}{6}\right)\ln^3 x\right].\end{aligned} \tag{3.88}$$

The temporal evolution of both the HFF and Hubble parameter around a reference conformal time τ_* requires the following expansions:

$$\begin{aligned}\epsilon_i(\tau) \simeq \epsilon_{i*} & \left[1 - \epsilon_{i+1*}(1 + \epsilon_{1*} + \epsilon_{1*}^2 + \epsilon_{1*}\epsilon_{2*})\ln\left(\frac{\tau}{\tau_*}\right)\right. \\ & + \frac{\epsilon_{i+1*}}{2}(\epsilon_{i+1*} + \epsilon_{i+2*} + \epsilon_{1*}\epsilon_{2*} + 2\epsilon_{1*}\epsilon_{i+1*} + 2\epsilon_{1*}\epsilon_{i+2*})\ln^2\left(\frac{\tau}{\tau_*}\right) \\ & \left. - \frac{\epsilon_{i+1*}}{6}\left(\epsilon_{i+1*}^2 + \epsilon_{i+2*}^2 + 3\epsilon_{i+1*}\epsilon_{i+2*} + \epsilon_{i+2*}\epsilon_{i+3*}\right)\ln^3\left(\frac{\tau}{\tau_*}\right)\right],\end{aligned} \tag{3.89}$$

$$\begin{aligned}H(\tau) \simeq H_* & \left[1 + \left(\epsilon_{1*} + \epsilon_{1*}^2 + \epsilon_{1*}^3 + \epsilon_{1*}^2\epsilon_{2*}\right)\ln\left(\frac{\tau}{\tau_*}\right)\right. \\ & + \left(\frac{\epsilon_{1*}^2}{2} + \epsilon_{1*}^3 - \frac{1}{2}\epsilon_{1*}\epsilon_{2*} - \frac{3}{2}\epsilon_{1*}^2\epsilon_{2*}\right)\ln^2\left(\frac{\tau}{\tau_*}\right) \\ & \left. + \left(\frac{\epsilon_{1*}^3}{6} - \frac{1}{2}\epsilon_{1*}^2\epsilon_{2*} + \frac{1}{6}\epsilon_{1*}\epsilon_{2*}^2 + \frac{1}{6}\epsilon_{1*}\epsilon_{2*}\epsilon_{3*}\right)\ln^3\left(\frac{\tau}{\tau_*}\right)\right].\end{aligned} \tag{3.90}$$

For scalar PPS calculations, the squared Hubble parameter expansion becomes essential:

$$\begin{aligned}H^2(\tau) \simeq H_*^2 & \left[1 + \left(2\epsilon_{1*} + 2\epsilon_{1*}^2 + 2\epsilon_{1*}^3 + 2\epsilon_{1*}^2\epsilon_{2*}\right)\ln\left(\frac{\tau}{\tau_*}\right)\right. \\ & + \left(2\epsilon_{1*}^2 + 4\epsilon_{1*}^3 - \epsilon_{1*}\epsilon_{2*} - 3\epsilon_{1*}^2\epsilon_{2*}\right)\ln^2\left(\frac{\tau}{\tau_*}\right) \\ & \left. + \left(\frac{4\epsilon_{1*}^3}{3} - 2\epsilon_{1*}^2\epsilon_{2*} + \frac{1}{3}\epsilon_{1*}\epsilon_{2*}^2 + \frac{1}{3}\epsilon_{1*}\epsilon_{2*}\epsilon_{3*}\right)\ln^3\left(\frac{\tau}{\tau_*}\right)\right].\end{aligned} \tag{3.91}$$

Through the combination of eq. (3.87) with eqs. (3.70), (3.73), (3.88), (3.89) and (3.91), the dimensionless PPS for scalar fluctuations expanded around the pivot scale k_* becomes:

$$\begin{aligned}
\mathcal{P}_\zeta(k) =& \frac{H_*^2}{8\pi^2\epsilon_{1*}}\Bigg\{\Bigg[1-2(1-\alpha)\epsilon_{1*}+\left(-3-2\alpha+2\alpha^2+\frac{\pi^2}{2}\right)\epsilon_{1*}^2+\alpha\epsilon_{2*}\\
&+\left(-6+\alpha+\alpha^2+\frac{7\pi^2}{12}\right)\epsilon_{1*}\epsilon_{2*}+\frac{1}{8}\left(-8+4\alpha^2+\pi^2\right)\epsilon_{2*}^2\\
&+\frac{1}{24}\left(-12\alpha^2+\pi^2\right)\epsilon_{2*}\epsilon_{3*}-\frac{1}{24}\left(-16+24\alpha-4\alpha^3-3\alpha\pi^2+6\mathcal{Z}\right)\left(8\epsilon_{1*}^3+\epsilon_{2*}^3\right)\\
&+\frac{1}{12}\left(-72\alpha+36\alpha^2+13\pi^2+8\alpha\pi^2-36\mathcal{Z}\right)\epsilon_{1*}^2\epsilon_{2*}\\
&-\frac{1}{24}\left(16+24\alpha-12\alpha^2-8\alpha^3-15\pi^2-6\alpha\pi^2+84\mathcal{Z}\right)\epsilon_{1*}\epsilon_{2*}^2\\
&+\frac{1}{24}\left(16+4\alpha^3-\alpha\pi^2-24\mathcal{Z}\right)\left(\epsilon_{2*}\epsilon_{3*}^2+\epsilon_{2*}\epsilon_{3*}\epsilon_{4*}\right)\\
&+\frac{1}{24}\left(48\alpha-12\alpha^3-5\alpha\pi^2\right)\epsilon_{2*}^2\epsilon_{3*}\\
&+\frac{1}{12}\left(-8+72\alpha-12\alpha^2-8\alpha^3+\pi^2-6\alpha\pi^2-24\mathcal{Z}\right)\epsilon_{1*}\epsilon_{2*}\epsilon_{3*}\Bigg]\\
&+\Bigg[-2\epsilon_{1*}+2(-2\alpha+1)\epsilon_{1*}^2-\epsilon_{2*}+(-2\alpha-1)\epsilon_{1*}\epsilon_{2*}-\alpha\epsilon_{2*}^2+\alpha\epsilon_{2*}\epsilon_{3*}\\
&-\frac{1}{8}\left(-8+4\alpha^2+\pi^2\right)\left(8\epsilon_{1*}^3+\epsilon_{2*}^3\right)-\frac{2}{3}\left(-9+9\alpha+\pi^2\right)\epsilon_{1*}^2\epsilon_{2*}\\
&-\frac{1}{4}\left(-4+4\alpha+4\alpha^2+\pi^2\right)\epsilon_{1*}\epsilon_{2*}^2+\frac{1}{2}\left(-12+4\alpha+4\alpha^2+\pi^2\right)\epsilon_{1*}\epsilon_{2*}\epsilon_{3*}\\
&+\frac{1}{24}\left(-12\alpha^2+\pi^2\right)\left(\epsilon_{2*}\epsilon_{3*}^2+\epsilon_{2*}\epsilon_{3*}\epsilon_{4*}\right)+\frac{1}{24}\left(-48+36\alpha^2+5\pi^2\right)\epsilon_{2*}^2\epsilon_{3*}\Bigg]\ln\left(\frac{k}{k_*}\right)\\
&+\frac{1}{2}\Bigg[4\epsilon_{1*}^2+2\epsilon_{1*}\epsilon_{2*}+6\epsilon_{1*}^2\epsilon_{2*}+\epsilon_{2*}^2-\epsilon_{2*}\epsilon_{3*}+(1+2\alpha)(\epsilon_{1*}\epsilon_{2*}^2-2\epsilon_{1*}\epsilon_{2*}\epsilon_{3*})\\
&+\alpha(8\epsilon_{1*}^3+\epsilon_{2*}^3-3\epsilon_{2*}^2\epsilon_{3*}+\epsilon_{2*}\epsilon_{3*}^2+\epsilon_{2*}\epsilon_{3*}\epsilon_{4*})\Bigg]\ln^2\left(\frac{k}{k_*}\right)\\
&+\frac{1}{6}\left(-8\epsilon_{1*}^3-2\epsilon_{1*}\epsilon_{2*}^2-\epsilon_{2*}^3+4\epsilon_{1*}\epsilon_{2*}\epsilon_{3*}+3\epsilon_{2*}^2\epsilon_{3*}-\epsilon_{2*}\epsilon_{3*}^2-\epsilon_{2*}\epsilon_{3*}\epsilon_{4*}\right)\ln^3\left(\frac{k}{k_*}\right)\Bigg\}
\end{aligned} \tag{3.92}$$

where all divergent terms in eq. (3.86) proportional to $\ln x$ cancel exactly. This scalar PPS expression utilizes a fixed pivot scale k_*, with $k_*\tau_* = -1$ yielding:

$$\frac{\tau}{\tau_*} = -\frac{k}{k_*}\,. \tag{3.93}$$

From eq. (3.92), one can derive the third-order slow-roll expansion for the scalar spectral index n_s and its runnings α_s and β_s. The scalar spectral index is defined as:

$$n_\mathrm{s}(k) \equiv 1 + \frac{\mathrm{d}\ln \mathcal{P}_\zeta}{\mathrm{d}\ln k} \tag{3.94}$$

$$\begin{aligned} &= \Big[1 - 2\epsilon_{1*} - \epsilon_{2*} - 2\epsilon_{1*}^2 - (3-2\alpha)\epsilon_{1*}\epsilon_{2*} + \alpha\epsilon_{2*}\epsilon_{3*} - 2\epsilon_{1*}^3 \\ &\quad + (-15 + 6\alpha + \pi^2)\epsilon_{1*}^2\epsilon_{2*} + \frac{1}{12}(-84 + 36\alpha - 12\alpha^2 + 7\pi^2)\epsilon_{1*}\epsilon_{2*}^2 \\ &\quad + \frac{1}{12}(-72 + 48\alpha - 12\alpha^2 + 7\pi^2)\epsilon_{1*}\epsilon_{2*}\epsilon_{3*} + \frac{1}{4}(-8+\pi^2)\epsilon_{2*}^2\epsilon_{3*} \\ &\quad + \left(-\frac{\alpha^2}{2} + \frac{\pi^2}{24}\right)\epsilon_{2*}\epsilon_{3*}^2 + \left(-\frac{\alpha^2}{2} + \frac{\pi^2}{24}\right)\epsilon_{2*}\epsilon_{3*}\epsilon_{4*}\Big] \\ &\quad + \big(-2\epsilon_{1*}\epsilon_{2*} - 6\epsilon_{1*}^2\epsilon_{2*} - 3\epsilon_{1*}\epsilon_{2*}^2 + 2\alpha\epsilon_{1*}\epsilon_{2*}^2 - \epsilon_{2*}\epsilon_{3*} - 4\epsilon_{1*}\epsilon_{2*}\epsilon_{3*} \\ &\quad + 2\alpha\epsilon_{1*}\epsilon_{2*}\epsilon_{3*} + \alpha\epsilon_{2*}\epsilon_{3*}^2 + \alpha\epsilon_{2*}\epsilon_{3*}\epsilon_{4*}\big)\ln\left(\frac{k}{k_*}\right) \\ &\quad + \left(-\epsilon_{1*}\epsilon_{2*}^2 - \epsilon_{1*}\epsilon_{2*}\epsilon_{3*} - \frac{1}{2}\epsilon_{2*}\epsilon_{3*}^2 - \frac{1}{2}\epsilon_{2*}\epsilon_{3*}\epsilon_{4*}\right)\ln^2\left(\frac{k}{k_*}\right). \end{aligned} \tag{3.95}$$

The running of the scalar spectral index [68] is given by the derivative with respect to $\ln k$:

$$\alpha_\mathrm{s}(k) \equiv \frac{\mathrm{d}n_\mathrm{s}}{\mathrm{d}\ln k} \tag{3.96}$$

$$\begin{aligned} &= \big[-2\epsilon_{1*}\epsilon_{2*} - \epsilon_{2*}\epsilon_{3*} - 6\epsilon_{1*}^2\epsilon_{2*} + (-3+2\alpha)\epsilon_{1*}\epsilon_{2*}^2 - 2(2-\alpha)\epsilon_{1*}\epsilon_{2*}\epsilon_{3*} + \alpha\epsilon_{2*}\epsilon_{3*}^2 \\ &\quad + \alpha\epsilon_{2*}\epsilon_{3*}\epsilon_{4*}\big] + \big(-2\epsilon_{1*}\epsilon_{2*}^2 - 2\epsilon_{1*}\epsilon_{2*}\epsilon_{3*} - \epsilon_{2*}\epsilon_{3*}^2 - \epsilon_{2*}\epsilon_{3*}\epsilon_{4*}\big)\ln\left(\frac{k}{k_*}\right). \end{aligned} \tag{3.97}$$

The running of the running of the scalar spectral index takes the form:

$$\beta_\mathrm{s}(k) \equiv \frac{\mathrm{d}\alpha_\mathrm{s}}{\mathrm{d}\ln k} \tag{3.98}$$

$$= -2\epsilon_{1*}\epsilon_{2*}^2 - 2\epsilon_{1*}\epsilon_{2*}\epsilon_{3*} - \epsilon_{2*}\epsilon_{3*}^2 - \epsilon_{2*}\epsilon_{3*}\epsilon_{4*}\,. \tag{3.99}$$

The Primordial Power Spectrum of Tensor Perturbations

For tensor perturbations, the dimensionless PPS characterizing the two polarization modes of gravitational waves generated during inflation is defined as:

$$\mathcal{P}_\mathrm{t}(k) = \frac{k^2}{\pi^2}\lim_{x\to 0}\left|\frac{y^{(\mathrm{t})}}{a}\right|^2, \tag{3.100}$$

This quantity can be computed using the identical procedure outlined previously, by substituting eq. (3.72) into the asymptotic solutions given in eq. (3.86). For primordial tensor fluctuations, the necessary expansion takes the form:

$$\begin{aligned} \left|\frac{1}{xa}\right|^2 \simeq \left(\frac{H}{k}\right)^2 \Big[&1 - 2\epsilon_1 - 2\epsilon_1\epsilon_2 + \epsilon_1^2 - 2\epsilon_1\epsilon_2^2 - 2\epsilon_1\epsilon_2\epsilon_3 \\ &+ \big(2\epsilon_1 + 2\epsilon_1\epsilon_2 - 2\epsilon_1^2 - 2\epsilon_1^2\epsilon_2 + 2\epsilon_1\epsilon_2^2 + 2\epsilon_1\epsilon_2\epsilon_3\big)\ln x \\ &+ \big(2\epsilon_1^2 - \epsilon_1\epsilon_2 + 3\epsilon_1^2\epsilon_2 - \epsilon_1\epsilon_2^2 - \epsilon_1\epsilon_2\epsilon_3\big)\ln^2 x \\ &+ \frac{1}{3}\big(4\epsilon_1^3 - 6\epsilon_1^2\epsilon_2 + \epsilon_1\epsilon_2^2 + \epsilon_1\epsilon_2\epsilon_3\big)\ln^3 x\Big]. \end{aligned} \tag{3.101}$$

The expressions for the dimensionless PPS, tensor spectral index, running of the tensor spectral index, and running of the running of the tensor spectral index, expanded around a pivot scale k_*, are presented below:

$$
\begin{aligned}
\mathcal{P}_{\mathrm{t}}(k) = \frac{2H_*^2}{\pi^2}\Bigg\{\Bigg[&1 + (-2+2\alpha)\epsilon_{1*} + \frac{1}{2}(-6-4\alpha+4\alpha^2+\pi^2)\epsilon_{1*}^2 \\
&+ \left(-2+2\alpha-\alpha^2+\frac{\pi^2}{12}\right)\epsilon_{1*}\epsilon_{2*} - \frac{1}{3}(-16+24\alpha-4\alpha^3-3\alpha\pi^2+6\mathcal{Z})\epsilon_{1*}^3 \\
&+ \frac{1}{12}(-96+72\alpha+36\alpha^2-24\alpha^3+13\pi^2-10\alpha\pi^2)\epsilon_{1*}^2\epsilon_{2*} \\
&- \frac{1}{12}(8-24\alpha+12\alpha^2-4\alpha^3-\pi^2+\alpha\pi^2+24\mathcal{Z})(\epsilon_{1*}\epsilon_{2*}^2+\epsilon_{1*}\epsilon_{2*}\epsilon_{3*})\Bigg] \\
&+ \Bigg[-2\epsilon_{1*} + 2\epsilon_{1*}^2 - 4\alpha\epsilon_{1*}^2 + (-2+2\alpha)\epsilon_{1*}\epsilon_{2*} - (-8+4\alpha^2+\pi^2)\epsilon_{1*}^3 \\
&+ \frac{1}{6}(-36-36\alpha+36\alpha^2+5\pi^2)\epsilon_{1*}^2\epsilon_{2*} \\
&+ \frac{1}{12}(-24+24\alpha-12\alpha^2+\pi^2)(\epsilon_{1*}\epsilon_{2*}^2+\epsilon_{1*}\epsilon_{2*}\epsilon_{3*})\Bigg]\ln\left(\frac{k}{k_*}\right) \\
&+ \left[2\epsilon_{1*}^2 + 4\alpha\epsilon_{1*}^3 - \epsilon_{1*}\epsilon_{2*} + (3-6\alpha)\epsilon_{1*}^2\epsilon_{2*} - (-\alpha+1)(\epsilon_{1*}\epsilon_{2*}^2+\epsilon_{1*}\epsilon_{2*}\epsilon_{3*})\right]\ln^2\left(\frac{k}{k_*}\right) \\
&+ \frac{1}{3}\left(-4\epsilon_{1*}^3 + 6\epsilon_{1*}^2\epsilon_{2*} - \epsilon_{1*}\epsilon_{2*}^2 - \epsilon_{1*}\epsilon_{2*}\epsilon_{3*}\right)\ln^3\left(\frac{k}{k_*}\right)\Bigg\}, \qquad (3.102)
\end{aligned}
$$

$$
\begin{aligned}
n_{\mathrm{t}}(k) = &-2\epsilon_{1*} - 2\epsilon_{1*}^2 - 2(1-\alpha)\epsilon_{1*}\epsilon_{2*} - 2\epsilon_{1*}^3 + (-14+6\alpha+\pi^2)\epsilon_{1*}^2\epsilon_{2*} \\
&+ \left(-2+2\alpha-\alpha^2+\frac{\pi^2}{12}\right)(\epsilon_{1*}\epsilon_{2*}^2+\epsilon_{1*}\epsilon_{2*}\epsilon_{3*}) \\
&+ \left(-2\epsilon_{1*}\epsilon_{2*} - 6\epsilon_{1*}^2\epsilon_{2*} - 2\epsilon_{1*}\epsilon_{2*}^2 + 2\alpha\epsilon_{1*}\epsilon_{2*}^2 - 2\epsilon_{1*}\epsilon_{2*}\epsilon_{3*} + 2\alpha\epsilon_{1*}\epsilon_{2*}\epsilon_{3*}\right)\ln\left(\frac{k}{k_*}\right) \\
&+ \left(-\epsilon_{1*}\epsilon_{2*}^2 - \epsilon_{1*}\epsilon_{2*}\epsilon_{3*}\right)\ln^2\left(\frac{k}{k_*}\right), \qquad (3.103)
\end{aligned}
$$

$$
\begin{aligned}
\alpha_{\mathrm{t}}(k) = &-2\epsilon_{1*}\epsilon_{2*} - 6\epsilon_{1*}^2\epsilon_{2*} - 2(1-\alpha)\epsilon_{1*}\epsilon_{2*}^2 - 2(1-\alpha)\epsilon_{1*}\epsilon_{2*}\epsilon_{3*} \\
&+ 2\left(-\epsilon_{1*}\epsilon_{2*}^2 - \epsilon_{1*}\epsilon_{2*}\epsilon_{3*}\right)\ln\left(\frac{k}{k_*}\right), \qquad (3.104)
\end{aligned}
$$

$$
\beta_{\mathrm{t}}(k) = -2\epsilon_{1*}\epsilon_{2*}^2 - 2\epsilon_{1*}\epsilon_{2*}\epsilon_{3*}\,. \qquad (3.105)
$$

These expressions for the dimensionless PPS of scalar and tensor perturbations, computed to third order in the slow-roll expansion through the integrals and their super-Hubble limits documented in appendices D and E respectively, demonstrate agreement with results previously reported in [57], exhibiting only minor discrepancies in the numerical coefficients of the constant terms in eqs. (3.92) and (3.102).

These different coefficients only appear in the constant part of the PPS without affecting the results obtained for the spectral indices and their slopes. The differences in PPS are numerically negligible.

Alternative formulations for the PPS are documented in appendix F.

3.3 Numerical Solution of the Primordial Power Spectra

To assess the effects of third-order corrections relative to second-order approximations, the work presented in [1] develops a comprehensive numerical approach that solves the coupled system of background and perturbation equations. This system encompasses the Friedmann equation for a spatially flat universe dominated by a scalar field ϕ, the Klein-Gordon equation governing the background dynamics of a scalar field with standard kinetic term and minimal coupling to gravity, and the Mukhanov-Sasaki equation eq. (3.12) that describes the evolution of scalar and tensor primordial perturbations. The numerical implementation strategy adopted to ensure computational stability is detailed in this section.

3.3.1 Models

The numerical code `PyPPSinflation`, developed specifically for this research, numerically solves both the background dynamics and the Mukhanov-Sasaki equation to obtain the numerical primordial power spectra. Additionally, the code implements analytical solutions up to first, second, and third order. The implementation is designed to work with any single-field slow-roll model. This code has been made publicly available[2]. In [1], two specific models are analyzed:

$$V_{\mathrm{T-model}}(\phi) = V_0 \tanh^2\left(\frac{\phi}{\sqrt{6\alpha}}\right) , \qquad V_{\mathrm{KKLT}}(\phi) = V_0\left(1+\frac{m}{|\phi|}\right)^{-1} . \tag{3.106}$$

The first corresponds to the T-model of α-attractor inflation [69, 70, 71, 72, 73, 74], while the second represents the inverse linear case of KKLT inflation [75] associated with D6-$\overline{\mathrm{D6}}$ potential in type IIA string theory [76, 77]. The two potentials are shown in fig. 3.1.

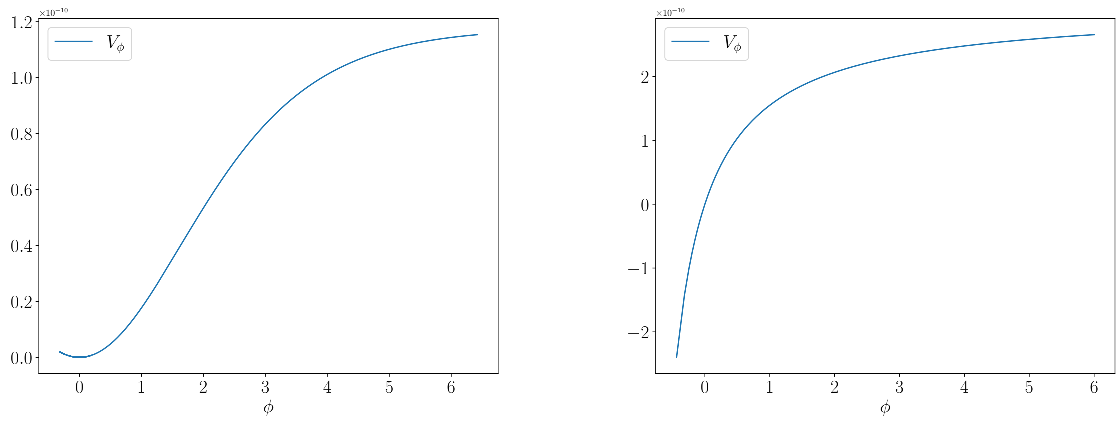

Figure 3.1: Left panel: $V_{\mathrm{T-model}}(\phi)$. Right panel: $V_{\mathrm{KKLT}}(\phi)$.

For T-model inflation, the field values at k_* and at the end of inflation are respectively:

$$\phi_*^{\mathrm{T}}(N,\alpha) = \sqrt{\frac{3\alpha}{2}}\mathrm{sech}^{-1}\left(\frac{3\alpha}{\alpha\sqrt{\frac{12}{\alpha}+9+4N}}\right) , \tag{3.107}$$

$$\phi_{\mathrm{end}}^{\mathrm{T}}(\alpha) = \sqrt{\frac{3\alpha}{2}}\sinh^{-1}\left(\frac{2}{\sqrt{3\alpha}}\right) , \tag{3.108}$$

[2] https://github.com/SirlettiSS/PyPPSinflation

while for KKLT inflation:

$$\phi_*^{\mathrm{KKLT}}(N,\,m) = \frac{1}{2}\Bigg\{\Bigg[12Nm + \left(\sqrt{2}-m\right)m\sqrt{m\left(2\sqrt{2}+m\right)}$$
$$+\sqrt{2m^2\left[\left(2\sqrt{2}-3m\right)m + 12N\left(6N+\left(\sqrt{2}-m\right)\sqrt{m\left(2\sqrt{2}+m\right)}\right)\right]}\Bigg]^{1/3}$$
$$- m + m^2\Bigg[12Nm + \left(\sqrt{2}-m\right)m\sqrt{m\left(2\sqrt{2}+m\right)}$$
$$+\sqrt{2m^2\left[\left(2\sqrt{2}-3m\right)m + 12N\left(6N+\left(\sqrt{2}-m\right)\sqrt{m\left(2\sqrt{2}+m\right)}\right)\right]}\Bigg]^{-1/3}\Bigg\}\,, \tag{3.109}$$

$$\phi_{\mathrm{end}}^{\mathrm{KKLT}}(m) = \frac{1}{2}\left[\sqrt{m\left(2\sqrt{2}+m\right)} - m\right]. \tag{3.110}$$

3.3.2 Background dynamics

The fundamental background equations consist of the Friedmann and Klein-Gordon equations for ϕ, expressed as:

$$H^2 = \frac{1}{3M_{\mathrm{Pl}}^2}\left(\frac{\dot{\phi}^2}{2}+V\right)\,, \qquad \ddot{\phi} + 3H\dot{\phi} + V_\phi = 0\,. \tag{3.111}$$

The temporal evolution of the background equations in eq. (3.111) is performed using the number of e-folds as the time parameter:

$$N = \int_{t_i}^{t} \mathrm{d}t\ H(t) = \ln\left[\frac{a(t)}{a(t_i)}\right]. \tag{3.112}$$

Additionally, the background system is reformulated by adopting the field redefinition $\psi = \dot{\phi}$. This transformation enables the reduction of the background equations to a system of first-order differential equations. Under these conditions, the background system becomes:

$$\begin{cases} \phi_N \equiv \frac{\psi}{H} = \psi M_{\mathrm{Pl}}\sqrt{\frac{3}{\frac{\psi^2}{2}+V(\phi)}} \\ \psi_N = -3\psi - V_\phi M_{\mathrm{Pl}}\sqrt{\frac{3}{\frac{\psi^2}{2}+V(\phi)}} \end{cases}\,, \tag{3.113}$$

where the subscript N denotes differentiation with respect to N. In fig. 3.2 the evolution of $\phi(N)$ and $\psi(N)$ for the T-model with $\alpha = 1$ is shown.

3.3.3 Perturbations

The Mukhanov-Sasaki equation eq. (3.12) can be expressed in general form for both scalar and tensor perturbations as:

$$\varphi_k^{(\mathrm{s,t})\,\prime\prime}(\tau) + \left[k^2 - U^{(\mathrm{s,t})}(\tau)\right]\varphi_k^{(\mathrm{s,t})}(\tau) = 0\,. \tag{3.114}$$

When transformed to the e-folds parametrization, equations eq. (3.114) take the form:

$$\varphi_{k\,NN}^{(\mathrm{s,t})} = [\epsilon_1(N)-1]\varphi_{k\,N}^{(\mathrm{s,t})} + \frac{1}{a^2H^2}\left[U^{(\mathrm{s,t})}(N) - k^2\right]\varphi_k^{(\mathrm{s,t})}\,, \tag{3.115}$$

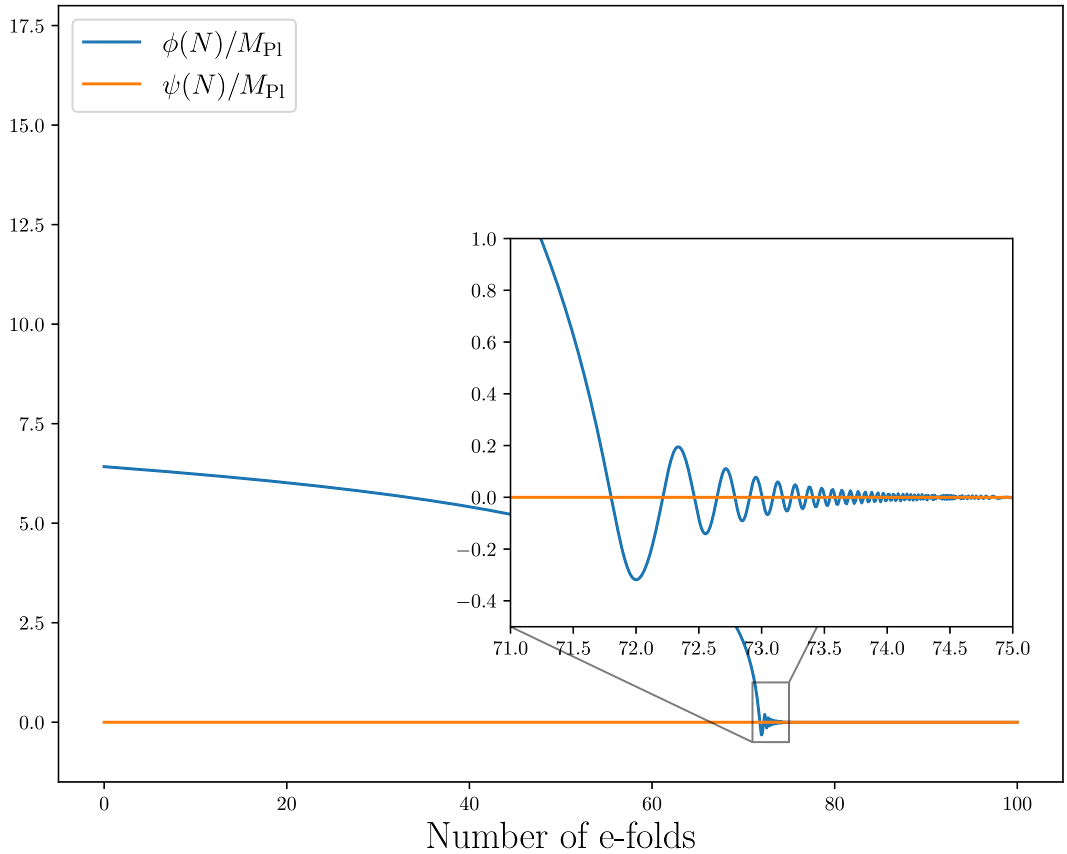

Figure 3.2: Background dynamics of $\phi(N)$ and its derivative with respect to the time $\psi = \dot{\phi}$ using the T-model of α-attractor inflation with $\alpha = 1$.

where the effective potentials are given by:

$$U^{(\rm s)}(N) = \frac{z''}{z} = a^2H^2\left(2 - \epsilon_1 + \frac{3\epsilon_2}{2} - \frac{\epsilon_1\epsilon_2}{2} + \frac{\epsilon_2^2}{4} + \frac{\epsilon_2\epsilon_3}{2}\right) , \tag{3.116}$$

$$U^{(\rm t)}(N) = \frac{a''}{a} = a^2H^2\left(2 - \epsilon_1\right) . \tag{3.117}$$

The perturbation equations are solved separately for the real and imaginary components of the mode functions, expressed as $\varphi_k^{(\rm s,t)} = \mathrm{Re}\left[\varphi_k^{(\rm s,t)}\right] + i\,\mathrm{Im}\left[\varphi_k^{(\rm s,t)}\right]$.

Regarding initial conditions, the background scalar field value ϕ_i is chosen to ensure that 55 e-folds occur between the time when the mode $k_* = 0.05\,\mathrm{Mpc}^{-1}$ crosses the Hubble radius and the end of inflation. The initial value of $\dot{\phi}$ is determined using slow-roll initial conditions corresponding to $\phi_N|_i \simeq -M_{\rm Pl}^2 V_\phi/V|_i$.

For the perturbation equations, Bunch-Davies initial conditions are imposed for each mode when $k = 10^2\,aH$. The factor 10^2 is selected to ensure that all evolved modes are well within the Hubble horizon at the beginning of their evolution, allowing the safe implementation of the Bunch-Davies vacuum. Modes are subsequently evolved until they become super-Hubble when $k = 10^{-3}\,aH$. The factor 10^{-3} ensures that all evolved modes exit the horizon before their evolution terminates. These values define the integration interval for the number of e-folds. The Bunch-Davies initial conditions eq. (3.13) for the real and imaginary components of the mode function are:

$$\mathrm{Re}\left[\varphi_k^{(\mathrm{s,t})}\right] = \frac{1}{\sqrt{2k}}\,, \qquad \mathrm{Re}\left[\varphi_{k\,N}^{(\mathrm{s,t})}\right] = 0\,, \tag{3.118}$$

and

$$\mathrm{Im}\left[\varphi_k^{(\mathrm{s,t})}\right] = 0\,, \qquad \mathrm{Im}\left[\varphi_{k\,N}^{(\mathrm{s,t})}\right] = -\frac{1}{aH}\sqrt{\frac{k}{2}}\,. \tag{3.119}$$

Since curvature and tensor perturbations become frozen on super-Hubble scales, it is sufficient to calculate the power spectrum for modes in the super-Hubble regime (post-horizon crossing) rather than computing it at the end of inflation. This is shown in fig. 3.3 where from the scalar solution $\varphi_k^{(\mathrm{s})}$ the curvature perturbation ζ and its derivative ζ_N with respect to N are recovered.

For the numerical implementation, the background equations are solved for a given potential, and the resulting scalar field background solution is incorporated into the Hubble flow functions entering the perturbation equations:

$$\epsilon_1(N) = \frac{\phi_N^2}{2M_{\mathrm{Pl}}^2}\,, \tag{3.120}$$

$$\epsilon_2(N) = \frac{\mathrm{d}\ln|\epsilon_1|}{\mathrm{d}N} = \frac{2\phi_{NN}}{\phi_N}\,, \tag{3.121}$$

$$\epsilon_3(N) = \frac{\mathrm{d}\ln|\epsilon_2|}{\mathrm{d}N} = \frac{\phi_{NNN}}{\phi_{NN}} - \frac{\phi_{NN}}{\phi_N}\,. \tag{3.122}$$

For the analytical approach, the Hubble flow functions are calculated as functions of the potential slow-roll parameters [78], following the detailed procedures outlined in [67, 79]. The analysis begins with the leading-order expressions:

$$\epsilon_1^{\mathrm{LO}} \simeq \frac{M_{\mathrm{Pl}}^2}{2}\left(\frac{V_\phi}{V}\right)^2\,, \tag{3.123}$$

$$\epsilon_2^{\mathrm{LO}} \simeq 2M_{\mathrm{Pl}}^2\left(\frac{V_\phi^2}{V^2} - \frac{V_{\phi\phi}}{V}\right)\,, \tag{3.124}$$

$$\epsilon_3^{\mathrm{LO}} \simeq \frac{2M_{\mathrm{Pl}}^4}{\epsilon_2}\left(\frac{2V_\phi^4}{V^4} - \frac{3V_\phi^2 V_{\phi\phi}}{V^3} + \frac{V_\phi V_{\phi\phi\phi}}{V^2}\right)\,, \tag{3.125}$$

$$\begin{aligned}\epsilon_4^{\mathrm{LO}} \simeq \frac{2M_{\mathrm{Pl}}^6}{\epsilon_2\epsilon_3}\Bigg[&\frac{8V_\phi^6}{V^6} - \frac{17V_\phi^4 V_{\phi\phi}}{V^5} + \frac{6V_\phi^2 V_{\phi\phi}^2}{V^4} + \frac{5V_\phi^3 V_{\phi\phi\phi}}{V^4} - \frac{V_\phi V_{\phi\phi} V_{\phi\phi\phi}}{V^3} - \frac{V_\phi^2 V_{\phi\phi\phi\phi}}{V^3} + \\ &+ \frac{2M_{\mathrm{Pl}}^2}{\epsilon_2}\left(-\frac{4V_\phi^8}{V^8} + \frac{12V_\phi^6 V_{\phi\phi}}{V^7} - \frac{9V_\phi^4 V_{\phi\phi}^2}{V^6} - \frac{4V_\phi^5 V_{\phi\phi\phi}}{V^6} + \frac{6V_\phi^3 V_{\phi\phi} V_{\phi\phi\phi}}{V^5} - \frac{V_\phi^2 V_{\phi\phi\phi}^2}{V^4}\right)\Bigg]\,.\end{aligned} \tag{3.126}$$

These expressions are derived by approximating the Hubble parameter at leading order as $H^2 \simeq V/(3M_{\mathrm{Pl}}^2)$, which yields the leading-order formula for the derivative with respect to N [79]:

$$\left.\frac{\mathrm{d}}{\mathrm{d}N}\right|_{\mathrm{LO}} = -M_{\mathrm{Pl}}^2\frac{V_\phi}{V}\frac{\mathrm{d}}{\mathrm{d}\phi}\,. \tag{3.127}$$

To enable comparison between analytical and numerical solutions, corrections up to third order in terms of potential slow-roll parameters must be incorporated. The third-order equations have been previously calculated in [67]; the results are presented here in terms of the leading-order Hubble flow functions:

$$\epsilon_1^{\mathrm{N3LO}} = \left.\left(\epsilon_1 - \frac{1}{3}\epsilon_1\epsilon_2 - \frac{1}{9}\epsilon_1^2\epsilon_2 + \frac{5}{36}\epsilon_1\epsilon_2^2 + \frac{1}{9}\epsilon_1\epsilon_2\epsilon_3\right)\right|_{\mathrm{LO}}\,, \tag{3.128}$$

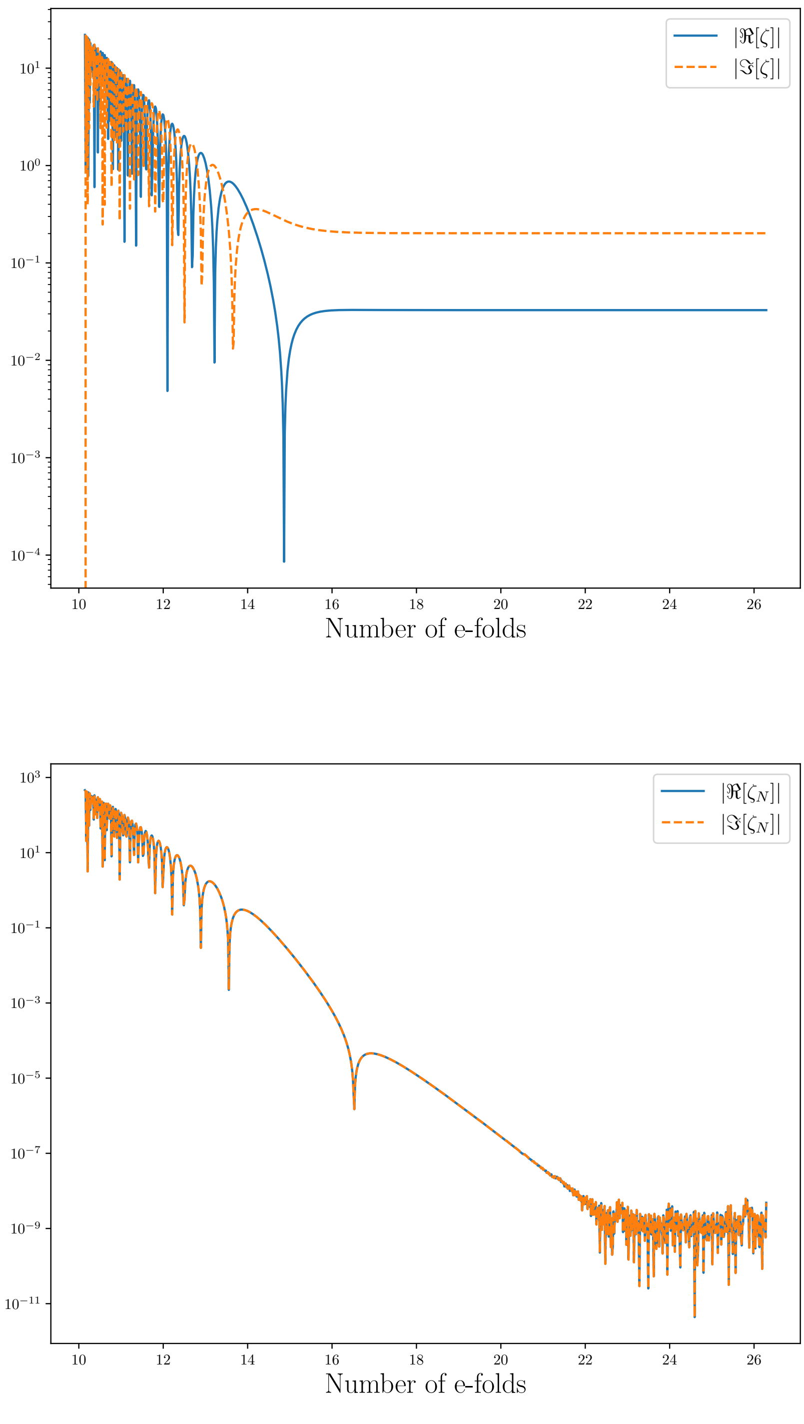

Figure 3.3: Upper panel: absolute value of the real and imaginary components of the curvature perturbation ζ. Lower panel: absolute value of the real and imaginary components of the the derivative with respect to N of the curvature perturbation, ζ_N. The curvature perturbation is a conserved quantity at super-Hubble scales and its derivative goes to zero.

$$\epsilon_2^{\text{N3LO}} = \left(\epsilon_2 - \frac{1}{6}\epsilon_2^2 - \frac{1}{3}\epsilon_2\epsilon_3 - \frac{1}{6}\epsilon_1\epsilon_2^2 + \frac{1}{18}\epsilon_2^3 - \frac{1}{9}\epsilon_1\epsilon_2\epsilon_3 + \frac{5}{18}\epsilon_2^2\epsilon_3 + \frac{1}{9}\epsilon_2\epsilon_3^2 + \frac{1}{9}\epsilon_2\epsilon_3\epsilon_4\right)\Bigg|_{\text{LO}}, \tag{3.129}$$

$$\epsilon_3^{\rm N3LO} = \left(\epsilon_3 - \frac{1}{3}\epsilon_2\epsilon_3 - \frac{1}{3}\epsilon_3\epsilon_4 - \frac{1}{6}\epsilon_1\epsilon_2^2 - \frac{1}{3}\epsilon_1\epsilon_2\epsilon_3 + \frac{1}{6}\epsilon_2^2\epsilon_3 + \frac{5}{18}\epsilon_2\epsilon_3^2 - \frac{1}{9}\epsilon_1\epsilon_3\epsilon_4 \right.$$
$$\left. + \frac{5}{18}\epsilon_2\epsilon_3\epsilon_4 + \frac{1}{9}\epsilon_3^2\epsilon_4 + \frac{1}{9}\epsilon_3\epsilon_4^2 + \frac{1}{9}\epsilon_3\epsilon_4\epsilon_5\right)\Big|_{\rm LO}, \tag{3.130}$$

$$\epsilon_4^{\rm N3LO} = \left(\epsilon_4 - \frac{1}{3}\epsilon_2\epsilon_3 - \frac{1}{6}\epsilon_2\epsilon_4 - \frac{1}{3}\epsilon_4\epsilon_5\right)\Big|_{\rm LO}, \tag{3.131}$$

where all HHFs on the right-hand side are evaluated at leading order using eqs. (3.123) to (3.126), and the analysis sets $\epsilon_5 = 0$.

To express the HHFs in terms of the number of e-folds rather than scalar field values, the classical inflationary trajectory $\phi(N)$ must be solved analytically. This is accomplished at leading order by solving:

$$N(\phi) \simeq -\frac{1}{M_{\rm Pl}^2}\int_{\phi}^{\phi_{\rm end}} \frac{V}{V_\phi}{\rm d}\phi\,, \tag{3.132}$$

and inverting this relationship. The value $\phi_{\rm end}$ represents the field value at the end of inflation, determined by imposing $\epsilon_{1,\,\rm end} \equiv \epsilon_1(\phi_{\rm end}) = 1$, corresponding to the point where the kinetic term begins to dominate over the potential energy.

Once the trajectory $\phi(N)$ is obtained, the analytical HHFs at leading order can be expressed with respect to the number of e-folds, yielding $\epsilon_i^{\rm LO}(N)$. Subsequently, the third-order expressions can be derived using eqs. (3.128) to (3.131). Finally, the scalar and tensor primordial power spectra can be calculated using eqs. (3.92) and (3.102).

The potential amplitude V_0 is fixed to normalize the dimensionless scalar power spectrum to $\mathcal{P}_\zeta(k_*) = 2\times 10^{-9}$ at $k_* = 0.05\,{\rm Mpc}^{-1}$.

3.4 Accuracy of Slow-Roll Analytic Power Spectra Against the Exact Numerical Solution

This section presents a comprehensive comparison between the analytical results derived in section 3.2.1 at various orders in the slow-roll expansion and the numerical solutions for the primordial power spectra obtained for two distinct single-field slow-roll inflationary models.

The analysis examines the T-model of α-attractor inflation with $\alpha = 1$ (results shown in figs. 3.4 and 3.5) and KKLT inflation with $m = 1$ (results presented in figs. 3.6 and 3.7). The comparison evaluates numerical solutions against analytical results computed at first-, second-, and third-order slow-roll expansions across the wavenumber range $k \in \left[10^{-4}, 10^{2}\right]$ Mpc^{-1}. Additionally, the analysis includes a comparison for the third-order case with $\epsilon_4 = 0$. Similar comparative studies between first- and second-order corrections can be found in the literature, as documented in [56, 80].

The power spectra comparisons and their corresponding relative deviations of analytical results from numerical solutions are displayed in figs. 3.4 and 3.6. Furthermore, figs. 3.5 and 3.7 present the relative deviations for the spectral indices $n_{\rm s}$ and $n_{\rm t}$, their respective runnings $\alpha_{\rm s}$ and $\alpha_{\rm t}$, and the runnings of the running $\beta_{\rm s}$ and $\beta_{\rm t}$. For any observable quantity X, where $X = \{\mathcal{P}_\zeta,\, \mathcal{P}_{\rm t},\, n_{\rm s},\, n_{\rm t},\, \alpha_{\rm s},\, \alpha_{\rm t},\, \beta_{\rm s},\, \beta_{\rm t}\}$, the corresponding percentage deviation $\%X$ is quantified as:

$$\%X = \left(1 - \frac{X_{\rm analytical}}{X_{\rm numerical}}\right)\times 100\,. \tag{3.133}$$

The results presented in figs. 3.4 and 3.6 reveal that relative deviations for the tensor power spectrum are approximately one order of magnitude smaller than those for the scalar power spectrum. Across the entire wavenumber range, the relative errors demonstrate the anticipated perturbative hierarchy, whereby higher-order approximations yield progressively smaller errors.

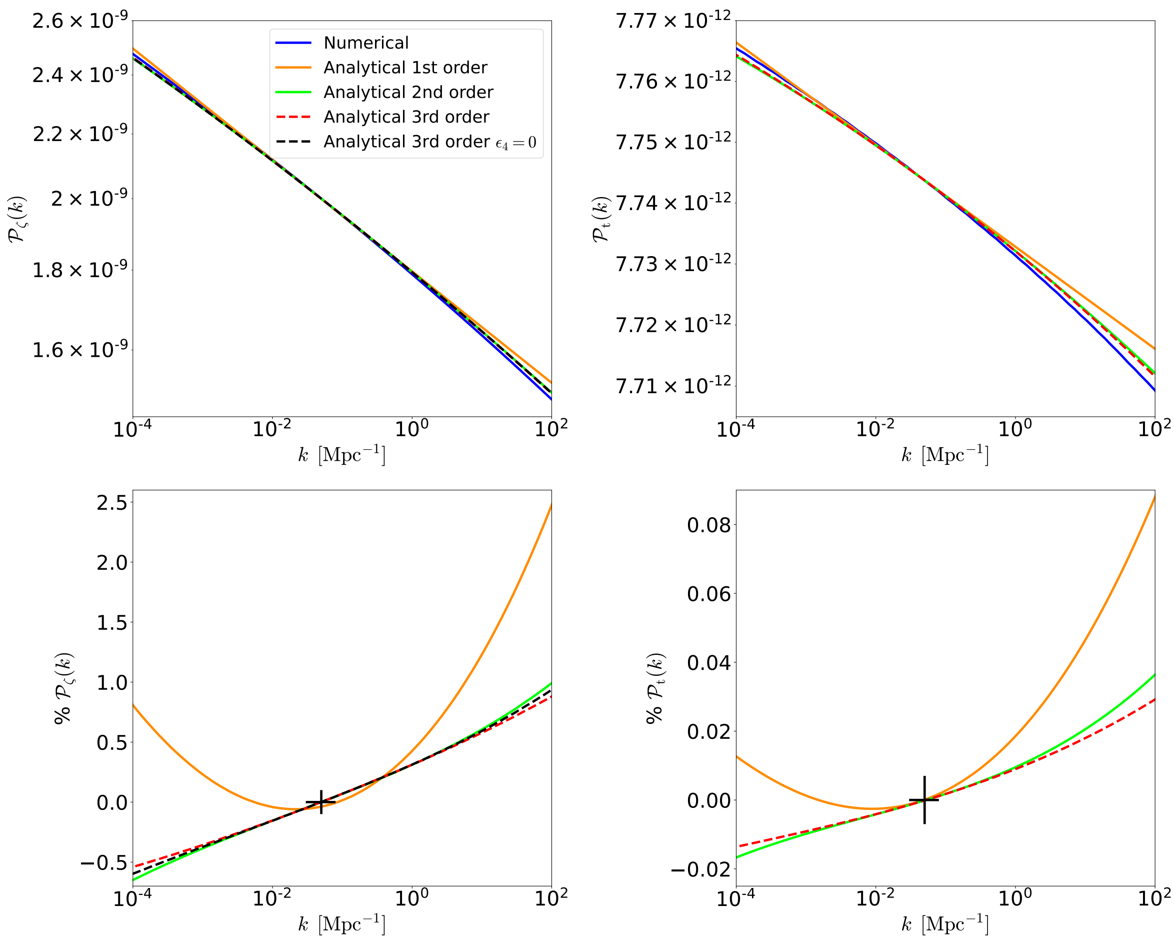

Figure 3.4: Comparison of scalar (left panels) and tensor (right panels) primordial power spectra for T-model α-attractor inflation with $\alpha = 1$. The pivot scale crosses the Hubble horizon 55 e-folds before inflation ends. Upper panels display the dimensionless power spectra, while lower panels show the relative deviations of analytical spectra from the numerical benchmark solution.

It is noteworthy that the third-order case with $\epsilon_4 = 0$ behaves as an intermediate case between the second- and full third-order approximations. For both inflationary models, the second- and third-order power spectrum relative deviations are nearly indistinguishable around the pivot scale k_* and closely match the numerical results due to the normalization procedure employed. Discrepancies between second and third order begin to emerge around $k \sim 10\,\mathrm{Mpc}^{-1}$ at the 0.1% level, with the curves becoming visibly distinct at $k \sim 10^2\,\mathrm{Mpc}^{-1}$ where maximum differences reach 0.5% and 0.3% for T-model and KKLT inflation, respectively. For the tensor power spectrum, small differences between second and third order commence at $k \sim 1\,\mathrm{Mpc}^{-1}$ with relative errors at the 0.01% level, increasing to 0.02% at $k \sim 10^2\,\mathrm{Mpc}^{-1}$.

The analysis of spectral parameters presented in figs. 3.5 and 3.7 examines the relative deviations for $n_{\mathrm{s/t}}$, $\alpha_{\mathrm{s/t}}$, and $\beta_{\mathrm{s/t}}$ for T-model and KKLT inflation models. Generally, larger deviations are observed for tensor quantities, though these are typically associated with greater observational uncertainties. For the spectral indices n_{s} and n_{t}, relative deviations are nearly identical around the pivot scale, beginning to diverge from $k \sim 10\,\mathrm{Mpc}^{-1}$. Conversely, for wavenumbers below the pivot scale, differences emerge from $k \sim 10^{-2}\,\mathrm{Mpc}^{-1}$. When incorporating second and third-order corrections, the relative deviations for n_{s} in both models remain consistently at or below 0.1%, while for n_{t} they stay at or below 10% in absolute terms. For the runnings of the spectral indices α_{s} and α_{t}, increasing differences between second and third order are observed

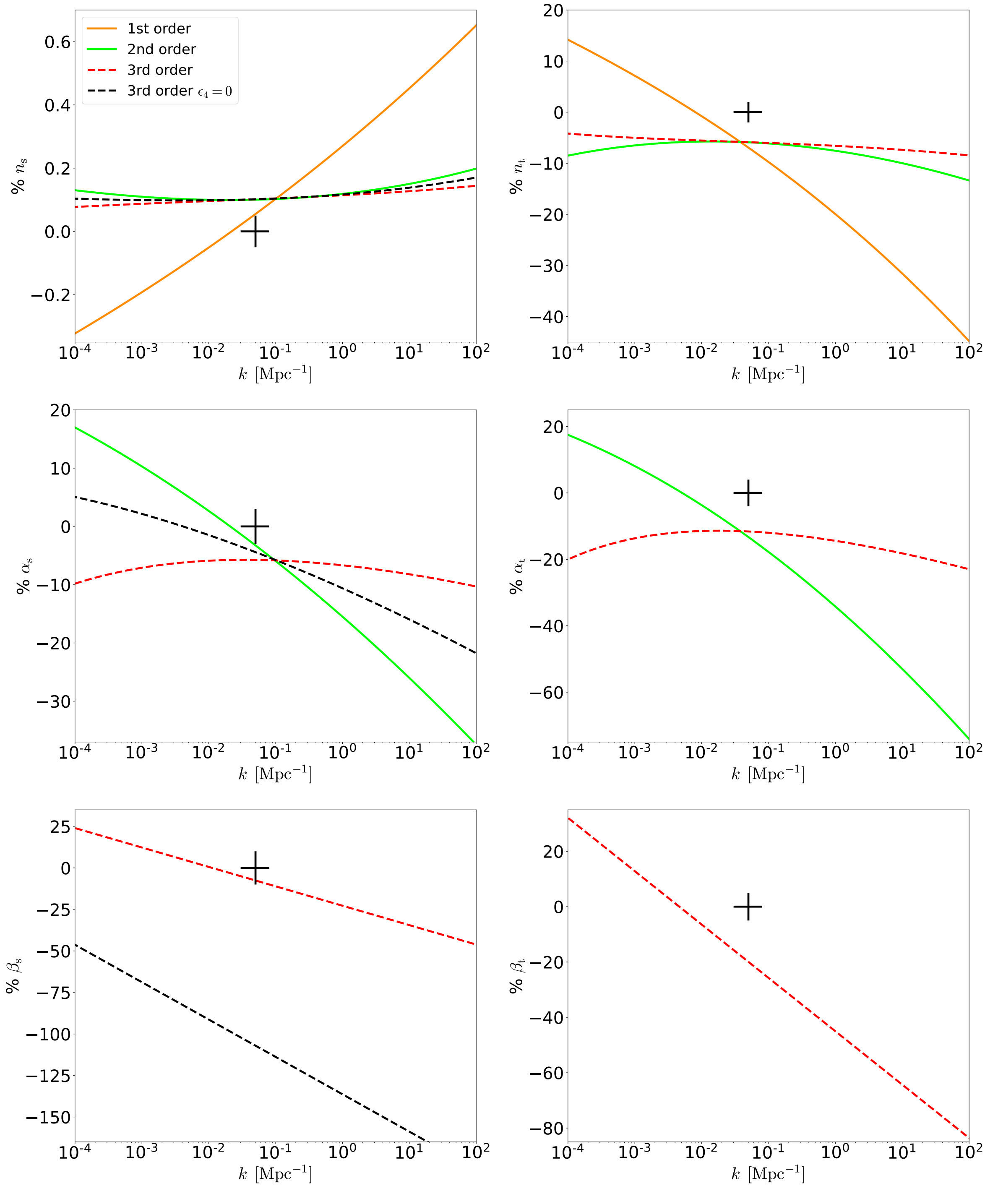

Figure 3.5: Relative deviations from the numerical solution for the scalar spectral index (upper panels), its running (central panels), and the running of the running (lower panels) in T-model α-attractor inflation with $\alpha = 1$. The comparison demonstrates the progressive improvement in accuracy with increasing order of slow-roll approximation.

as one moves away from the pivot scale; these differences consistently remain around $\sim 1\%$ near the pivot scale and increase to approximately $\sim 10\%$ at larger separations.

The third-order relative deviations for β_s and β_t consistently remain around $\sim 10\%$ for both models across the scale range accessible to CMB measurements; errors become larger at scales distant from the pivot. When considering the third-order case with $\epsilon_4 = 0$, β_s exhibits

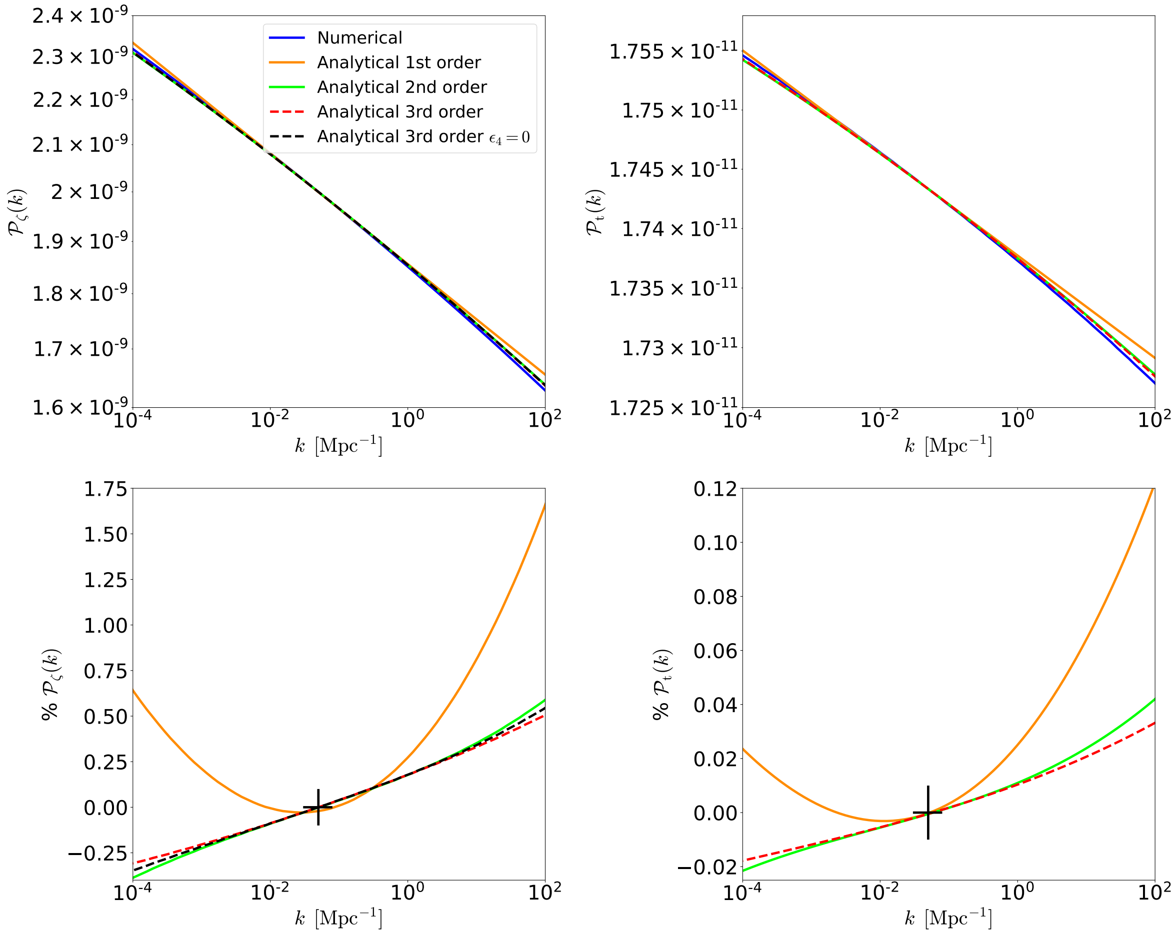

Figure 3.6: Primordial power spectra comparison for KKLT inflation with $m = 1$, following the same format as fig. 3.4. The analysis reveals similar convergence patterns to the T-model case.

substantially larger deviations compared to the numerical benchmark: these errors begin at approximately 50% for $k \sim 10^{-4}\,\mathrm{Mpc}^{-1}$ and increase to 150% at $k \sim 10^{2}\,\mathrm{Mpc}^{-1}$.

Additionally, the comparison was extended to larger values of the inflationary parameters, specifically $\alpha = 100$ for T-model inflation and $m = 100$ for KKLT inflation. No significant differences were observed compared to the cases presented here for $\alpha = 1$ and $m = 1$.

These results demonstrate that higher-order corrections significantly enhance the accuracy of the predicted power spectra, spectral indices, and their derivatives. Nevertheless, the transition from second to third-order expansion yields noticeable improvements only at very small scales, specifically for $k \gtrsim 10\,\mathrm{Mpc}^{-1}$, as illustrated in figs. 3.4 to 3.7. At higher scales, the CMB angular power spectra remain largely unchanged.

Given that scalar perturbations demand higher precision requirements compared to tensor modes, the primary focus should be directed toward the scalar sector.

3.5 Data Analysis and Cosmological Constraints

Having derived the third-order PPS solution and validated it against the results of [57], this third-order expansion is employed to constrain the HFFs using observational data. To assess the significance of including third-order corrections, a comparative analysis is performed with constraints obtained using first- and second-order truncations.

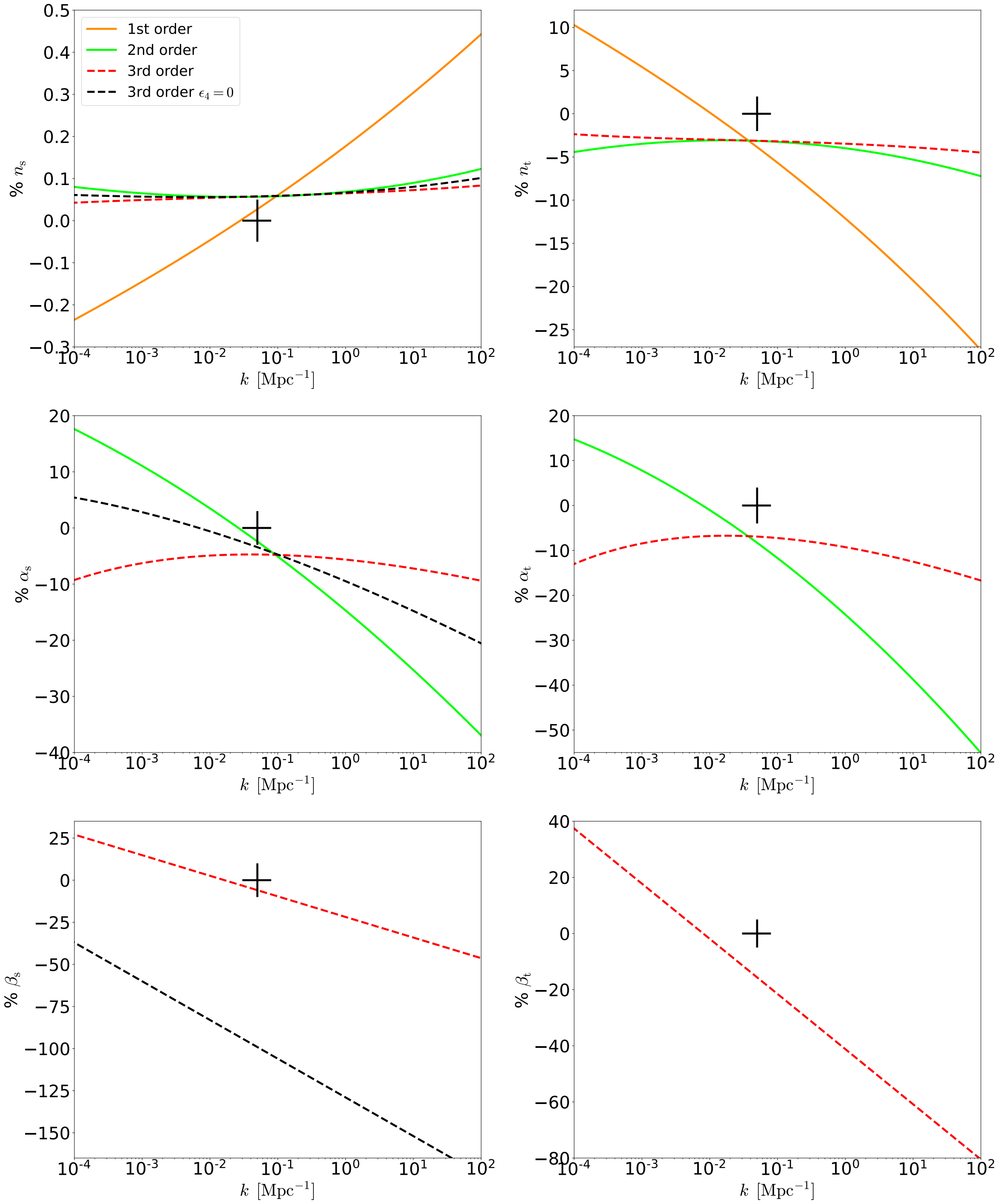

Figure 3.7: Spectral parameter deviations for KKLT inflation with $m = 1$, presented in the same format as fig. 3.5. The results demonstrate the enhanced precision achieved through third-order corrections.

3.5.1 Methodology and datasets

This section presents the determination of uncertainties on the HFFs by considering the PPS expansion truncated at first, second, and third order. The analysis employs `CosmoMC` [81][3] in-

[3] https://github.com/cmbant/CosmoMC

terfaced with a modified version of `CAMB` [82, 83].[4] Parameter estimates with their associated uncertainties, along with the posterior contours, have been derived using `GetDist` [84].[5] The Markov chain Monte Carlo (MCMC) sampling explores the standard cosmological parameters of a flat ΛCDM concordance model: ω_b, ω_c, H_0, τ, and $\ln\left(10^{10}A_\mathrm{s}\right)$, supplemented by the HFFs ϵ_i. Nuisance and foreground parameters associated with each likelihood are also varied. The neutrino sector assumes two massless species with $N_\mathrm{eff} = 2.046$ and one massive neutrino with a fixed minimum mass $m_\nu = 0.06\,\mathrm{eV}$.

The primary objective is to compare constraints derived from various cosmological datasets based on primary CMB observations, specifically temperature and polarisation anisotropies. Additionally, the impact of incorporating non-primary CMB datasets is examined. The following data combinations are considered:

- P18 denotes *Planck* PR3 primary CMB data [85]. At low multipoles ($\ell < 30$), the analysis uses the `commander` likelihood for temperature and `SimAll` for E-mode polarisation. At high multipoles ($\ell \geq 30$), the `Plik` likelihood is employed, incorporating CMB temperature up to $\ell_\mathrm{max} = 2508$, and E-mode polarisation along with temperature-polarisation cross-correlation up to $\ell_\mathrm{max} = 1996$.[6]

- ACT denotes ACT DR4 TT, EE, and TE power spectra [20, 65] spanning the multipole range [350, 4000]. When combining ACT with *Planck* data, temperature measurements are excluded at specific multipole thresholds to mitigate unaccounted correlations between the two datasets. Two multipole cut strategies are implemented: the first removes *Planck* temperature data for $\ell > 650$, while the second excludes ACT temperature data for $\ell < 1800$.

- SPT denotes SPT-3G 2018 TT, EE, and TE power spectra covering the angular multipole range $750 < \ell < 3000$ [19]. When combining SPT with *Planck* data, no multipole cuts are applied, since *Planck* observations cover a substantial sky fraction not observed by SPT.

- BK18 denotes the B-mode polarisation spectrum over $20 < \ell < 330$ from BICEP2, Keck Array, and BICEP3 observations through 2018 [39].

- *ext* (external) denotes the combination of late-time cosmological probes and non-primary CMB data. This includes baryon acoustic oscillations (BAO) and redshift space distortions (RSD) measurements at low redshift $0.07 < z < 0.2$ from the SDSS-I and -II *Main Galaxy Sample* (MGS), BOSS DR12 galaxy observations over $0.2 < z < 0.6$, eBOSS luminous red galaxies (LRG) and quasars covering $0.6 < z < 2.2$, and Lyman-α forest data spanning $1.8 < z < 3.5$. The Pantheon compilation of uncalibrated Type Ia Supernovae (SNe) over the redshift range $0.01 < z < 2.3$ [86] is also included.[7] Finally, CMB lensing measurements from *Planck* PR3 are incorporated using the conservative multipole range $8 < \ell < 400$ [87].

When analyzing ACT or SPT data independently of *Planck* observations, the *Planck* low-ℓ E-mode polarisation likelihood `SimAll` is included to constrain the optical depth τ, thereby avoiding reliance on a Gaussian *Planck*-based prior. The data combinations examined include P18+BK18, ACT+BK18, SPT+BK18, P18+ACT+BK18, P18+SPT+BK18, with each combination also tested with the external datasets. For precedents on combining *Planck*, ACT, and SPT data in extensions of the ΛCDM model, see [88, 89, 90, 91].

The prior ranges for cosmological parameters are summarized in table 3.1. Uniform priors are adopted for all HFF parameters ϵ_i. To maintain the validity of the slow-roll framework derived in section 3.2.1 and implemented in this analysis, the HFFs must satisfy $|\epsilon_i| < 1$.

[4] https://github.com/cmbant/CAMB
[5] https://github.com/cmbant/getdist
[6] https://pla.esac.esa.int/pla/#cosmology
[7] https://github.com/dscolnic/Pantheon/

Parameter	Uniform prior
$\Omega_b h^2$	[0.019, 0.025]
$\Omega_c h^2$	[0.095, 0.145]
$100\theta_{MC}$	[1.03, 1.05]
τ	[0.01, 0.4]
$\ln\left(10^{10} A_s\right)$	[2.5, 3.7]
ϵ_1	[0, 0.1]
ϵ_2	[-0.5, 0.5]
ϵ_3	[-0.5, 0.5]
ϵ_4	[-0.5, 0.5]

Table 3.1: Prior ranges for cosmological parameters used in the Bayesian analysis.

3.5.2 Results

Constraints on the slow-roll parameters are first presented, derived from the analytic perturbative expansion of the primordial spectra in terms of the HFFs ϵ_i during slow-roll inflation. Truncating the expansion at first order yields

$$\epsilon_1 < 0.0022 \qquad (95\%\ \text{CL},\ \text{P18} + \text{BK18})\,, \tag{3.134}$$
$$\epsilon_2 = 0.0332 \pm 0.0046 \qquad (68\%\ \text{CL},\ \text{P18} + \text{BK18})\,, \tag{3.135}$$

$$\epsilon_1 < 0.0023 \qquad (95\%\ \text{CL},\ \text{ACT} + \text{BK18})\,, \tag{3.136}$$
$$\epsilon_2 = -0.005 \pm 0.014 \qquad (68\%\ \text{CL},\ \text{ACT} + \text{BK18})\,, \tag{3.137}$$

$$\epsilon_1 < 0.0024 \qquad (95\%\ \text{CL},\ \text{SPT} + \text{BK18})\,, \tag{3.138}$$
$$\epsilon_2 = 0.032 \pm 0.015 \qquad (68\%\ \text{CL},\ \text{SPT} + \text{BK18})\,. \tag{3.139}$$

Extending the expansion to second order in the HFFs provides

$$\epsilon_1 < 0.0023 \qquad (95\%\ \text{CL},\ \text{P18} + \text{BK18})\,, \tag{3.140}$$
$$\epsilon_2 = 0.0379 \pm 0.0078 \qquad (68\%\ \text{CL},\ \text{P18} + \text{BK18})\,, \tag{3.141}$$
$$\epsilon_3 = 0.13^{+0.19}_{-0.12} \qquad (68\%\ \text{CL},\ \text{P18} + \text{BK18})\,, \tag{3.142}$$

$$\epsilon_1 < 0.0023 \qquad (95\%\ \text{CL},\ \text{ACT} + \text{BK18})\,, \tag{3.143}$$
$$\epsilon_2 = -0.007^{+0.016}_{-0.014} \qquad (68\%\ \text{CL},\ \text{ACT} + \text{BK18})\,, \tag{3.144}$$
$$\epsilon_3\ \text{unconstrained} \qquad (95\%\ \text{CL},\ \text{ACT} + \text{BK18})\,, \tag{3.145}$$

$$\epsilon_1 < 0.0025 \qquad (95\%\ \text{CL},\ \text{SPT} + \text{BK18})\,, \tag{3.146}$$
$$\epsilon_2 = 0.035 \pm 0.017 \qquad (68\%\ \text{CL},\ \text{SPT} + \text{BK18})\,, \tag{3.147}$$
$$\epsilon_3\ \text{unconstrained} \qquad (95\%\ \text{CL},\ \text{SPT} + \text{BK18})\,. \tag{3.148}$$

At third order in the HFF expansion, the results closely mirror those obtained at second order, with ϵ_4 remaining unconstrained, as detailed in table 3.2. Incorporating external datasets—specifically BAO and RSD measurements, SNe, and CMB lensing—produces marginally tighter uncertainties while maintaining consistent central values for ϵ_2 and ϵ_3, as shown in table 3.3.

The upper bound on ϵ_1, along with the derived constraint on r ($\lesssim 0.04$ at 95% CL), remains largely insensitive to the choice of dataset combination and truncation order, being predominantly determined by the BK18 data present in all cases. Conversely, ϵ_2 and ϵ_3 exhibit substantial variations between *Planck* and ACT datasets. This discrepancy stems from the nearly

	P18 + BK18	ACT + BK18	SPT + BK18
	FIRST ORDER		
$\ln\left(10^{10} A_s\right)$	3.046 ± 0.015	3.030 ± 0.019	3.038 ± 0.016
ϵ_1 (at 95% CL)	< 0.0022	< 0.0023	< 0.0024
ϵ_2	0.0332 ± 0.0046	-0.005 ± 0.014	0.032 ± 0.015
$n_{s,\,0.05}$	0.9647 ± 0.0043	1.003 ± 0.014	0.966 ± 0.015
$r_{0.05}$ (at 95% CL)	< 0.035	< 0.037	< 0.039
$n_{t,\,0.05}$	$-0.0020^{+0.0015}_{-0.0009}$	$-0.0022^{+0.0015}_{-0.0009}$	$-0.0024^{+0.0017}_{-0.0010}$
	SECOND ORDER		
$\ln\left(10^{10} A_s\right)$	3.050 ± 0.017	3.029 ± 0.019	3.040 ± 0.017
ϵ_1 (at 95% CL)	< 0.0023	< 0.0023	< 0.0025
ϵ_2	0.0379 ± 0.0078	$-0.007^{+0.016}_{-0.014}$	0.035 ± 0.017
ϵ_3 (at 95% CL)	$0.13^{+0.30}_{-0.35}$	–	–
$n_{s,\,0.05}$	0.9641 ± 0.0046	$1.003^{+0.015}_{-0.013}$	0.967 ± 0.014
$\alpha_{s,\,0.05}$	-0.0059 ± 0.0067	$0.0020^{+0.0029}_{-0.0051}$	$-0.006^{+0.012}_{-0.010}$
$r_{0.05}$ (at 95% CL)	< 0.036	< 0.038	< 0.038
$n_{t,\,0.05}$	$-0.0022^{+0.0016}_{-0.0010}$	$-0.0022^{+0.0016}_{-0.0010}$	$-0.0024^{+0.0017}_{-0.0010}$
$10^5\alpha_{t,\,0.05}$	$-8.1^{+5.9}_{-3.3}$	$1.9^{+2.3}_{-4.4}$	$-7.8^{+6.8}_{-3.4}$

Table 3.2: Constraints on the primary inflationary parameters and their derived quantities (reported at 68% CL unless otherwise indicated) for the data combinations P18+BK18, ACT+BK18, and SPT+BK18.

	P18 + BK18 + ext	ACT + BK18 + ext	SPT + BK18 + ext
	FIRST ORDER		
$\ln\left(10^{10} A_s\right)$	$3.052^{+0.013}_{-0.015}$	3.042 ± 0.014	3.043 ± 0.011
ϵ_1 (at 95% CL)	< 0.0022	< 0.0023	< 0.0025
ϵ_2	0.0306 ± 0.0039	0.003 ± 0.010	0.034 ± 0.012
$n_{s,\,0.05}$	0.9673 ± 0.0036	0.995 ± 0.010	0.963 ± 0.012
$r_{0.05}$ (at 95% CL)	< 0.036	< 0.036	< 0.039
$n_{t,\,0.05}$	$-0.0021^{+0.0015}_{-0.0009}$	$-0.0022^{+0.0015}_{-0.0009}$	$-0.0024^{+0.0016}_{-0.0010}$
	SECOND ORDER		
$\ln\left(10^{10} A_s\right)$	3.055 ± 0.015	3.041 ± 0.014	3.045 ± 0.012
ϵ_1 (at 95% CL)	< 0.0023	< 0.0023	< 0.0024
ϵ_2	0.0342 ± 0.0071	$0.002^{+0.012}_{-0.010}$	$0.036^{+0.012}_{-0.014}$
ϵ_3 (at 95% CL)	$0.11^{+0.33}_{-0.38}$	–	–
$n_{s,\,0.05}$	0.9669 ± 0.0038	$0.995^{+0.011}_{-0.010}$	0.965 ± 0.012
$\alpha_{s,\,0.05}$	-0.0048 ± 0.0065	$0.0011^{+0.0022}_{-0.0031}$	$-0.005^{+0.012}_{-0.010}$
$r_{0.05}$ (at 95% CL)	< 0.037	< 0.037	< 0.038
$n_{t,\,0.05}$	$-0.0023^{+0.0016}_{-0.0010}$	$-0.0022^{+0.0016}_{-0.0010}$	$-0.0024^{+0.0016}_{-0.0010}$
$10^5\alpha_{t,\,0.05}$	$-7.6^{+5.4}_{-3.1}$	$-0.3^{+2.0}_{-0.2.4}$	$-8.4^{+6.6}_{-3.3}$

Table 3.3: Same as table 3.2 but including external datasets: BAO and RSD measurements, SNe, and CMB lensing.

3σ tension in the inferred scalar spectral index n_s between these two experiments. The *Planck* result (combining temperature, E-mode polarisation, and lensing) yields $n_s = 0.9649 \pm 0.0044$ [22], consistent with predictions from the simplest single-field slow-roll inflationary scenarios. In contrast, ACT data [65] favor $n_s = 1.008 \pm 0.015$ (at 2.8σ deviation), compatible with the scale-invariant Harrison-Zel'dovich (HZ) primordial power spectrum [92, 93, 94].

This tension between *Planck* and ACT persists at the level of the scalar PPS parameters even when allowing for a running spectral index α_s [93, 94]—in the present analysis, when advancing to the second-order expansion. Despite this ongoing disagreement, *Planck* data are consistent with vanishing running, $\alpha_s = -0.0045 \pm 0.0067$ at 68% CL [22], in agreement with single-field slow-roll inflation predictions [95]. ACT data, however, exhibit a 2.5σ preference for positive running,

$\alpha_s = 0.069 \pm 0.029$ [65]. The inferred value of n_s shows a discrepancy of 3.8σ using primary CMB data alone and 3.2σ when combined with external datasets—tensions larger than those obtained when retaining only second-order terms. At second order in the slow-roll expansion, the inferred values of α_s differ by 0.9σ between *Planck* ($\alpha_s = -0.0059 \pm 0.0067$ at 68% CL) and ACT ($\alpha_s = 0.0020^{+0.0029}_{-0.0051}$ at 68% CL), both for primary CMB alone and in combination with external datasets; see tables 3.2 and 3.3. SPT data are consistent with *Planck* findings, albeit with larger uncertainties.

3.5.3 Combined Results

This section presents the constraints obtained for the combined datasets P18+ACT+BK18, implemented with two distinct multipole cut strategies, and P18+SPT+BK18. Truncating the expansion at first order provides

$$\epsilon_1 < 0.0024 \qquad 95\%\text{ CL},\ \text{P18}\ (\ell_{\text{TT}} < 650) + \text{ACT} + \text{BK18}\,, \tag{3.149}$$
$$\epsilon_2 = 0.0183 \pm 0.0059 \qquad 68\%\text{ CL},\ \text{P18}\ (\ell_{\text{TT}} < 650) + \text{ACT} + \text{BK18}\,, \tag{3.150}$$

$$\epsilon_1 < 0.0022 \qquad 95\%\text{ CL},\ \text{P18} + \text{ACT}\ (\ell_{\text{TT}} > 1800) + \text{BK18}\,, \tag{3.151}$$
$$\epsilon_2 = 0.0312 \pm 0.0044 \qquad 68\%\text{ CL},\ \text{P18} + \text{ACT}\ (\ell_{\text{TT}} > 1800) + \text{BK18}\,, \tag{3.152}$$

$$\epsilon_1 < 0.0022 \qquad 95\%\text{ CL},\ \text{P18} + \text{SPT} + \text{BK18}\,, \tag{3.153}$$
$$\epsilon_2 = 0.0327 \pm 0.0044 \qquad 68\%\text{ CL},\ \text{P18} + \text{SPT} + \text{BK18}\,. \tag{3.154}$$

Extending to second order in the HFFs yields

$$\epsilon_1 < 0.0023 \qquad 95\%\text{ CL},\ \text{P18}\ (\ell_{\text{TT}} < 650) + \text{ACT} + \text{BK18}\,, \tag{3.155}$$
$$\epsilon_2 = 0.0166^{+0.0045}_{-0.0057} \qquad 68\%\text{ CL},\ \text{P18}\ (\ell_{\text{TT}} < 650) + \text{ACT} + \text{BK18}\,, \tag{3.156}$$
$$\epsilon_3 < -0.053 \qquad 68\%\text{ CL},\ \text{P18}\ (\ell_{\text{TT}} < 650) + \text{ACT} + \text{BK18}\,, \tag{3.157}$$

$$\epsilon_1 < 0.0023 \qquad 95\%\text{ CL},\ \text{P18} + \text{ACT}\ (\ell_{\text{TT}} > 1800) + \text{BK18}\,, \tag{3.158}$$
$$\epsilon_2 = 0.0274^{+0.0047}_{-0.0063} \qquad 68\%\text{ CL},\ \text{P18} + \text{ACT}\ (\ell_{\text{TT}} > 1800) + \text{BK18}\,, \tag{3.159}$$
$$\epsilon_3 = -0.08^{+0.23}_{-0.19} \qquad 68\%\text{ CL},\ \text{P18} + \text{ACT}\ (\ell_{\text{TT}} > 1800) + \text{BK18}\,, \tag{3.160}$$

$$\epsilon_1 < 0.0024 \qquad 95\%\text{ CL},\ \text{P18} + \text{SPT} + \text{BK18}\,, \tag{3.161}$$
$$\epsilon_2 = 0.0354 \pm 0.0066 \qquad 68\%\text{ CL},\ \text{P18} + \text{SPT} + \text{BK18}\,, \tag{3.162}$$
$$\epsilon_3 = 0.13^{+0.19}_{-0.12} \qquad 68\%\text{ CL},\ \text{P18} + \text{SPT} + \text{BK18}\,. \tag{3.163}$$

Minimal differences emerge between second- and third-order expansions, with ϵ_4 remaining unconstrained in both cases; see table 3.4 and table 3.5 for results incorporating external datasets. Complete third-order results are reported exclusively for the combined datasets augmented with external data in table 3.5.

The P18+ACT combination more closely resembles the *Planck*-only results regardless of the temperature multipole cut strategy employed. When applying the cut to ACT data with $\ell_{\text{TT}}^{\text{ACT}} > 1800$, the inferred spectral index $n_s = 0.9694 \pm 0.0034$ at 68% CL (0.3σ difference) aligns well with *Planck* findings. Conversely, restricting *Planck* temperature data to $\ell_{\text{TT}}^{\text{P18}} < 650$ yields $n_s = 0.9796 \pm 0.0049$ at 68% CL (2.1σ difference) when considering primary CMB alone; these tensions become 0.6σ and 2.3σ, respectively, upon including second-order corrections. The constraints on the scalar running further demonstrate this pattern: the P18+ACT combination with $\ell_{\text{TT}}^{\text{ACT}} > 1800$ yields results closer to those from *Planck* alone, with $\alpha_s = 0.0014^{+0.0062}_{-0.0040}$ when

	P18 ($\ell_{\mathrm{TT}} < 650$) + ACT + BK18	P18 + ACT ($\ell_{\mathrm{TT}} > 1800$) + BK18	P18 + SPT + BK18
	FIRST ORDER		
$\ln\left(10^{10} A_{\mathrm{s}}\right)$	3.041 ± 0.016	3.048 ± 0.015	$3.045^{+0.010}_{-0.015}$
ϵ_1 (at 95% CL)	< 0.0024	< 0.0022	< 0.0022
ϵ_2	0.0183 ± 0.0059	0.0312 ± 0.0044	0.0327 ± 0.0044
$n_{\mathrm{s},\,0.05}$	0.9794 ± 0.0056	0.9667 ± 0.0040	0.9651 ± 0.0041
$r_{0.05}$ (at 95% CL)	< 0.038	< 0.035	< 0.035
$n_{\mathrm{t},\,0.05}$	$-0.0023^{+0.0017}_{-0.0010}$	$-0.0021^{+0.0015}_{-0.0009}$	$-0.0021^{+0.0015}_{-0.0009}$
	SECOND ORDER		
$\ln\left(10^{10} A_{\mathrm{s}}\right)$	3.040 ± 0.016	3.047 ± 0.016	3.046 ± 0.012
ϵ_1 (at 95% CL)	< 0.0024	< 0.0022	< 0.0023
ϵ_2	$0.0166^{+0.0050}_{-0.0063}$	$0.0297^{+0.0055}_{-0.006}$	0.0383 ± 0.0071
ϵ_3 (at 95% CL)	< 0.27	$-0.06^{+0.33}_{-0.38}$	$0.15^{+0.27}_{-0.31}$
$n_{\mathrm{s},\,0.05}$	0.9796 ± 0.0055	0.9674 ± 0.0040	0.9640 ± 0.0041
$\alpha_{\mathrm{s},\,0.05}$	$0.0020^{+0.0045}_{-0.0027}$	$0.0010^{+0.0063}_{-0.0045}$	-0.0064 ± 0.0062
$r_{0.05}$ (at 95% CL)	< 0.038	< 0.035	< 0.036
$n_{\mathrm{t},\,0.05}$	$-0.0023^{+0.0016}_{-0.0010}$	$-0.0021^{+0.0016}_{-0.0010}$	$-0.0023^{+0.0016}_{-0.0010}$
$10^5 \alpha_{\mathrm{t},\,0.05}$	$-3.6^{+2.7}_{-1.4}$	$-6.1^{+4.4}_{-2.5}$	$-8.4^{+5.9}_{-3.5}$

Table 3.4: Constraints on the primary inflationary parameters and their derived quantities (reported at 68% CL unless otherwise indicated) for the combined datasets P18+ACT+BK18 with two distinct multipole cuts, and P18+SPT-3G+BK18.

cutting ACT data and $\alpha_{\mathrm{s}} = 0.0021^{+0.0045}_{-0.0026}$ when cutting *Planck* data, both at 68% CL. The P18+SPT combination remains consistent with *Planck* results while providing tighter error bars.

Figure 3.8 displays the 68% CL and 95% CL confidence regions for the HFFs obtained from the first-order analysis, both for individual experiments (*Planck* ACT, and SPT alone) and their combinations. The results align with the general observation that CMB data favor potentials with concave curvature, i.e., $V_{\phi\phi} < 0$, within the observable window, with the ACT+BK18 case representing a notable exception. Figure 3.9 presents the 68% CL and 95% CL confidence regions

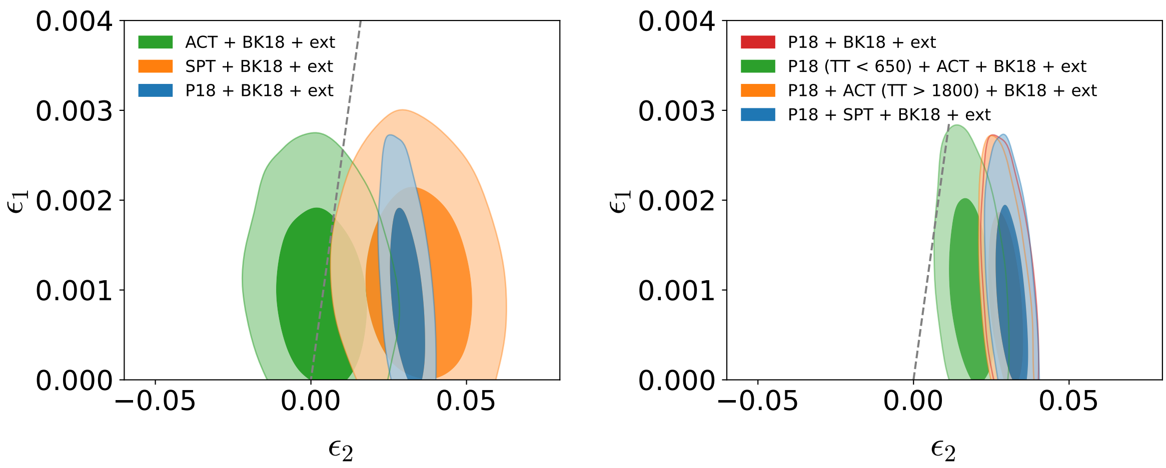

Figure 3.8: Marginalized joint confidence contours for the first two HFF parameters ϵ_1 and ϵ_2 under first-order slow-roll predictions. The grey dashed line delineates the parameter space separating convex (left) from concave (right) single-field slow-roll potentials.

for the HFFs obtained from the second-order analysis, shown for individual experiments on the left panel and for combined datasets on the right panel.

Finally, Figure 3.10 illustrates the 68% CL and 95% CL marginalized constraints on the scalar inflationary parameters derived via eqs. (F.20) to (F.22): for the second-order HFF expansion,

	P18 ($\ell_{\rm TT} < 650$) + ACT + BK18 + ext	P18 + ACT ($\ell_{\rm TT} > 1800$) + BK18 + ext	P18 + SPT + BK18 + ext
		FIRST ORDER	
$\ln\left(10^{10}A_{\rm s}\right)$	3.048 ± 0.014	3.052 ± 0.013	$3.052^{+0.026}_{-0.020}$
ϵ_1 (at 95% CL)	< 0.0024	< 0.0023	< 0.0022
ϵ_2	0.0183 ± 0.0051	0.0292 ± 0.0037	0.0311 ± 0.0036
$n_{\rm s,\,0.05}$	0.9794 ± 0.0049	0.9687 ± 0.0035	0.9667 ± 0.0033
$r_{0.05}$ (at 95% CL)	< 0.038	< 0.036	< 0.036
$n_{\rm t,\,0.05}$	$-0.0023^{+0.0016}_{-0.0010}$	$-0.0021^{+0.0016}_{-0.0009}$	$-0.0022^{+0.0016}_{-0.0009}$
		SECOND ORDER	
$\ln\left(10^{10}A_{\rm s}\right)$	3.047 ± 0.014	3.051 ± 0.014	3.048 ± 0.011
ϵ_1 (at 95% CL)	< 0.0023	< 0.0023	< 0.0024
ϵ_2	$0.0166^{+0.0045}_{-0.0057}$	$0.0274^{+0.0047}_{-0.0063}$	0.0354 ± 0.0066
ϵ_3 (at 95% CL)	< 0.26	$-0.08^{+0.32}_{-0.40}$	$0.13^{+0.30}_{-0.34}$
$n_{\rm s,\,0.05}$	0.9796 ± 0.0049	0.9694 ± 0.0034	0.9661 ± 0.0035
$\alpha_{\rm s,\,0.05}$	$0.0021^{+0.0045}_{-0.0026}$	$0.0014^{+0.0062}_{-0.0040}$	-0.0055 ± 0.0062
$r_{0.05}$ (at 95% CL)	< 0.037	< 0.035	< 0.037
$n_{\rm t,\,0.05}$	$-0.0023^{+0.0016}_{-0.0010}$	$-0.0022^{+0.0016}_{-0.0010}$	$-0.0023^{+0.0016}_{-0.0010}$
$10^5\alpha_{\rm t,\,0.05}$	$-3.6^{+2.6}_{-1.4}$	$-5.7^{+4.0}_{-2.4}$	$-8.0^{+5.5}_{-3.3}$
		THIRD ORDER	
$\ln\left(10^{10}A_{\rm s}\right)$	3.046 ± 0.014	3.052 ± 0.014	3.048 ± 0.011
ϵ_1 (at 95% CL)	< 0.0024	< 0.0022	< 0.0023
ϵ_2	$0.0166^{+0.0047}_{-0.0063}$	$0.0291^{+0.0049}_{-0.0066}$	$0.0363^{+0.0068}_{-0.0085}$
ϵ_3 (at 95% CL)	< 0.34	$0.00^{+0.37}_{-0.35}$	> -0.13
ϵ_4	–	–	–
$n_{\rm s,\,0.05}$	0.9804 ± 0.0049	0.9695 ± 0.0035	0.9673 ± 0.0038
$\alpha_{\rm s,\,0.05}$	$0.0019^{+0.0046}_{-0.0039}$	$-0.0002^{+0.0054}_{-0.0047}$	$-0.0056^{+0.0064}_{-0.0051}$
$\beta_{\rm s,\,0.05}$	$-0.0011^{+0.0018}_{-0.0007}$	$-0.0010^{+0.0020}_{-0.0006}$	$-0.0025^{+0.0043}_{-0.0012}$
$r_{0.05}$ (at 95% CL)	< 0.037	< 0.035	< 0.036
$n_{\rm t,\,0.05}$	$-0.0023^{+0.0016}_{-0.0010}$	$-0.0022^{+0.0015}_{-0.0010}$	$-0.0023^{+0.0016}_{-0.0010}$
$10^5\alpha_{\rm t,\,0.05}$	$-3.6^{+2.7}_{-1.3}$	$-6.2^{+4.5}_{-2.5}$	$-8.9^{+6.4}_{-3.7}$
$10^5\beta_{\rm t,\,0.05}$	$0.2^{+1.0}_{-0.6}$	$-0.4^{+1.4}_{-0.7}$	$-2.2^{+2.6}_{-1.1}$

Table 3.5: Same as table 3.4 but including external datasets: BAO and RSD measurements, SNe, and CMB lensing.

these include the scalar spectral index $n_{\rm s}$ and its running $\alpha_{\rm s}$, while the third-order expansion additionally incorporates the running of the running $\beta_{\rm s}$. Although current constraints are consistent with the small values of $1-n_{\rm s}$, $\alpha_{\rm s}$, and $\beta_{\rm s}$ predicted by single-field slow-roll inflationary models, substantially larger values remain permitted by present CMB measurements. The light shaded regions correspond to $|\alpha_{\rm s}| > |n_{\rm s}-1|^2$ and $|\beta_{\rm s}| > |n_{\rm s}-1|^3$, indicating regimes where single-field slow-roll predictions are qualitatively violated, as discussed in [96].

In summary, this analysis establishes a stringent upper bound on the first HFF, $\epsilon_1 \lesssim 0.002$ at 95% CL, primarily driven by BICEP/Keck data. This constraint demonstrates remarkable stability across diverse combinations of observational datasets. Combining *Planck* data with late-time cosmological probes yields $\epsilon_2 \simeq 0.031 \pm 0.004$ at 68% CL when retaining only first-order corrections. Incorporating second- and third-order corrections broadens this to $\epsilon_2 \simeq 0.034 \pm 0.007$ at 68% CL. For the third HFF, the analysis indicates $\epsilon_3 \simeq 0.1 \pm 0.4$ at 95% CL, with consistent values across second- and third-order treatments. The fourth HFF ϵ_4 remains beyond the reach of current data, as also demonstrated in [67].

Incorporating small-scale CMB measurements from ACT and SPT alongside *Planck* data provides additional insight. The combination of *Planck* with ACT data (after removing temperature data below $\ell = 1800$ as recommended by the ACT collaboration to avoid inter-dataset correlations) and with SPT yields results consistent with *Planck*-only constraints while offering slightly tighter bounds on ϵ_2 and ϵ_3. However, ACT data alone, as well as the ACT+*Planck* combination with *Planck* temperature data removed above $\ell = 650$, produce shifts in the central values of ϵ_2 and ϵ_3, indicating a preference for higher scalar spectral indices and positive values of the spectral running.

3.5.4 Future CMB Constraints

This subsection explores the anticipated constraining power of a conceptual future CMB space mission. Under the assumption that CMB anisotropies follow a Gaussian distribution and exhibit statistical isotropy, the analysis employs the following Gaussian likelihood $\mathcal{L}$ [97, 98]

$$-2\ln\mathcal{L} = \sum_{\ell}(2\ell+1)f_{\rm sky}\left(\mathrm{Tr}[\hat{\mathbf{C}}_\ell\bar{\mathbf{C}}_\ell^{-1}] + \ln|\hat{\mathbf{C}}_\ell\bar{\mathbf{C}}_\ell^{-1}| - 4\right), \tag{3.164}$$

where $\bar{\mathbf{C}}_\ell$ denote the theoretical data covariance matrices

$$\bar{\boldsymbol{C}}_\ell \equiv \begin{bmatrix} \bar{C}_\ell^{TT} + N_\ell^{TT} & \bar{C}_\ell^{TE} & 0 & 0 \\ \bar{C}_\ell^{TE} & \bar{C}_\ell^{EE} + N_\ell^{EE} & 0 & 0 \\ 0 & 0 & \bar{C}_\ell^{BB} + N_\ell^{BB} & 0 \\ 0 & 0 & 0 & \bar{C}_\ell^{\phi\phi} + N_\ell^{\phi\phi} \end{bmatrix}, \tag{3.165}$$

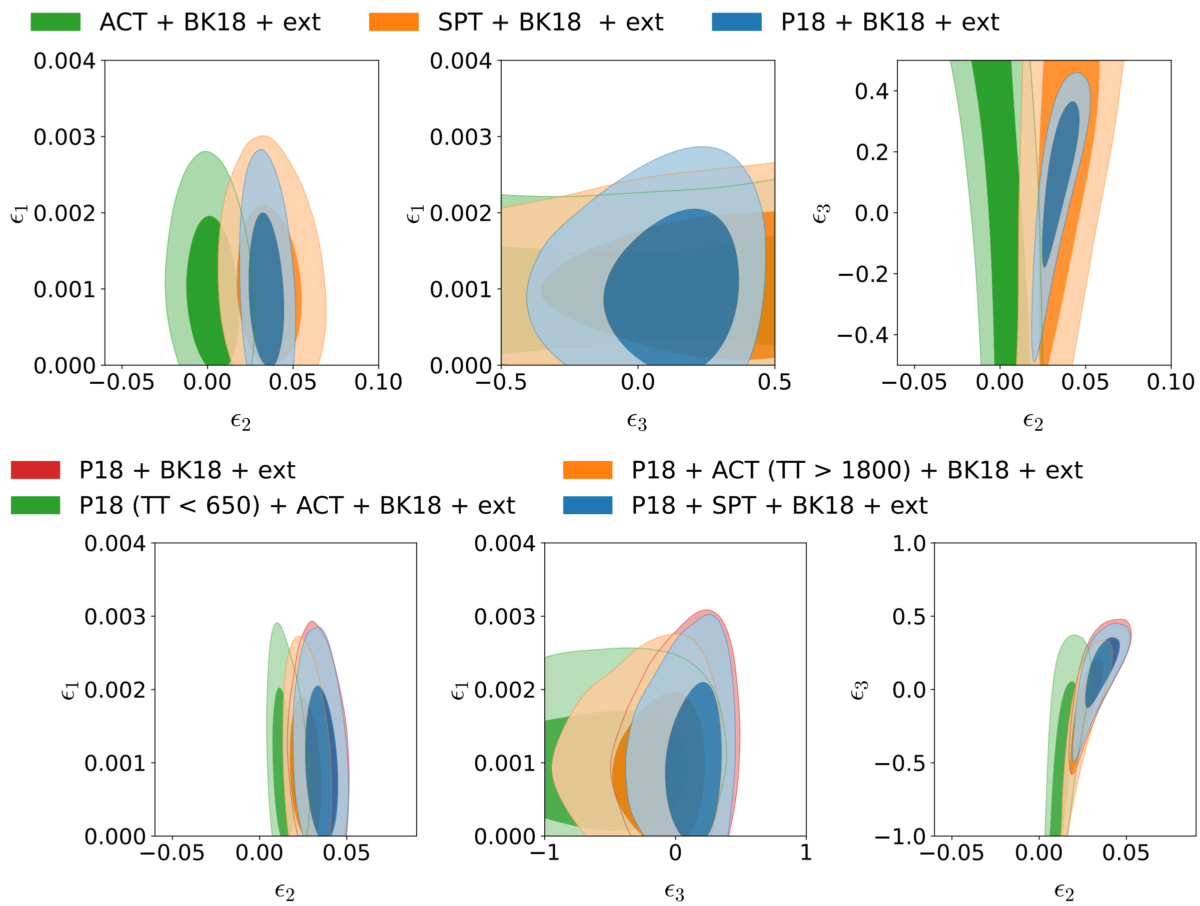

Figure 3.9: Marginalized joint confidence contours for the first three HFF parameters ϵ_1, ϵ_2, and ϵ_3 under second-order slow-roll predictions.

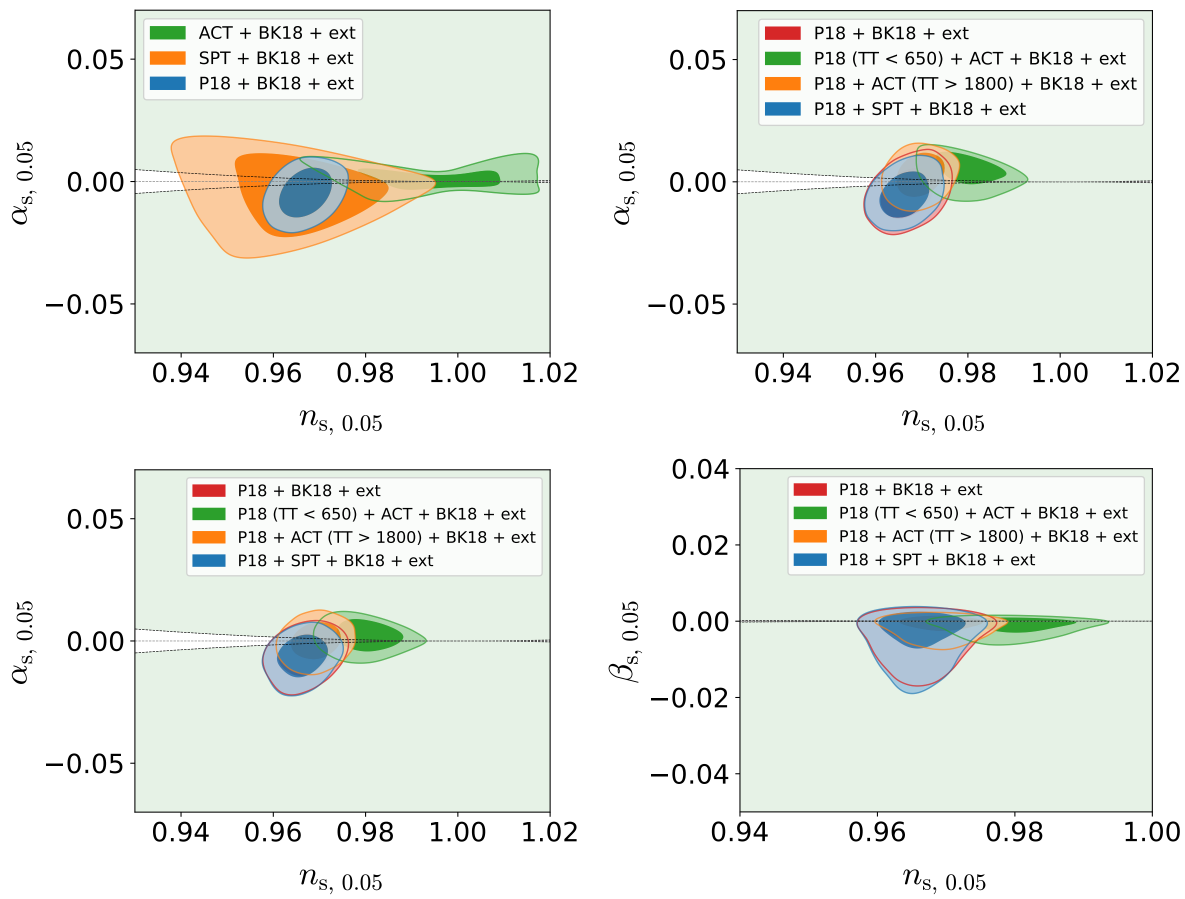

Figure 3.10: Marginalized joint confidence contours for the scalar spectral index n_s and its running α_s under second-order slow-roll predictions (upper panels), and for the scalar spectral index n_s, its running α_s, and the running of the running β_s under third-order slow-roll predictions (lower panels).

and $\hat{\mathbf{C}}_\ell$ are the fiducial data covariance matrices

$$\hat{\boldsymbol{C}}_\ell \equiv \begin{bmatrix} \hat{C}_\ell^{TT} & \hat{C}_\ell^{TE} & 0 & 0 \\ \hat{C}_\ell^{TE} & \hat{C}_\ell^{EE} & 0 & 0 \\ 0 & 0 & \hat{C}_\ell^{BB} & 0 \\ 0 & 0 & 0 & \hat{C}_\ell^{\phi\phi} \end{bmatrix} . \tag{3.166}$$

The noise power spectra for temperature and polarisation angular power spectra account for isotropic noise deconvolved with the instrumental Gaussian beam as

$$N_\ell^{\mathrm{XX}} = w_{\mathrm{XX}}^{-1}\, e^{\ell(\ell+1)\frac{\theta^2_{\mathrm{FWHM}}}{8\ln 2}} . \tag{3.167}$$

The forecast assumes an effective noise variance $w_{\mathrm{TT}}^{-1/2} = 1.2\,\mu\mathrm{K\,arcmin}$ with $w_{\mathrm{EE}}^{-1/2} = w_{\mathrm{BB}}^{-1/2} = \sqrt{2}\, w_{\mathrm{TT}}^{-1/2}$ and an effective beam resolution of $\theta_{\mathrm{FWHM}} = 5.5\,\mathrm{arcmin}$ over 70% of the sky, spanning the multipole range $2 \leq \ell \leq 3000$. These instrumental specifications correspond to a CMB experiment achieving cosmic-variance-limited sensitivity up to $\ell = 2800$ in temperature, $\ell = 2000$ in E-mode polarisation, and $\ell = 800$ in gravitational lensing reconstruction over nearly the full sky.

Beyond primary temperature and polarisation anisotropies, the analysis incorporates information from CMB weak lensing through the lensing potential power spectrum $C_\ell^{\phi\phi}$. For the

CMB lensing noise power spectrum, the minimum-variance quadratic estimator for lensing reconstruction [99] is adopted over the range $30 \leq \ell \leq 3000$, combining the TT, EE, BB, TE, TB, and EB estimators with iterative lensing reconstruction following [100, 101].

Additionally, internal delensing [102, 103, 104] of the B-mode angular power spectrum is implemented using the specifications above to suppress the non-primordial lensing-induced contribution. The delensing procedure removes the lensing component from the B-mode power spectrum while incorporating an additional error term into the instrumental noise $N_\ell^{\rm BB}$.

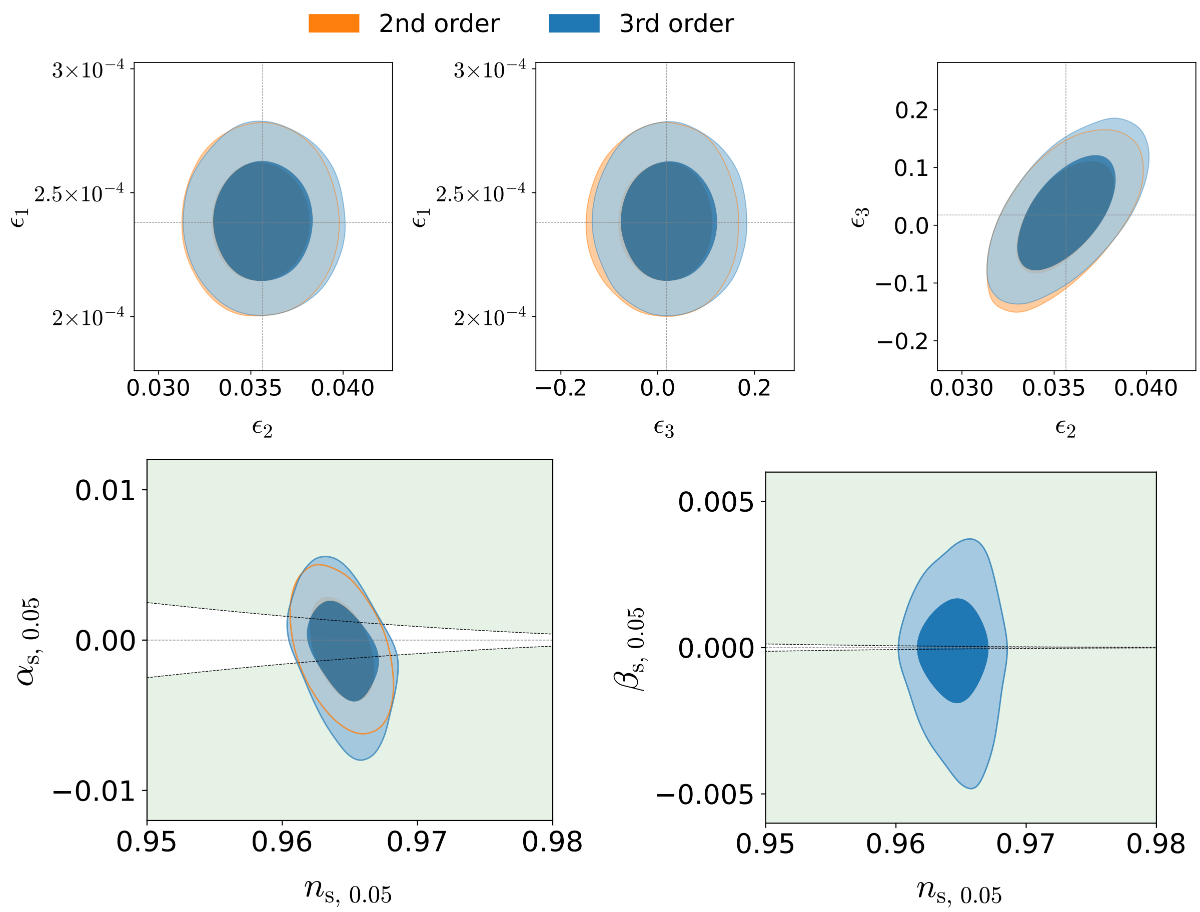

Figure 3.11: Marginalized joint confidence contours for the first three HFF parameters ϵ_1, ϵ_2, and ϵ_3 under second- and third-order slow-roll predictions (upper panels). Marginalized joint confidence contours for the scalar spectral index $n_{\rm s}$ and its running $\alpha_{\rm s}$ under second- and third-order slow-roll predictions (lower left panel), and for the scalar spectral index $n_{\rm s}$ and the running of the running $\beta_{\rm s}$ under third-order slow-roll predictions (lower right panel).

The forecast assumes a flat Universe with a cosmological constant, two massless neutrinos with $N_{\rm eff} = 2.046$, and one massive neutrino with fixed minimum mass $m_\nu = 0.06\,$eV. The fiducial angular power spectra are generated using HFF values corresponding to the T-model of α-attractor inflation with $\alpha = 1$ evaluated at $N_* = 55$ e-folds and pivot scale $k_* = 0.05\,{\rm Mpc}^{-1}$. This yields $\epsilon_1 = 0.000235$, $\epsilon_2 = 0.0352$, $\epsilon_3 = 0.0175$, and $\epsilon_4 = 0.0175$. The simulated measurements are analyzed using both the second-order PPS equations (with $\epsilon_4 = 0$ and neglecting third-order corrections) and the complete third-order expressions. The results are displayed in fig. 3.11. The analysis of this futuristic CMB experiment reveals:

- The HFFs are accurately recovered without bias or significant degradation in uncertainties when truncating at second order.
- The fourth HFF ϵ_4 remains beyond the reach of CMB experiments alone.

- Uncertainties on the HFFs are substantially reduced, enabling high-significance statistical detection of ϵ_2 (and, for this specific fiducial, ϵ_1 as well). Specifically, the forecast yields $\epsilon_1 = 0.000239 \pm 0.000016$, $\epsilon_2 = 0.0357 \pm 0.0018$, and $\epsilon_3 = 0.023 \pm 0.066$ at 68% CL, consistent with previous forecast studies [105].

These results demonstrate that second-order equations provide sufficient accuracy for modeling both current and future CMB observations, as illustrated in fig. 3.11. The parameter ϵ_4 remains unconstrained even with next-generation CMB measurements.

In conclusion to this chapter, it is important to stress that future small-scale CMB observations from ACT, SPT, and the Simons Observatory will be essential for further testing higher-order terms in the slow-roll expansion and validating single-field slow-roll predictions. Beyond CMB measurements, as demonstrated throughout this chapter, observations spanning broader scales—including large-scale structure (LSS) measurements from *Euclid* [106], CMB spectral distortions [107], 21 cm experiments [108], and constraints on primordial black hole abundance at smaller scales [109]—can provide valuable constraints on the primordial curvature power spectrum. Collectively, these multi-scale observations are vital for confirming or refuting the single-field slow-roll inflation paradigm, and third-order corrections to the PPS will play a crucial role in this assessment.

Chapter 4

Planck constraints on the scale dependence of isotropic cosmic birefringence

As discussed in section 2.4, cosmic birefringence (CB) is the rotation of the linear polarisation plane of photons during their propagation through the vacuum. This phenomenon serves as a powerful probe of parity-violating extensions of standard electromagnetism. While various theoretical frameworks can produce this effect—including interpretations based on non-trivial spatial topology that leave standard electromagnetism unchanged, as proposed by the COMPACT collaboration [110], or kinetic mixing between the standard electromagnetic sector and a dark one [111]—the most prominent example is Chern-Simons (ChS) theory [50]. In this framework, a pseudo-scalar field such as an axion or axion-like particle (ALP) a couples to the electromagnetic field tensor via the Lagrangian[1]:

$$\mathcal{L} \supset -\frac{g_{a\gamma\gamma}}{4} a F_{\mu\nu}\tilde{F}^{\mu\nu}. \tag{4.1}$$

Although the CB effect is a general phenomenon, the Cosmic Microwave Background (CMB) provides an ideal laboratory for its detection. Thomson scattering at the last scattering surface generates linear polarisation in the CMB at the few percent level, making it the most distant known source of linear polarised photons in nature. Consequently, CMB polarisation observations have become the standard tool for constraining cosmic birefringence [49].

Isotropic cosmic birefringence (ICB) induces a mixing between E- and B-mode polarisation, thereby affecting the CMB angular power spectra (APS). As derived in section 2.4.1, when no parity-violation signals are present at the last scattering surface and the birefringence angle β remains constant [112, 113, 114], the observed power spectra are given by eq. (2.127) through eq. (2.132), which we report here for the reader's convenience:

$$C_\ell^{EE,\mathrm{obs}} = C_\ell^{EE}\cos^2(2\beta) + C_\ell^{BB}\sin^2(2\beta), \tag{4.2}$$

$$C_\ell^{BB,\mathrm{obs}} = C_\ell^{EE}\sin^2(2\beta) + C_\ell^{BB}\cos^2(2\beta), \tag{4.3}$$

$$C_\ell^{EB,\mathrm{obs}} = \frac{1}{2}\sin(4\beta)\left(C_\ell^{EE} - C_\ell^{BB}\right), \tag{4.4}$$

$$C_\ell^{TT,\mathrm{obs}} = C_\ell^{TT}, \tag{4.5}$$

$$C_\ell^{TE,\mathrm{obs}} = C_\ell^{TE}\cos(2\beta), \tag{4.6}$$

$$C_\ell^{TB,\mathrm{obs}} = C_\ell^{TE}\sin(2\beta). \tag{4.7}$$

[1]Following the convention introduced in section 2.4, a denotes the axion field when no ambiguity with the scale factor arises.

These relations demonstrate that ICB affects only CMB polarisation, leaving the TT APS unaltered. It should be noted that these equations are valid when the axion field a remains constant in time during the recombination epoch [115]. This condition is satisfied only if the field mass is sufficiently small for a given coupling constant $g_{a\gamma\gamma}$ [116]. For larger masses, the field a exhibits time-evolution characterized by decay followed by damped oscillations, which modifies these relations.

The *Planck* collaboration has consistently detected a non-zero EB APS signal across all four component separation methods[2]. Within the framework of Chern-Simons theory, this signal can be interpreted as arising from a combination of a cosmological birefringence angle β and an instrumental polarisation miscalibration angle α, yielding $\beta + \alpha = 0.31 \pm 0.05\,(\mathrm{stat}) \pm 0.28\,(\mathrm{sys})$ [deg] [124]. The systematic uncertainty, dominated by the instrumental polarisation angle α, significantly exceeds the statistical error. This degeneracy arises because the instrumental polarisation angle *alpha* affects the CMB APS through the same mathematical framework as the cosmological CB effect [125], making it difficult to disentangle genuine cosmic birefringence from systematic miscalibration.

To break this degeneracy, a novel technique—now known as the Minami-Komatsu method—was proposed in [126, 127] and subsequently applied to *Planck* data in [128] and [129, 130]. These analyses suggest a detection of β around 0.3 [deg] with a statistical significance approaching the 3σ confidence level (CL). More recently, the ACT collaboration has independently estimated $\beta_{\mathrm{ACT}} = 0.20 \pm 0.08$ [deg] [20, 21, 131].

The validity of eq. (4.2) through eq. (4.7) depends critically on the mass of the ALP field a. The degeneracy between the instrumental angle α and the birefringence angle β is exact only when the ALP mass falls within the ultra-light range [116, 132]:

$$10^{-33}\,\mathrm{eV} \lesssim m \lesssim 10^{-28}\,\mathrm{eV} \tag{4.8}$$

Outside this mass range, the degeneracy is broken [133, 134, 135]. From an observational perspective, the degeneracy is maximised when β is independent of the harmonic scale. Previous analyses of *Planck* measurements [136] indicate that this scenario is currently favoured by the data. Similar conclusions have been reached in [137], where constraints on ALP parameters are derived from the full shape of the *Planck* EB spectrum.

The work on Isotropic Cosmic Birefringence presented in [3] proposes a new test to assess whether β exhibits any dependence on the harmonic scale or remains constant across all scales. Using *Planck* Public Data Release 3 (PR3) [64], the birefringence angles are estimated at different harmonic scales and their consistency is tested across the entire harmonic range. Two complementary approaches are employed: first, fitting the birefringence angle estimated at different multipoles, β_ℓ, with a power-law model; second, performing a non-parametric Bayesian reconstruction. Both methods yield results consistent with a non-vanishing constant birefringence angle. The power-law analysis shows no significant dependence on the harmonic scale (up to 1.8σ CL), while the Bayesian reconstruction demonstrates that a constant model is favoured by the Bayesian evidence. Additionally, forecasts for future CMB observations are explored to assess how they could improve this type of analysis.

It is important to emphasise that the goal of this work [3] is not to address the degeneracy between β and α directly, although the proposed test may help to distinguish between the two effects.

The test has been performed using two different methodologies:

1. The estimated angles at different angular scales are fitted using a two-parameter power-law

[2] The analysis of Planck satellite data is performed using four different techniques to account for the foreground emissions that contaminate the CMB signal [117]. These techniques are `Commander` [118, 119], `NILC` [120], `SEVEM` [121], and `SMICA` [122, 123].

model, (β_0, n), defined as

$$\beta_\ell = \beta_0 \left(\frac{\ell}{\ell_0}\right)^n \tag{4.9}$$

where ℓ_0 is a suitable harmonic pivot scale. In this approach, the power n is the key parameter, as it quantifies the consistency of a constant birefringence angle across the entire harmonic range under consideration.

2. In the second approach, β_ℓ is fitted using a non-parametric Bayesian reconstruction for a given number of moving knots [138, 139, 140]. In this case, the best-fit curve is statistically evaluated against constant behaviour in ℓ.

The analysis presented in the following sections is based on the work [3].

4.1 Planck data and simulations

4.1.1 Data and Simulations

The analysis presented in [3] relies on the *Planck* Public Release 3 (PR3) dataset and associated simulations [64]. As mentioned in the previous section, the study utilizes CMB maps reconstructed through the four *Planck*'s different component-separation (CS) techniques: `Commander`, `NILC`, `SEVEM`, and `SMICA`.

To characterize the statistical properties of the observational data, the official *Planck* PR3 simulation set has been employed. For each component-separation method, this set comprises 1000 full focal plane (FFP) CMB Monte Carlo realizations based on the *Planck* ΛCDM best-fit cosmology (hereafter referred to as the **fiducial model**) [117]. These simulations incorporate an effective Gaussian beam with a full width at half maximum (FWHM) of 5 arcmin [141, 142]. Additionally, the set includes 300 noise realizations for the first half-mission (HM1) and 300 for the second half-mission (HM2). Importantly, the *Planck* PR3 simulations account for residual contributions from various systematic effects, including beam leakage, analog-to-digital converter (ADC) non-linearities, thermal fluctuations, and other instrumental systematics [143, 144].

All data products employed in this analysis are publicly available through the ESA *Planck* Legacy Archive[3] and have been processed at resolution parameter $N_{\rm side} = 2048$. This parameter is defined within the Hierarchical Equal Area isoLatitude Pixelization (`HEALPix`) scheme [145],[4] where the total number of pixels on the sphere, $N_{\rm pix}$, is related to the resolution parameter through $N_{\rm pix} = 12N_{\rm side}^2$.

4.1.2 Angular power spectra

For each component-separation method, two independent data splits have been constructed by combining the 300 HM1 and 300 HM2 noise realizations with the first 300 CMB simulations. Cross-correlation between these splits is then employed to estimate the CMB angular power spectra, a procedure known to yield auto-spectra with reduced sensitivity to noise characteristics and residual systematic contamination [117].

The angular power spectra are computed using the `NaMaster` Python package [146], which implements the pseudo-C_ℓ estimator [147, 148]. This calculation incorporates the *Planck* PR3 common masks for both temperature and polarisation, as well as the masks identifying unobserved pixels in HM1 and HM2, as illustrated in fig. 4.1. Neither apodization nor purification techniques [149, 150, 151] have been applied to the masks.

[3] http://pla.esac.esa.int/pla
[4] https://sourceforge.net/projects/healpix/

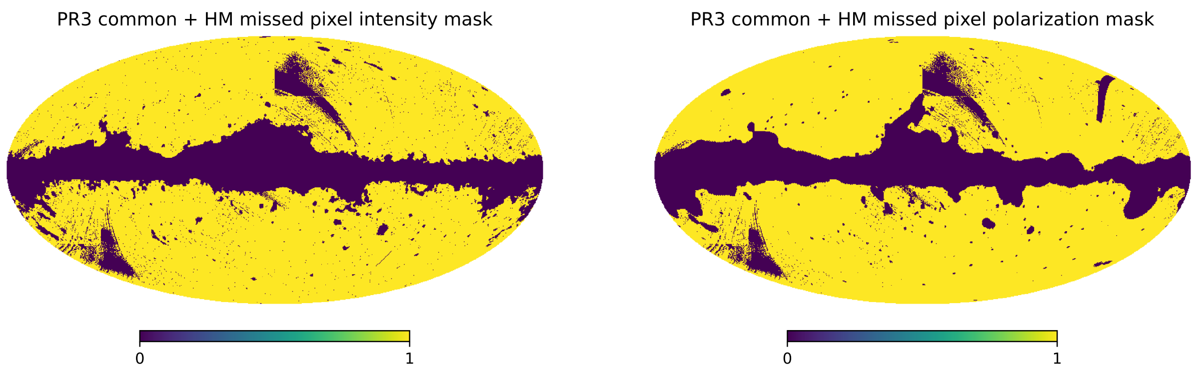

Figure 4.1: Masks employed in [3]. Both the intensity (left panel) and polarization (right panel) masks correspond to an effective sky fraction of $f_{\rm sky} \simeq 75\%$.

In CMB data analysis, it is standard practice to work with the dimensionless power spectrum $\mathcal{D}_\ell^{XY}$, defined as

$$\mathcal{D}_\ell^{XY} = \frac{\ell(\ell+1)}{2\pi} C_\ell^{XY}. \tag{4.10}$$

The analysis pipeline presented in [3] primarily exploits the EB spectrum and the combined $(EE - BB)/2$ signal:

$$\mathcal{D}_\ell^{EB} \equiv \frac{\ell(\ell+1)}{2\pi} C_\ell^{EB} \quad \text{and} \quad \mathcal{D}_\ell^{(EE-BB)/2} \equiv \frac{\ell(\ell+1)}{2\pi} \left(\frac{C_\ell^{EE} - C_\ell^{BB}}{2} \right). \tag{4.11}$$

Figures 4.2 and 4.3 present $\mathcal{D}_\ell^{EB}$ and $\mathcal{D}_\ell^{(EE-BB)/2}$, respectively. Each figure comprises four panels corresponding to the four CS methods, showing the binned APS with bandpowers of width $\Delta\ell = 20$ extending to a maximum multipole $\ell_{\rm max} \simeq 1550$. Within each panel, the measured data APS with error bars (derived from simulations) are shown in black, the ΛCDM fiducial spectrum is indicated by a dotted gray line, and the simulation mean along with its one-σ dispersion is displayed in orange.

The lower portion of each panel demonstrates the consistency between simulations and the expected fiducial APS, denoted by $\mathcal{D}_\ell^{X,\rm fid}$, where $X = \{EB, (EE-BB)/2\}$. This is achieved by plotting the *standardised* APS, defined as:

$$\Delta\mathcal{D}_\ell^X \cdot (\bar{\rm C}^X)_{\ell\ell'}^{-1/2}, \tag{4.12}$$

where $\Delta\mathcal{D}_\ell^X = \langle \mathcal{D}_\ell^X - \mathcal{D}_\ell^{X,\rm fid} \rangle$ denotes the mean deviation from the fiducial spectrum, and $(\bar{\rm C}^{\rm X})_{\ell\ell'}^{-1/2}$ represents the Cholesky decomposition of the inverse mean covariance matrix $\bar{\rm C}_{\ell\ell'}^X$. The mean covariance is obtained as ${\rm C}_{\ell\ell'}^X/300$, where ${\rm C}_{\ell\ell'}^X$ denotes the full covariance of X.

Under the assumption of Gaussian statistics, these standardised quantities should follow a normal distribution with zero mean and unit variance at each harmonic bandpower, and are therefore expected to remain within $\pm 3\sigma$ for most multipoles. The covariances ${\rm C}_{\ell\ell'}^X$ are computed using the analytical approach implemented in the `NaMaster` code, which accounts for signal and noise fluctuations as well as mode coupling induced by sky masking [146].

The lower panels of figs. 4.2 and 4.3 reveal that the simulation ensemble mean remains within 3.5σ of the fiducial model across all the four component-separation methods. This demonstrates that residual effects included in the official *Planck* simulations do not produce any statistically significant systematic bias. The only notable exception occurs for `SMICA` in $\mathcal{D}_\ell^{EB}$ near $\ell \simeq 300$, where a deviation of approximately 5σ is observed. However, this fluctuation corresponds to merely 30% of the statistical uncertainty of the APS at those angular scales, and is therefore not expected to significantly affect the final results. Furthermore, the `SMICA` estimates remain

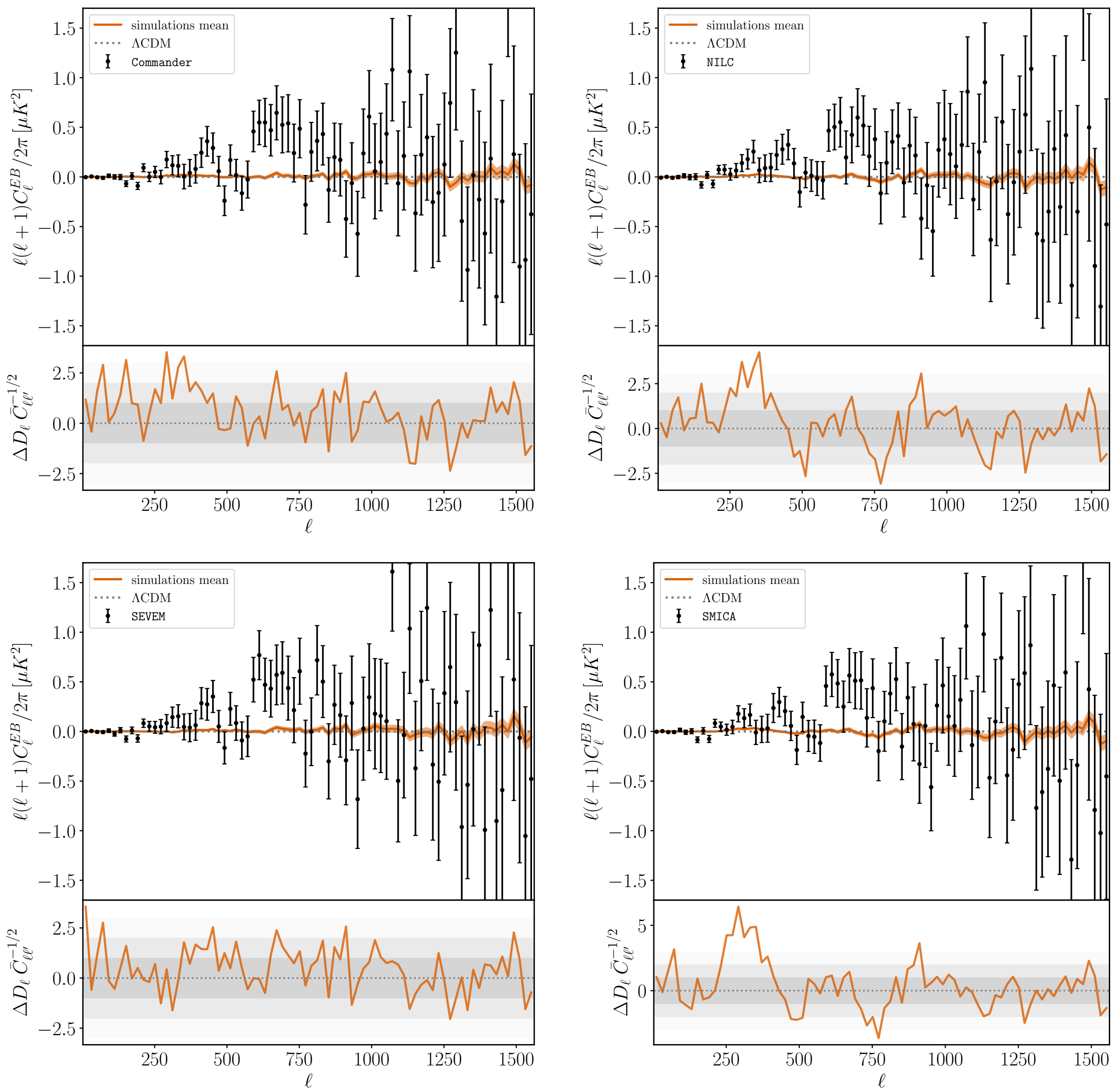

Figure 4.2: Dimensionless EB power spectrum $\mathcal{D}_\ell^{EB} \equiv \ell(\ell+1)C_\ell^{EB}/2\pi\ [\mu\mathrm{K}^2]$ as a function of ℓ from *Planck* PR3 data with bandpower width $\Delta\ell = 20$. The panels are organized by component-separation method: upper left for `Commander`, upper right for `NILC`, lower left for `SEVEM`, and lower right for `SMICA`. In each panel, the upper portion displays the measured APS with error bars (black), the ΛCDM fiducial spectrum (dotted gray), and the simulation mean with its one-σ dispersion (orange). The lower portion shows the deviation of the simulation mean from the fiducial spectrum in units of the standard deviation of the mean.

in excellent agreement with those obtained from the other CS methods, even around $\ell \simeq 300$ where the simulations from other methods show no significant departure from expected statistical fluctuations.

Overall, the APS estimates for both $\mathcal{D}_\ell^{EB}$ and $\mathcal{D}_\ell^{(EE-BB)/2}$ exhibit excellent consistency at better than the 2σ level across all component-separation methods. Additionally, a harmonic χ^2 analysis, where

$$\chi^2 = \sum_{\ell,\ell'} \mathcal{D}_\ell^X \mathrm{C}_{\ell\ell'}^{\mathrm{X}\ -1} \mathcal{D}_{\ell'}^X \quad \text{with} \quad \mathrm{X} = \{EB, (EE-BB)/2\}, \tag{4.13}$$

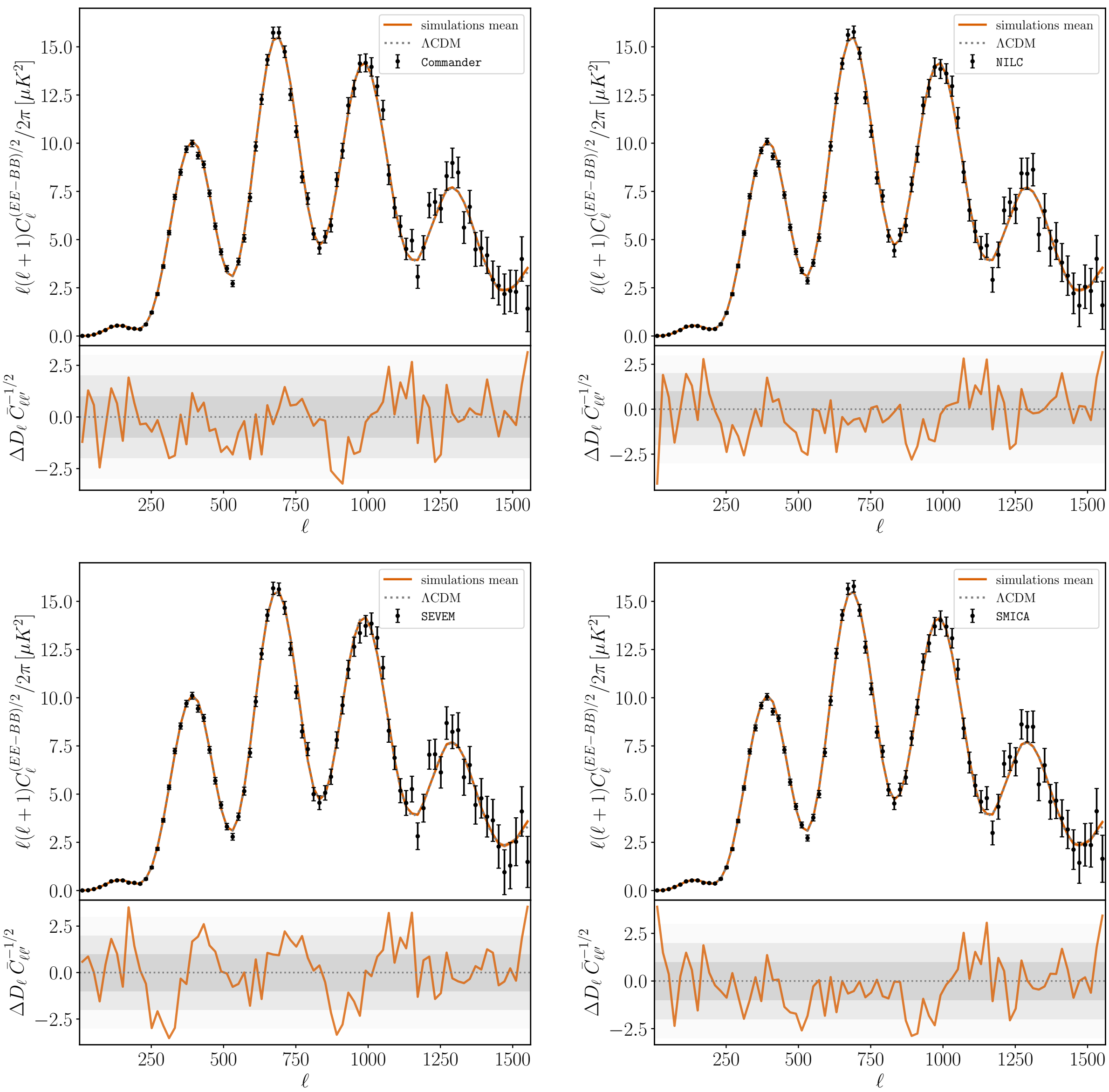

Figure 4.3: $\mathcal{D}_\ell^{(EE-BB)/2} \equiv \ell(\ell+1)[(C_\ell^{EE} - C_\ell^{BB})/2]/2\pi$ [μK^2] as a function of ℓ from *Planck* PR3 data with bandpower width $\Delta\ell = 20$. The panels are organized by component-separation method: upper left for `Commander`, upper right for `NILC`, lower left for `SEVEM`, and lower right for `SMICA`. In each panel, the upper portion displays the measured APS with error bars (black), the ΛCDM fiducial spectrum (dotted gray), and the simulation mean with its one-σ dispersion (orange). The lower portions of the single sub-plots show the deviation of the simulation mean from the fiducial spectrum in units of the standard deviation of the mean.

reveals a moderate excess for $\mathcal{D}_\ell^{EB}$, while showing very good agreement for $\mathcal{D}_\ell^{(EE-BB)/2}$ across all methods. Specifically, the measured $\chi^2_{\rm data}$ for $\mathcal{D}_\ell^{EB}$ ranges from 96 to 115 depending on the CS method, compared to an expected value of 73 for the harmonic range [42, 1501]. These values correspond to a probability to exceed (PTE) ranging from 0.2% for `Commander`, 0.3% for `NILC`, 0.1% for `SEVEM`, to 0.7% for `SMICA`, indicating tension with the null hypothesis of vanishing EB correlation.

Concluding this section, the analysis of data and simulations described in section 4.1 has confirmed the presence of an excess EB signal across all four component separation methods, whose physical origin remains unclear. The estimated birefringence angle β over the full harmonic range $[42, 1501]$ is consistent with values reported in the literature [128, 129], regardless of the impact of the instrumental polarization angle α.

4.2 Testing the harmonic-scale dependence of the isotropic cosmic birefringence

4.2.1 Estimators

Starting from eqs. (4.2) and (4.7), it is possible to construct two harmonic-based estimators for β, known as D-estimators [124, 152, 153]:

$$D_\ell^{TB,\mathrm{obs}}(\hat{\beta}) \equiv C_\ell^{TB,\mathrm{obs}} \cos(2\hat{\beta}) - C_\ell^{TE,\mathrm{obs}} \sin(2\hat{\beta}) \,, \tag{4.14}$$

$$D_\ell^{EB,\mathrm{obs}}(\hat{\beta}) \equiv C_\ell^{EB,\mathrm{obs}} \cos(4\hat{\beta}) - \frac{1}{2}\left(C_\ell^{EE,\mathrm{obs}} - C_\ell^{BB,\mathrm{obs}}\right) \sin(4\hat{\beta}) \,, \tag{4.15}$$

where $\hat{\beta}$ denotes the estimate of the CB angle β. It can be demonstrated that

$$D_\ell^{Y,\mathrm{obs}}(\hat{\beta} = \beta) = 0 \,, \tag{4.16}$$

for $Y = TB$ or EB [153], indicating that β can be determined by identifying the zeros of the D-estimators.

The analysis presented in [3] relies exclusively on $D_\ell^{EB,\mathrm{obs}}(\hat{\beta})$. This estimator has been shown to provide stronger constraints than $D_\ell^{TB,\mathrm{obs}}(\hat{\beta})$ for *Planck* data, as demonstrated in [124]. However, it must be pointed out that this result holds only when the complete available harmonic range is employed, whereas the estimator's performance has not been investigated for particular harmonic subranges. Therefore, it is possible that within specific multipole intervals, the two estimators exhibit comparable statistical efficiency, or at least similar constraining power, making the analysis with D^{TB} as statistically efficient as the one on D^{EB}. A possible follow-up to test the consistency of the results is discussed in [3]. Furthermore, when working with the TE and TB signals, one must account for the fact that beam deconvolution affects both temperature and polarization channels and it does it in a different way, necessitating significantly greater care in the computation of the spectra and interpretation of the results. For these reasons, the work presented in [3] focuses exclusively on $D_\ell^{EB,\mathrm{obs}}(\hat{\beta})$.

4.2.2 Estimates of the β_ℓ

The initial step of the analysis consists in reproducing established results from the literature. The cosmic birefringence angle is estimated by minimizing the $\chi^2(\hat{\beta})$ function defined as

$$\chi^2(\hat{\beta}) = \sum_{b,b'} D_b^{EB,\mathrm{obs}}(\hat{\beta}) (\mathrm{C}^{EB})^{-1}_{bb'} D_{b'}^{EB,\mathrm{obs}}(\hat{\beta}) \,, \tag{4.17}$$

over the complete multipole range, where $b, b' = 1, \dots, 73$ correspond to the harmonic interval $[42, 1501]$ with uniform spacing $\Delta\ell = 20$. Here, $\mathrm{C}^{EB}_{bb'}$ denotes the analytical covariance matrix for the EB spectrum computed via `NaMaster`, as discussed in section 4.1.2. Following standard practice in previous studies [124]), the lowest multipoles are excluded to reduce potential contamination from residual systematic effects, including those of astrophysical origin.

For each component-separation method, β is computed for every simulation and for the corresponding *Planck* CMB map. These values are used to construct fig. 4.4, where histograms show the expected distribution derived from simulations (generated with ΛCDM) for each CS method, while vertical bars mark the observed CB angle. Each panel additionally displays a

Gaussian distribution whose mean and standard deviation are extracted from the corresponding histogram. This normal approximation is employed to assess the statistical significance of the observed value, which is reported above the arrow connecting the histogram mean to the measured angle. The significance levels associated with the observations span from 5σ for the `SMICA` solution to 6.2σ for `NILC`, with `Commander` and `SEVEM` yielding 5.4σ and 5.3σ, respectively.

The Hartlap factor

The Hartlap factor was originally studied in [154]. It is a correction that allows one to obtain an unbiased estimate of the inverse covariance matrix when the covariance is estimated from a finite number of simulations or independent realizations.

Let $\mathbf{s} = (s_1, .., s_r)$ be a set of r random variables drawn from a multivariate Gaussian distribution with mean $\boldsymbol{\mu} = (\mu_1, ..., \mu_r)$ and population covariance Σ, i.e.,

$$P(\mathbf{s}) = \frac{1}{(2\pi)^{r/2}\sqrt{\det\Sigma}} \exp\left[-\frac{1}{2}(\mathbf{s}-\boldsymbol{\mu})^T\Sigma^{-1}(\mathbf{s}-\boldsymbol{\mu})\right]. \quad (4.18)$$

A standard estimator for the components of the covariance matrix is the maximum-likelihood estimator

$$\hat{C}^{\mathrm{ML}}_{ij} = \frac{1}{n}\sum_{k=1}^{n}(s_i^{(k)} - \mu_i)(s_j^{(k)} - \mu_j), \quad (4.19)$$

where k denotes the k-th realization among the total number of realizations n. From this estimator, an estimator for Σ^{-1} can be obtained by matrix inversion:

$$\hat{C}_*^{-1} = (\hat{C}^{\mathrm{ML}})^{-1}. \quad (4.20)$$

Unfortunately, due to the noise in $\hat{C}^{\mathrm{ML}}$, the estimator in eq. (4.20) is consistent but biased. In [154], building upon previous results explained in [155], the authors demonstrate that an unbiased estimator of Σ^{-1} is given by

$$\hat{C}^{-1} = \frac{n-r-2}{n-1}\hat{C}_*^{-1} \quad \text{for} \quad r < n-2, \quad (4.21)$$

i.e., the estimated inverse covariance matrix must be multiplied by the factor

$$H = \frac{n-r-2}{n-1}, \quad (4.22)$$

commonly known as the Hartlap factor.

The estimated means and standard deviations of β are summarized in table 4.1, together with the residual CB angle $\beta_{\mathrm{res}} = \langle\beta_i\rangle_{i\in\mathrm{sims}}$ computed from the simulations. It should be noted that this residual represents only a fraction of the statistical uncertainty on β and therefore does not account for the overall measured CB effect. Nevertheless, it can be interpreted as contributing to the systematic uncertainty budget.

In fig. 4.5 it is possible to see that for all four component-separation methods an EB signal appears when analyzing the data. Equation (4.4), using the values from table 4.1 and section 4.2.2, appears to fit these data well, as shown for four different values of the birefringence angle.

The CB angle β_B is subsequently determined over four aggregated harmonic bins, labeled by B, by minimizing

$$\chi^2_B(\hat{\beta}_B) = \sum_{b,b'} D_b^{EB,\mathrm{obs}}(\hat{\beta}_B)(\mathrm{C}^{EB})^{-1}_{bb'}D_{b'}^{EB,\mathrm{obs}}(\hat{\beta}_B)\,, \quad (4.23)$$

Method	β [deg]	$\beta_{\rm res}$ [deg]
PR3 `Commander`	0.30 ± 0.05	0.02
PR3 `NILC`	0.32 ± 0.05	0.01
PR3 `SEVEM`	0.31 ± 0.06	0.01
PR3 `SMICA`	0.27 ± 0.05	0.02

Table 4.1: Estimated values of β over the harmonic range $[42, 1501]$ for the four component-separation methods employed in this work. These values have been used in eq. (4.4) to compare the resulting APS with *Planck* PR3 data, as shown in fig. 4.5. The third column of the table reports the mean birefringence angle estimated from the simulations, denoted as $\beta_{\rm res}$.

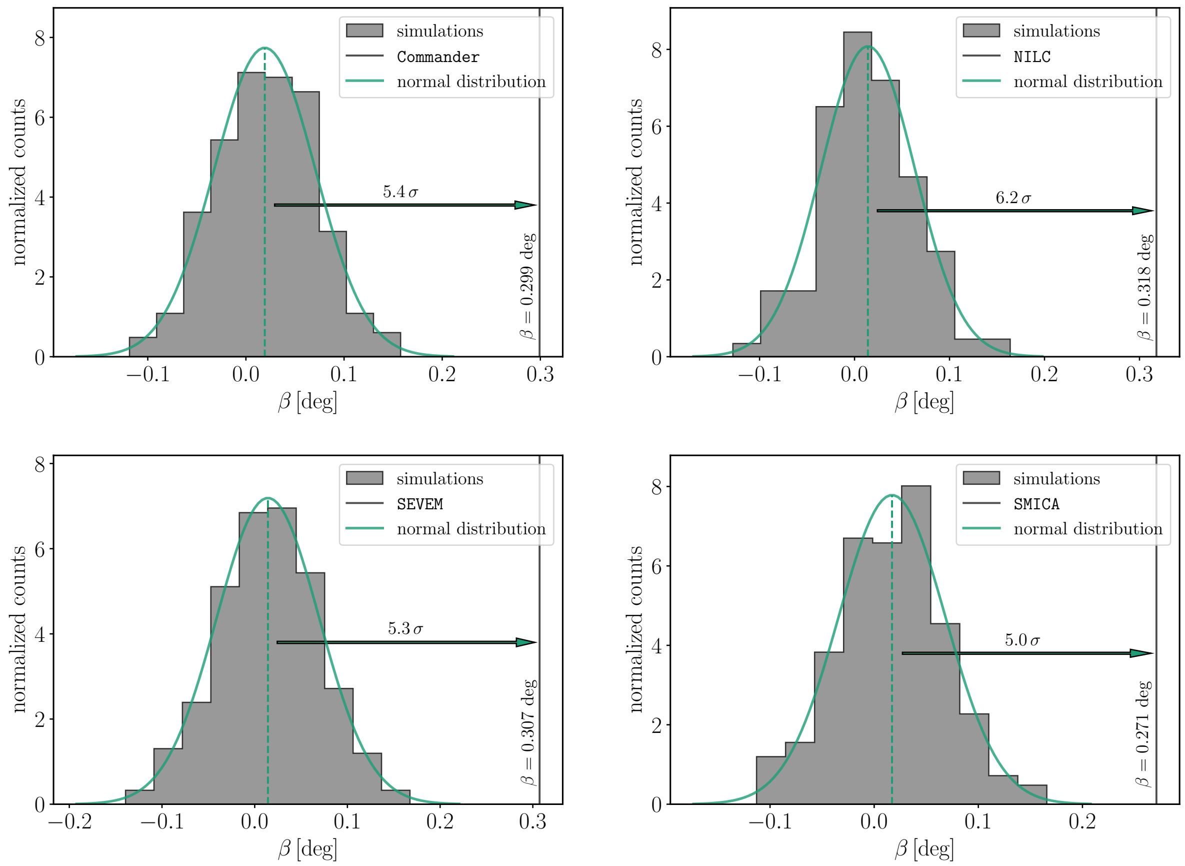

Figure 4.4: Estimated β for all component-separation methods: upper left panel for `Commander`, upper right for `NILC`, lower left for `SEVEM`, and lower right for `SMICA`. In each panel, the gray histogram constructed from simulations represents the expected distribution for β, while the black vertical bar indicates the observed value. The green curve shows a Gaussian distribution whose mean and standard deviation are derived from the corresponding histogram. This normal approximation is used to calculate the significance of the observed value, which is also reported above the arrow connecting the histogram mean to the estimated angle.

where the index B labels four consecutive aggregated bins b to span the multipole range $[42, 1481]$. Thus, $B \in [1, 18]$ maps onto $b \in [1, 72]$. It important to point out that the final bin, $b = 73$, is excluded to ensure the total number of bins is divisible by four. Additionally, it has been found that estimating β over the aggregated bins corresponding to the multipole range $\ell \in [2, 41]$ yields an uncertainty approximately 10 times larger than that obtained from the analysis conducted on aggregated harmonic bins in $\ell \in [42, 1481]$.

For each CS method and for each of the 300 corresponding simulations, the values β_B that

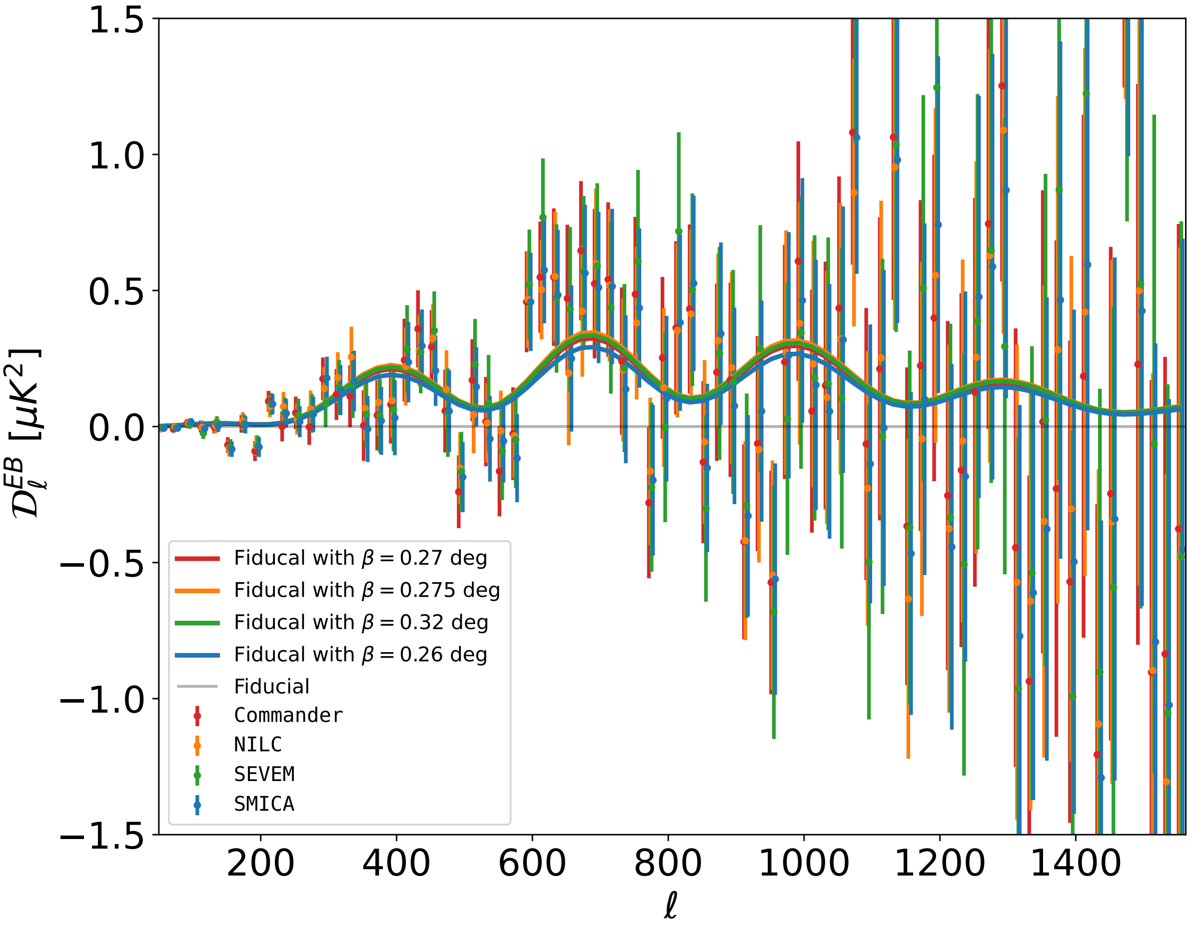

Figure 4.5: C_ℓ^{EB} data from *Planck* PR3, for all four component-separation methods (cf. section 4.1). The four β values are those obtained from the whole-range analysis performed in [3] (cf. table 4.1 and section 4.2.2).

minimize eq. (4.23) are computed. The covariance matrix is then estimated from simulations as

$$\mathrm{C}^{\beta}_{BB'} = \big\langle \left(\beta_B - \langle\beta_B\rangle\right)\left(\beta_{B'} - \langle\beta_{B'}\rangle\right) \big\rangle\,, \tag{4.24}$$

where $\langle\beta_B\rangle$ denotes the ensemble mean over simulations for each bin B. Employing the identical procedure, β_B is estimated from *Planck* data.

The results are presented in fig. 4.6. For each panel, the compatibility of $\langle\beta_B\rangle$ with the null hypothesis is illustrated in the lower tiles through the standardised quantity $\langle\beta_B\rangle \left[H \cdot (\mathrm{C}^{\beta}_{BB'})^{-1}\right]^{1/2}$ (solid orange lines), which should remain predominantly within $\pm 3\sigma$ for each bin B. The inverse covariance matrix is adjusted using the Hartlap factor H to account for the finite number of effective degrees of freedom in the simulation-based covariance estimate [154]. As previously, the power of 1/2 applied to a matrix denotes its Cholesky decomposition.

The same calculation is also performed using only the diagonal elements of $\mathrm{C}^{\beta}_{BB'}$, in this case without applying the Hartlap correction (dashed lines). As evident from fig. 4.6, the off-diagonal terms contribute negligibly to the total uncertainty.

This validation reveals only partial consistency of the *Planck* simulations for `Commander`, `NILC`, and `SMICA`, as evidenced by excess power around $\ell \approx 300$ for all three CS methods, and additionally near $\ell \approx 500$ and 700 for `NILC` and `SMICA`. To address this issue, a debiasing procedure has been applied, subtracting the constant residual value β_{res}—reported in table 4.1—from each β_B, separately for each CS method.

The standardised quantities are then re-evaluated and the debiased results are presented in the same lower tiles of fig. 4.6, using indigo lines to indicate the corrected curves. This procedure restores full compatibility with the null hypothesis for `Commander`, while only partially mitigating the residual excess for `NILC` and `SMICA`. `SEVEM` exhibits full compatibility regardless of whether the debiasing procedure is applied. The impact of the residual excess on the analysis will be discussed in the following section.

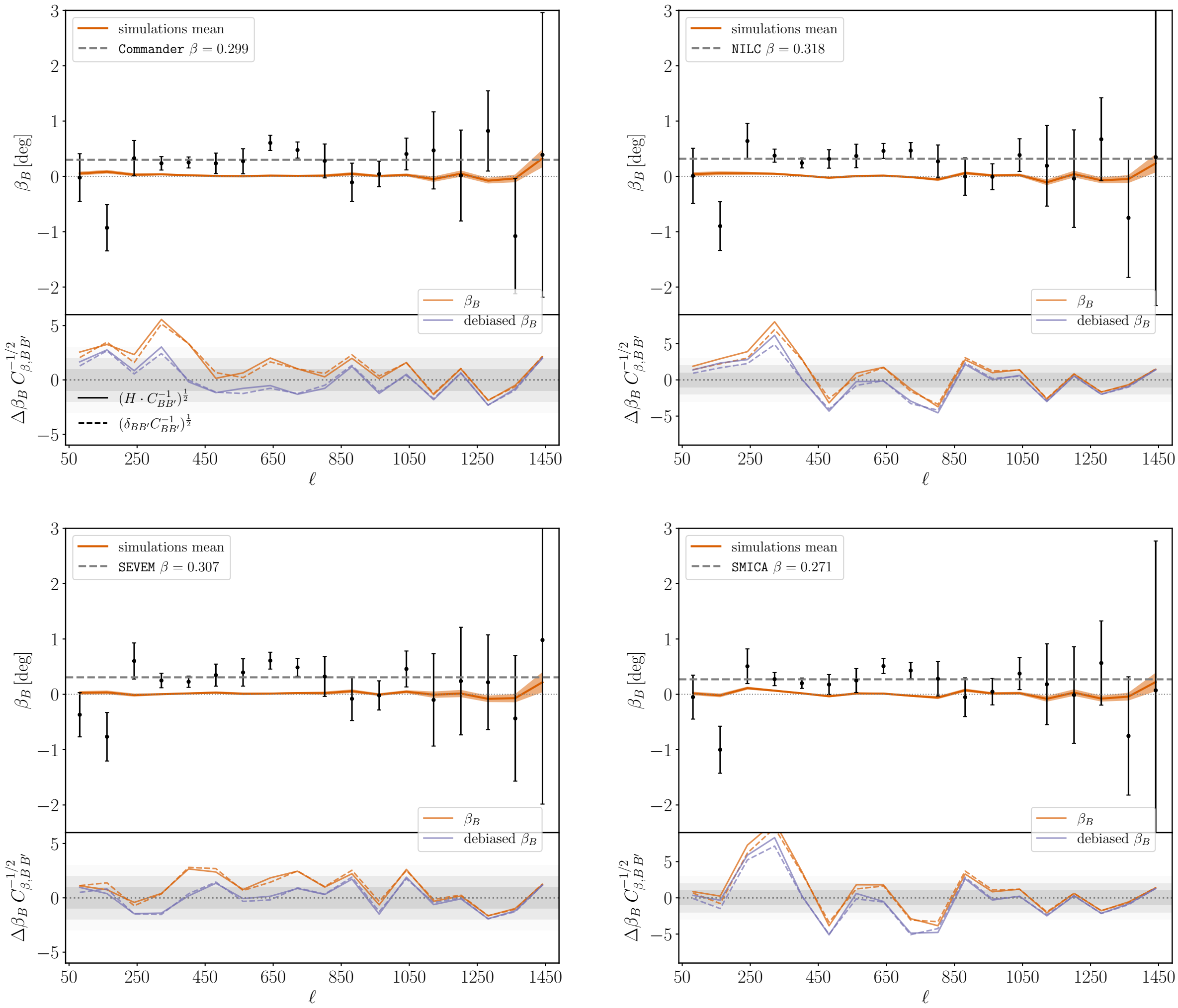

Figure 4.6: Estimated β_B for all component-separation methods: upper left panel for `Commander`, upper right for `NILC`, lower left for `SEVEM`, and lower right for `SMICA`. In each panel, the black points with error bars represent β_B from data, where error bars are computed from the numerical covariance $C^{\beta}_{BB'}\delta_{BB'}$. The orange band shows the mean value $\langle\beta_B\rangle$ with its 1σ region from the corresponding simulations. Gray dashed horizontal lines indicate the value of β computed over the complete multipole range. In the lower tiles, the fluctuation of the simulation mean relative to the null hypothesis is displayed before removing the constant value of $\beta_{\rm res}$ at each multipole (orange) and after its removal (indigo), considering either the full dense covariance matrix corrected by the Hartlap factor (solid lines) or only its diagonal elements (dashed lines).

Nevertheless, it should be emphasized that all estimates obtained from the different CS methods are in very good agreement, with relative fluctuations typically at the 1σ level.

Par.	Data	Commander	NILC	SEVEM	SMICA
β_0 [deg]	β_B	0.28 ± 0.05	0.31 ± 0.05	0.30 ± 0.06	0.26 ± 0.05
	$\beta_{\rm res}$	0.019 ± 0.003	0.013 ± 0.003	0.013 ± 0.003	0.017 ± 0.003
	$\beta_B - \beta_{\rm res}$	0.26 ± 0.05	0.29 ± 0.05	0.29 ± 0.06	0.25 ± 0.05
n	β_B	$0.60^{+0.34}_{-0.31}$	$0.29^{+0.31}_{-0.29}$	$0.57^{+0.33}_{-0.31}$	$0.52^{+0.36}_{-0.34}$
	$\beta_{\rm res}$	$0.00^{+0.35}_{-0.31}$	$0.00^{+0.45}_{-0.41}$	$0.00^{+0.49}_{-0.41}$	$0.00^{+0.38}_{-0.33}$
	$\beta_B - \beta_{\rm res}$	$0.62^{+0.36}_{-0.33}$	0.30 ± 0.31	$0.59^{+0.34}_{-0.32}$	$0.54^{+0.38}_{-0.35}$

Table 4.2: Best-fit values and 1σ confidence intervals for the parameters (β_0, n) obtained from different component-separation methods and datasets: measured data β_B, systematic residual $\beta_{\rm res}$, and debiased data $\beta_B - \beta_{\rm res}$.

4.2.3 Fitting β_ℓ with a power-law like functional

In this section, the birefringence angles β_B across different angular scales are modeled using a two-parameter power-law functional form given by

$$\beta(B) = \beta_0 \left(\frac{\ell_B}{\ell_{B_0}}\right)^n , \tag{4.25}$$

where β_0 represents the amplitude and n denotes the power index (or slope) that characterizes the harmonic scale dependence at a reference pivot scale ℓ_{B_0}. Since the power-law parametrization in eq. (4.25) exhibits sensitivity to the pivot choice, B_0 is fixed to the bin that minimizes the correlation between β_0 and n while simultaneously yielding the smallest systematic uncertainty arising from $\beta_{\rm res}$. This corresponds to the sixth bin with $\ell_{B_0=6} \in [442, 522]$, a choice that remains consistent across all four CS methods (appendix G for details). The power index n serves as the key parameter in this analysis, as it quantifies departures from scale-independent birefringence behavior across multipoles.

The following analysis pipeline has been developed to test the power-law model described in eq. (4.25):

1. A two-dimensional grid in the parameter space (β_0, n) is constructed, centered at the origin $(0, 0)$. The grid consists of 1000×1000 points spanning the ranges $\beta_0 \in [-1, 1]$ deg and $n \in [-1.5, 2.5]$.

2. The two-dimensional χ^2 function is evaluated at each grid point (β_0, n) under the assumption of the theoretical power law given in eq. (4.25).

3. The best-fit values (β_0, n) are determined by minimizing the two-dimensional χ^2 function.

The $\chi^2(\beta_0, n)$ function is expressed as

$$\chi^2(\beta_0, n) = \sum_{B,B'}^{18} \left[\beta(B) - \beta_B\right] \left(\mathrm{C}^\beta\right)^{-1}_{BB'} \left[\beta(B') - \beta_{B'}\right] , \tag{4.26}$$

where $\chi^2(\beta_0, n)$ quantifies the goodness of fit for each point in the parameter space. This procedure is applied to three distinct datasets: the measured β_B values from each CS method, the residual $\beta_{\rm res}$ to propagate systematic effects into the parameter constraints, and the debiased dataset $\beta_B - \beta_{\rm res}$.

The marginal distributions for (β_0, n) are displayed in fig. 4.7, while the constraints on β_0 and n are reported in table 4.2. The constraints derived from $\beta_{\rm res}$ represent a systematic contribution that affects β_0 at approximately 40% of its statistical uncertainty. Notably, the systematic uncertainty on n is peaked at zero, indicating that residuals from the *Planck* analysis pipeline do not impose a significant limitation on this analysis.

The estimates of n are found to be compatible with zero within the total error budget at confidence levels of 1.8σ for `Commander`, 1.0σ for `NILC`, 1.7σ for `SEVEM`, and 1.5σ for `SMICA`. However, when template corrections are constructed for `NILC` and `SMICA` to account for the excess power identified at $\ell \approx 300$, 500, and 700 (cf. fig. 4.6), the analysis yields $\beta_0 = 0.30 \pm 0.05$ [deg] with $n = 0.40 \pm 0.33$ for `NILC`, and $\beta_0 = 0.25 \pm 0.05$ [deg] with $n = 0.68 \pm 0.36$ for `SMICA`. This corresponds to shifts in the power index of $\Delta n = -0.11$ for `NILC` and $\Delta n = -0.16$ for `SMICA`, representing 0.36σ and 0.51σ variations, respectively. These results suggest a non-negligible interplay between foreground contamination and systematic residuals. When properly accounted for, the updated power index estimates become mutually consistent among the different CS methodologies within one standard deviation.

The template corrections are constructed using the ensemble mean of β_B computed from simulations (without debiasing, corresponding to the orange curves in fig. 4.6), retaining only those fluctuations exceeding 3.5σ. The parameters β_0 and n are then re-estimated from the dataset after template subtraction.

4.2.4 Fitting β_ℓ with a non-parametric Bayesian reconstruction

To model the data without introducing theoretical biases, a model-independent reconstruction approach is adopted based on a flexible representation using moving nodes or knots. This methodology provides a versatile framework enabling the data to determine the shape of the reconstructed function without imposing a specific parametric form, in contrast to the power-law approach employed in the previous section.

The reconstruction procedure operates by placing a set of nodes along the data domain. Both the amplitudes and positions of these nodes are treated as free parameters to be inferred through Bayesian analysis. Between nodes, the function is interpolated using linear splines. This approach, commonly referred to as the `FlexKnot` model [156], enables the reconstruction to adapt flexibly to the underlying data structure.

To ensure robustness and generality of the reconstruction, the two domain endpoints are fixed at $\ell_{\min} = 42$ and $\ell_{\max} = 1481$, while the intermediate nodes are permitted to vary in a sorted configuration, maintaining the ordering $\ell_i < \ell_{i+1}$ for any node i to prevent non-physical configurations. The number of nodes is increased incrementally, beginning with a single node ($N = 1$)—corresponding to constant amplitude—and progressively adding additional nodes ($N = 2, 3, 4, \ldots$). This iterative strategy allows for assessment of the trade-off between model complexity and goodness of fit.

Bayesian inference is performed using the nested sampling algorithm implemented in `PyPolyChord` [138, 139][5] with 800 live points. The isotropic birefringence angle estimates obtained in section 4.2.2 are considered for all four CS methods. The log-likelihood function follows the form given in eq. (4.26), incorporating the observed data and their uncertainties. The priors are chosen to reflect reasonable physical constraints: node amplitudes are sampled from a uniform prior over $[-20°, 20°]$, while node positions are sampled uniformly within $[\ell_{\min}, \ell_{\max}]$, applying a *forced identifiability prior* transformation [139, 157].

For each configuration of node number, the posterior distributions of the parameters are obtained and the model evidence is computed. The Bayesian evidence provides a quantitative criterion for comparing reconstructions with different numbers of nodes, enabling identification of the optimal balance between model simplicity and explanatory power. The posterior distributions of the reconstructed functions are visualized using the `fgivenx` package [158],[6] which provides a clear representation of the reconstruction uncertainty.

[5] https://github.com/PolyChord/PolyChordLite
[6] https://github.com/handley-lab/fgivenx

Figure 4.8 presents the reconstructed function obtained with the four CS methods assuming $N = 4$. The shaded regions represent the credible intervals derived from the posterior samples. The reconstructed β_ℓ spectra for $N = 4$ are compared with the results obtained in the single-node case ($N = 1$), displayed as grey shaded regions in fig. 4.8 and numerically reported in table 4.3. While all four CS methods yield mutually consistent results that broadly support a constant CB angle, minor deviations at the 68% confidence level emerge at large angular scales ($\ell \lesssim 350$) for `Commander`, `SEVEM`, and `SMICA`, where the results become more compatible with a vanishing angle.

Method	β [deg]
PR3 `Commander`	0.30 ± 0.05
PR3 `NILC`	0.32 ± 0.05
PR3 `SEVEM`	0.31 ± 0.06
PR3 `SMICA`	0.28 ± 0.05

Table 4.3: Mean values of β with uncertainties at 68% confidence level obtained using `PolyChord` for the single-node case ($N = 1$).

In appendix H, the complete set of results obtained from this pipeline is collected for various node numbers, comparing them with the $N = 4$ case presented here. Additionally, Bayes factors calculated relative to the single-node baseline are provided.

To conclude this section, the investigation of the harmonic dependence of the excess EB signal identified in section 4.1 is summarized. This analysis employed two complementary approaches: a parametric method fitting the data with a power-law template (eq. (4.25)) and a non-parametric approach based on the `FlexKnot` model. The results indicate that the excess is consistent with being independent of harmonic scale, at the $\lesssim 2\sigma$ level, for all component separation methods, as demonstrated in table 4.2 and fig. 4.7. The non-parametric reconstruction using the `FlexKnot` model reveals a strong preference for a constant birefringence angle β across the harmonic range, as shown in fig. 4.8.

The principal finding of the work presented in [3] is therefore the *Planck* data's preference for a scale-invariant cosmic birefringence angle.

4.3 Forecasts for future CMB experiments

This section presents forecasts on the ability to recover β_0 and n using upcoming CMB experiments, focusing particularly on LiteBIRD (LB) [41, 159], Simons Observatory - Large Aperture Telescope (SO-LAT) [43, 160], and CMB Stage 4 (CMB-S4) [161, 162].

For each experiment, 500 simulated datasets were generated with identical underlying cosmological parameters, including a scale-invariant angle $\beta = 0.3$ deg, but with different noise realizations corresponding to the experimental configurations summarized in the upper section of table 4.4. The analysis pipeline described in section 4.2.3 was then applied to constrain β_0 and n. To ensure comparability with the *Planck* analysis results presented in this work, the same pivot scale was maintained, though it should be noted that this choice does not necessarily represent the optimal configuration. The resulting forecasts for β_0 and n are presented in table 4.5, while the contour plots are shown in fig. 4.9. The uncertainty on β_0 is found to be up to 5 times smaller than that obtained with *Planck* data, while the error on n can be reduced by up to ~ 7 times compared to the larger uncertainty found with *Planck* data.

In conclusion, this section demonstrates that future CMB experiments will reduce the current *Planck* uncertainties by up to a factor of 7. If the observed effect originate from new physics, these improved measurements would provide stringent constraints on ultra-light axion fields, with even greater potential for future observational probes.

Parameter	LiteBIRD	SO-LAT	CMB-S4
beam [arcmin]	30	1.4	1
Q, U sensitivity [μK $\cdot$ arcmin]	3.26	8.49	4.24
sky fraction	70%	40%	2%
$N_{\rm side}$	1024	1024	2048
$\ell_{\rm min}$	11	11	51
$\ell_{\rm max}$	811	3011	3011

Table 4.4: Summary of the experimental specifications for the considered upcoming CMB surveys (upper block), and the set-up for the analysis pipeline (lower block).

Par.	LiteBIRD	SO-LAT	CMB-S4
β_0 [deg]	0.30 ± 0.01	0.30 ± 0.01	0.30 ± 0.02
n	0.00 ± 0.07	0.00 ± 0.05	0.00 ± 0.07

Table 4.5: Forecasted best-fit values and 1σ errors for (β_0, n) from upcoming CMB experiments.

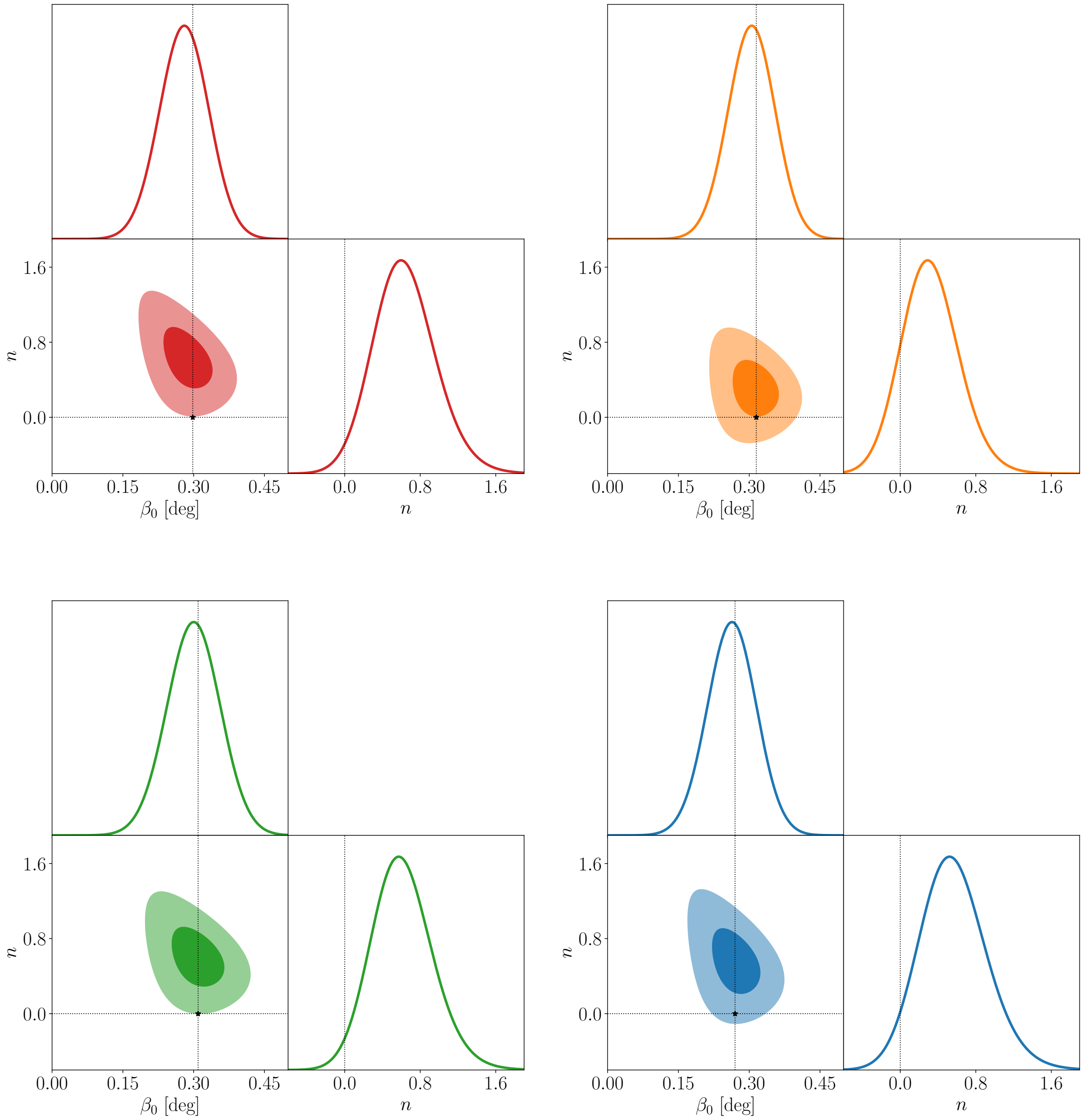

Figure 4.7: Triangular contour plots illustrating the power-law constraints for all four component-separation methods using the D^{EB} estimator: upper left panel for `Commander`, upper right for `NILC`, lower left for `SEVEM`, and lower right for `SMICA`. The stars ($\star$) indicate the points $(\beta, 0)$ where β values are taken from table 4.1.

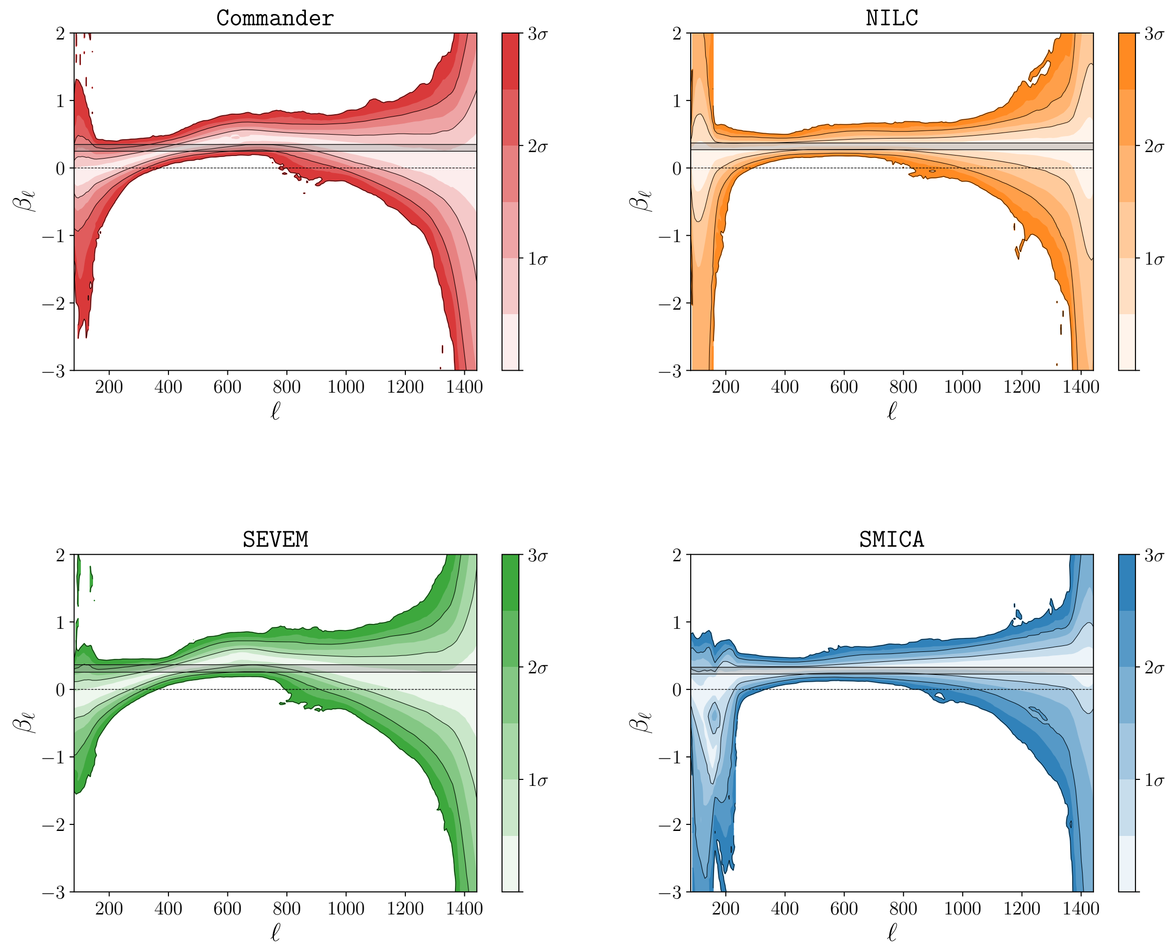

Figure 4.8: Reconstruction of the angular-dependent isotropic cosmic birefringence angle displayed using iso-probability credibility intervals in the (β_ℓ, ℓ) plane, with probability masses converted to σ values via an inverse error function transformation. Results are obtained from the EB-based estimator applied to the `Commander` (upper left), `NILC` (upper right), `SEVEM` (lower left), and `SMICA` (lower right) maps, assuming four nodes ($N = 4$). The grey shaded regions correspond to the 68% confidence level obtained from the single-node analysis ($N = 1$), with numerical values reported in table 4.3.

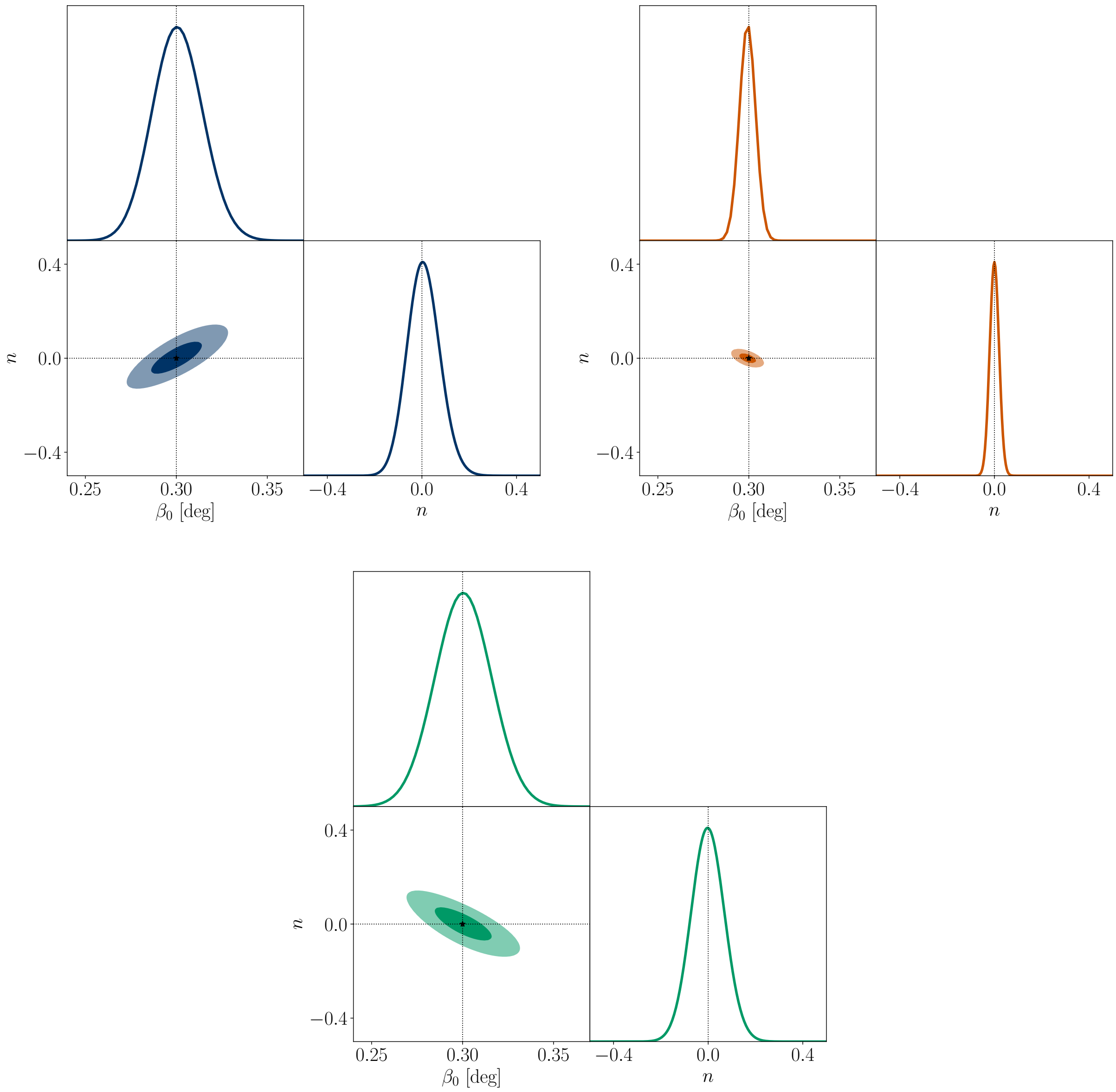

Figure 4.9: Triangular contour plots illustrating the forecast of power-law constraints for different future CMB experiments: LiteBIRD (dark blue), Simons Observatory - Large Aperture Telescope (brick red), and CMB Stage 4 (emerald green). The stars ($\star$) indicate the constant values ($\beta = 0.3$ deg , $n = 0$) used to produce the simulations.

Chapter 5

Photon-to-axion conversion in cosmological environments

Starting from the Chern-Simons Lagrangian introduced in eq. (2.89), a photon γ can interact with an external magnetic field and convert into an axion a. This process can be viewed as the axion analog of the Mikheyev-Smirnov-Wolfenstein (MSW) effect in neutrino oscillations [163, 164]. In the MSW effect, neutrinos traveling through matter of varying density can undergo resonant flavor conversion—for instance, from electron neutrinos to muon neutrinos—due to coherent forward scattering off particles in the medium. Similarly, photons propagating through matter can resonantly convert into axions when certain conditions are met. The system can be studied as a two-level quantum system described by a Schrödinger-like equation, whose solution yields the conversion probability.

This conversion probability strongly depends on the properties of the medium through which the photon propagates. In particular, through scattering within the medium, the photon acquires an effective mass proportional to the electron density distribution. When the effective photon mass equals the axion mass, a resonance is induced between the quantum states $|\gamma\rangle$ and $|a\rangle$, and the conversion probability—which can be assumed negligible away from resonance—is significantly enhanced. For this reason, the large-scale structure and galaxy halos, characterized by extended magnetic fields and free electron densities, provide a powerful environment in which to search for photon-to-axion conversion. In this context, CMB photons serve as an ideal source for this phenomenon.

As discussed in [165, 166, 167], CMB photon conversion into axions can induce secondary anisotropies in the intensity and polarization of CMB maps and power spectra, manifesting as CMB spectral distortions [168]. These spectral distortions are deviations of the CMB frequency spectrum from a perfect blackbody, which can arise when energy is injected into or removed from the CMB photon field after the epoch at which thermalization processes (such as Compton scattering and photon production mechanisms) become inefficient. In the context of photon-to-axion conversion, the distortion arises because photons that convert into axions are effectively removed from the CMB spectrum, creating a spatially-dependent (or patchy) temperature deficit. This leads to a patchy screening of the CMB temperature, which can be correlated with the positions of galaxies themselves through a cross-correlation power spectrum between the anisotropic spectral distortion in the CMB temperature signal and the projected galaxy overdensity [169, 170]. A schematic illustration of this phenomenon is shown in fig. 5.1.

The same phenomenology applies to the conversion of photons into another hypothetical massive particle of the dark sector known as the dark photon [171]. In this latter case, as discussed in the following sections, the interacting Lagrangian is described by a kinetic mixing term between the standard electromagnetic sector and the dark one. Consequently, the presence of an external magnetic field becomes unnecessary, meaning that conversion can occur regardless of whether an external magnetic field is present. This leads to a simpler study of the patchy

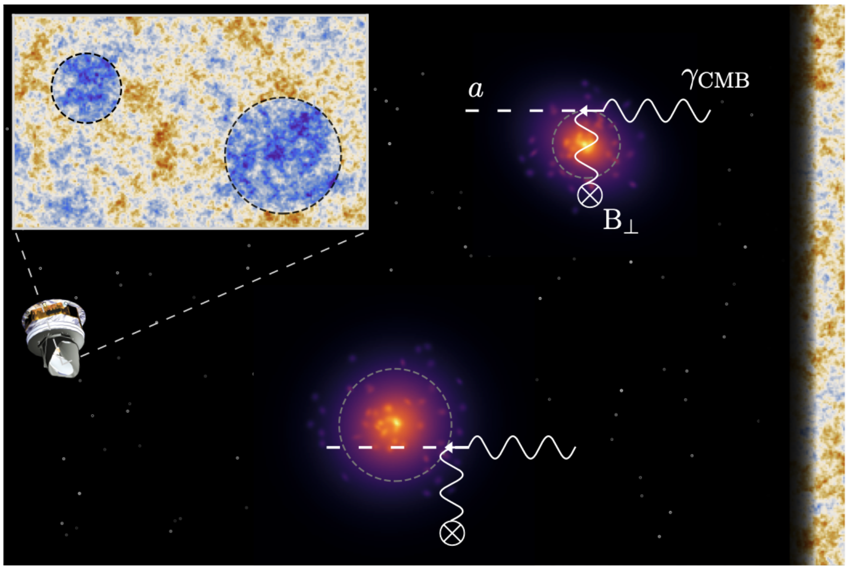

Figure 5.1: Photons emitted at the CMB surface of last scattering, passing through galactic halos and interacting with the magnetic fields within these halos, can convert into axions, inducing secondary anisotropies in the CMB signal due to energy loss. Image from [170].

screening effect, as complications arising from the description of large-scale galactic magnetic fields are avoided.

CMB spectral distortions induced by this effect can be used to test the axion mass range and set an upper bound on the photon-axion coupling constant $g_{a\gamma\gamma}$ described by the Chern-Simons Lagrangian in eq. (2.89).

As described in detail throughout this chapter, the two-level Schrödinger equation can be solved under certain assumptions, yielding a conversion probability proportional to the coupling constant and inversely proportional to the derivative of the halo density profile. This result is known as the Landau-Zener approximation [172, 173].

The astrophysical case is defined by halo models that are symmetric or approximately symmetric around the center. In such cases, a resonance shell is present rather than a single resonance point. When multiple resonance points occur along a given line of sight, interference patterns between the two quantum states $|\gamma\rangle$ and $|a\rangle$ arise, and the final probability cannot simply be taken as the sum of Landau-Zener probabilities at each point. Previous works on this matter have not addressed this issue in detail, generally arguing that on average the interference patterns cancel out [169, 170, 171]. While this may be generally true, the literature lacks any comprehensive study addressing this problem.

The goal of the project described in this chapter is to refine the theoretical modeling of these effects by comparing analytic halo-model predictions with results from state-of-the-art cosmological hydrodynamical simulations. This is achieved by: (a) numerically solving the Schrödinger equation along realistic, inhomogeneous lines of sight to validate the Landau-Zener approximation for photon-axion conversion; (b) comparing halo-model-based predictions with outputs from full hydrodynamical simulations such as Auriga and Illustris-TNG [174, 175]; (c) studying signal production in poorly understood regimes, such as voids, where analytic techniques fail.

To address these issues, a systematic numerical approach has been employed, and a stable numerical code has been developed to test possible scenarios. The theoretical framework and numerical methods described in the following sections of this chapter are based on work in preparation [4].

5.1 Photon-to-axion coupling in an external magnetic field

The analysis begins by considering a photon interacting with an external magnetic field, as illustrated in fig. 5.2. The Lagrangian includes a Chern-Simons interaction term between the photon γ and the axion field a is

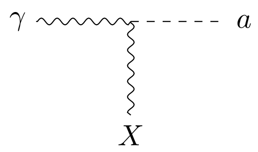

Figure 5.2: Photon converting into an axion in the presence of a background electromagnetic field X. The case of interest corresponds to X being a magnetic field. Time flows from left to right.

$$\mathscr{S} = \int \mathrm{d}x^4 \left[-\frac{1}{2}\partial^\mu a \partial_\mu a - \frac{1}{2}m_a^2 a^2 - \frac{1}{4}F_{\mu\nu}F^{\mu\nu} - \frac{1}{4}g_{a\gamma\gamma} a F_{\mu\nu}\tilde{F}^{\mu\nu} + A_\mu J^\mu \right], \tag{5.1}$$

where $F_{\mu\nu}$ and its dual are defined in eq. (2.90).

By deriving the Euler–Lagrange equations with respect to the axion field a and the electromagnetic field A_μ, the equations of motion for the system can be obtained:

$$\partial_\mu \left(\frac{\partial \mathscr{L}}{\partial(\partial_\mu a)} \right) = \frac{\partial \mathscr{L}}{\partial a}, \tag{5.2}$$

$$\partial_\mu \left(\frac{\partial \mathscr{L}}{\partial(\partial_\mu A_\nu)} \right) = \frac{\partial \mathscr{L}}{\partial A_\nu}, \tag{5.3}$$

where the first equation leads to the modified Klein–Gordon equation and the second gives the modified Maxwell equations. Both are altered due to the presence of the Chern–Simons interaction term.

The Euler–Lagrange equation for a is considered first:

$$\frac{\partial \mathscr{L}}{\partial a} = -m_a^2 a - \frac{1}{4}g_{a\gamma\gamma}F_{\mu\nu}\tilde{F}^{\mu\nu}, \tag{5.4}$$

and, recalling that $\partial^\mu = \eta^{\mu\nu}\partial_\nu$, one computes:

$$\frac{\partial \mathscr{L}}{\partial(\partial_\mu a)} = -\frac{1}{2} \cdot 2\partial^\mu a = -\partial^\mu a, \tag{5.5}$$

thus,

$$\partial_\mu \left(\frac{\partial \mathscr{L}}{\partial(\partial_\mu a)} \right) = -\partial_\mu \partial^\mu a = -\Box a. \tag{5.6}$$

Hence, the full Euler–Lagrange equation becomes:

$$-\Box a = -m_a^2 a - \frac{1}{4}g_{a\gamma\gamma}F_{\mu\nu}\tilde{F}^{\mu\nu}, \tag{5.7}$$

or equivalently

$$\boxed{(\Box - m_a^2)a = \frac{1}{4}g_{a\gamma\gamma}F_{\mu\nu}\tilde{F}^{\mu\nu} = g_{a\gamma\gamma}\mathbf{E}\cdot\mathbf{B}} \tag{5.8}$$

where in the last equality the explicit form of the electromagnetic field tensor is used, as expressed in eq. (2.92).

The Euler–Lagrange equation for A_ν is now examined:

$$\frac{\partial \mathscr{L}}{\partial A_\nu} = \frac{\partial}{\partial A_\nu}(A_\nu J^\nu) = J^\nu, \tag{5.9}$$

and recall that $F_{\mu\nu}$ and its dual are defined as in eq. (2.90), so that

$$\frac{\partial \mathscr{L}}{\partial(\partial_\mu A_\nu)} = -\frac{1}{4}\frac{\partial}{\partial(\partial_\mu A_\nu)}(F_{\mu\nu}F^{\mu\nu}) - \frac{1}{4}\frac{\partial}{\partial(\partial_\mu A_\nu)}(g_{a\gamma\gamma} a F_{\mu\nu}\tilde{F}^{\mu\nu}). \tag{5.10}$$

From electrodynamics it is known that

$$\frac{\partial}{\partial(\partial_\mu A_\nu)}(F_{\mu\nu}F^{\mu\nu}) = +4F^{\mu\nu}, \tag{5.11}$$

thus, applying this to the second term as well, one obtains

$$\frac{\partial \mathscr{L}}{\partial(\partial_\mu A_\nu)} = -F^{\mu\nu} - g_{a\gamma\gamma} a \tilde{F}^{\mu\nu}. \tag{5.12}$$

Recalling that in standard relativistic algebra the Bianchi identity holds:

$$\partial_\mu \tilde{F}^{\mu\nu} = 0, \tag{5.13}$$

one finds:

$$\partial_\mu \left(\frac{\partial \mathscr{L}}{\partial(\partial_\mu A_\nu)} \right) = \partial_\mu(-F^{\mu\nu} - g_{a\gamma\gamma} a \tilde{F}^{\mu\nu}) = -\partial_\mu F^{\mu\nu} - g_{a\gamma\gamma}\tilde{F}^{\mu\nu}\partial_\mu a, \tag{5.14}$$

so the Euler–Lagrange equation becomes

$$\boxed{\partial_\mu F^{\mu\nu} = -g_{a\gamma\gamma}\tilde{F}^{\mu\nu}\partial_\mu a - J^\nu} \tag{5.15}$$

This is essentially Maxwell's equation ($\partial_\mu F^{\mu\nu} = -J^\nu$), modified by the interaction term $-g_{a\gamma\gamma}\tilde{F}^{\mu\nu}\partial_\mu a$.

The equations of motion associated with the Lagrangian are then

$$\begin{cases} (\Box - m_a^2)a = \frac{1}{4} g_{a\gamma\gamma} F_{\mu\nu}\tilde{F}^{\mu\nu} = g_{a\gamma\gamma}\mathbf{E}\cdot\mathbf{B} \\ \partial_\mu F^{\mu\nu} = -g_{a\gamma\gamma}\tilde{F}^{\mu\nu}\partial_\mu a - J^\nu \end{cases} . \tag{5.16}$$

5.1.1 Setting a working coordinate system

For the purposes of this analysis, it is convenient to rewrite the equations of motion in eq. (5.16) in terms of the physical electric and magnetic fields relevant to the setup. To accomplish this, a suitable coordinate system is first defined.

A coordinate system is adopted in which the photon propagates along the z-axis, so that $\hat{z} = \hat{k}$, and the external background magnetic field points in an arbitrary direction. Given the magnetic field $\mathbf{B}$, it can be decomposed into two components: the projection along the direction of propagation, $\mathbf{B}_k = B_k\hat{k}$, and the transverse projection in the xy-plane, $\mathbf{B}_T$. The transverse component $\mathbf{B}_T$ defines a preferred direction in the xy-plane, which is labeled $\hat{\parallel}$, and from this a perpendicular direction, $\hat{\perp}$, is defined.

It is convenient to work in the rotated basis $(\hat{\perp}, \hat{\parallel}, \hat{k}) \equiv (e_\perp, e_\parallel, e_k)$, which simplifies both the discussion and the calculations.

Since the magnetic field is external[1], it may have a component along the photon's direction of propagation. In contrast, the electric field associated with the photon lies entirely in the transverse xy-plane. In this new basis, one writes

$$\mathbf{E} = \mathbf{E}_\perp + \mathbf{E}_\parallel, \tag{5.17}$$

[1]The photon wave also generates a magnetic field, but it is not of interest here, and thus is not included in the analysis.

and

$$\mathbf{B} = \mathbf{B}_k + \mathbf{B}_T. \tag{5.18}$$

Therefore, the scalar product becomes

$$\mathbf{E} \cdot \mathbf{B} = \mathbf{E} \cdot \mathbf{B}_T = E_{\|} B_T. \tag{5.19}$$

The coordinate system is illustrated more clearly in fig. 5.3.

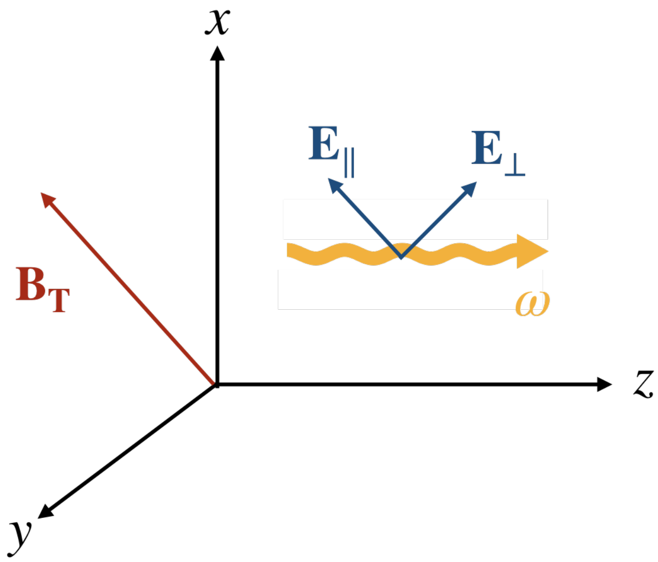

Figure 5.3: Coordinate system $(\hat{\perp}, \hat{\|}, \hat{z})$ described with respect to $(\hat{x}, \hat{y}, \hat{z})$.

This result is physically important: only the transverse component of the external magnetic field contributes to the photon-axion interaction, leading to axion production.

In the coordinate basis $(e_{\perp}, e_{\|}, e_k)$, the electric and magnetic fields take the form $\mathbf{E} = (E_{\perp}, E_{\|}, 0)$ and $\mathbf{B} = (0, B_T, B_k)$. As demonstrated by eq. (5.19), the B_k component does not contribute to the scalar product $\mathbf{E} \cdot \mathbf{B}$ and therefore does not appear in the equations of motion. Consequently, the B_k component can be set to zero without loss of generality, yielding $\mathbf{B} = (0, B_T, 0)$.

Considering the potential field $A_\mu = (\phi, \mathbf{A})$, in the chosen coordinate system one has $A_\mu = (\phi, A_{\perp}, A_{\|}, 0)$. Furthermore, working in the Lorenz gauge, $\partial_\mu A^\mu = 0$, allows expressing the electric and (external) magnetic fields as

$$\partial_\mu A^\mu = 0 \iff \begin{cases} \mathbf{E} = -\nabla\phi - \frac{\partial \mathbf{A}}{\partial t} \\ \mathbf{B} = \nabla \times \mathbf{A}. \end{cases} \tag{5.20}$$

5.1.2 Rewriting the equations in terms of vectors

The equations of motion in eq. (5.16) are now revisited using the coordinate system established above. The equations are rewritten for the case where the external magnetic field $\mathbf{B}$ is transverse[2] to the photon's propagation direction. Additionally, the case with no external source of photons is considered, so $J^\mu = 0$ can be set in eq. (5.16).

[2]Again, it is irrelevant whether $\mathbf{B}$ has a B_k component or not, since only the transverse component relative to the photon's propagation direction contributes to the interaction.

The goal is to express the equations in terms of $\mathbf{E}\cdot\mathbf{B}^{\text{ext}}$ and/or in terms of A^μ. In fact, the first equation in eq. (5.16) is already written in the desired form, so the focus is now on rewriting the second one.

First, the left-hand side is expanded explicitly

$$\partial_\mu F^{\mu\nu} = \partial_\mu(\partial^\mu A^\nu - \partial^\nu A^\mu) = \partial_\mu\partial^\mu A^\nu - \partial^\nu\partial_\mu A^\mu = \partial_\mu\partial^\mu A^\nu = \Box A^\nu, \tag{5.21}$$

where in the final step the Lorenz gauge condition is used.

In the absence of external electromagnetic sources ($q = 0$ and $J^\mu = 0$), the modified Maxwell equation reduces to

$$\Box A^\nu = -g_{a\gamma\gamma}\tilde{F}^{\mu\nu}\partial_\mu a\,, \tag{5.22}$$

where the right-hand side represents an effective source term induced by the axion field.

Recalling that $\mathbf{A}^\mu = (\phi, \mathbf{A})$, as seen in (2.91), the latter equations are now computed component by component.

- **Time component (0-th):**

$$\Box A^0 = -g_{a\gamma\gamma}\tilde{F}^{\mu 0}\partial_\mu a\,. \tag{5.23}$$

  It is now assumed that the scalar potential ϕ is constant and that the propagation of the photon is described by waves in $\mathbf{A}$ only. For simplicity, one sets

$$A^0 = \phi = \text{const} = 0, \tag{5.24}$$

  so that the 0th component equation vanishes identically.

- **Spatial component (k-th):**

$$\Box A^k = -g_{a\gamma\gamma}\tilde{F}^{\mu k}\partial_\mu a. \tag{5.25}$$

  The right-hand side expands as

$$-g_{a\gamma\gamma}\left(\tilde{F}^{0k}\partial_0 a + \tilde{F}^{jk}\partial_j a\right).$$

  From the definition of the dual field strength tensor

$$\tilde{F}_{0k} = \frac{\varepsilon_{0k\rho\sigma}}{2}F^{\rho\sigma} = -B^k, \tag{5.26}$$

  so the equation becomes

$$\Box A^k = -g_{a\gamma\gamma}\left(-B^k\partial_0 a + \frac{1}{2}\varepsilon_{jk\rho\sigma}F^{\rho\sigma}\partial_j a\right). \tag{5.27}$$

  Note that $\varepsilon_{jk\rho\sigma} \neq 0$ only when either $\rho = 0$ or $\sigma = 0$, so the second term can be rewritten explicitly as

$$\frac{1}{2}\varepsilon_{jk\rho\sigma}F^{\rho\sigma}\varepsilon_{jk0i}\partial^0 A^i = -\varepsilon_{jk0i}E^i, \tag{5.28}$$

  where the antisymmetry of $F^{\mu\nu}$, the condition $A^0 = 0$, and the definition of the electric field $E^i = -\partial^0 A^i$ are used.

  Therefore, the equation for the spatial components becomes

$$\Box A^k = -g_{a\gamma\gamma}\left(-B^k\partial_0 a - \varepsilon_{jk0i}E^i\partial_j a\right), \tag{5.29}$$

  which can be rewritten using index notation as a vector product

$$\Box A^k = -g_{a\gamma\gamma}\left(-B^k\partial_0 a + \partial_i a \times E^i\right). \tag{5.30}$$

Finally, the equations of motion in eq. (5.16) can be rewritten in vector form as

$$\boxed{\begin{cases}(\Box - m_a^2)a = g_{a\gamma\gamma}\mathbf{E}\cdot\mathbf{B} \\ \Box\mathbf{A} = g_{a\gamma\gamma}\left(\mathbf{B}\,\partial_0 a + \nabla a\times\mathbf{E}\right)\end{cases}.} \tag{5.31}$$

5.1.3 Rewriting the equations in the fixed coordinate system

The coordinate system previously defined is now adopted and real wave solutions are considered. Specifically, it is assumed

$$\mathbf{A}(z,t) = (A_\perp(z), A_\parallel(z), 0)e^{i\omega_\gamma t}, \tag{5.32}$$

where the photon γ is polarized perpendicularly to the direction of propagation. The axion field is generated perpendicular to the photon's plane and thus also depends only on the $z = k$ direction

$$a(z,t) = a(z)e^{i\omega_a t}. \tag{5.33}$$

Assuming the system is in resonance, one imposes

$$\omega_\gamma = \omega_a = \omega. \tag{5.34}$$

Again, $\mathbf{B} = (0, B_T, 0)$ is taken, although in principle it may also have a component along $z = k$.

- **First equation:**

$$(\Box - m_a^2)a = g_{a\gamma\gamma}\mathbf{E}\cdot\mathbf{B}. \tag{5.35}$$

The left-hand side becomes

$$(\Box - m_a^2)a(z,t) = \left(-\partial^0\partial_0 a(z,t) + \nabla^2 a(z,t) - m_a^2 a(z,t)\right), \tag{5.36}$$

and since

$$\nabla^2 a(z,t) = \partial_z^2 a(z,t), \tag{5.37}$$

and

$$-\partial^0\partial_0 a(z,t) = -a(z)\frac{\partial^2}{\partial t^2}(e^{i\omega t}) = \omega^2 a(z,t), \tag{5.38}$$

the full expression becomes

$$(\Box - m_a^2)a(z,t) = (\omega^2 + \partial_z^2 - m_a^2)a(z,t). \tag{5.39}$$

The right-hand side evaluates to

$$g_{a\gamma\gamma}\mathbf{E}\cdot\mathbf{B} = -g_{a\gamma\gamma}B_T\partial_t A_\parallel(z,t) = -i\omega g_{a\gamma\gamma}B_T A_\parallel(z), \tag{5.40}$$

so the equation becomes

$$(\omega^2 + \partial_z^2 - m_a^2)a(z,t) = -i\omega g_{a\gamma\gamma}B_T A_\parallel(z,t). \tag{5.41}$$

- **Second equation:**

The second equation of motion is now split into two components, one along $\hat{e}_\perp$ and the other along $\hat{e}_\parallel$.

In both cases, the term $\nabla a \times \mathbf{E}$ is neglected, as it is subdominant (the axion field varies slowly in space). Thus, one has:

$$\Box A_\perp(z,t) = g_{a\gamma\gamma}B_\perp\partial_0 a = 0, \tag{5.42}$$

since $B_\perp = 0$. Making the d'Alembertian explicit

$$(\omega^2 + \partial_z^2)A_\perp(z,t) = 0. \tag{5.43}$$

For the parallel component, still neglecting the $\nabla a \times \mathbf{E}$ term, one obtains

$$(\omega^2 + \partial_z^2)A_\parallel(z,t) = i\omega g_{a\gamma\gamma} B_T a(z,t). \tag{5.44}$$

Thus, the system in eq. (5.16) in the chosen coordinate system becomes

$$\begin{cases} (\omega^2 + \partial_z^2 - m_a^2)a(z,t) = -i\omega g_{a\gamma\gamma} B_T A_\parallel(z,t) \\ (\omega^2 + \partial_z^2)A_\perp(z,t) = 0 \\ (\omega^2 + \partial_z^2)A_\parallel(z,t) = i\omega g_{a\gamma\gamma} B_T a(z,t) \end{cases}. \tag{5.45}$$

By applying the transformation $\mathbf{A} \to i\mathbf{A} = e^{i\frac{\pi}{2}}\mathbf{A}$, which corresponds to a phase shift in the photon field, the system can be further rewritten as

$$\begin{cases} (\omega^2 + \partial_z^2 - m_a^2)a(z,t) = \omega g_{a\gamma\gamma} B_T A_\parallel(z,t) \\ (\omega^2 + \partial_z^2)A_\perp(z,t) = 0 \\ (\omega^2 + \partial_z^2)A_\parallel(z,t) = \omega g_{a\gamma\gamma} B_T a(z,t) \end{cases}. \tag{5.46}$$

This system can be compactly expressed by defining

$$\mathcal{M} = \begin{pmatrix} 0 & 0 & 0 \\ 0 & 0 & \omega g_{a\gamma\gamma} B_T \\ 0 & \omega g_{a\gamma\gamma} B_T & -m_a^2 \end{pmatrix} \quad \text{and} \quad \Psi(z,t) = \begin{pmatrix} A_\perp(z,t) \\ A_\parallel(z,t) \\ a(z,t) \end{pmatrix}, \tag{5.47}$$

so that the system becomes

$$\left[\omega^2 + \partial_z^2 + \mathcal{M}\right]\Psi(z,t) = 0. \tag{5.48}$$

Another useful approximation can also be made. The first two terms can be factorized as:

$$\omega^2 + \partial_z^2 = (\omega + i\partial_z)(\omega - i\partial_z), \tag{5.49}$$

which suggests a possible simplification. In fact, the factor $e^{-i\omega t}$ appearing in the components of $\Psi(z,t)$ now behaves as an overall phase (i.e., a constant with respect to the differential operator) and can be factored out. The problem is then reduced to a dependence on z only:

$$\Psi(z) = \begin{pmatrix} A_\perp(z) \\ A_\parallel(z) \\ a(z) \end{pmatrix}. \tag{5.50}$$

For slowly varying amplitudes (as in this case), where $\partial_z|\mathbf{A}(z)| \ll k|\mathbf{A}(z)|$, the **WKB approximation** can be applied [176]. One writes[3]

$$\mathbf{A}(z) = |\mathbf{A}(z)|e^{-ikz}, \tag{5.51}$$

implying

$$\tilde{\Psi} = \Psi e^{-ikz}. \tag{5.52}$$

This allows the approximation:

$$\partial_z\Psi \sim -ik\Psi + \cancel{\ldots} \quad \Longrightarrow \quad i\partial_z\Psi \sim k\Psi. \tag{5.53}$$

[3]Note that the phase could also be defined with the opposite sign, i.e., e^{+ikz}.

As a result, one arrives at the approximation

$$\omega^2 + \partial_z^2 = (\omega + i\partial_z)(\omega - i\partial_z) \simeq (\omega + k)(\omega - i\partial_z). \tag{5.54}$$

Since $\omega = \frac{k}{n}$, and assuming approximate vacuum conditions ($n \simeq 1$), one takes $\omega \simeq k$. This gives

$$\omega^2 + \partial_z^2 \simeq 2\omega(\omega - i\partial_z). \tag{5.55}$$

The equation of motion can then be rewritten in the form

$$\left[\omega - i\partial_z + \begin{pmatrix} 0 & 0 & 0 \\ 0 & 0 & \frac{g_{a\gamma\gamma}B_T}{2} \\ 0 & \frac{g_{a\gamma\gamma}B_T}{2} & -\frac{m_a^2}{2\omega} \end{pmatrix}\right]\tilde{\Psi} = 0, \tag{5.56}$$

with

$$\tilde{\Psi}(z) = \begin{pmatrix} A_\perp(z) \\ A_\parallel(z) \\ a(z) \end{pmatrix} = \begin{pmatrix} |A_\perp(z)| \\ |A_\parallel(z)| \\ |a(z)| \end{pmatrix} e^{-i\omega z} = \Psi e^{-ikz}, \tag{5.57}$$

where it is emphasized that the phase introduced by the WKB approximation does not affect physical probabilities but helps simplify the structure of the equation.

The following quantities are now defined:

$$\Delta_{a\gamma} = \frac{g_{a\gamma\gamma}B_T}{2}, \qquad \Delta_a = -\frac{m_a^2}{2\omega}, \tag{5.58}$$

so that the mass matrix becomes

$$\left[\omega - i\partial_z + \begin{pmatrix} 0 & 0 & 0 \\ 0 & 0 & \Delta_{a\gamma} \\ 0 & \Delta_{a\gamma} & \Delta_a \end{pmatrix}\right]\Psi = 0. \tag{5.59}$$

This equation is formally equivalent to a **Schrödinger-like equation** for a three-level system described by $\tilde{\Psi}$. Indeed, by distributing the operator:

$$\omega\tilde{\Psi} - i\partial_z\tilde{\Psi} + \mathcal{M}\tilde{\Psi} = \cancel{\omega\tilde{\Psi}} - i\partial_z(\Psi)e^{-i\omega z} - \cancel{i(-i\omega)\tilde{\Psi}} + \mathcal{M}\tilde{\Psi} = 0, \tag{5.60}$$

and simplifying the phase factor, one obtains

$$\boxed{i\frac{\mathrm{d}}{\mathrm{d}z}\Psi = \mathcal{M}\Psi\ .} \tag{5.61}$$

5.2 Photon-to-axion oscillation

The goal is now to demonstrate that the evolution equations, written compactly in eq. (5.61), lead to photon-to-axion (and *vice versa*) oscillations, as represented in the Feynman diagram in fig. 5.2. The equation for $A_\perp$ describes a simple propagation mode and does not couple to either B_T or a. Therefore, it can be set aside and the focus placed on the coupled system described by the Klein–Gordon equation and the equation for $A_\parallel(z)$, which are the relevant components for the mixing dynamics.

5.2.1 Adding other interaction terms

Up to this point, quantum corrections to the Lagrangian have not been included, such as those arising from the **Euler–Heisenberg** effective Lagrangian, which introduces next-to-leading-order (NLO) corrections to Maxwell's equations. The **Cotton–Mouton effect**, a birefringence effect that occurs in a liquid when it is subjected to a constant magnetic field perpendicular to the light direction [177], has also been neglected [178].

Including these corrections introduces two additional terms, $\Delta_\parallel = \Delta_\gamma$ and $\Delta_\perp$, modifying the mass matrix $\mathcal{M}$ to

$$\mathcal{M} = \begin{pmatrix} \Delta_\perp & 0 & 0 \\ 0 & \Delta_\parallel & \Delta_{\gamma a} \\ 0 & \Delta_{\gamma a} & \Delta_a \end{pmatrix} = \begin{pmatrix} \Delta_\perp & 0 \\ 0 & \mathcal{M}_\parallel \end{pmatrix}, \tag{5.62}$$

where

$$\mathcal{M}_\parallel = \begin{pmatrix} \Delta_\parallel & \Delta_{\gamma a} \\ \Delta_{\gamma a} & \Delta_a \end{pmatrix}. \tag{5.63}$$

The terms $\Delta_\parallel$ and $\Delta_\perp$ can be generalized as

$$\Delta_* = \Delta_{\text{QED}} + \Delta_{\text{CM}} + \Delta_{\text{Plasma}} \quad \text{where} \quad * = \{\parallel, \perp\}. \tag{5.64}$$

In principle, higher-order corrections could also be considered, which would render $\mathcal{M}$ fully populated. However, such contributions are neglected here. The conclusions reached earlier remain valid: the equation for $A_\perp$ continues to describe the free propagation of the photon, possibly modified by QED self-interactions, but it remains decoupled from axion dynamics and can be safely ignored in what follows.

However, the equation for $A_\parallel$ is modified due to these additional interaction terms. In particular: - Δ_{QED} arises from vacuum polarization effects, - Δ_{CM} accounts for birefringence due to the Cotton–Mouton effect, - Δ_{Plasma} describes the photon's effective mass induced by scattering with free electrons in a plasma.

Among these, only Δ_{Plasma} is dominant and essential for describing the interaction between photons and the intergalactic medium, especially in cosmological and astrophysical contexts. Photons propagating through the large-scale structure (LSS) interact with electrons in galactic halos, gaining an effective mass. Thus, one sets

$$\Delta_{\text{QED}} = 0 \quad \text{and} \quad \Delta_{\text{CM}} = 0. \tag{5.65}$$

Had the plasma interaction been included from the start, an effective photon mass term would have been added to the Lagrangian, appearing in the system in eq. (5.46) as a modification to the second and third equations.

As for the remaining Δ terms (see also eq. (5.58)), one has[4]

$$\Delta_\parallel = \Delta_\gamma = -\frac{m_\gamma^2}{2\omega}. \tag{5.66}$$

Here, m_γ^2 depends on the electron density encountered by the photon along its trajectory:

$$m_\gamma^2(z) = e^2 \frac{n_e(z)}{m_e} = \frac{4\pi\alpha n_e(z)}{m_e}, \tag{5.67}$$

leading to

$$\Delta_\parallel = -\frac{1}{2\omega} \cdot \frac{4\pi\alpha n_e(z)}{m_e}, \tag{5.68}$$

where $n_e(z)$ is the number density of electrons, e is the elementary charge, and m_e is the electron mass.

[4]The notation $\Delta_\parallel$ and Δ_γ are used interchangeably, following standard conventions in the literature.

5.2.2 Diagonalizing the Schrödinger equation in the case of constant parameters

Attention is now restricted to the reduced two-level Schrödinger equation

$$i\frac{\mathrm{d}}{\mathrm{d}z}\begin{pmatrix} A_\parallel(z) \\ a(z) \end{pmatrix} = \begin{pmatrix} \Delta_\parallel & \Delta_{\gamma a} \\ \Delta_{\gamma a} & \Delta_a \end{pmatrix}\begin{pmatrix} A_\parallel(z) \\ a(z) \end{pmatrix} = \mathcal{M}_\parallel \begin{pmatrix} A_\parallel(z) \\ a(z) \end{pmatrix} . \tag{5.69}$$

In realistic settings, $B_T = B_T(z)$ and $m_\gamma^2 = m_\gamma^2(z) \sim n_e(z)$. However, the problem is simplified by assuming both B_T and n_e are constant. In this idealized case, the Hamiltonian $H = \mathcal{M}_\parallel$ is symmetric and constant, making it straightforward to diagonalize and solve the system for $A_\parallel(z)$ and $a(z)$.

The Hamiltonian can be diagonalized as

$$D = P^{-1}\mathcal{M}_\parallel P = P^T\mathcal{M}_\parallel P = \begin{pmatrix} \lambda_+ & 0 \\ 0 & \lambda_- \end{pmatrix}, \tag{5.70}$$

where P is a unitary matrix ($\det P = 1$ and $P^T = P^{-1}$) representing a basis rotation

$$P = \begin{pmatrix} \cos\vartheta & -\sin\vartheta \\ \sin\vartheta & \cos\vartheta \end{pmatrix}. \tag{5.71}$$

To find the eigenvalues $\lambda_\pm$, the characteristic equation is solved:

$$\det\left(\mathcal{M}_\parallel - \lambda\mathbb{1}\right) = 0 \quad\Rightarrow\quad (\Delta_\parallel - \lambda)(\Delta_a - \lambda) - \Delta_{\gamma a}^2 = 0, \tag{5.72}$$

which yields

$$\lambda^2 - (\Delta_a + \Delta_\parallel)\lambda + (\Delta_\parallel\Delta_a - \Delta_{\gamma a}^2) = 0. \tag{5.73}$$

Solving this quadratic equation gives

$$\lambda_\pm = \frac{\Delta_a + \Delta_\parallel \pm \sqrt{(\Delta_a - \Delta_\parallel)^2 + 4\Delta_{\gamma a}^2}}{2} = \frac{\Delta_a + \Delta_\parallel \pm \Delta_{\mathrm{osc}}}{2}, \tag{5.74}$$

where the following quantity is defined:

$$\Delta_{\mathrm{osc}} = \sqrt{(\Delta_a - \Delta_\parallel)^2 + 4\Delta_{\gamma a}^2}. \tag{5.75}$$

The mixing angle ϑ satisfies

$$\sin(2\vartheta) = \frac{2\Delta_{\gamma a}}{\Delta_{\mathrm{osc}}}, \qquad \cos(2\vartheta) = \frac{\Delta_\parallel - \Delta_a}{\Delta_{\mathrm{osc}}}, \tag{5.76}$$

which implies

$$\tan(2\vartheta) = \frac{2\Delta_{\gamma a}}{\Delta_\parallel - \Delta_a}. \tag{5.77}$$

[5] This result is particularly relevant in vacuum, i.e., in the absence of plasma ($\Delta_\parallel = 0$) and under a constant magnetic field:

$$\sin(2\vartheta) = \frac{2g_{a\gamma\gamma}B_T\omega}{\sqrt{m_a^4 + (2g_{a\gamma\gamma}B_T\omega)^2}}, \qquad \cos(2\vartheta) = \frac{m_a^2}{\sqrt{m_a^4 + (2g_{a\gamma\gamma}B_T\omega)^2}}, \tag{5.78}$$

$$\Downarrow$$

$$\tan(2\vartheta) = \frac{2g_{a\gamma\gamma}B_T\omega}{m_a^2}. \tag{5.79}$$

[5] This is the standard diagonalization procedure for a symmetric 2×2 matrix. Indeed, for a matrix $A = \begin{pmatrix} a & c \\ c & b \end{pmatrix}$, the mixing angle satisfies $\tan(2\vartheta) = \frac{2c}{a-b}$.

5.2.3 Solving the Schrödinger equation in the case of constant quantities

Once the Hamiltonian $H = \mathcal{M}_\parallel$ is diagonalized in the simple case of z-independent quantities, it becomes possible to solve the Schrödinger equation explicitly. The solution to eq. (5.69) follows from solving the corresponding diagonalized equation (with components denoted by tildes)

$$i\frac{\mathrm{d}}{\mathrm{d}z}\begin{pmatrix}\tilde{A}_\parallel(z)\\ \tilde{a}(z)\end{pmatrix} = \begin{pmatrix}\lambda_+ & 0\\ 0 & \lambda_-\end{pmatrix}\begin{pmatrix}\tilde{A}_\parallel(z)\\ \tilde{a}(z)\end{pmatrix}. \tag{5.80}$$

In general, the solution $\Psi(z) = \begin{pmatrix}\Psi_1(z)\\ \Psi_2(z)\end{pmatrix}$ of the non-diagonalized system is recovered from the solution $\tilde{\Psi}(z) = \begin{pmatrix}\tilde{\Psi}_1(z)\\ \tilde{\Psi}_2(z)\end{pmatrix}$ of the diagonalized one via the transformation

$$\Psi = P\tilde{\Psi}. \tag{5.81}$$

Since the Schrödinger equation describes wave-like propagation, the time evolution (in this context, along z) of the eigenstates is

$$\tilde{\Psi}_i(z) = \tilde{\Psi}_i(z_0)e^{-i\lambda_i z}, \tag{5.82}$$

with $\lambda_1 \equiv \lambda_+$ and $\lambda_2 \equiv \lambda_-$. Substituting into eq. (5.81), the solution becomes

$$\Psi_i(z) = \sum_{j=1}^{2} P_{ij}^{-1}\tilde{\Psi}_j(z) = \sum_{j=1}^{2} P_{ij}^{-1}P_{kj}\Psi_j(z_0)e^{-i\lambda_j z} = \sum_{j=1}^{2} P_{ij}^{-1}[P\Psi(z_0)]_j e^{-i\lambda_j z}. \tag{5.83}$$

In this case:

$$\begin{pmatrix}A_\parallel(z)\\ a(z)\end{pmatrix} = P\begin{pmatrix}e^{-i\lambda_+ z} & 0\\ 0 & e^{-i\lambda_- z}\end{pmatrix}P^{-1}\begin{pmatrix}A_\parallel(z_0)\\ a(z_0)\end{pmatrix}. \tag{5.84}$$

By specifying initial and final states appropriately, the desired physical process can be described. For example, taking

$$\Psi_0 = \begin{pmatrix}A_\parallel(z_0)\\ a(z_0)\end{pmatrix} = \begin{pmatrix}1\\ 0\end{pmatrix}, \quad \Psi(z) = \begin{pmatrix}A_\parallel(z)\\ a(z)\end{pmatrix}, \tag{5.85}$$

models a scenario in which the initial state at z_0 contains only a photon, and the probability of conversion into an axion at position z is computed.

Carrying out the matrix multiplications yields

$$\begin{cases} A_\parallel(z) = \cos\vartheta\sin\vartheta\left(e^{-i\lambda_+ z} - e^{-i\lambda_- z}\right)a(z_0) + \left(\sin^2\vartheta\, e^{-i\lambda_+ z} + \cos^2\vartheta\, e^{-i\lambda_- z}\right)A_\parallel(z_0),\\ a(z) = \left(\cos^2\vartheta\, e^{-i\lambda_+ z} + \sin^2\vartheta\, e^{-i\lambda_- z}\right)a(z_0) + \cos\vartheta\sin\vartheta\left(e^{-i\lambda_+ z} - e^{-i\lambda_- z}\right)A_\parallel(z_0), \end{cases} \tag{5.86}$$

which in the case $\Psi_0 = \begin{pmatrix}1\\ 0\end{pmatrix}$ reduces to

$$\begin{cases} A_\parallel(z) = \sin^2\vartheta\, e^{-i\lambda_+ z} + \cos^2\vartheta\, e^{-i\lambda_- z},\\ a(z) = \cos\vartheta\sin\vartheta\left(e^{-i\lambda_+ z} - e^{-i\lambda_- z}\right). \end{cases} \tag{5.87}$$

The conversion probability can now be computed. Denoting $|\gamma\rangle \equiv |\Psi_0\rangle$ and $|a\rangle \equiv |\Psi\rangle$, one obtains

$$P_{\gamma\to a}(z) = |\langle a|\gamma\rangle|^2 = |a(z)|^2 \tag{5.88}$$

$$= 2\cos^2\vartheta\sin^2\vartheta\,\sin^2\left(\frac{\lambda_- - \lambda_+}{2}z\right) \tag{5.89}$$

$$= \sin^2(2\vartheta)\,\sin^2\left(\frac{\Delta_{\mathrm{osc}}}{2}z\right) \tag{5.90}$$

$$= \frac{(\Delta_{\gamma a}z)^2}{\left(\frac{\Delta_{\mathrm{osc}}}{2}z\right)^2}\,\sin^2\left(\frac{\Delta_{\mathrm{osc}}}{2}z\right), \tag{5.91}$$

where in the last step the expression for $\sin(2\vartheta)$ in terms of $\Delta_{\gamma a}$ and $\Delta_{\rm osc}$ is used.

This result assumes a constant transverse magnetic field B_T and a constant effective photon mass m_γ^2 (i.e., constant electron density n_e) over a domain of size $L_{\rm dom} = z$. The conversion probability across this domain is therefore

$$P_{\gamma\to a}(L_{\rm dom}) = \frac{(g_{a\gamma\gamma} B_T L_{\rm dom})^2}{(\Delta_{\rm osc} L_{\rm dom})^2} \sin^2\left(\frac{\Delta_{\rm osc}}{2} L_{\rm dom}\right). \tag{5.92}$$

A particularly important case is that of **resonance**, where

$$\text{Resonance:} \quad m_a = m_\gamma, \tag{5.93}$$

which implies $\vartheta = \frac{\pi}{4}$, and the probability simplifies to [173]

$$P^{\rm res}_{\gamma\to a} = \sin^2\left(\Delta_{\gamma a} L_{\rm dom}\right) = \sin^2\left(\frac{g_{a\gamma\gamma} B_T}{2} L_{\rm dom}\right), \tag{5.94}$$

a particularly elegant result as it is independent of the frequency ω. Substituting the relevant parameters confirms the qualitative insight:

$$P^{\rm res}_{\gamma\to a} \gg P_{\gamma\to a}, \tag{5.95}$$

highlighting that **when resonance occurs, the conversion probability is significantly enhanced**. This emphasizes the relevance of the resonant regime in both theoretical analyses and observational searches for photon–axion conversion.

5.3 The real two-level photon-to-axion system

In the previous section, the probability of photon-to-axion conversion was derived for the case of constant quantities—namely, constant $m_\gamma^2 \sim n_e$ and B_T.

In the realistic case, however, these quantities depend on the spatial coordinate z: $B_T = B_T(z)$ and $m_\gamma^2 = m_\gamma^2(z) \sim n_e(z)$. Consequently, the Hamiltonian $H = \mathcal{M}_\parallel$ is also z-dependent.[6]

The Schrödinger equation in eq. (5.69) is thus more accurately expressed as

$$i\frac{\mathrm{d}}{\mathrm{d}z}\begin{pmatrix} A_\parallel(z) \\ a(z)\end{pmatrix} = \begin{pmatrix} \Delta_\parallel(z) & \Delta_{\gamma a}(z) \\ \Delta_{\gamma a}(z) & \Delta_a \end{pmatrix}\begin{pmatrix} A_\parallel(z) \\ a(z)\end{pmatrix} = \mathcal{M}_\parallel(z)\begin{pmatrix} A_\parallel(z) \\ a(z)\end{pmatrix}, \tag{5.96}$$

where

$$\begin{cases} \Delta_\parallel(z) = -\frac{1}{2\omega}\left(\frac{4\pi\alpha n_e(z)}{m_e}\right) = -\frac{m_\gamma^2(z)}{2\omega}, \\ \Delta_{\gamma a}(z) = \frac{g_{a\gamma\gamma}}{2} B_T(z), \\ \Delta_a = -\frac{m_a^2}{2\omega}. \end{cases} \tag{5.97}$$

In this case, it is no longer possible to diagonalize the Hamiltonian globally, due to its dependence on z (or analogously, on t). Therefore, the problem must be treated differently.

As shown in the next sections, it is still possible to reformulate the problem in terms of a second-order differential equation. Under certain simplifying assumptions, this equation yields an approximate but tractable solution for the conversion probability.

The appropriate framework for analyzing such a situation is provided by the **Landau-Zener approximation**, developed independently by Landau and Zener in 1938. The probability formula derived under this approximation is known as the **Landau-Zener formula**.

This section follows the discussion in [173], together with the original, pedagogically clear treatment by Zener [172].

[6] An identical treatment can be carried out for the full three-level system, but the focus continues on the two-level case.

5.3.1 General case and Landau-Zener approximation

A general two-level system described by a time-dependent Hamiltonian $H_0(t)$ is considered, characterized by instantaneous energy levels $E_i(t)$:

$$H_0(t) = \begin{pmatrix} E_1(t) & 0 \\ 0 & E_2(t) \end{pmatrix}. \tag{5.98}$$

Suppose the system is initially prepared in the state $|E_2\rangle$. At a given time t_0, the energy levels cross

$$E_1(t_0) = E_2(t_0). \tag{5.99}$$

At this point, a transition $\psi_2 \to \psi_1$ becomes possible.

Now consider adding a perturbation $V(t)$ to the system, such that the full Hamiltonian becomes $H(t) = H_0(t) + V(t)$. This perturbation prevents an exact level crossing, transforming it into an *avoided crossing*. The system, initially in ψ_2 with energy E_2, ends up in a superposition

$$\psi(t \to \infty) = \alpha\psi_1 + \beta\psi_2,$$

with transition probability $P = |\alpha|^2$ and survival probability $|\beta|^2$, subject to normalization: $|\alpha|^2 + |\beta|^2 = 1$.

The full time-dependent Hamiltonian is then

$$H(t) = \begin{pmatrix} \varepsilon_1(t) & \varepsilon_{12}(t) \\ \varepsilon_{12}(t) & \varepsilon_2(t) \end{pmatrix}, \tag{5.100}$$

and the evolution is governed by the Schrödinger equation

$$i\frac{\mathrm{d}}{\mathrm{d}t}\begin{pmatrix} \psi_1(t) \\ \psi_2(t) \end{pmatrix} = H(t)\begin{pmatrix} \psi_1(t) \\ \psi_2(t) \end{pmatrix}. \tag{5.101}$$

This is formally equivalent to eq. (5.96). Following Zener [172], it is convenient to define

$$\Psi_1(t) = e^{-i\int \varepsilon_1(t)\mathrm{d}t}\psi_1(t), \qquad \Psi_2(t) = e^{-i\int \varepsilon_2(t)\mathrm{d}t}\psi_2(t). \tag{5.102}$$

This redefinition only introduces a global phase and does not affect transition probabilities. The transformed system reads:

$$i\frac{\mathrm{d}}{\mathrm{d}t}\begin{pmatrix} \Psi_1(t) \\ \Psi_2(t) \end{pmatrix} = H(t)\begin{pmatrix} \Psi_1(t) \\ \Psi_2(t) \end{pmatrix}, \tag{5.103}$$

which gives

$$\begin{cases} i\dot{\psi}_1(t) = \varepsilon_{12}(t)\psi_2(t)e^{-i\int \Delta\varepsilon(t)\mathrm{d}t}, \\ i\dot{\psi}_2(t) = \varepsilon_{12}(t)\psi_1(t)e^{+i\int \Delta\varepsilon(t)\mathrm{d}t}, \end{cases} \tag{5.104}$$

with $\Delta\varepsilon(t) = \varepsilon_2(t) - \varepsilon_1(t)$. Differentiating again and substituting yields the second-order equation

$$\ddot{\psi}_1 + \left[i\Delta\varepsilon - \frac{\dot{\varepsilon}_{12}}{\varepsilon_{12}}\right]\dot{\psi}_1 + \varepsilon_{12}^2\psi_1 = 0. \tag{5.105}$$

This equation is exact but difficult to solve. The **Landau-Zener approximation** introduces two simplifications

1. **Linear crossing:** near t_0, the energy difference is approximated as linear

$$\Delta\varepsilon(t) \approx \varepsilon_0\frac{t}{t_0}.$$

2. **Slow coupling variation:** ε_{12} varies slowly compared to $\Delta\varepsilon(t)$ and is treated as constant.

With these assumptions, eq. (5.105) reduces to Weber's equation

$$\frac{\mathrm{d}^2\Psi_1}{\mathrm{d}w^2} + \left(1 - \frac{1}{2n} - \frac{w^2}{4n^2}\right)\Psi_1 = 0, \tag{5.106}$$

with the definitions

$$\Psi_1 = e^{\frac{i}{2}\int \Delta\varepsilon \mathrm{d}t}\psi_1, \quad w = \sqrt{\frac{\varepsilon_0}{t_0}}t, \quad \gamma = \frac{\varepsilon_{12}^2}{\left|\frac{\mathrm{d}}{\mathrm{d}t}\Delta\varepsilon\right|}, \quad n = i\gamma. \tag{5.107}$$

Assuming initial conditions

$$\psi_1(-\infty) = 0, \qquad |\psi_2(-\infty)|^2 = 1, \tag{5.108}$$

the solution is expressed in terms of parabolic cylinder functions:

$$\Psi_1(w) = \sqrt{\gamma}e^{-\frac{\pi}{4}\gamma}\mathcal{D}_{-1-n}\left(\frac{iw}{\sqrt{n}}\right). \tag{5.109}$$

The Landau-Zener transition probability is then

$$P_{\psi_2\to\psi_1} = \lim_{w\to+\infty}|\Psi_1(w)|^2 = 1 - e^{-2\pi\gamma}. \tag{5.110}$$

5.3.2 Solving the photon-to-axion system

This formalism is now applied to the photon-to-axion system in eq. (5.96), using the redefinition

$$\begin{pmatrix} A_\parallel(z) \\ a(z) \end{pmatrix} = \begin{pmatrix} e^{-i\int_{z_i}^{z}\Delta_\parallel(z')\mathrm{d}z'}\tilde{A}_\parallel(z) \\ e^{-i\int_{z_i}^{z}\Delta_a\,\mathrm{d}z'}\tilde{a}(z) \end{pmatrix}. \tag{5.111}$$

This yields to

$$\begin{cases} iA_\parallel'(z) = \Delta_{\gamma a}(z)\,a(z)\,e^{-i\int_{z_i}^{z}(\Delta_a-\Delta_\parallel(z'))\mathrm{d}z'}, \\ ia'(z) = \Delta_{\gamma a}(z)\,A_\parallel(z)\,e^{+i\int_{z_i}^{z}(\Delta_a-\Delta_\parallel(z'))\mathrm{d}z'}. \end{cases} \tag{5.112}$$

Defining $\Delta\varepsilon(z) = \Delta_a - \Delta_\parallel(z)$, and using prime notation to denote z-derivatives, a second-order ODE for $A_\parallel(z)$ is derived

$$\boxed{A_\parallel''(z) + \left[i(\Delta_a - \Delta_\parallel(z)) - \frac{\Delta_{\gamma a}'}{\Delta_{\gamma a}}\right]A_\parallel'(z) + \Delta_{\gamma a}^2(z)A_\parallel(z) = 0.} \tag{5.113}$$

Alternatively, working with $a(z)$, one finds

$$\boxed{a''(z) + \left[i(\Delta_\parallel(z) - \Delta_a) - \frac{\Delta_{\gamma a}'(z)}{\Delta_{\gamma a}(z)}\right]a'(z) + \Delta_{\gamma a}^2(z)a(z) = 0.} \tag{5.114}$$

With initial conditions

$$\begin{cases} A_\parallel(z_i) = 1, \\ a(z_i) = 0, \\ a'(z_i) = -i\Delta_{\gamma a}(z_i). \end{cases} \tag{5.115}$$

Equations eqs. (5.113) and (5.114) are the **master equations** governing photon-to-axion conversion. They are equivalent and can be used interchangeably. Importantly, they are derived without any approximation.

5.4 Approaches to the master equation

In this section, various approaches to solving the master equation in eq. (5.114) (or equivalently eq. (5.113)) are discussed.

5.4.1 Constant magnetic field and electron density

In this case, both the transverse magnetic field and the electron number density are constant: $B_T(z) = B_T$ and $n_e(z) = n_e$. This reduces the problem to the constant-coefficient case studied analytically in section 5.2.3.

The master equation in eq. (5.114) becomes

$$a''(z) + i(\Delta_\parallel - \Delta_a)a'(z) + \Delta_{a\gamma}^2 a(z) = 0, \tag{5.116}$$

where all the Δ parameters are constant. The initial conditions are given in eq. (5.115).

The solution to this equation is given in eq. (5.87), and the corresponding probability is provided in eq. (5.94).

5.4.2 Complete Landau-Zener approach

In the general case governed by the master equation in eq. (5.105), it was shown that, under the Landau-Zener approximation, an analytic expression for the transition probability can be derived, known as the Landau-Zener formula in eq. (5.110).

In this specific case, the two simplifying assumptions of the Landau-Zener approximation are

1. **Simplification 1:** The resonance at z_0 occurs over a short enough interval such that the energy gap
$$\Delta\varepsilon(z) = \Delta_a - \Delta_\parallel(z) \tag{5.117}$$
can be approximated as linear
$$\Delta\varepsilon(z) \sim \Delta_0 \frac{z}{z_0}. \tag{5.118}$$
Since $\Delta_\parallel(z) \sim m_\gamma^2(z) \sim n_e(z)$, this implies a linear electron density
$$n_e(z) \sim n_e(z_0)\frac{z}{z_0}. \tag{5.119}$$

2. **Simplification 2:** The photon-axion coupling term $\Delta_{\gamma a}(z)$ varies slowly compared to $\Delta\varepsilon(z)$, so it can be approximated as constant
$$\Delta'_{\gamma a}(z) \simeq 0 \quad \Longleftrightarrow \quad \Delta_{\gamma a} \sim \text{const.} \tag{5.120}$$
That is,
$$B_T = \text{const.} \tag{5.121}$$

Under these assumptions, the master equation becomes

$$a''(z) + i(\Delta_\parallel(z) - \Delta_a)a'(z) + \Delta_{a\gamma}^2 a(z) = 0, \tag{5.122}$$

where $\Delta_{a\gamma}^2$ is constant and $\Delta_\parallel(z)$ is linear. The initial conditions remain those in eq. (5.115).

A known issue is that the original Landau-Zener formula assumes asymptotic boundary conditions. Nevertheless, if it is assumed that the initial and final conditions effectively approximate asymptotic behavior, the Landau-Zener formula for the $\gamma \to a$ transition can be adopted:

$$P_{\gamma\to a} = 1 - e^{-2\pi\gamma}, \quad \text{with} \quad \gamma = \frac{\Delta_{a\gamma}^2}{\left|\frac{\mathrm{d}\Delta_\parallel(z)}{\mathrm{d}z}\right|}. \tag{5.123}$$

In most realistic cases, $\gamma \ll 1$ is expected, so the exponential can be Taylor-expanded to first order:

$$P \simeq 2\pi\gamma. \tag{5.124}$$

This can be recast in a more convenient form widely used in cosmology and astroparticle physics, [169, 171].

Recall that:

$$\frac{\mathrm{d}\Delta_\parallel}{\mathrm{d}z} = -\frac{1}{2\omega}\frac{4\pi\alpha}{m_e}\frac{\mathrm{d}n_e(z)}{\mathrm{d}z} = -\frac{1}{2\omega}\frac{\mathrm{d}m_\gamma^2(z)}{\mathrm{d}z}. \tag{5.125}$$

At resonance, $\Delta_\parallel(z_{\mathrm{res}}) = \Delta_a$ is imposed, and for simplicity $z_{\mathrm{res}} = 0$ can be set. This leads to

$$\Delta_\varepsilon(z_{\mathrm{res}}) = 0 \quad \Rightarrow \quad n_e(z_{\mathrm{res}}) = \frac{m_a^2 m_e}{4\pi\alpha}. \tag{5.126}$$

Substituting into the formula for γ and the probability

$$\begin{aligned} P_{\gamma\to a} &= \frac{2\pi\,\frac{g_{a\gamma\gamma}^2}{4}B_T^2}{\frac{1}{2\omega}\frac{\mathrm{d}m_\gamma^2}{\mathrm{d}z}} = \frac{2\pi\,\frac{g_{a\gamma\gamma}^2}{4}B_T^2}{\frac{1}{2\omega}m_\gamma^2(z_{\mathrm{res}})\left|\frac{\mathrm{d}\ln m_\gamma^2}{\mathrm{d}z}\right|_{z_{\mathrm{res}}}} \\ &= \frac{2\pi\,\frac{g_{a\gamma\gamma}^2}{4}B_T^2}{\frac{1}{2\omega}\frac{4\pi\alpha}{m_e}n_e(z_{\mathrm{res}})}\left|\frac{\mathrm{d}\ln m_\gamma^2}{\mathrm{d}z}\right|_{z_{\mathrm{res}}}^{-1} \\ &= \frac{2\pi\,\frac{g_{a\gamma\gamma}^2}{4}B_T^2}{\frac{1}{2\omega}\frac{4\pi\alpha}{m_e}\cdot\frac{m_a^2 m_e}{4\pi\alpha}}\left|\frac{\mathrm{d}\ln m_\gamma^2}{\mathrm{d}z}\right|_{z_{\mathrm{res}}}^{-1}. \end{aligned}$$

$$\Downarrow$$

$$P_{\gamma\to a}^{\mathrm{res}} \sim \frac{\omega\pi g_{a\gamma\gamma}^2 B_T^2}{m_a^2}\left|\frac{\mathrm{d}\ln m_\gamma^2}{\mathrm{d}z}\right|_{z_{\mathrm{res}}}^{-1}. \tag{5.127}$$

This is the most widely used expression for resonant photon-to-axion conversion in the cosmology and astroparticle physics literature. While this specific form appears in [169, 170] for axion conversion, a similar structure arises in photon-to-massive dark photon oscillations [171].

5.5 Interference and phase terms for multiple level crossings

In [179], a novel method for treating the Landau-Zener approximation is introduced. This approach not only recovers the standard Landau-Zener transition probability but also accounts for possible interference effects between the two states $|\gamma\rangle$ and $|a\rangle$. The computation starts from the standard perturbed two-level Hamiltonian

$$H = H_0 + H_1 = \begin{pmatrix} \Delta_\parallel(z) & \Delta_{\gamma a}(z) \\ \Delta_{\gamma a}(z) & \Delta_a \end{pmatrix} = \begin{pmatrix} \Delta_\parallel(z) & 0 \\ 0 & \Delta_a \end{pmatrix} + \begin{pmatrix} 0 & \Delta_{\gamma a}(z) \\ \Delta_{\gamma a}(z) & 0 \end{pmatrix}, \tag{5.128}$$

where H_1 is treated as a perturbation. Since $\Delta_{a\gamma} \ll \Delta_\parallel, \Delta_a$, and thus $H_1 \ll H_0$, perturbation theory is applicable.

The analysis proceeds in the interaction picture, where the evolution equation becomes

$$H_{\mathrm{int}}\begin{pmatrix} A \\ a \end{pmatrix} = i\frac{\mathrm{d}}{\mathrm{d}z}\begin{pmatrix} A_{\mathrm{int}} \\ a_{\mathrm{int}} \end{pmatrix}, \tag{5.129}$$

with the field redefinition

$$\begin{pmatrix} A_{\mathrm{int}} \\ a_{\mathrm{int}} \end{pmatrix} = \mathcal{U}^\dagger(z)\begin{pmatrix} A \\ a \end{pmatrix}, \tag{5.130}$$

and the interaction Hamiltonian defined by

$$H_{\rm int} = \mathcal{U}^\dagger(z) H_1 \mathcal{U}(z), \quad \mathcal{U}(z) = e^{-i\int_{z_i}^z \mathrm{d}z'\, H_0(z')}. \tag{5.131}$$

This is equivalent to the phase redefinitions performed in the works of Zener and Carenza–Marsh [173, 172], eqs. (5.102) and (5.111).

The initial condition is set by

$$\begin{pmatrix} A_i \\ a_i \end{pmatrix} = \mathcal{U}(z_i) \begin{pmatrix} A_{{\rm int},i} \\ a_{{\rm int},i} \end{pmatrix} = \begin{pmatrix} A_{{\rm int},i} \\ a_{{\rm int},i} \end{pmatrix}, \tag{5.132}$$

where $\mathcal{U}(z_i) = \mathbb{1}$ is assumed for simplicity.

The time evolution in the interaction picture is then governed by

$$\mathcal{U}_{\rm int} = e^{-i\int_{z_i}^z \mathrm{d}z'\, H_{\rm int}(z')}, \tag{5.133}$$

so the state evolves as

$$\begin{pmatrix} A_{\rm int}(z) \\ a_{\rm int}(z) \end{pmatrix} = \mathcal{U}_{\rm int} \begin{pmatrix} A(z_i) \\ a(z_i) \end{pmatrix}. \tag{5.134}$$

Switching back to the Schrödinger picture

$$\begin{pmatrix} A \\ a \end{pmatrix} = \mathcal{U}(z) \begin{pmatrix} A_{\rm int} \\ a_{\rm int} \end{pmatrix}, \tag{5.135}$$

one arrives at:

$$\begin{pmatrix} A(z) \\ a(z) \end{pmatrix} = e^{-i\int_{z_i}^z \mathrm{d}z'\, H_0(z')} e^{-i\int_{z_i}^z \mathrm{d}z'\, H_{\rm int}(z')} \begin{pmatrix} A(z_i) \\ a(z_i) \end{pmatrix}. \tag{5.136}$$

Using the Baker–Campbell–Hausdorff formula and assuming first-order perturbation in $\Delta_{a\gamma}$, the interaction Hamiltonian becomes

$$H_{\rm int}(z) = \Delta_{a\gamma}(z) \begin{pmatrix} 0 & e^{i\Phi(z)} \\ e^{-i\Phi(z)} & 0 \end{pmatrix}, \tag{5.137}$$

where the phase is defined as

$$\Phi(z) = \int_{z_i}^z \mathrm{d}z'\, [\Delta_a - \Delta_\parallel(z')]. \tag{5.138}$$

This leads to

$$\begin{pmatrix} A(z) \\ a(z) \end{pmatrix} = \begin{pmatrix} 1 & -ic_+ \\ ic_- e^{i\Phi(z)} & e^{i\Phi(z)} \end{pmatrix} \begin{pmatrix} A(z_i) \\ a(z_i) \end{pmatrix} + \mathcal{O}(\Delta_{a\gamma}^2), \tag{5.139}$$

where:

$$c_\pm = \int_{z_i}^z \mathrm{d}z'\, \Delta_{a\gamma}(z') e^{\pm i\Phi(z')}. \tag{5.140}$$

From this, the transition probability is directly extracted from the modulus square of the off-diagonal term

$$\boxed{P_{\gamma\to a} = \left| \int_{z_i}^z \mathrm{d}z'\, \Delta_{a\gamma}(z') e^{i\Phi(z')} \right|^2 + \mathcal{O}(\Delta_{a\gamma}^2).} \tag{5.141}$$

This is an exact result, obtained without any approximations.

If there is only a single resonance point, then applying the Landau-Zener approximation yields

$$P_{\gamma\to a} \simeq 2\pi\gamma. \tag{5.142}$$

However, if multiple resonance points are present, the total probability is not simply the sum of the individual Landau-Zener probabilities

$$P_{\gamma \to a} \not\simeq \sum_n 2\pi\gamma_n. \tag{5.143}$$

This discrepancy arises due to interference between wave packets, which can either enhance or suppress the transition probability (constructive or destructive interference).

The resonance points correspond to stationary points of the phase $\Phi(z)$, satisfying $\Phi'(z_n) = 0$, i.e., where $\Delta_\parallel(z_n) = \Delta_a$.

To evaluate eq. (5.141), the **stationary phase approximation** is used, expanding

$$\Phi(z') \approx \Phi(z_n) + \frac{1}{2}\Phi''(z_n)(z' - z_n)^2, \tag{5.144}$$

$$\Delta_{a\gamma}(z') \approx \Delta_{a\gamma}(z_n). \tag{5.145}$$

This gives:

$$P_{\gamma \to a} = \left| \int \mathrm{d}z'\, \Delta_{a\gamma}(z_n) e^{i\Phi(z_n) + \frac{i}{2}\Phi''(z_n)(z'-z_n)^2} \right|^2 \tag{5.146}$$

$$= \left| \Delta_{a\gamma} e^{i\Phi(z_n)} \int \mathrm{d}z'\, e^{\frac{i}{2}\Phi''(z_n)(z'-z_n)^2} \right|^2. \tag{5.147}$$

The integral is a Fresnel-type Gaussian

$$\int_{\mathbb{R}} e^{\frac{i}{2}cx^2} \mathrm{d}x = \sqrt{\frac{2\pi i}{c}} = \sqrt{\frac{2\pi}{|c|}} e^{i\frac{\pi}{4}\,\mathrm{sgn}(c)}. \tag{5.148}$$

Thus, the probability becomes

$$P_{\gamma \to a} = \left| \Delta_{a\gamma} \sqrt{\frac{2\pi}{|\Phi''(z_n)|}} e^{i\Phi(z_n) + i\frac{\pi}{4}\,\mathrm{sgn}(\Phi''(z_n))} \right|^2. \tag{5.149}$$

Defining

$$\gamma_n = \frac{\Delta_{a\gamma}^2(z_n)}{|\Phi''(z_n)|}, \quad A_n = 2\pi\gamma_n, \tag{5.150}$$

one recovers

$$P_{\gamma \to a} = 2\pi\gamma_n, \tag{5.151}$$

in the single-resonance case.

In the case of two resonance points z_1 and z_2, one finds

$$P_{\gamma \to a} = \left| \sum_{n=1}^{2} \sqrt{2\pi\gamma_n} e^{i\Phi(z_n) + i\frac{\pi}{4}\,\mathrm{sgn}(\Phi''(z_n))} \right|^2 \tag{5.152}$$

$$= 2\pi(\gamma_1 + \gamma_2) + 2\sqrt{(2\pi\gamma_1)(2\pi\gamma_2)}\cos(\Phi_{12}), \tag{5.153}$$

where:

$$\Phi_{12} = \Phi(z_1) - \Phi(z_2) + \frac{\pi}{4}\left[\mathrm{sgn}(\Phi''(z_1)) - \mathrm{sgn}(\Phi''(z_2))\right]. \tag{5.154}$$

Therefore, in general, the total transition probability is not additive.

In the general case of N resonance points

$$P_{\gamma \to a} = \left| \sum_n \sqrt{2\pi\gamma_n} e^{i\Phi(z_n) + i\frac{\pi}{4}\,\mathrm{sgn}(\Phi''(z_n))} \right|^2 = \sum_n 2\pi\gamma_n + 2\sum_{n<m}\sqrt{4\pi^2\gamma_n\gamma_m}\cos(\Phi_{nm}). \tag{5.155}$$

5.6 Photon-to-dark photon conversion

Up to this point, the focus has been on photon-to-axion conversion. However, the same formalism can be extended to describe the conversion of photons into massive **dark photons**. These are hypothetical massive spin-1 particles that arise naturally in extensions of the Standard Model featuring a hidden sector with an additional abelian $U(1)$ gauge symmetry. The associated gauge boson—the dark photon—can mix kinetically with the ordinary photon, providing a portal between the dark sector and visible matter [180].

Dark photons are well-motivated candidates for physics beyond the Standard Model. Kinetic mixing with ordinary photons offers a non-gravitational window into dark matter interactions, such particles emerge ubiquitously in grand unified theories and string theory constructions, and massive dark photons can themselves constitute dark matter through various production mechanisms [180, 181].

In this context, the relevant Lagrangian is given by [171]

$$\mathscr{L} = -\frac{1}{4}F_{\mu\nu}F^{\mu\nu} - \frac{1}{4}F'_{\mu\nu}F'^{\mu\nu} - \frac{m_{\mathcal{A}}^2}{2}\mathcal{A}_\mu\mathcal{A}^\mu - \frac{\varepsilon}{2}F_{\mu\nu}F'^{\mu\nu}, \tag{5.156}$$

where $\mathcal{A}_\mu$ denotes the dark photon field, and ε is the kinetic mixing parameter.

Unlike the axion case, where the interaction is mediated by an external magnetic field through a Chern-Simons-like term, the coupling here is direct via the kinetic mixing term $\frac{\varepsilon}{2}F_{\mu\nu}F'^{\mu\nu}$. Therefore, an external magnetic field is not required to trigger the transition.

By deriving the equations of motion, one finds that the dynamics of the photon–dark photon system are governed by a Schrödinger-like equation structurally analogous to the axion case

$$i\frac{\mathrm{d}}{\mathrm{d}z}\begin{pmatrix} A(z) \\ \mathcal{A}(z) \end{pmatrix} = \begin{pmatrix} \Delta(z) & \varepsilon\Delta_{\mathcal{A}} \\ \varepsilon\Delta_{\mathcal{A}} & \Delta_{\mathcal{A}} \end{pmatrix}\begin{pmatrix} A(z) \\ \mathcal{A}(z) \end{pmatrix}, \tag{5.157}$$

where

$$\Delta = \Delta_\parallel = -\frac{m_{\mathrm{eff}}^2}{2\omega}, \qquad \Delta_{\mathcal{A}} = -\frac{m_{\mathcal{A}}^2}{2\omega}. \tag{5.158}$$

As a result, the equations governing dark photon dynamics can be obtained directly from those of the axion case via the substitution

$$\Delta_{a\gamma} \quad \longrightarrow \quad \varepsilon\Delta_{\mathcal{A}}. \tag{5.159}$$

For instance, within the Landau-Zener framework, the adiabaticity parameter γ for photon-to-axion conversion is

$$\gamma_{\gamma\to a} = \frac{\Delta_{a\gamma}^2}{\left|\frac{\mathrm{d}\Delta_\parallel}{\mathrm{d}z}\right|}, \tag{5.160}$$

which becomes, in the dark photon case

$$\gamma_{\gamma\to\mathcal{A}} = \frac{\varepsilon^2\Delta_{\mathcal{A}}^2}{\left|\frac{\mathrm{d}\Delta}{\mathrm{d}z}\right|}. \tag{5.161}$$

This correspondence allows the full machinery developed for photon–axion mixing—including exact solutions, approximations, and numerical methods—to be applied directly to the case of dark photon production.

5.7 Numerical approach

Solving the exact master equation analytically, without any approximation, is extremely difficult—if not impossible. However, a numerical approach can be developed. Obtaining numerical results is crucial, as it allows the incorporation of any functional form of $B_T(z)$ and $n_e(z)$, and from the solution, the corresponding probability can be extracted.

5.7.1 Numerical approach in the case of Landau-Zener approximation

In the Landau-Zener approximation, the key parameter is the factor γ. In this context, Carenza and Marsh [173] used a reparametrization involving a phase of the state and expressed the master equation in units of $\Delta_{a\gamma}$. Starting from the master equation in eq. (5.122), the following quantity can be defined

$$u(z) = e^{\frac{i}{2}\int_{z_i}^{z} \mathrm{d}z'(\Delta_\parallel - \Delta_a)} a(z), \tag{5.162}$$

and, under the Landau-Zener approximation, one can write (cf. eq. (5.117))

$$\Delta_\parallel - \Delta_a = \Delta\varepsilon = \frac{\Delta_0}{z_0} z = \frac{\Delta_{a\gamma}^2}{\gamma} z, \tag{5.163}$$

This allows expressing $a''(z)$, $a'(z)$, and $a(z)$ in terms of $u''(z)$, $u'(z)$, $u(z)$, and γ, and rewriting the master equation accordingly. Defining the dimensionless quantity

$$\tilde{z} = \Delta_{a\gamma} z, \tag{5.164}$$

after a straightforward (albeit algebraically intensive) derivation, one arrives at

$$u''(\tilde{z}) + \left(1 + \frac{1}{2n} - \frac{\tilde{z}^2}{(2n)^2}\right) u(\tilde{z}) = 0, \tag{5.165}$$

where

$$n = i\gamma \tag{5.166}$$

and the initial condition is

$$u'(\tilde{z}_i) = -i. \tag{5.167}$$

In this formulation, the entire equation is expressed in terms of γ. This is the equation used by Carenza and Marsh, and is referred to as the **Carenza and Marsh equation**.

It is also possible, specifically within the Landau-Zener approximation, to work with the master equation expressed in terms of γ without redefining the field $a \to u$. This can be done as follows: starting from eq. (5.163) (valid only under the Landau-Zener approximation), this is substituted into the master equation in eq. (5.122) to obtain

$$a''(z) + \left[i \frac{\Delta_{a\gamma}^2}{\gamma} z \right] a'(z) + \Delta_{a\gamma}^2 a = 0. \tag{5.168}$$

To relate this equation to the one by Carenza and Marsh, one switches to $\tilde{z} = \Delta_{a\gamma} z$

$$\frac{\mathrm{d}^2 a(z)}{\mathrm{d}\tilde{z}^2} \Delta_{a\gamma}^2 + i \frac{\Delta_{a\gamma}^2}{\gamma} z \Delta_{a\gamma} \frac{\mathrm{d}a(z)}{\mathrm{d}\tilde{z}} + \Delta_{a\gamma}^2 a(z) = 0, \tag{5.169}$$

which simplifies to

$$\frac{\mathrm{d}^2 a(z)}{\mathrm{d}\tilde{z}^2} + \frac{i}{\gamma} \tilde{z} \frac{\mathrm{d}a(z)}{\mathrm{d}\tilde{z}} + a(z) = 0, \tag{5.170}$$

where the initial condition is

$$\left.\frac{\mathrm{d}a(z)}{\mathrm{d}z}\right|_{z_i} = \left.\frac{\mathrm{d}a(z)}{\mathrm{d}\tilde{z}}\right|_{\tilde{z}_i} \Delta_{a\gamma} = -i\Delta_{a\gamma},$$

hence:

$$a'(\tilde{z}_i) = \left.\frac{\mathrm{d}a(z)}{\mathrm{d}\tilde{z}}\right|_{\tilde{z}_i} = -i. \tag{5.171}$$

5.7.2 Numerical approach in the general case

The equations above assume a linear form of $n_e(z)$ and do not account for possible changes in its slope, even if γ remains unchanged. For instance, $n_e(z)$ could increase linearly up to a certain point and then decrease linearly with the same magnitude but opposite sign. Since γ depends on the absolute value of the slope of $n_e(z)$—i.e., the absolute derivative of $\Delta_\parallel$ with respect to z—γ remains constant in this case. However, both the Carenza and Marsh equation and the previous formulation fail to capture this change in the behavior of $n_e(z)$.

Moreover, interest lies in solving the equation in a more general case where γ is not constant, while the Landau-Zener approximation still holds at first order.

Starting from the master equation, the dimensionless variable is defined as

$$\tilde{z} = \Delta_{a\gamma} z, \tag{5.172}$$

and using $\mathrm{d}\tilde{z} = \Delta_{a\gamma}\mathrm{d}z$, one obtains

$$\frac{\mathrm{d}^2 a(\tilde{z})}{\mathrm{d}\tilde{z}^2} + i\frac{\Delta_\parallel(\tilde{z}) - \Delta_a}{\Delta_{a\gamma}(\tilde{z})}\frac{\mathrm{d}a(\tilde{z})}{\mathrm{d}\tilde{z}} + a = 0, \tag{5.173}$$

with the initial condition

$$\left.\frac{\mathrm{d}a}{\mathrm{d}\tilde{z}}\right|_{\tilde{z}_i} = a'(\tilde{z}_i) = -i. \tag{5.174}$$

By defining

$$f \equiv \frac{\mathrm{d}a}{\mathrm{d}\tilde{z}}, \tag{5.175}$$

the equation becomes

$$f'(\tilde{z}) + i\frac{\Delta_\parallel(\tilde{z}) - \Delta_a}{\Delta_{a\gamma}(\tilde{z})} f(\tilde{z}) + a = 0, \tag{5.176}$$

and the initial conditions $a(z_i) = 0$ and $a'(z_i) = -i\Delta_{a\gamma}$ become

$$\text{Initial conditions}: \begin{cases} a(\tilde{z}_i) = 0 \\ f(\tilde{z}_i) = -i \end{cases}. \tag{5.177}$$

Naturally, if the equation is solved numerically using a dimensionless quantity z_A, and $1\,\mathrm{Mpc} = 1.564 \times 10^{29}\,\mathrm{eV}^{-1}$ is expressed, with $z = \mathrm{Mpc} \times z_A$, this must be accounted for when restoring physical units

$$z_{\text{physical}} = \frac{\tilde{z}}{\Delta_{a\gamma} \times \mathrm{Mpc}}. \tag{5.178}$$

Working with $\tilde{z}$ leads to the definition of γ with respect to it:

$$\gamma = \frac{\Delta_{a\gamma}(\tilde{z})}{\left|\frac{\mathrm{d}\Delta_\parallel(\tilde{z})}{\mathrm{d}\tilde{z}}\right|}. \tag{5.179}$$

5.7.3 Halo model

The trajectory of a photon passing through a spherical halo can be represented by a single parameter r_{min}. Given the electron density as a function of the halo radius, i.e., $n_e(r)$, there exists a certain resonance shell where the value of $n_e(r_{\text{res}})$ is such that $\Delta_\parallel = \Delta_a$. Such a scenario is well described in [171] (cf. fig. 5.4).

As a first test, a well-known halo profile with fixed quantities is employed. The electron number density profile is taken from a Battaglia profile [182], and the relevant parameters are summarized in section 5.7.3.

The radial profile and its projection $n_e(\mathbf{x}(t))$ along the photon trajectory are shown in fig. 5.5.

In fig. 5.6 the obtained probability is shown. The case displayed exhibits an enhancement of the probability after the second resonance point, as described by the two-point interference formula in eq. (5.153).

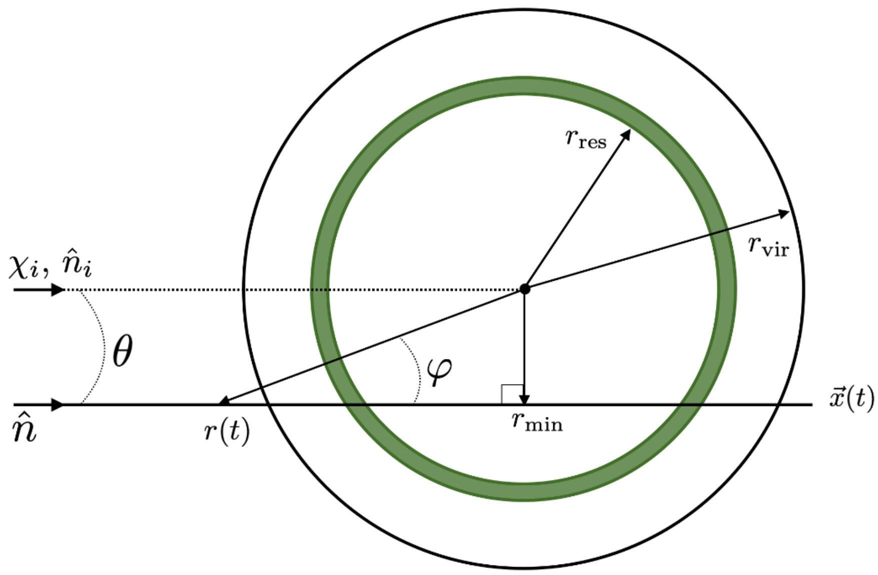

Figure 5.4: The photon trajectory, denoted as $\mathbf{x}(t)$, passes through a dark matter halo centered at the comoving position χ_i and direction $\hat{n}_i$ on the observer's sky and with a total radius defined by $r_{\rm vir}$. The resonant conversion takes place when the photon intersects a spherical shell located at radius $r_{\rm res}$. Since the trajectory passes through the shell twice, each path involves two resonance zones. Figure from [171].

Parameter	**Value**
Axion mass, m_a	$3 \times 10^{-13}\,\mathrm{eV}$
Photon-axion coupling, $g_{a\gamma\gamma}$	$10^{-10}\,\mathrm{GeV}^{-1}$
Transverse magnetic field, $\lvert\mathbf{B}_\perp\rvert$	$1\,\mu\mathrm{G}$
Photon frequency, ν	$145\,\mathrm{GHz}$
Halo mass, M	$10^{13.5}\,M_\odot$
Virial radius, $r_{\rm vir}$	$2\,\mathrm{Mpc}$
Redshift, z	0
Impact parameter	$1.435\,\mathrm{Mpc}$

Table 5.1: Parameters used for the halo model test case using the Battaglia profile.

5.7.4 Global and cut integrations

In the $\tilde{z}$ parametrization, typical halo distances of the order of several Mpc are transformed into extremely large values, and the solution oscillates hundreds of thousands of times between the two points of resonance. This is clean if for instance one compares the scale of the right plot of fig. 5.5 (in z) with that in fig. 5.6 (in $\tilde{z}$). For this reason, the solution over the whole interval becomes computationally expensive, even when using numerical acceleration tools such as `Numba`[7]. At first glance, one might consider further reducing the interval by selecting a smaller one that contains both resonance points. However, despite this reduction, the computational cost remains excessive, making it impractical to analyze (many) multiple trajectories.

Most of the oscillations occur far from the two resonance points, whereas all the relevant physical processes take place near them. Therefore, we can consider a *cut integration*, defining two intervals I_1 and I_2 around the two resonance points, and integrating only over these two regions, while propagating the solution from the endpoint of the first interval to the starting point

[7] `https://numba.pydata.org`

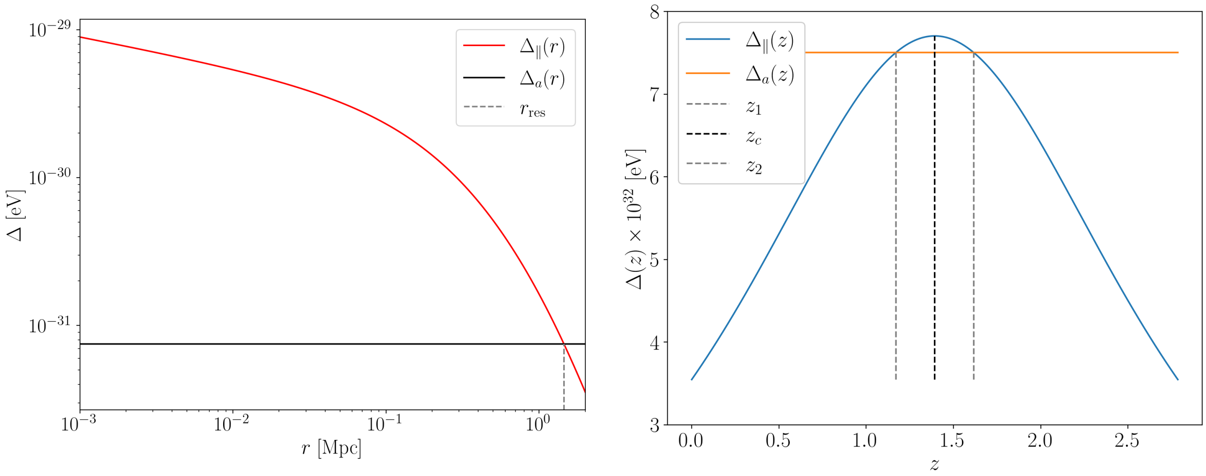

Figure 5.5: Left panel: the radial halo profile converted to $\Delta_\parallel(r)$ and Δ_a. Right panel: the same profile projected along the chosen photon trajectory. The two resonance points z_1 and z_2, together with the critical point z_c, are indicated.

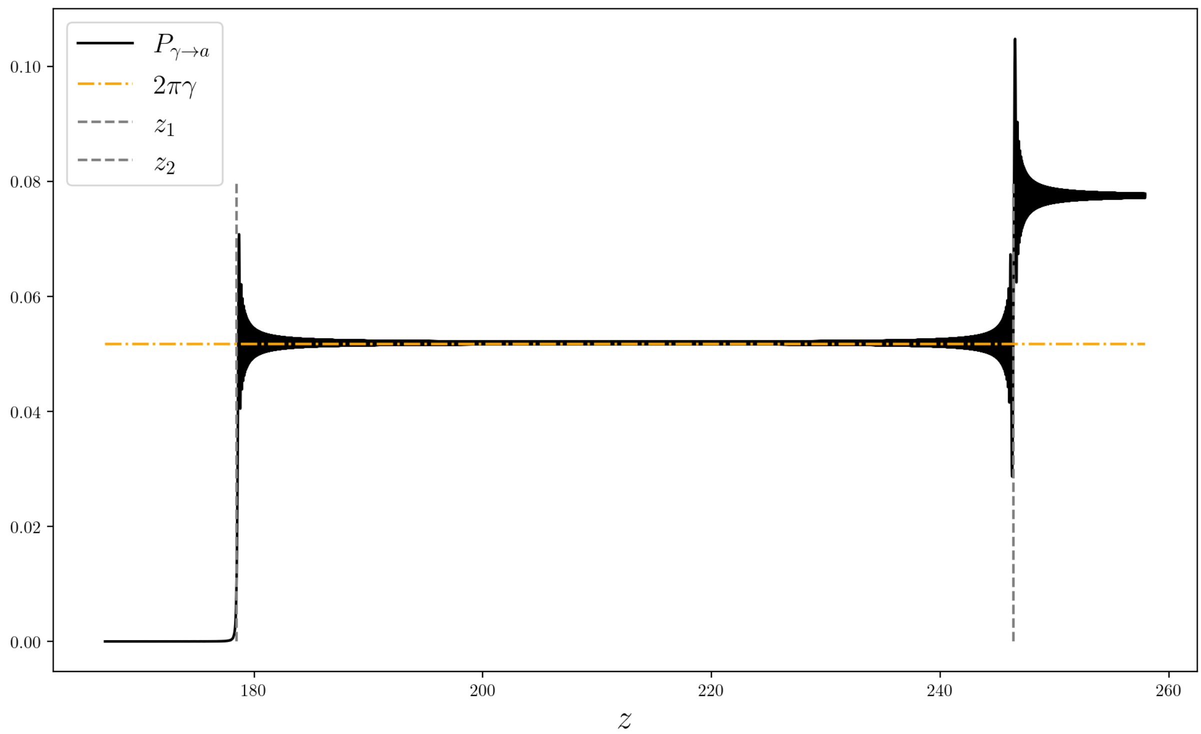

Figure 5.6: Probability as a function of $\tilde{z} = \Delta_{a\gamma} z$ in the case of Battaglia's halo model shown in fig. 5.5. The solution between the first and second resonance points, z_1 and z_2 respectively, is compared to the value $2\pi\gamma$. Since the profile is symmetric along the trajectory, the parameters γ at the resonance points are identical, i.e., $\gamma_1 = \gamma_2 = \gamma$.

of the second. This propagation can be performed by introducing an oscillation wavelength $\lambda_{\rm osc}$ that depends on z,

$$\lambda(z) = \frac{2\pi}{\Delta_\parallel(z) - \Delta_a}, \tag{5.180}$$

and assuming the phase evolves as

$$\frac{d\varphi(z)}{dz} = \frac{2\pi}{\lambda(z)}, \tag{5.181}$$

so that

$$\varphi_{\text{cumulative}}(z) = \int_{z_1^{\max}}^{z} \frac{2\pi}{\lambda(z)} \mathrm{d}z = \int_{z_1^{\max}}^{z} \left[\Delta_{\parallel}(z) - \Delta_a\right] \mathrm{d}z. \tag{5.182}$$

We aim to set the initial conditions (ICs) for the integration over I_2 in such a way as to match the global solution perfectly and correctly capture the interference between the two wave packets $|a\rangle$ and $|\gamma\rangle$. This can be done by starting from $z_1^{\max}$ and defining the point $z_2^{\min}$ as a location after N oscillations. That is, we define $z_2^{\min}$ from $\varphi_{\text{cumulative}}(z)$ such that

$$\varphi_{\text{cumulative}}(z_2^{\min}) = \int_{z_1^{\max}}^{z_2^{\min}} \left[\Delta_{\parallel}(z) - \Delta_a\right] \mathrm{d}z = 2\pi N. \tag{5.183}$$

We adopt the following algorithm to achieve this:

1. Compute $\varphi_{\text{cumulative}}(z)$ over a certain interval I starting from $z_1^{\max}$ and ending before the second point of resonance.
2. Define N. From $\varphi_{\text{cumulative}}$, we can also compute its value over I, and then:

$$\frac{\varphi_{\text{cumulative}}(I)}{2\pi} = \mathcal{N}. \tag{5.184}$$

   This $\mathcal{N}$ is not an integer, $\mathcal{N} \not\in \mathbb{N}$. However, we can define N as the lowest integer near this value.
3. Interpolate the inverse function $(z, \varphi_{\text{cumulative}})$ to obtain $z(\varphi_{\text{cumulative}})$.
4. Set $z_2^{\min} = z(\varphi_{\text{cumulative}} = 2\pi N)$.
5. Set the ICs at $z_2^{\min}$ as

$$\begin{cases} a(z_1^{\max}) = a(z_2^{\min}) \\ \left.\frac{\mathrm{d}a}{\mathrm{d}z}\right|_{z_1^{\max}} = \left.\frac{\mathrm{d}a}{\mathrm{d}z}\right|_{z_2^{\min}} \end{cases}. \tag{5.185}$$

This approach seems to work in *most cases*, but in several others we observe an error at the second resonance point, due to an incorrect setting of the ICs on I_2. The error in the probability of the cut solution with respect to the global integration remains below $\sim 10\%$, but our goal is to achieve high precision.

It is possible to identify that the issue lies in how the ICs on I_2 are set. By inspecting the solutions $|a\rangle$ and $\frac{\mathrm{d}|a\rangle}{\mathrm{d}z}$, one notices that—beyond the expected amplitude modulation $A(z)$—in some cases (such as the one shown) a slope appears in the curves, as shown in fig. 5.8.

Because of this issue, the naive approach of setting $|a\rangle$ and its derivative at the starting point of I_2 equal to their values at the end of I_1, under the assumption that only a phase evolution occurs in between, does not hold.

5.7.5 Cut and WKB implementation

Performing a cut remains an optimal choice, as it allows for reducing the computational time from minutes or hours to just a few seconds[8]. However, a more precise mathematical implementation is needed.

If the ODE is rewritten in an alternative form, valid far from the resonance points—i.e., in the region to be skipped—the Wentzel–Kramers–Brillouin (WKB) approximation holds.

By redefining $|a\rangle$ with a phase, it becomes possible to eliminate the derivative term in the ODE in eq. (5.114), obtaining a Schrödinger-like equation. This is particularly useful because,

[8] All computations have been performed both on a personal laptop (Apple MacBook Air M1, 8-core CPU) and on CINECA HPC facilities (Leonardo cluster).

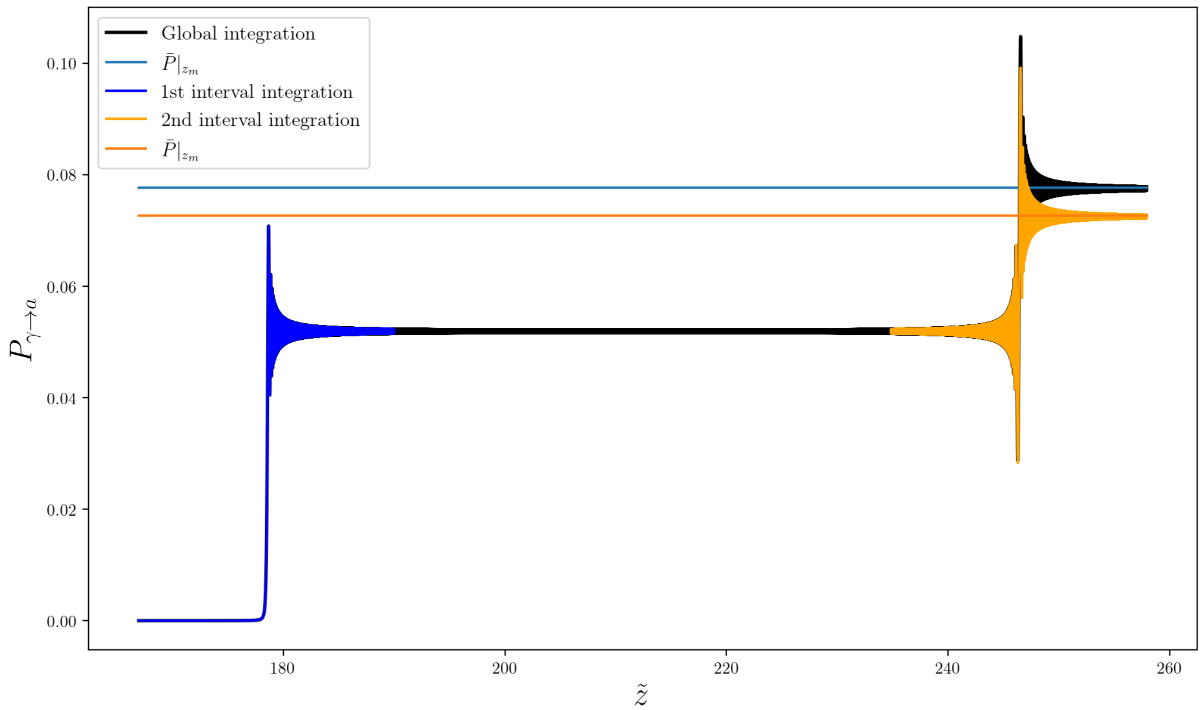

Figure 5.7: Comparison between the global numerical solution and the truncated one obtained in the same identical case as fig. 5.6.

far from resonance, the solution can be expressed analytically using the WKB method. In this way, the solution can be propagated from $z_1^{\max}$ to $z_2^{\min}$ and highly accurate initial conditions on I_2 can be imposed.

The following quantity is defined:

$$u(z) = e^{\frac{i}{2}\Phi(z)}a(z) \quad \Leftrightarrow \quad a(z) = e^{-\frac{i}{2}\Phi(z)}u(z), \tag{5.186}$$

where

$$\Phi(z) = \int_{z_i}^{z} \left[\Delta_\parallel(z) - \Delta_a\right] \,\mathrm{d}z \quad \Leftrightarrow \quad \Phi(\tilde{z}) = \int_{\tilde{z}_i}^{\tilde{z}} \frac{\Delta_\parallel(\tilde{z}) - \Delta_a}{\Delta_{a\gamma}} \,\mathrm{d}\tilde{z}. \tag{5.187}$$

From the expression of $a(z)$, both the first and second derivatives appearing in eq. (5.114) can be computed and the equation rewritten in terms of u. Carrying out the full computation, one arrives at the **master equation in terms of** u:

$$\boxed{u''(z) + \left[1 + \left(\frac{\Phi'(z)}{2}\right)^2 - \frac{i}{2}\Phi''(z)\right] u(z) = 0,} \tag{5.188}$$

which is exactly the desired WKB form, where

$$\Phi'(z) = \frac{\mathrm{d}\Phi}{\mathrm{d}z} = \Delta_\parallel - \Delta_a, \tag{5.189}$$

$$\Phi''(z) = \frac{\mathrm{d}\Phi'}{\mathrm{d}z} = \frac{\mathrm{d}\Delta_\parallel}{\mathrm{d}z}, \tag{5.190}$$

and $\Phi'(\tilde{z})$ and $\Phi''(\tilde{z})$ are obtained by rescaling with $\Delta_{a\gamma}$. *The form of the equation remains identical in the $\tilde{z}$ parametrization.*

In the WKB approximation, starting from the Schrödinger equation

$$\frac{\mathrm{d}^2\Psi(x)}{\mathrm{d}x^2} = \frac{2m}{\hbar^2}\left(V(x) - E\right)\Psi(x), \tag{5.191}$$

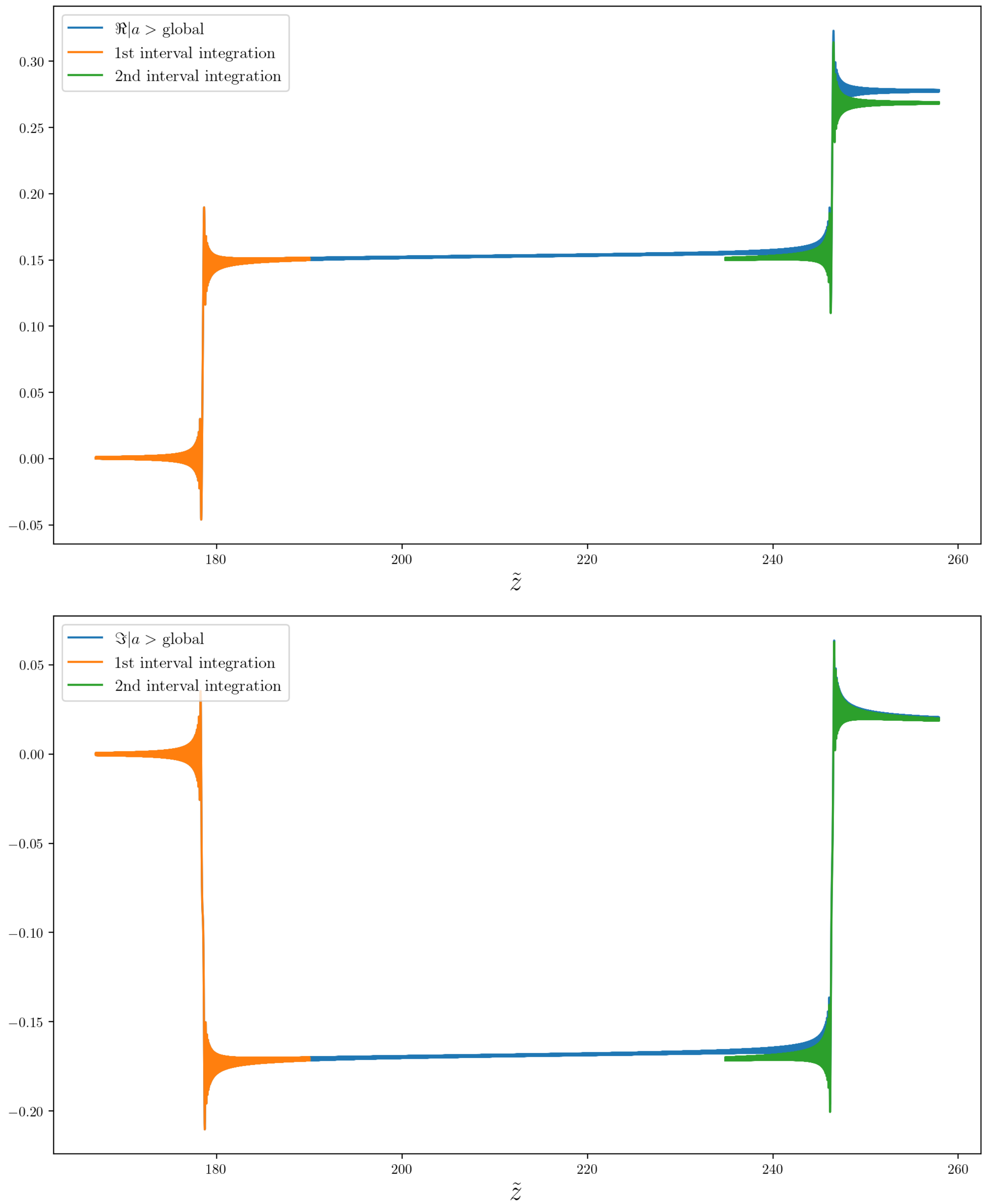

Figure 5.8: Global and cut plots of $\Re\,|a\rangle$ and $\Im\,|a\rangle$. For this solution a slope is evident. The slope presence let the initial condizions eq. (5.185) higly wrong inducing a big error between the global and the cut solutions.

one obtains:

$$\frac{\mathrm{d}^2\Psi(x)}{\mathrm{d}x^2} = \frac{p^2(x)}{\hbar^2}\Psi(x), \tag{5.192}$$

where $p(x) = \sqrt{2m(E - V(x))}$, leading to the following solution:

$$\Psi(x) \simeq \frac{C_+ e^{\frac{i}{\hbar}\int p(x)\mathrm{d}x} + C_- e^{-\frac{i}{\hbar}\int p(x)\mathrm{d}x}}{\sqrt{\frac{|p(x)|}{\hbar}}} = \frac{C_+ e^{\frac{i}{\hbar}\int \sqrt{2m(E-V(x))}\mathrm{d}x} + C_- e^{-\frac{i}{\hbar}\int \sqrt{2m(E-V(x))}\mathrm{d}x}}{\frac{1}{\hbar}[2m|E - V(x)|]^{1/4}}. \tag{5.193}$$

In this case, one has

$$\Omega = \sqrt{1 + \left(\frac{\Phi'(z)}{2}\right)^2 - \frac{i}{2}\Phi''(z)}, \tag{5.194}$$

$$|\Omega| = \left[\left(1 + \frac{\Phi'^2}{4}\right)^2 + \frac{\Phi''^2}{4}\right]^{1/4}, \tag{5.195}$$

so

$$\frac{|p|}{\hbar} = \left[\left(1 + \frac{\Phi'^2}{4}\right) + \frac{\Phi''^2}{4}\right]^{1/4}, \tag{5.196}$$

and therefore, far from the resonance point where the WKB approximation holds, one can write:

$$u_{\mathrm{WKB}}(z) = \frac{C_+ e^{i\int \Omega(z)\,\mathrm{d}z} + C_- e^{-i\int \Omega(z)\,\mathrm{d}z}}{\left[\left(1 + \frac{\Phi'^2}{4}\right) + \frac{\Phi''^2}{4}\right]^{1/8}}. \tag{5.197}$$

Defining $\Xi(z) = \int \Omega(z)\mathrm{d}z$, this can be rewritten in a more manageable form:

$$u_{\mathrm{WKB}}(z) = \frac{C_+ e^{i\Xi(z)} + C_- e^{-i\Xi(z)}}{\sqrt{|\Omega(z)|}}. \tag{5.198}$$

The goal is now to determine $C_\pm$, which can be achieved by integrating over I_1 and matching u_{WKB} at $z_1^{\max}$ with the numerical solution. Once $C_\pm$ are known, u_{WKB} can be propagated to $z_2^{\min}$ to set the initial conditions. To determine $C_\pm$, two equations are needed; the second comes from the derivative u'_{WKB}, which is derived from the expression above.

Recalling that

$$\frac{\mathrm{d}}{\mathrm{d}z}\left(\frac{1}{\sqrt{|\Omega(z)|}}\right) = -\frac{1}{2}\frac{1}{|\Omega(z)|^{3/2}}\frac{\mathrm{d}|\Omega(z)|}{\mathrm{d}z}, \tag{5.199}$$

and that

$$\frac{\mathrm{d}\Xi}{\mathrm{d}z} = \Omega(z), \tag{5.200}$$

one can write

$$u'_{\mathrm{WKB}}(z) = A_+(z)C_+ e^{i\Xi(z)} + A_-(z)C_- e^{-i\Xi(z)}, \tag{5.201}$$

where

$$A_\pm(z) = -\frac{1}{2}\frac{D[|\Omega(z)|]}{|\Omega(z)|^{3/2}} \pm \frac{i\Omega(z)}{|\Omega(z)|^{1/2}}, \tag{5.202}$$

and $D[\cdot]$ denotes the derivative with respect to z. Developing $D[|\Omega(z)|]$, the full form of $A_\pm$ becomes:

$$A_\pm(z) = -\frac{1}{2}\frac{\Re[\Omega(z)]\Re[\Omega'(z)] + \Im[\Omega(z)]\Im[\Omega'(z)]}{|\Omega(z)|^{5/2}} \pm \frac{i\Omega(z)}{|\Omega(z)|^{1/2}}. \tag{5.203}$$

In this case

$$\Omega'(z) = \frac{\Phi'(z)\Phi''(z) - i\Phi'''(z)}{4\sqrt{1 + \left(\frac{\Phi'(z)}{2}\right)^2 - \frac{i}{2}\Phi''(z)}}. \tag{5.204}$$

A convenient choice is to set the lower limit of the integral defining Ξ as $z_0 \equiv z_1^{\max}$, so that $\Xi(z_1^{\max}) = 0$ and the exponentials reduce to unity at $z_1^{\max}$. Therefore, the system of equations to solve for $C_\pm$ is

$$\begin{cases} u_{\text{numeric}}(z_1^{\max}) = \frac{C_+ + C_-}{\sqrt{|\Omega(z_1^{\max})|}} \\ u'_{\text{numeric}}(z_1^{\max}) = C_+ A_+(z_1^{\max}) + C_- A_-(z_1^{\max}) \end{cases} . \tag{5.205}$$

Once $C_\pm$ are determined, $u_{\text{WKB}}(z)$ and $u'_{\text{WKB}}(z)$ can be propagated up to $z_2^{\min}$ and the initial conditions on I_2 can be set as $\text{IC}_{I_2} = [u_{\text{WKB}}(z_2^{\min}), u'_{\text{WKB}}(z_2^{\min})]$. In this way, the cut becomes precise and the two integrations (global vs. cut) agree, as shown in fig. 5.9. Moreover, it is observed that both $\Re[u]$ and $\Im[u]$ do not display any significant slope, as shown in fig. 5.10. By starting from $u(z)$ and transforming back to $a(z)$, the eventual slope observed when working directly with a is recovered, indicating that this slope is physical and arises from the phase factor $e^{-i\Phi(z)/2}$, which depends on z.

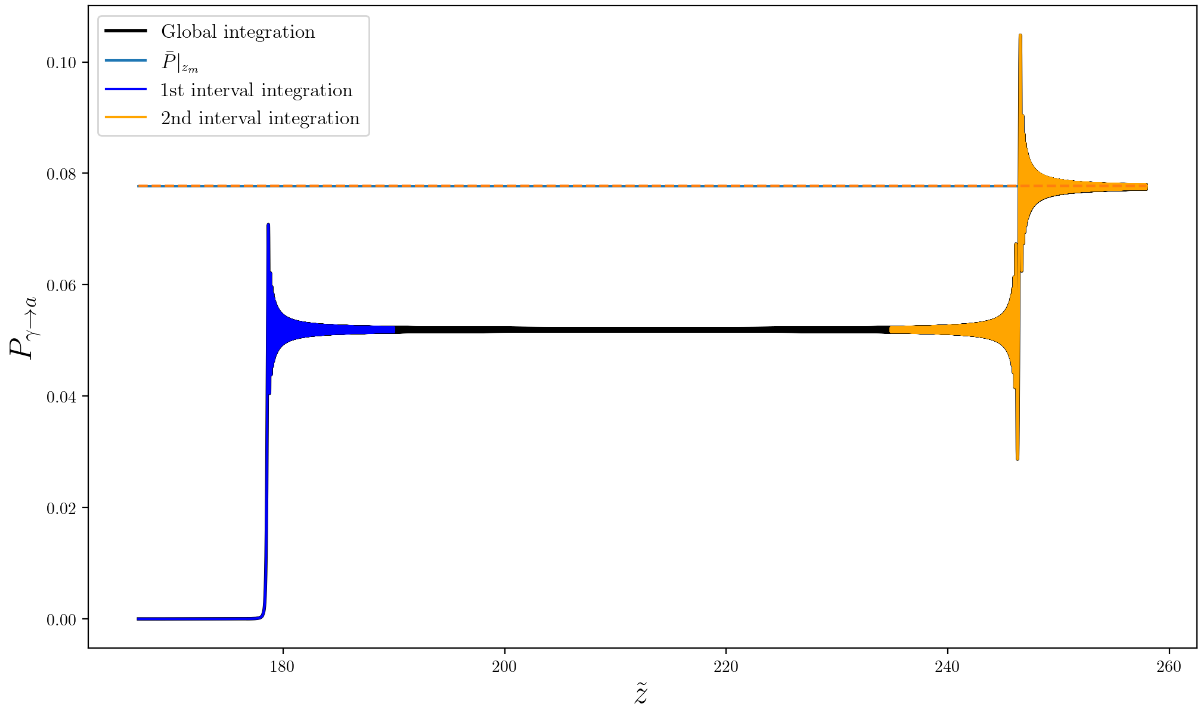

Figure 5.9: Comparison between global and cut solutions using $|u\rangle$ with initial conditions implemented via the WKB method. The cut solution on the second interval perfectly recovers the global one (cf. fig. 5.6).

The general case with N resonance points is treated in the same way, by defining N distinct intervals I_i centered on each resonance point z_i, along with $N-1$ intermediate intervals between I_i and I_{i+1}. In each intermediate interval, the WKB solution is applied and then the pairs $(u_{\text{num}}, u'_{\text{num}})$ are found by integrating the ODE. The integration at each interval I_i allows setting the initial conditions on the I_{i+1} interval: $\text{IC}_{I_{i+1}} = (u_{\text{num}}(z_{i+1}^{\max}), u'_{\text{num}}(z_{i+1}^{\max}))$.

An example with $N = 14$ resonance points is shown in fig. 5.11. This has been obtained by adding an oscillatory noise on top of the Battaglia profile.

5.8 Results with Illustris-TNG simulations

To validate the theoretical framework developed in the previous sections, realistic electron density profiles from state-of-the-art cosmological hydrodynamical simulations are employed. Specifi-

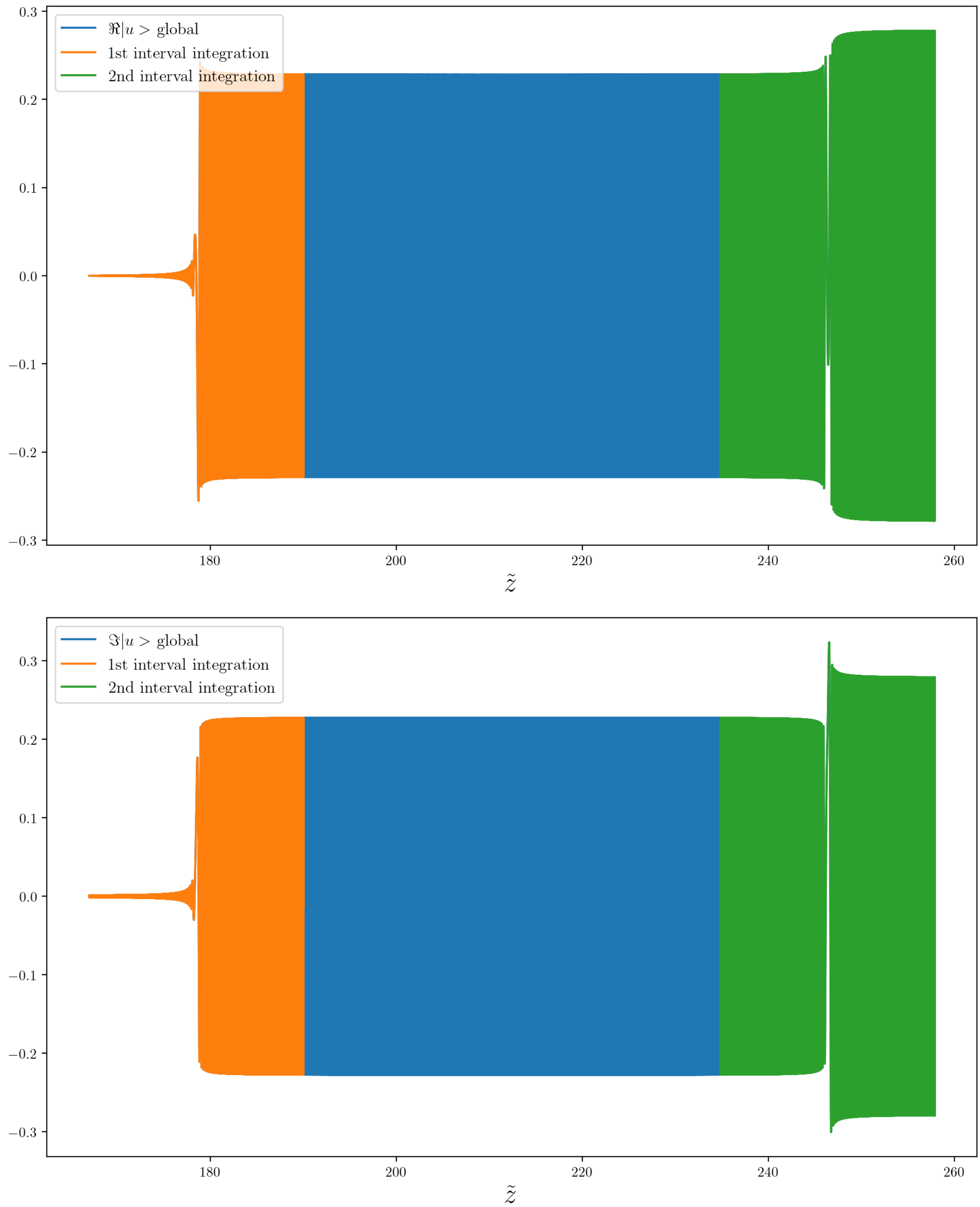

Figure 5.10: Global and cut plots of $\Re[|u\rangle]$ and $\Im[|u\rangle]$.

cally, the Illustris-TNG suite [175], a series of large-volume magnetohydrodynamical simulations modeling galaxy formation and evolution, provides a comprehensive set of halo profiles with varying masses and morphologies. The TNG300-1 simulation, with a box size of $(300\,\mathrm{Mpc})^3$ and high mass resolution, is particularly well-suited for this analysis.

Two distinct datasets extracted from the TNG300-1 simulation are analyzed, corresponding to different halo mass ranges:

- **Dataset 1**: Halo mass range $M \in [10^{13.50}, 10^{14.00}]\,M_\odot$, with characteristic virial radius

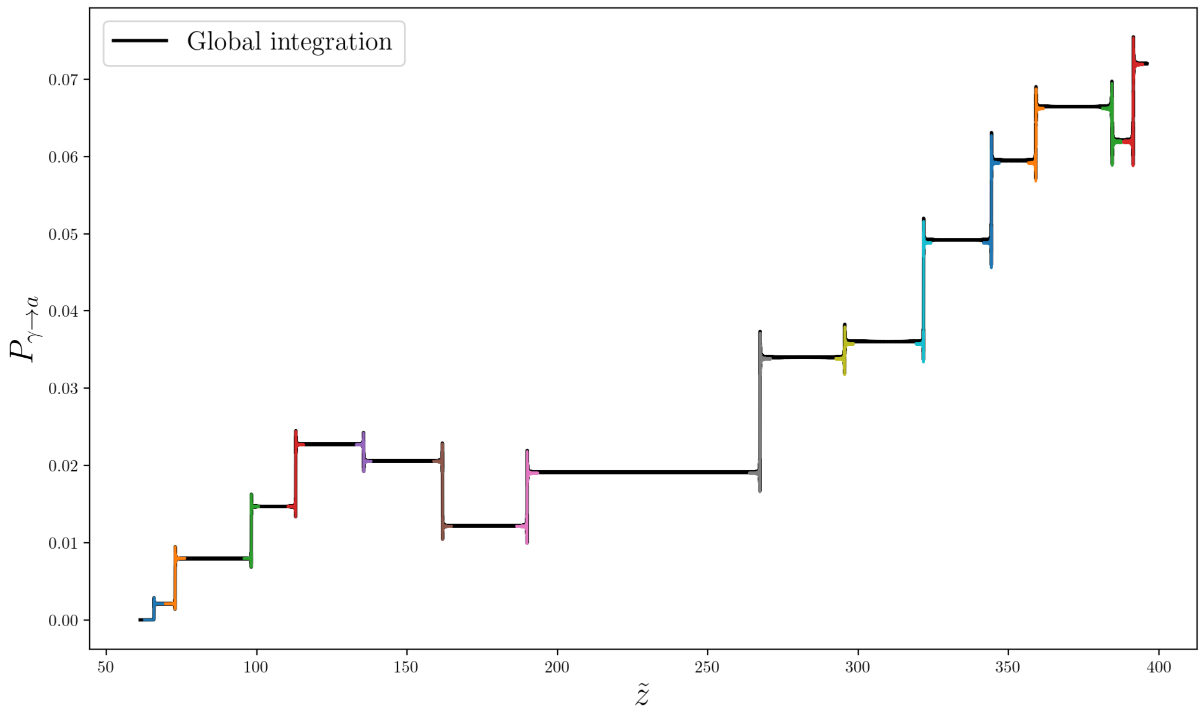

Figure 5.11: Situation with $N = 14$ resonance points obtained by adding oscillatory noise on top of the Battaglia profile. Also in this case, the WKB solution matches almost perfectly the global integration.

$R_{200c} \simeq 0.7876\,\mathrm{Mpc}$, comprising 866 individual electron density profiles.

- **Dataset 2**: Halo mass range $M \in [10^{13.00}, 10^{13.50}]\,M_\odot$, with characteristic virial radius $R_{200c} \simeq 0.5353\,\mathrm{Mpc}$, comprising 2587 individual electron density profiles.

These datasets are constructed from volume-weighted halo profiles, excluding star-forming regions, and are binned radially over the range $[0.05, 2.0]\,R_{200c}$ with 40 radial bins and a displacement parameter of 5. Figure 5.12 displays all individual $n_e(r)$ profiles for both datasets, together with their respective mean profiles, which are used as representative density distributions for subsequent validation tests.

For each profile—including the mean profiles—the resonance condition $\Delta_\parallel = \Delta_a$ yields not a single resonance point but rather a resonance shell at radius $r_{\rm res}$, due to the spherical symmetry of the halo. Photons propagating along different trajectories characterized by different impact parameters $r_{\rm min}$ encounter two resonance points symmetrically located with respect to the halo center, provided $r_{\rm min} < r_{\rm res}$, as shown in fig. 5.4. This geometric configuration leads to interference effects between the two conversion amplitudes, which must be accounted for when computing the total conversion probability.

To assess the validity of the Landau-Zener approximation (5.124) and the interference formula for multiple resonances (5.155), numerical integrations of the master equation are performed over 3000 distinct trajectories for each of the two mean profiles. The trajectories are parametrized by impact parameter $r_{\rm min}$, uniformly sampled in the interval $[r_{\rm min}^{\rm min}, r_{\rm min}^{\rm max}]$, where $r_{\rm min}^{\rm min} = 0$ and $r_{\rm min}^{\rm max} = 0.9999 \cdot r_{\rm res}$. This sampling strategy ensures comprehensive coverage of the resonance shell, including trajectories passing arbitrarily close to the critical radius $r_{\rm res}$, where the two resonance points approach each other. All other physical parameters are fixed according to section 5.7.3.

Figure 5.13 presents the ratio $P_{\gamma\to a}^{\rm LR}/(2\pi\gamma)$, where LR denotes "last resonance", as a function of trajectory number. The conversion probability $P_{\gamma\to a}^{\rm LR}$ is computed after the photon has crossed

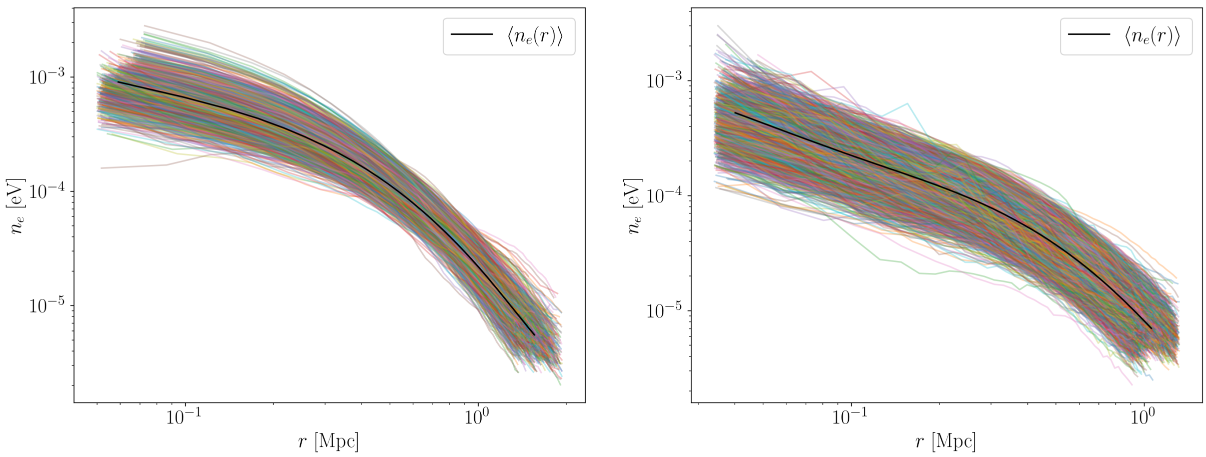

Figure 5.12: Electron density profiles $n_e(r)$ as a function of normalized radius r/R_{200c} extracted from the TNG300-1 simulation. Ensemble mean profiles highlighted in black. Left panel: Dataset 1. Right panel: Dataset 2.

both resonance points and is evaluated by averaging over oscillations in the final 10% of the integration domain. Remarkably, even for trajectories extremely close to the critical configuration $r_{\rm min} \simeq r_{\rm res}$—where the two resonance points nearly coincide—the numerical results satisfy

$$\frac{P^{\rm LR}_{\gamma\to a}}{2\pi\gamma} \sim 2 + 2\cos\Phi_{nm}, \tag{5.206}$$

in excellent agreement with the interference prediction in eq. (5.155). This behavior is expected given the spherical symmetry of the halo, which ensures $\gamma_1 = \gamma_2 = \gamma$, and the phase Φ_{nm} depends on the accumulated action between the two resonance points. Furthermore, the ensemble average over all trajectories yields

$$\left\langle \frac{P^{\rm LR}_{\gamma\to a}}{2\pi\gamma} \right\rangle \sim \langle 2 + 2\cos\Phi_{nm}\rangle = 2, \tag{5.207}$$

confirming that destructive and constructive interference cancel on average, as anticipated from phase randomization.

A focused analysis of trajectories in the vicinity of $r_{\rm res}$ demonstrates that, except for a small subset of trajectories, the interference formula remains accurate even in this challenging regime. This validates the applicability of eq. (5.155) across the entire range of physically relevant impact parameters.

Figure 5.14 displays the ratio $P^{\rm FR}_{\gamma\to\gamma'}/(2\pi\gamma)$, where FR denotes "first resonance", computed after the photon crosses the first resonance point. It is evident that for trajectories approaching $r_{\rm res}$, the standard Landau-Zener approximation in eq. (5.124) systematically deviates from the numerical solution. This deviation persists even when the more refined expression in eq. (5.123) is employed. The breakdown of the Landau-Zener approximation in this regime is attributed to violations of the underlying assumptions: the resonance width becomes comparable to the scale over which the electron density varies, invalidating the local linearity assumption, and the adiabaticity parameter γ approaches unity, violating the condition $\gamma \ll 1$ required for the exponential suppression formula.

Nevertheless, the relative error remains below 1% for the vast majority of trajectories, and only a small fraction near $r_{\rm res}$ exhibit discrepancies up to 2%. Consequently, when averaged over the ensemble of trajectories, the Landau-Zener approximation provides a good estimate for both the first-resonance probability and the final exit probability from the halo in agreement with previous studies in the literature [169, 171, 170], which assumed this result without rigorous numerical verification. The present analysis thus provides the first detailed validation of this

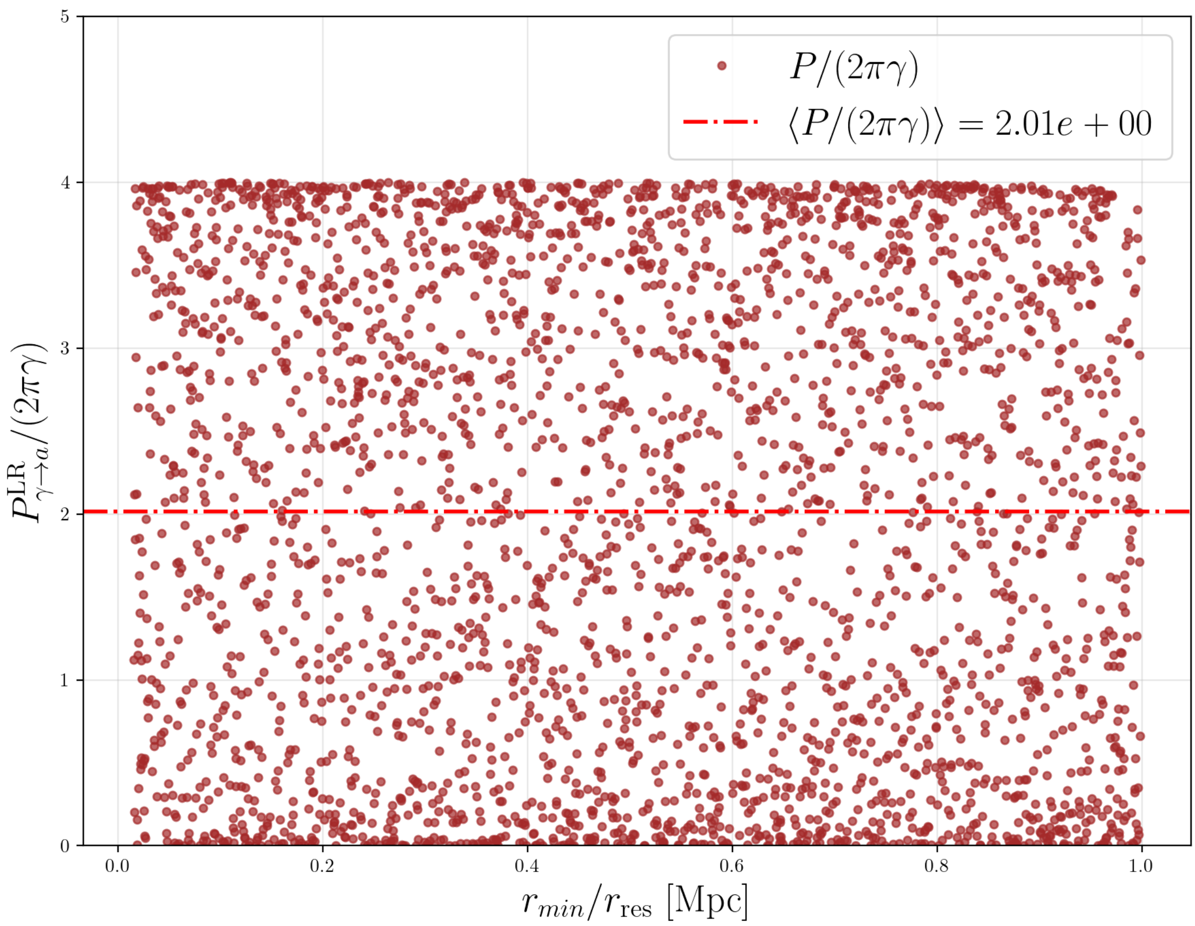

Figure 5.13: Normalized conversion probability $P^{\mathrm{LR}}_{\gamma\to a}/(2\pi\gamma)$ evaluated after the second (last) resonance point as a function of trajectory number for the mean profile of Dataset 1. Each point corresponds to a distinct trajectory characterized by impact parameter r_{min}. The numerical solution exhibits rapid oscillations consistent with the interference term $2 + 2\cos\Phi_{nm}$ predicted by eq. (5.155).

widely adopted approximation using realistic halo profiles from cosmological simulations.

Subsequently, a complementary analysis was performed by running multiple simulations using individual halo profiles along a single fixed trajectory. Specifically, a central trajectory passing through the halo center was selected, corresponding to an impact parameter $r_{\mathrm{min}} = 0$. For this fixed trajectory, each of the N individual profiles from the dataset (e.g., 866 profiles for Dataset 1, or 2587 for Dataset 2) was integrated separately. In this framework, the individual profiles are treated as noise realizations around the mean profile, reflecting the intrinsic scatter in halo morphologies and thermal histories within the simulation.

Importantly, some individual profiles exhibit resonance shells located beyond the virial radius, i.e., $r_{\mathrm{res}} > r_{\mathrm{vir}}$, such that no resonance occurs along the trajectory. In these cases, the conversion probability is effectively zero, as the photon never encounters the resonance condition. These non-resonant profiles were included in the ensemble average to obtain a statistically meaningful comparison with the mean profile.

The conversion probabilities were computed and averaged over all profile realizations for both the first and last resonance points. These ensemble-averaged probabilities were then compared with the corresponding values obtained from the single run using the mean profile along the same trajectory ($r_{\mathrm{min}} = 0$). The results reveal a striking asymmetry. For the first resonance point, the

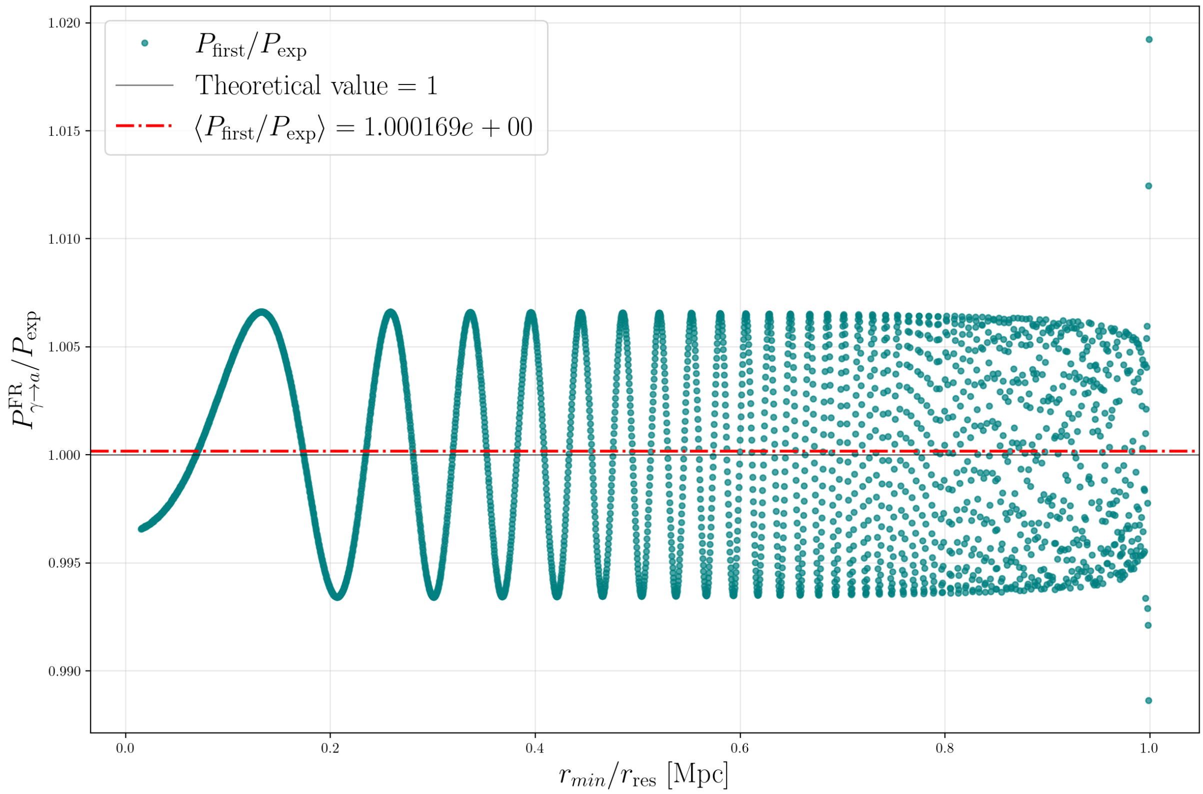

Figure 5.14: Normalized conversion probability $P^{\text{FR}}_{\gamma\to\gamma'}/P_{\text{exp}}$, where $P_{\text{exp}} = 1 - e^{-2\pi\gamma}$, evaluated after the first resonance point as a function of impact parameter r_{min} for the mean profile of Dataset 1. The horizontal axis spans trajectories from $r_{\text{min}} = 0$ (central passage through the halo) to $r_{\text{min}} \approx r_{\text{res}}$ (grazing trajectories tangent to the resonance shell).

ensemble-averaged probability over the 866 individual profiles (Dataset 1) converges to the value obtained from the mean profile, as expected from statistical averaging. However, the probability evaluated after the last resonance point is found to be completely incompatible with the mean profile prediction.

This discrepancy is a clear signature of the breakdown of the ensemble-averaging assumption when interference effects between multiple resonances are present. The phase accumulated between the first and second resonance points depends sensitively on the detailed shape of the electron density profile along the trajectory. Even small variations in the profile morphology—arising from halo-to-halo scatter, substructure, or numerical noise—can lead to large variations in the interference phase Φ_{nm} defined in eq. (5.155). Consequently, while the probability at the first resonance is well-approximated by the Landau-Zener formula and exhibits stable ensemble behavior, the probability at the second resonance is dominated by stochastic interference terms that do not average coherently.

Chapter 6

Conclusions

This thesis has explored three distinct yet interconnected aspects of physics beyond the standard cosmological model, all sharing the Cosmic Microwave Background (CMB) as the central observational probe. The work presented addresses fundamental questions in early-universe physics, parity-violating interactions, and photon-axion conversions, combining rigorous theoretical developments with confrontation against current and forecasted observational data. The structure follows both a chronological perspective and the thermal history of the Universe—from inflationary dynamics in the earliest moments, through CMB generation, to photon propagation and conversion processes in the late-time Universe.

The first original contribution concerns the computation of scalar and tensor Primordial Power Spectra (PPS) at third order in the slow-roll approximation. Higher-order corrections have been demonstrated to significantly enhance the accuracy of predicted power spectra, spectral indices, and their derivatives. By comparing different orders of approximation, it has been shown that the improvement from second to third order becomes appreciable at very small scales, $k \gtrsim 10\,\mathrm{Mpc}^{-1}$, while leaving CMB angular power spectra nearly unaffected. For current and upcoming CMB experiments, the third-order solution provides no significant improvement over the second-order treatment, confirming that this order is sufficiently accurate for CMB observational analyses. However, thanks to third-order solutions and by combining late-time cosmological datasets with CMB measurements, stringent upper limits have been placed on the first three Hubble Flow Functions, although the fourth remains unconstrained by present data. While the third-order solution offers minimal benefit for CMB science, it becomes crucial at small scales for other cosmological observables. Future surveys covering broader scale ranges—such as large-scale structure (LSS) measurements from *Euclid*, CMB spectral distortions experiments, 21 cm observations, and primordial black hole abundance studies—will be essential to test higher-order terms in the slow-roll expansion and probe the validity of single-field slow-roll predictions.

The second project presented in this thesis addresses the Cosmic Birefringence effect possibly induced by parity-violating coupling between CMB photons and axions. In this work, confirming previous results, the analysis of *Planck* PR3 data has revealed a non-zero EB cross-correlation signal, inconsistent with zero at more than 5σ confidence level when compared with the standard ΛCDM prediction. Regardless of whether this signal originates from new physics beyond the Standard Model or from systematic effects due to polarimeter miscalibrations, a comprehensive investigation of its scale dependence has been performed. The isotropic cosmic birefringence (ICB) signal has been analyzed not only over the full harmonic range but also across distinct subsets of multipoles. To understand the fundamental nature of this signal, its potential scale dependence has been investigated using two complementary approaches: a parametric power-law model and a non-parametric Bayesian reconstruction. The results demonstrate that the birefringence angle β is scale-independent at the $\lesssim 2\sigma$ level across all four *Planck* component separation methods.

Forecasts for future CMB polarization experiments—including LiteBIRD, Simons Observatory, and the now-cancelled CMB-S4—have been computed in this work, demonstrating that uncertainties on scale dependence can be reduced by up to a factor of seven, enabling decisive tests of both systematic and fundamental interpretations of the observed signal. These upcoming missions will play a crucial role in resolving the degeneracy between fundamental parity violation and instrumental systematics.

The final chapter provides an extensive treatment of photon-to-axion conversion phenomena in cosmological contexts, developing the complete quantum mechanical framework required for accurate predictions. Previous approaches in the literature have been shown to contain approximations that, while acceptable in certain limiting cases, fail to correctly address the general problem. A rigorous solution method for the relevant second-order ordinary differential equations—the Schrödinger equation in astrophysical and cosmological environments—has been presented, including mathematical techniques to drastically reduce computational cost without sacrificing precision. The developed approach is general and applicable to a broad class of problems in astrophysics involving similar differential equations. Application to realistic physical scenarios demonstrates that the Landau-Zener approximation provides acceptable accuracy when applied to smooth, spherically-averaged halo profiles obtained from hydrodynamical simulations. The refined theoretical framework developed in this work enables the derivation of stringent constraints on the axion-photon coupling constant and axion mass through accurate modeling of photon-to-axion conversion probabilities in realistic cosmological environments. Future CMB spectral distortion experiments will leverage these improved predictions to constrain axion parameter space via cross-correlation analyses between CMB temperature anisotropies and large-scale structure tracers.

Overall, the results presented in this thesis demonstrate the power of precision cosmology to address fundamental questions in theoretical physics. In the coming decades, improved datasets from multiple observational channels will dramatically narrow the parameter space of slow-roll inflation models, potentially excluding entire classes of scenarios. Within this context, third-order corrections will become increasingly important as observations extend to smaller scales where ΛCDM predictions must be tested with unprecedented accuracy.

The *Euclid* mission, which began science operations in 2023 and released its first images in early 2025, is already delivering large-scale structure measurements that will complement CMB constraints on cosmic inflation and dark energy. Upcoming CMB polarization missions —particularly LiteBIRD (planned launch in early 2033) and Simons Observatory—are specifically designed to achieve the sensitivity required to definitively characterize the EB signal and resolve its physical origin. These experiments will provide critical insights into the nature and role of axions, one of the most compelling candidates for physics beyond the Standard Model and a potential component of dark matter or dark energy.

Future CMB experiments will also open new observational windows through improved sensitivity to secondary anisotropies and small-scale power spectrum measurements, providing complementary probes of early-universe physics and enabling tests of exotic processes such as photon-to-axion and photon-to-dark-photon conversions. Realizing the full scientific potential of these observations requires continued development of accurate and efficient theoretical predictions, as demonstrated throughout this work. The interplay between theoretical refinement and observational advancement will remain central to cosmology's role as one of the most productive arenas for testing fundamental physics in the decades ahead.

Appendix A

Isometries

This appendix provides the detailed mathematical derivations supporting the construction of the FLRW metric presented in section 1.2. The first section derives the fundamental Killing equation from isometry conditions, while the second section applies this equation to determine the form factor $F(r)$ that constrains the spatial curvature structure of cosmological spacetimes.

A.1 The Killing Equation

Starting from the definition of isometry given in eq. (1.15), the general criterion for defining isometries is constructed, recalling that the metric transforms as a rank-2 tensor under coordinate transformation:

$$\tilde{g}_{\alpha\beta}(\tilde{x}) = \frac{\partial x^\mu}{\partial \tilde{x}^\alpha}\frac{\partial x^\nu}{\partial \tilde{x}^\beta} g_{\mu\nu}(x) \quad \Longleftrightarrow \quad g_{\mu\nu}(x) = \frac{\partial \tilde{x}^\alpha}{\partial x^\mu}\frac{\partial \tilde{x}^\beta}{\partial x^\nu}\tilde{g}_{\alpha\beta}(\tilde{x}), \tag{A.1}$$

provided the transformation is admissible, i.e., the Jacobians and their inverses exist and are non-singular. For an isometric transformation, the condition becomes:

$$g_{\mu\nu}(x^\alpha) = \frac{\partial \tilde{x}^\alpha}{\partial x^\mu}\frac{\partial \tilde{x}^\beta}{\partial x^\nu} g_{\alpha\beta}(\tilde{x}^\alpha). \tag{A.2}$$

This equation provides the isometries but is computationally challenging to solve directly. However, a manageable formula characterizing isometries can be derived by considering reference systems that are infinitesimally close. Consider the transformation:

$$\tilde{x}^\alpha = x^\alpha + \varepsilon\xi^\alpha(x), \tag{A.3}$$

which is infinitesimal with $\varepsilon \ll 1$ and where ξ^α represents the connection vector.

The Jacobian becomes:

$$\frac{\partial \tilde{x}^\alpha}{\partial x^\mu} = \delta^\alpha_\mu + \varepsilon\frac{\partial \xi^\alpha}{\partial x^\mu}; \tag{A.4}$$

from which the metric transformation can be rewritten as:

$$g_{\mu\nu}(x) = \left(\delta^\alpha_\mu + \varepsilon\frac{\partial \xi^\alpha}{\partial x^\mu}\right)\left(\delta^\beta_\nu + \varepsilon\frac{\partial \xi^\beta}{\partial x^\nu}\right) g_{\alpha\beta}(\tilde{x}). \tag{A.5}$$

Expanding the products and neglecting second-order terms in ε yields:

$$g_{\mu\nu}(x) = \delta^\alpha_\mu\delta^\beta_\nu g_{\alpha\beta}(\tilde{x}) + \varepsilon\frac{\partial \xi^\alpha}{\partial x^\mu}\delta^\beta_\nu g_{\alpha\beta}(\tilde{x}) + \varepsilon\frac{\partial \xi^\beta}{\partial x^\nu}\delta^\alpha_\mu g_{\alpha\beta}(\tilde{x}) + \mathcal{O}(\varepsilon^2)$$

$$\Downarrow$$

$$g_{\mu\nu}(x) = g_{\mu\nu}(\tilde{x}) + \varepsilon\frac{\partial \xi^\alpha}{\partial x^\mu} g_{\alpha\nu}(\tilde{x}) + \varepsilon\frac{\partial \xi^\beta}{\partial x^\nu} g_{\beta\mu}(\tilde{x}). \tag{A.6}$$

The term $g_{\mu\nu}(\tilde{x})$ can be expanded in Taylor series with $\tilde{x} \simeq x$ (since $\varepsilon \to 0$), again neglecting second-order terms:

$$g_{\mu\nu}(\tilde{x}) = g_{\mu\nu}(x + \varepsilon\xi) \simeq g_{\mu\nu}(x) + \varepsilon\xi^\alpha \frac{\partial g_{\mu\nu}}{\partial x^\alpha}. \tag{A.7}$$

Substituting the series expansion gives:

$$\varepsilon \left[\xi^\alpha \frac{\partial g_{\mu\nu}}{\partial x^\alpha} + \frac{\partial \xi^\alpha}{\partial x^\mu} g_{\alpha\nu} + \frac{\partial \xi^\beta}{\partial x^\nu} g_{\mu\beta} \right] = 0. \tag{A.8}$$

The term in square brackets represents the **metric deformation induced by the transformation**. For the metric tensor to be invariant under coordinate transformations—the fundamental requirement defining isometric transformations—the metric deformation must vanish.

The **condition for isometries** is therefore:

$$\xi^\alpha \frac{\partial g_{\mu\nu}}{\partial x^\alpha} + \frac{\partial \xi^\alpha}{\partial x^\mu} g_{\alpha\nu} + \frac{\partial \xi^\beta}{\partial x^\nu} g_{\mu\beta} = 0, \tag{A.9}$$

which can be rewritten equivalently by changing the dummy index β to α:

$$\xi^\alpha \frac{\partial g_{\mu\nu}}{\partial x^\alpha} + \frac{\partial \xi^\alpha}{\partial x^\mu} g_{\alpha\nu} + \frac{\partial \xi^\alpha}{\partial x^\nu} g_{\mu\alpha} = 0. \tag{A.10}$$

Since this equation is written in terms of the metric, it is convenient to reformulate it without explicit metric dependence.

Expressing ξ^α in covariant form:

$$\xi_\nu = g_{\alpha\nu}\xi^\alpha \quad \text{and} \quad \xi_\mu = g_{\alpha\mu}\xi^\alpha; \tag{A.11}$$

the derivatives of ξ_ν and ξ_μ become:

$$\begin{aligned}
\frac{\partial \xi_\nu}{\partial x^\mu} &= \frac{\partial g_{\alpha\nu}}{\partial x^\mu}\xi^\alpha + g_{\alpha\nu}\frac{\partial \xi^\alpha}{\partial x^\mu} \quad &\Longrightarrow \quad g_{\alpha\nu}\frac{\partial \xi^\alpha}{\partial x^\mu} &= \frac{\partial \xi_\nu}{\partial x^\mu} - \frac{\partial g_{\alpha\nu}}{\partial x^\mu}\xi^\alpha \\
\frac{\partial \xi_\mu}{\partial x^\nu} &= \frac{\partial g_{\alpha\mu}}{\partial x^\nu}\xi^\alpha + g_{\alpha\mu}\frac{\partial \xi^\alpha}{\partial x^\nu} \quad &\Longrightarrow \quad g_{\alpha\mu}\frac{\partial \xi^\alpha}{\partial x^\nu} &= \frac{\partial \xi_\mu}{\partial x^\nu} - \frac{\partial g_{\alpha\mu}}{\partial x^\nu}\xi^\alpha.
\end{aligned}$$

Substituting into the isometry condition yields:

$$\xi^\alpha \frac{\partial g_{\mu\nu}}{\partial x^\alpha} + \frac{\partial \xi_\nu}{\partial x^\mu} - \frac{\partial g_{\alpha\nu}}{\partial x^\mu}\xi^\alpha + \frac{\partial \xi_\mu}{\partial x^\nu} - \frac{\partial g_{\alpha\mu}}{\partial x^\nu}\xi^\alpha = 0,$$

which can be reordered and factorized as:

$$\frac{\partial \xi_\nu}{\partial x^\mu} + \frac{\partial \xi_\mu}{\partial x^\nu} - \xi^\alpha \left[\frac{\partial g_{\alpha\mu}}{\partial x^\nu} + \frac{\partial g_{\alpha\nu}}{\partial x^\mu} - \frac{\partial g_{\mu\nu}}{\partial x^\alpha} \right] = 0. \tag{A.12}$$

The term in square brackets resembles a Christoffel symbol of the first kind. Recalling the definition of the Christoffel symbol of the second kind:

$$\Gamma^\rho_{\mu\nu} = \frac{1}{2} g^{\rho\alpha} \left(\frac{\partial g_{\alpha\mu}}{\partial x^\nu} + \frac{\partial g_{\alpha\nu}}{\partial x^\mu} - \frac{\partial g_{\mu\nu}}{\partial x^\alpha} \right),$$

and multiplying both members by $2g_{\rho\alpha}$ gives:

$$2g_{\rho\alpha}\Gamma^\rho_{\mu\nu} = g_{\rho\alpha} g^{\rho\alpha} \left(\frac{\partial g_{\alpha\mu}}{\partial x^\nu} + \frac{\partial g_{\alpha\nu}}{\partial x^\mu} - \frac{\partial g_{\mu\nu}}{\partial x^\alpha} \right),$$

where $g_{\rho\alpha}g^{\rho\alpha} = 1$ (not equal to 4, as the sum over ρ and α extends to the entire right-hand side). Thus:

$$\left(\frac{\partial g_{\alpha\mu}}{\partial x^\nu} + \frac{\partial g_{\alpha\nu}}{\partial x^\mu} - \frac{\partial g_{\mu\nu}}{\partial x^\alpha} \right) = 2g_{\rho\alpha}\Gamma^\rho_{\mu\nu}, \tag{A.13}$$

and the main equation becomes:

$$\frac{\partial \xi_\nu}{\partial x^\mu} + \frac{\partial \xi_\mu}{\partial x^\nu} - 2\xi^\alpha g_{\rho\alpha}\Gamma^\rho_{\mu\nu} = 0$$

$$\Downarrow$$

$$\frac{\partial \xi_\nu}{\partial x^\mu} + \frac{\partial \xi_\mu}{\partial x^\nu} - 2\xi_\rho\Gamma^\rho_{\mu\nu} = 0. \tag{A.14}$$

This expression can be written more compactly using the definition of covariant derivative from eq. (1.15):

$$\xi_{\nu;\mu} + \xi_{\mu;\nu} = 0. \tag{A.15}$$

A.2 From Isometries to the FLRW Form Factor $F(r)$

To determine the form of the term $F(r)$ in the FLRW metric, metric invariance under affine transformations at fixed times is imposed, i.e., the isometry $\tilde{g}_{\mu\nu}(\tilde{x}) = g_{\mu\nu}(\tilde{x}^\alpha)$ under the transformation $x^\alpha \to \tilde{x}^\alpha = \varepsilon + \xi^\alpha$. Given temporal invariance—time is measured uniformly throughout $\mathcal{M}^3$—the condition becomes:

$$x^0 \equiv \tilde{x}^0 \quad \Rightarrow \quad \xi^0 = \xi_0 = 0, \tag{A.16}$$

as expected from the fact that in this foliation situation, the isometries act on $\mathcal{M}^3$ at fixed time.

With the metric form specified, the Killing equation written in terms of the metric—the isometry condition eq. (A.10)—is most convenient for calculations:

$$g_{\alpha\beta,\lambda}\xi^\lambda + \xi^\lambda{}_{,\alpha} g_{\lambda\beta} + \xi^\lambda{}_{,\beta} g_{\alpha\lambda} = 0. \tag{A.17}$$

The form of $F(r)$ is determined by writing the Killing equations for various components. The case $\alpha = \beta = 0$ yields a trivial equality $0 = 0$ due to $\xi^0 = 0$, $g_{00} = 1$, and $g_{0\lambda} = 0$. Following the approach typically used for the Schwarzschild solution [8], the components $\alpha = 1, \beta = 2$ are considered instead of $\alpha = \beta = 3$.

- **Case** $\alpha = \beta = 1$**:**

The Killing equation becomes:

$$g_{11,\lambda}\xi^\lambda + \xi^\lambda{}_{,1} g_{\lambda 1} + \xi^\lambda{}_{,1} g_{1\lambda} = 0. \tag{A.18}$$

Recall that $x^1 = r$, $x^2 = \vartheta$, and $x^3 = \phi$. From the metric symmetry, the last two terms combine and the equation simplifies to:

$$g_{11,\lambda}\xi^\lambda + 2\xi^\lambda{}_{,r} g_{1\lambda} = 0. \tag{A.19}$$

Since the metric is diagonal, $g_{1\lambda} \neq 0$ only for $\lambda = 1 = r$, so the second term involves g_{11}:

$$g_{11,\lambda}\xi^\lambda + 2\xi^r{}_{,r} g_{11} = 0. \tag{A.20}$$

Given that $g_{11} = -a^2(t)F(r)$ depends only on $t = \frac{x^0}{c}$ and $x^1 = r$, and expanding the sum over λ with $\xi^0 = 0$, the formula reduces to:

$$g_{11,1}\xi^r + 2\xi^r{}_{,r} g_{11} = 0. \tag{A.21}$$

Substituting $g_{11} = -a^2(t)F(r)$ and

$$g_{11,1} = -a^2(t)\frac{\mathrm{d}F(r)}{\mathrm{d}r}, \tag{A.22}$$

yields the differential equation:

$$2F(r)\xi^r{}_{,r} + \frac{\mathrm{d}F(r)}{\mathrm{d}r}\xi^r = 0 \quad \Longrightarrow \quad 2F(r)\frac{\mathrm{d}\xi^r}{\mathrm{d}r} + \frac{\mathrm{d}F(r)}{\mathrm{d}r}\xi^r = 0. \tag{A.23}$$

This represents a separable differential equation:

$$\frac{\mathrm{d}\xi^r}{\xi^r} = -\frac{1}{2F(r)}\mathrm{d}F,$$

which integrates to:

$$\ln \xi^r = -\frac{1}{2}\ln F(r) + \text{const},$$

i.e.:

$$\xi^r \sqrt{F} = \text{const}, \tag{A.24}$$

where the constant is with respect to r but may depend on ϑ and ϕ, while being independent of t since the transformation is purely spatial:

$$\xi^r \sqrt{F} = C(\vartheta, \phi). \tag{A.25}$$

This equation will be used later; now consider the other Killing equations.

• **Case** $\alpha = \beta = 2$**:**

The Killing equation becomes:

$$g_{22,\lambda}\xi^\lambda + \xi^\lambda{}_{,\vartheta}g_{\lambda 2} + \xi^\lambda{}_{,\vartheta}g_{2\lambda} = 0, \tag{A.26}$$

which, by symmetry and since $g_{\lambda 2} \neq 0$ only for $\lambda = 2$, simplifies to:

$$g_{22,\lambda}\xi^\lambda + 2\xi^\vartheta{}_{,\vartheta}g_{22} = 0. \tag{A.27}$$

Given that $g_{22,\lambda} \neq 0$ only for $\lambda = 0$ and $\lambda = 1$, and with $\xi^0 = 0$:

$$g_{22,1}\xi^r + 2\xi^\vartheta{}_{,\vartheta}g_{22} = 0. \tag{A.28}$$

Substituting $g_{22} = -r^2 a^2(t)F(r)$ and

$$g_{22,1} = -a^2(t)\frac{\mathrm{d}}{\mathrm{d}r}[r^2 F(r)], \tag{A.29}$$

and simplifying the common factor $-a^2(t)$, yields:

$$2\xi^\vartheta{}_{,\vartheta}r^2 F(r) + \frac{\mathrm{d}}{\mathrm{d}r}[r^2 F(r)]\xi^r = 0. \tag{A.30}$$

This equation introduces $\xi^\vartheta{}_{,\vartheta}$ as another unknown, necessitating consideration of another equation. The case $\alpha = 1$ and $\beta = 2$ is examined.

• **Case** $\alpha = 1$ **and** $\beta = 2$**:**

The Killing equation becomes:

$$g_{12,\lambda}\xi^\lambda + \xi^\lambda{}_{,r}g_{\lambda 2} + \xi^\lambda{}_{,\vartheta}g_{1\lambda} = 0. \tag{A.31}$$

Since $g_{12} = 0$ and $g_{ij} \neq 0$ only if $i = j$, the equation reduces to:

$$\xi^\vartheta{}_{,r}g_{22} + \xi^r{}_{,\vartheta}g_{11} = 0. \tag{A.32}$$

Substituting g_{11} and g_{22}, which differ only by the factor r^2, and simplifying the common term $a^2(t)F(r)$, gives:

$$\xi^\vartheta{}_{,r}r^2 + \xi^r{}_{,\vartheta} = 0, \tag{A.33}$$

i.e.:

$$\xi^\vartheta{}_{,r} = -\frac{1}{r^2}\xi^r{}_{,\vartheta}. \tag{A.34}$$

The equations eq. (A.25), eq. (A.30) and eq. (A.34) form the system:

$$\begin{cases} \xi^r\sqrt{F} = C(\vartheta,\phi) \\ 2\xi^\vartheta{}_{,\vartheta} r^2 F(r) + \frac{\mathrm{d}}{\mathrm{d}r}[r^2F(r)]\xi^r = 0 \\ \xi^\vartheta{}_{,r} = -\frac{1}{r^2}\xi^r{}_{,\vartheta} \end{cases} . \tag{A.35}$$

This system is solved using appropriate mathematical techniques. Differentiating both sides of eq. (A.34) with respect to ϑ yields:

$$\xi^\vartheta{}_{,r\vartheta} = -\frac{1}{r^2}\xi^r{}_{,\vartheta\vartheta}. \tag{A.36}$$

Now dividing eq. (A.30) by $2r^2F(r)$:

$$\xi^\vartheta{}_{,\vartheta} + \frac{\xi^r}{2r^2F}\frac{\mathrm{d}}{\mathrm{d}r}[r^2F(r)] = 0, \tag{A.37}$$

and differentiating both sides with respect to r allows substitution of the differentiated eq. (A.34):

$$\frac{\mathrm{d}}{\mathrm{d}r}\left[\frac{\xi^r}{2r^2F}\frac{\mathrm{d}}{\mathrm{d}r}(r^2F(r))\right] = -\xi^\vartheta{}_{,\vartheta r} = \frac{1}{r^2}\xi^r{}_{,\vartheta\vartheta}. \tag{A.38}$$

Returning to equation eq. (A.25), an ansatz arising from the invariance under rotations on the manifold $\mathcal{M}^3$ is made. Given the symmetry, reference systems on $\mathcal{M}^3$ can be chosen such that r is fixed and ϕ is fixed, allowing only rotations along ϑ. This permits imposition of harmonic dependence of ξ^r only on ϑ:

$$\xi^r\sqrt{F} = A\cos\vartheta \quad \Rightarrow \quad \xi^r = \frac{A\cos\vartheta}{\sqrt{F}}; \tag{A.39}$$

differentiating twice with respect to ϑ gives:

$$\xi^r{}_{,\vartheta\vartheta} = \frac{-A\cos\vartheta}{\sqrt{F}} = -\xi^r. \tag{A.40}$$

Substituting into equation eq. (A.38) yields:

$$\frac{\mathrm{d}}{\mathrm{d}r}\left[\frac{\xi^r}{2r^2F}\frac{\mathrm{d}}{\mathrm{d}r}(r^2F(r))\right] = -\frac{1}{r^2}\xi^r. \tag{A.41}$$

Developing the derivative in square brackets using the notation $\frac{\mathrm{d}F}{\mathrm{d}r} = F'$:

$$\frac{\mathrm{d}}{\mathrm{d}r}\left[\frac{\xi^r}{2r^2F}(r^2F' + 2rF)\right] = -\frac{1}{r^2}\xi^r,$$

and substituting the harmonic form ξ^r:

$$\frac{\mathrm{d}}{\mathrm{d}r}\left[\frac{A\cos\vartheta}{2r^2F^{3/2}}(r^2F' + 2rF)\right] = -\frac{A\cos\vartheta}{r^2\sqrt{F}}$$

$$\Downarrow$$

$$\frac{\mathrm{d}}{\mathrm{d}r}\left[\frac{1}{2r^2F^{3/2}}(r^2F' + 2rF)\right] = -\frac{1}{r^2\sqrt{F}}.$$

Developing the derivative on the left-hand side:

$$\frac{\mathrm{d}}{\mathrm{d}r}\left[\frac{1}{2r^2F^{3/2}}\right] = \frac{\mathrm{d}}{\mathrm{d}r}\left[\frac{1}{2}r^{-2}F^{-3/2}\right] = \frac{1}{2}\left[-\frac{2}{r^3F^{3/2}} - \frac{3}{2}\frac{1}{r^2}\frac{F'}{F^{5/2}}\right],$$

gives:

$$\left(-\frac{1}{r^3F^{3/2}}-\frac{3}{4}\frac{1}{r^2F^{5/2}}\right)(r^2F'+2rF)+\frac{1}{2r^2F^{3/2}}\left(2rF'+r^2F''+2F+2rF'\right)=-\frac{1}{r^2\sqrt{F}}.$$

After performing all products and simplifications, the resulting equation is:

$$F''-\frac{1}{r}F'-\frac{3}{2}\frac{(F')^2}{F}=0. \tag{A.42}$$

This nonlinear differential equation has the solution:

$$F'=ArF^{3/2} \quad \text{with} \quad A=\text{const}, \tag{A.43}$$

which remains a differential equation with separable variables:

$$\frac{F'}{F^{3/2}}=Ar \quad \Rightarrow \quad \frac{\mathrm{d}F}{F^{3/2}}=Ar\mathrm{d}r \quad \Rightarrow \quad -\frac{2}{\sqrt{F}}=A\frac{r^2}{2}+B$$

$$\Downarrow$$

$$F(r)=\frac{4}{\left(B+\frac{Ar^2}{2}\right)^2}. \tag{A.44}$$

Since A and B are arbitrary integration constants, renormalization gives the appropriate values to the constants, yielding definitively:

$$F(r)=\frac{1}{\left(1+\frac{k}{4}r^2\right)^2} \quad \text{with} \quad k=-1,0,1\,; \tag{A.45}$$

this renormalization is possible because the reference system can be chosen to rescale r; once renormalized, only the sign or possible nullity of the constant matters, hence k takes the three values $1,0,-1$.

Appendix B

Christoffel Symbols and Ricci Tensor in FLRW Metric

This appendix presents the detailed calculations of the Christoffel symbols and the components of the Ricci tensor for the FLRW metric in the limit $r \to 0$, leading to the expressions for R_{00} and R_{11} given in eqs. (1.28) and (1.29).

B.1 Computation of the Christoffel Symbols

An alternative approach to using the Christoffel symbol definition eq. (1.8) is to start from the Lagrangian for a massive particle, compute the Euler-Lagrange equations, and compare them with the geodesic equation eq. (1.7). Denoting $\dot{x} = \frac{\mathrm{d}x}{\mathrm{d}s}$, the Lagrangian L is defined and normalized to unity for massive particles, as customary in General Relativity:

$$L = 1 = \frac{\mathrm{d}s^2}{\mathrm{d}s^2} = (\dot{x}^0)^2 - a^2(t)\left(1 - \frac{k}{2}r^2\right)[(\dot{x}^1)^2 + (\dot{x}^2)^2 + (\dot{x}^3)^2]; \tag{B.1}$$

while the Euler-Lagrange equations in the parametrization s are:

$$\frac{\mathrm{d}}{\mathrm{d}s}\frac{\partial L}{\partial \dot{x}^\alpha} = \frac{\partial L}{\partial x^\alpha}. \tag{B.2}$$

This approach is chosen here because it provides a more systematic and straightforward method compared to direct exploitation of eq. (1.8).

- **Component $\alpha = 0$:**

The Euler-Lagrange equation for $\alpha = 0$ is:

$$\frac{\mathrm{d}}{\mathrm{d}s}\frac{\partial L}{\partial \dot{x}^0} - \frac{\partial L}{\partial x^0} = 0. \tag{B.3}$$

From the Lagrangian:

$$\frac{\partial L}{\partial \dot{x}^0} = 2\dot{x}^0, \tag{B.4}$$

yielding the first term of the Euler-Lagrange equation:

$$\frac{\mathrm{d}}{\mathrm{d}s}\frac{\partial L}{\partial \dot{x}^0} = \frac{\partial(2\dot{x}^0)}{\partial \dot{x}^0}\frac{\partial \dot{x}^0}{\partial s} = 2\ddot{x}^0. \tag{B.5}$$

The second term becomes:

$$\frac{\partial L}{\partial x^0} = \frac{1}{c}\frac{\partial L}{\partial t} = -\frac{1}{c}2a\dot{a}\left[1 - \frac{k}{2}r^2\right][(\dot{x}^1)^2 + (\dot{x}^2)^2 + (\dot{x}^3)^2],$$

which in the limit $r \to 0$ can be written as:

$$\frac{\partial L}{\partial x^0} = -\frac{1}{c} 2a\dot{a}[(\dot{x}^1)^2 + (\dot{x}^2)^2 + (\dot{x}^3)^2]. \tag{B.6}$$

The Euler-Lagrange equation is therefore:

$$\ddot{x}^0 + \frac{1}{c} a\dot{a}[(\dot{x}^1)^2 + (\dot{x}^2)^2 + (\dot{x}^3)^2] = 0, \tag{B.7}$$

which, compared with the geodesic equation for $\alpha = 0$, $\ddot{x}^0 + \Gamma^0_{\mu\nu}\dot{x}^\mu\dot{x}^\nu = 0$, yields the following non-zero Christoffel symbols:

$$\Gamma^0_{11} = \Gamma^0_{22} = \Gamma^0_{33} = \frac{1}{c} a\dot{a}, \tag{B.8}$$

written compactly as:

$$\Gamma^0_{ij} = \frac{1}{c} a\dot{a}\delta_{ij}. \tag{B.9}$$

- **Component $\alpha = 1$:**

The Euler-Lagrange equation for $\alpha = 1$ is:

$$\frac{\mathrm{d}}{\mathrm{d}s}\frac{\partial L}{\partial \dot{x}^1} - \frac{\partial L}{\partial x^1} = 0. \tag{B.10}$$

From the Lagrangian:

$$\frac{\partial L}{\partial \dot{x}^1} = -2a^2\left(1 - \frac{k}{2}r^2\right)\dot{x}^1, \tag{B.11}$$

yielding the first term of the Euler-Lagrange equation:

$$\begin{aligned}\frac{\mathrm{d}}{\mathrm{d}s}\frac{\partial L}{\partial \dot{x}^1} &= -2\left\{\frac{\mathrm{d}}{\mathrm{d}s}\left[a^2\left(1 - \frac{k}{2}r^2\right)\right]\dot{x}^1 + a^2\left(1 - \frac{k}{2}r^2\right)\ddot{x}^1\right\} \\ &= -2\left[\frac{\mathrm{d}a^2}{\mathrm{d}s}\left(1 - \frac{k}{2}r^2\right)\dot{x}^1 + a^2\frac{\mathrm{d}}{\mathrm{d}s}\left(1 - \frac{k}{2}r^2\right)\dot{x}^1 + a^2\left(1 - \frac{k}{2}r^2\right)\ddot{x}^1\right].\end{aligned}$$

These calculations must account for $\frac{\partial f}{\partial s} = \frac{\partial f}{\partial x^\alpha}\frac{\partial x^\alpha}{\partial s}$ and the fact that, in Cartesian coordinates, $r^2 = (x^1)^2 + (x^2)^2 + (x^3)^2$. With algebraic development, the expression becomes:

$$\frac{\mathrm{d}}{\mathrm{d}s}\frac{\partial L}{\partial \dot{x}^1} = -2a\left(1 - \frac{k}{2}r^2\right)\ddot{x}^1 - \frac{4}{c}\left(1 - \frac{k}{2}r^2\right)\dot{x}^0\dot{x}^1 + 2ka^2\dot{x}^1\left[x^1\dot{x}^1 + x^2\dot{x}^2 + x^3\dot{x}^3\right]. \tag{B.12}$$

The second term of the Euler-Lagrange equation, expressing r^2 in Cartesian form, is:

$$\frac{\partial L}{\partial x^1} = a^2\frac{k}{2}2r\frac{x^1}{r}[(\dot{x}^1)^2 + (\dot{x}^2)^2 + (\dot{x}^3)^2]. \tag{B.13}$$

Combining the results and setting $r \to 0$, while dividing by $2a^2$, yields:

$$\ddot{x}^1 + \frac{2}{c}\frac{\dot{a}}{a}\dot{x}^0\dot{x}^1 - k\dot{x}^1\left[x^1\dot{x}^1 + x^2\dot{x}^2 + x^3\dot{x}^3\right] + \frac{1}{2}kx^1[(\dot{x}^1)^2 + (\dot{x}^2)^2 + (\dot{x}^3)^2] = 0. \tag{B.14}$$

Comparison with the geodesic equation for $\alpha = 1$, $\ddot{x}^1 + \Gamma^1_{\mu\nu}\dot{x}^\mu\dot{x}^\nu = 0$, yields the following non-zero Christoffel symbols:

$$\Gamma^1_{01} = \Gamma^1_{10} = \frac{1}{c}\frac{\dot{a}}{a}, \quad \Gamma^1_{11} = -kx^1 + \frac{1}{2}kx^1 = -\frac{1}{2}kx^1, \tag{B.15}$$

$$\Gamma^1_{13} = \Gamma^1_{31} = -\frac{kx^3}{2}, \quad \Gamma^1_{12} = \Gamma^1_{21} = -\frac{kx^2}{2}, \quad \Gamma^1_{22} = \Gamma^1_{33} = \frac{1}{2}kx^1. \tag{B.16}$$

- **Components $\alpha = 2$ and $\alpha = 3$:**

Given the symmetry of the equations, the results for $\alpha = 2$ and $\alpha = 3$ are completely analogous to those obtained for $\alpha = 1$. The Euler-Lagrange equations become:

$$\ddot{x}^2 + \frac{2}{c}\frac{\dot{a}}{a}\dot{x}^0\dot{x}^2 - k\dot{x}^2\left[x^1\dot{x}^1 + x^2\dot{x}^2 + x^3\dot{x}^3\right] + \frac{1}{2}kx^2[(\dot{x}^1)^2 + (\dot{x}^2)^2 + (\dot{x}^3)^2] = 0, \tag{B.17}$$

$$\ddot{x}^3 + \frac{2}{c}\frac{\dot{a}}{a}\dot{x}^0\dot{x}^3 - k\dot{x}^3\left[x^1\dot{x}^1 + x^2\dot{x}^2 + x^3\dot{x}^3\right] + \frac{1}{2}kx^3[(\dot{x}^1)^2 + (\dot{x}^2)^2 + (\dot{x}^3)^2] = 0, \tag{B.18}$$

with corresponding Christoffel symbols obtained by extending the previous results to $\alpha = 2$ and $\alpha = 3$.

The complete set of non-zero Christoffel symbols is:

$$\Gamma^0_{ij} = \frac{a\dot{a}}{c}\delta_{ij}, \tag{B.19}$$

$$\Gamma^i_{0k} = \Gamma^i_{k0} = \frac{1}{c}\frac{\dot{a}}{a}\delta_{ik}, \tag{B.20}$$

$$\Gamma^i_{ii} = -\frac{1}{2}kx^i, \tag{B.21}$$

$$\Gamma^i_{jj} = \frac{1}{2}kx^i, \tag{B.22}$$

$$\Gamma^i_{ij} = \Gamma^i_{ji} = -\frac{1}{2}kx^j. \tag{B.23}$$

B.2 Calculation of the Ricci Tensor Components

The Ricci tensor expression using the contracted Christoffel symbol formula is employed:

$$R_{\alpha\beta} = \frac{\partial}{\partial x^\sigma}\Gamma^\sigma_{\alpha\beta} - \frac{\partial^2}{\partial x^\beta \partial x^\alpha}\ln\sqrt{-g} + \Gamma^\tau_{\alpha\beta}\frac{\partial}{\partial x^\tau}\ln\sqrt{-g} - \Gamma^\sigma_{\tau\beta}\Gamma^\tau_{\alpha\sigma}. \tag{B.24}$$

From the metric form, with $g_{00} = 1$ and $g_{11} = g_{22} = g_{33} = -\frac{a^2}{\left(1+\frac{k}{4}r^2\right)^2}$, the determinant becomes:

$$g = \det(g_{\alpha\beta}) = -\frac{a^6}{\left(1+\frac{k}{4}r^2\right)^6} \quad \Longrightarrow \quad \sqrt{-g} = \frac{a^3}{\left(1+\frac{k}{4}r^2\right)^3}; \tag{B.25}$$

in the neighborhood of the origin ($r \to 0$):

$$g = -a^6 \quad \Longrightarrow \quad \sqrt{-g} = a^3, \tag{B.26}$$

and thus:

$$\text{For} \quad r \to 0 \quad \Rightarrow \quad \ln\sqrt{-g} = 3\ln a. \tag{B.27}$$

Given the homogeneity and isotropy of the metric, which ensures that only two components are linearly independent, Einstein's system of equations reduces to only two equations. The relevant components are R_{00} and R_{11}, with $R_{11} = R_{22} = R_{33}$ due to spatial symmetry.

- **Calculation of R_{00}:**

The expression is:

$$R_{00} = \frac{\partial}{\partial x^\sigma}\Gamma^\sigma_{00} - \frac{\partial^2}{\partial x^0 \partial x^0}\ln\sqrt{-g} + \Gamma^\tau_{00}\frac{\partial}{\partial x^\tau}\ln\sqrt{-g} - \Gamma^\sigma_{\tau 0}\Gamma^\tau_{0\sigma}. \tag{B.28}$$

Each term is calculated separately:

1. Term Γ^σ_{00}:

$$\Gamma^\sigma_{00} = 0 \quad \forall\sigma. \tag{B.29}$$

2. From the previous point, the third term $\Gamma^\tau_{00}\frac{\partial}{\partial x^\tau}\ln\sqrt{-g}$ is also zero.

3. Term $\frac{\partial^2}{\partial x^0\partial x^0}\ln\sqrt{-g}$:

$$\frac{\partial^2}{\partial x^0\partial x^0}\ln\sqrt{-g} = \frac{\partial^2}{\partial x^0\partial x^0}(3\ln a) = \frac{1}{c^2}\frac{\partial^2}{\partial t^2}(3\ln a) = \frac{1}{c^2}\frac{\partial}{\partial t}\left(\frac{\dot a}{a}\right)$$

$$\Downarrow$$

$$\frac{\partial^2}{\partial x^0\partial x^0}\ln\sqrt{-g} = \frac{3}{c^2}\frac{\ddot a}{a} - \frac{3}{c^2}\left(\frac{\dot a}{a}\right)^2. \tag{B.30}$$

4. Term $\Gamma^\sigma_{\tau 0}\Gamma^\tau_{0\sigma}$; developing the sums:

$$\Gamma^\sigma_{\tau 0}\Gamma^\tau_{0\sigma} = \Gamma^0_{0\sigma}\underbrace{\Gamma^\sigma_{00}}_{0} + \Gamma^i_{0\sigma}\Gamma^\sigma_{i0} = \underbrace{\Gamma^i_{00}}_{0}\Gamma^0_{i0} + \Gamma^i_{0k}\Gamma^k_{i0},$$

therefore:

$$\Gamma^\sigma_{\tau 0}\Gamma^\tau_{0\sigma} = \Gamma^i_{0k}\Gamma^k_{i0} = 3[\Gamma^i_{0k}]^2 = \frac{3}{c^2}\left(\frac{\dot a}{a}\right)^2. \tag{B.31}$$

Thus R_{00} becomes:

$$R_{00} = -\frac{3}{c^2}\frac{\ddot a}{a}. \tag{B.32}$$

- **Calculation of R_{11}:**

$$R_{11} = \frac{\partial}{\partial x^\sigma}\Gamma^\sigma_{11} - \frac{\partial^2}{\partial x^1\partial x^1}\ln\sqrt{-g} + \Gamma^\tau_{11}\frac{\partial}{\partial x^\tau}\ln\sqrt{-g} - \Gamma^\sigma_{\tau 1}\Gamma^\tau_{1\sigma}. \tag{B.33}$$

Each term is calculated separately:

1. Term $\frac{\partial}{\partial x^\sigma}\Gamma^\sigma_{11}$; summing over σ:

$$\frac{\partial}{\partial x^\sigma}\Gamma^\sigma_{11} = \frac{\partial}{\partial x^0}\Gamma^0_{11} + \frac{\partial}{\partial x^1}\Gamma^1_{11} + \frac{\partial}{\partial x^2}\Gamma^2_{11} + \frac{\partial}{\partial x^3}\Gamma^3_{11} = \frac{1}{c^2}\frac{\partial}{\partial t}(a\dot a) - \frac{1}{2}k + \frac{1}{2}k + \frac{1}{2}k,$$

so:

$$\frac{\partial}{\partial x^\sigma}\Gamma^\sigma_{11} = \frac{1}{c^2}\dot a^2 + \frac{1}{c^2}a\ddot a + \frac{1}{2}k. \tag{B.34}$$

2. Term $\frac{\partial^2}{\partial x^1\partial x^1}\ln\sqrt{-g}$; calculations must be performed without taking the limit initially, then setting $r\to 0$ at the end:

$$\sqrt{-g} = \frac{a^3}{\left(1+\frac{k}{4}r^2\right)^3} \simeq a^3\left(1-\frac{3}{4}kr^2\right), \tag{B.35}$$

where the second equality comes from Taylor expansion. The logarithm becomes:

$$\ln\sqrt{-g} \simeq \ln\left[a^3\left(1-\frac{3}{4}kr^2\right)\right] = 3\ln a + \ln\left(1-\frac{3}{4}kr^2\right). \tag{B.36}$$

Expressing r in Cartesian coordinates:

$$\frac{\partial^2}{\partial x^1\partial x^1}\ln\sqrt{-g} = 0 + \frac{\partial^2}{\partial x^1\partial x^1}\ln\left[1-\frac{3}{4}k((x^1)^2+(x^2)^2+(x^3)^2)\right] = -\frac{3}{2}k\frac{\partial}{\partial x^1}\left[\frac{x^1}{1-\frac{3}{4}kr^2}\right]$$
$$= -\frac{3}{2}k\left[\frac{1-\frac{3}{4}kr^2 - x^1\frac{\partial}{\partial x^1}\left(1-\frac{3}{4}kr^2\right)}{\left(1-\frac{3}{4}kr^2\right)^2}\right],$$

and in the limit $r\to 0$:

$$\text{For}\quad r\to 0 \quad\Rightarrow\quad \frac{\partial^2}{\partial x^1\partial x^1}\ln\sqrt{-g} = -\frac{3}{2}k. \tag{B.37}$$

3. Term $\Gamma^{\tau}_{11}\frac{\partial}{\partial x^{\tau}}\ln\sqrt{-g}$; restoring the contracted Christoffel symbol:
$$\Gamma^{\tau}_{11}\frac{\partial}{\partial x^{\tau}}\ln\sqrt{-g}=\Gamma^{\sigma}_{\tau\sigma}\Gamma^{\tau}_{11}; \tag{B.38}$$
summing first over σ and then over τ:
$$\Gamma^{\sigma}_{\tau\sigma}\Gamma^{\tau}_{11}=(\Gamma^{0}_{\tau 0}+\Gamma^{i}_{\tau i})\Gamma^{\tau}_{11}=\underbrace{\Gamma^{0}_{00}}_{0}\Gamma^{0}_{11}+\underbrace{\Gamma^{0}_{k0}}_{0}\Gamma^{k}_{11}+\Gamma^{i}_{0i}\Gamma^{0}_{11}+\Gamma^{i}_{ki}\Gamma^{k}_{11}.$$
The last term generally depends on x^1, x^2, x^3 and vanishes for $r\to 0$. Thus only the penultimate term remains:
$$\Gamma^{\sigma}_{\tau\sigma}\Gamma^{\tau}_{11}=\Gamma^{i}_{0i}\Gamma^{0}_{11}=3\Gamma^{1}_{01}\Gamma^{0}_{11}=\frac{3}{c^2}\dot{a}^2. \tag{B.39}$$

4. Term $\Gamma^{\sigma}_{\tau 1}\Gamma^{\tau}_{1\sigma}$; developing the sums:
$$\Gamma^{\tau}_{1\sigma}\Gamma^{\sigma}_{\tau 1}=\Gamma^{0}_{1\sigma}\Gamma^{\sigma}_{01}+\Gamma^{i}_{1\sigma}\Gamma^{\sigma}_{i1}=\underbrace{\Gamma^{0}_{10}}_{0}\Gamma^{0}_{01}+\Gamma^{0}_{1k}\Gamma^{k}_{01}+\Gamma^{i}_{10}\Gamma^{0}_{i1}+\Gamma^{i}_{1k}\Gamma^{k}_{i1};$$
- Second term: Γ^{0}_{1k} is non-zero only for $k=1$, leaving $\Gamma^{0}_{11}\Gamma^{1}_{01}$.
- Third term: Γ^{i}_{10} is non-zero only for $i=1$, leaving $\Gamma^{1}_{10}\Gamma^{0}_{11}$.
- Fourth term: generic elements are non-zero but contain factors of x^j that vanish for $r\to 0$.

Therefore:
$$\Gamma^{\tau}_{1\sigma}\Gamma^{\sigma}_{\tau 1}=\Gamma^{0}_{11}\Gamma^{1}_{01}+\Gamma^{1}_{10}\Gamma^{0}_{11}=2\Gamma^{0}_{11}\Gamma^{1}_{01}=\frac{2}{c^2}\dot{a}^2. \tag{B.40}$$

Thus R_{11} becomes:
$$R_{11}=\frac{1}{c^2}\dot{a}^2+\frac{1}{c^2}a\ddot{a}+\frac{1}{2}k+\frac{3}{2}k+\frac{3}{c^2}\dot{a}^2-\frac{2}{c^2}\dot{a}^2$$
$$\Downarrow$$
$$R_{11}=\frac{a^2}{c^2}\left[\frac{\ddot{a}}{a}+\frac{2\dot{a}^2}{a^2}+\frac{2kc^2}{a^2}\right]. \tag{B.41}$$

The Ricci scalar can now be calculated:
$$R=R^0{}_0+R^1{}_1+R^2{}_2+R^3{}_3=R^0{}_0+3R^1{}_1, \tag{B.42}$$
where the second equality follows from spatial homogeneity and isotropy. The components are:
$$R^0{}_0=g^{00}R_{00}=1\cdot R_{00}=-\frac{3}{c^2}\frac{\ddot{a}}{a}. \tag{B.43}$$
The inverse metric component g^{11} is needed for $R^1{}_1$:
$$g^{11}=\frac{1}{g_{11}}=-\frac{\left(1+\frac{k}{4}r^2\right)^2}{a^2}, \tag{B.44}$$
and in the limit at the origin:
$$\text{For}\quad r\to 0\quad\Rightarrow\quad g^{11}=-\frac{1}{a^2}. \tag{B.45}$$
Thus:
$$R^1{}_1=g^{11}R_{11}=-\frac{1}{c^2}\left[\frac{\ddot{a}}{a}+2\left(\frac{\dot{a}}{a}\right)^2+\frac{2kc^2}{a^2}\right]. \tag{B.46}$$
The Ricci curvature scalar becomes:
$$R=-\frac{6}{c^2}\left[\frac{\ddot{a}}{a}+\left(\frac{\dot{a}}{a}\right)^2+\frac{kc^2}{a^2}\right]. \tag{B.47}$$

Appendix C

Estimators of C_ℓ

The analysis begins by considering **estimators in the ideal case**, then examines how to adapt them for realistic observations. The ideal case assumes observation of only the CMB signal with no noise, no foregrounds, and full-sky coverage without obstructions.

For the ideal case, the estimator $\hat{C}_\ell$ that extracts C_ℓ from observations is given by (for fixed ℓ):

$$\hat{C}_\ell = \frac{1}{2\ell+1} \sum_{m=-\ell}^{\ell} |a_{\ell m}|^2. \tag{C.1}$$

The ensemble average of this estimator is:

$$\langle \hat{C}_\ell \rangle = \frac{1}{2\ell+1} \sum_{m=-\ell}^{\ell} \underbrace{\langle a_{\ell m} a^*_{\ell m} \rangle}_{C_\ell} = \frac{C_\ell}{2\ell+1} \sum_{m=-\ell}^{\ell} 1. \tag{C.2}$$

Since $\sum_{m=-\ell}^{\ell} 1 = 2\ell + 1$, the result becomes:

$$\langle \hat{C}_\ell \rangle = C_\ell, \tag{C.3}$$

demonstrating that the estimator $\hat{C}_\ell$ is **unbiased**: its expectation value equals the true parameter it estimates.

The **consistency** of the estimator is verified by examining its variance. By definition:

$$\mathrm{Var}(\hat{C}_\ell) = \langle (\hat{C}_\ell - \langle \hat{C}_\ell \rangle)^2 \rangle = \langle \hat{C}_\ell^2 \rangle - \langle \hat{C}_\ell \rangle^2 = \langle \hat{C}_\ell^2 \rangle - C_\ell^2. \tag{C.4}$$

To compute $\langle \hat{C}_\ell^2 \rangle$:

$$\langle \hat{C}_\ell^2 \rangle = \frac{1}{(2\ell+1)^2} \sum_{m=-\ell}^{\ell} \sum_{m'=-\ell}^{\ell} \langle a_{\ell m} a^*_{\ell m} a_{\ell m'} a^*_{\ell m'} \rangle. \tag{C.5}$$

Wick's theorem is applied to express the four-point correlation function as a sum over all possible pairings:

$$\langle a_{\ell m} a^*_{\ell m} a_{\ell m'} a^*_{\ell m'} \rangle = \langle a_{\ell m} a^*_{\ell m} \rangle \langle a_{\ell m'} a^*_{\ell m'} \rangle + \langle a_{\ell m} a_{\ell m'} \rangle \langle a^*_{\ell m} a^*_{\ell m'} \rangle + \langle a_{\ell m} a^*_{\ell m'} \rangle \langle a^*_{\ell m} a_{\ell m'} \rangle. \tag{C.6}$$

The first term gives C_ℓ^2. For the remaining terms, the reality condition of $\delta T(\hat{n})$ implies:

$$a_{\ell m} = (-1)^m a^*_{\ell(-m)}, \tag{C.7}$$

Therefore:

$$\langle a_{\ell m} a_{\ell m'} \rangle = (-1)^{m'} \langle a_{\ell m} a^*_{\ell(-m')} \rangle = (-1)^{m'} C_\ell \delta_{m(-m')} \tag{C.8}$$

$$\langle a^*_{\ell m} a^*_{\ell m'} \rangle = (-1)^{m+m'} \langle a_{\ell(-m)} a_{\ell(-m')} \rangle = (-1)^m C_\ell \delta_{(-m)m'}. \tag{C.9}$$

Substituting these results:

$$\langle \hat{C}_\ell^2 \rangle = \frac{1}{(2\ell+1)^2} \sum_{m,m'} \left[C_\ell^2 + (-1)^{m'} C_\ell^2 \delta_{m(-m')} + (-1)^m C_\ell^2 \delta_{mm'} \right]. \tag{C.10}$$

The sum over the first term gives $(2\ell+1)^2 C_\ell^2$. For the second term, $\delta_{m(-m')} = 1$ only when $m' = -m$, which occurs for $2\ell+1$ pairs. Similarly, $\delta_{mm'} = 1$ for $2\ell+1$ pairs when $m = m'$. The alternating signs from $(-1)^m$ factors cancel in the symmetric sum, yielding:

$$\langle \hat{C}_\ell^2 \rangle = C_\ell^2 + \frac{2C_\ell^2}{2\ell+1}. \tag{C.11}$$

Therefore, the variance of the estimator is:

$$\mathrm{Var}(\hat{C}_\ell) = \langle \hat{C}_\ell^2 \rangle - C_\ell^2 = \frac{2C_\ell^2}{2\ell+1}. \tag{C.12}$$

The variance is proportional to the signal itself. This irreducible variance, present even in the ideal case (no noise, full-sky coverage, no foregrounds), is known as **cosmic variance**. It arises from the fundamental statistical limitation that only one realization of the Universe can be observed, limiting the ability to precisely determine the underlying power spectrum.

C.1 The $\hat{C}_\ell$ Estimators in the Real Case

Despite cosmic variance, the estimators discussed above perform well under ideal conditions. However, realistic observations introduce several complications:

1. **Incomplete sky coverage**: Sky fraction $f_{\mathrm{sky}} < 1$ due to Galactic and foreground masking.
2. **Instrumental noise**: Stochastic noise from detectors and systematics.
3. **Finite angular resolution**: Instruments observe with a finite beam that smooths the signal.

These effects can be treated separately or collectively through a unified approach using **pseudo-C_ℓ estimators**. In this framework, the ideal $a_{\ell m}$ coefficients are replaced by $\tilde{a}_{\ell m}$ coefficients that incorporate information about noise, partial sky coverage, and finite instrumental resolution.

The observed temperature fluctuations can be written as:

$$\delta T^{\mathrm{obs}}(\hat{n}) = \delta T^{(b)}_{\mathrm{CMB}}(\hat{n}) + \delta T_n(\hat{n}), \tag{C.13}$$

where $\delta T^{(b)}_{\mathrm{CMB}}(\hat{n})$ represents the CMB fluctuations convolved with the instrumental beam, and $\delta T_n(\hat{n})$ represents the noise contribution.

The beam-convolved CMB signal is related to the true CMB signal through:

$$\delta T^{(b)}_{\mathrm{CMB}}(\hat{n}) = \int \mathrm{d}\Omega' \, \delta T_{\mathrm{CMB}}(\hat{n}') \, b(\hat{n}, \hat{n}'), \tag{C.14}$$

where $b(\hat{n}, \hat{n}')$ is the **beam function** that encodes all instrumental properties. In the ideal case of infinite resolution, $b(\hat{n}, \hat{n}') \to \delta(\hat{n} - \hat{n}')$ where δ is the Dirac delta function.

For many instruments, beams exhibit circular symmetry around the pointing direction, satisfying the **circularity condition**:

$$b(\hat{n}, \hat{n}') = b(\hat{n} \cdot \hat{n}'), \tag{C.15}$$

meaning the beam function depends only on the angular separation between directions, not on their individual orientations.

Under the circularity condition, the beam convolution becomes:

$$\delta T^{(b)}_{\mathrm{CMB}}(\hat{n}) = \int \mathrm{d}\Omega'\, b(\hat{n}\cdot\hat{n}')\, \delta T_{\mathrm{CMB}}(\hat{n}'). \tag{C.16}$$

The spherical harmonic coefficients from partial sky observations are defined as:

$$\tilde{a}_{\ell m} = \int_{4\pi - M} \mathrm{d}\Omega\, \delta T^{\mathrm{obs}}(\hat{n})\, Y^*_{\ell m}(\hat{n}), \tag{C.17}$$

where M represents the masked region (primarily the Galactic plane and point sources).

Substituting the expression for $\delta T^{\mathrm{obs}}(\hat{n})$:

$$\tilde{a}_{\ell m} = \int_{4\pi - M} \mathrm{d}\Omega \int \mathrm{d}\Omega'\, b(\hat{n}\cdot\hat{n}') \sum_{\ell' m'} a_{\ell' m'} Y_{\ell' m'}(\hat{n}') Y^*_{\ell m}(\hat{n}) + \tilde{a}^N_{\ell m}, \tag{C.18}$$

where $\tilde{a}^N_{\ell m}$ represents the noise contribution:

$$\tilde{a}^N_{\ell m} = \int_{4\pi - M} \mathrm{d}\Omega\, \delta T_n(\hat{n})\, Y^*_{\ell m}(\hat{n}). \tag{C.19}$$

For circular beams, the convolution can be expressed using beam transfer functions b_ℓ:

$$\int \mathrm{d}\Omega'\, b(\hat{n}\cdot\hat{n}')\, Y_{\ell' m'}(\hat{n}') = b_{\ell'} Y_{\ell' m'}(\hat{n}), \tag{C.20}$$

where b_ℓ characterizes the beam's effect on multipole ℓ.

This allows the expression to be rewritten as:

$$\tilde{a}_{\ell m} = \sum_{\ell' m'} a_{\ell' m'} b_{\ell'} \int_{4\pi - M} \mathrm{d}\Omega\, Y_{\ell' m'}(\hat{n}) Y^*_{\ell m}(\hat{n}) + \tilde{a}^N_{\ell m}. \tag{C.21}$$

The integral defines the **coupling kernel**:

$$K_{\ell m \ell' m'} = \int_{4\pi - M} \mathrm{d}\Omega\, Y_{\ell' m'}(\hat{n}) Y^*_{\ell m}(\hat{n}), \tag{C.22}$$

which encodes the effect of incomplete sky coverage. For full-sky observations, $K_{\ell m \ell' m'} = \delta_{\ell\ell'}\delta_{mm'}$.

Therefore:

$$\tilde{a}_{\ell m} = \sum_{\ell' m'} a_{\ell' m'} b_{\ell'} K_{\ell m \ell' m'} + \tilde{a}^N_{\ell m}. \tag{C.23}$$

This expression for $\tilde{a}_{\ell m}$ contains all non-idealities:

- $b_{\ell'}$: beam effects and finite resolution
- $K_{\ell m \ell' m'}$: mode coupling due to incomplete sky coverage
- $\tilde{a}^N_{\ell m}$: instrumental and systematic noise

The C_ℓ estimator is now defined as:

$$\hat{\tilde{C}}_\ell = \frac{1}{2\ell+1} \sum_{m=-\ell}^{\ell} |\tilde{a}_{\ell m}|^2. \tag{C.24}$$

However, this estimator is biased. Substituting the expression for $\tilde{a}_{\ell m}$ and taking the ensemble average yields:

$$\langle \hat{\tilde{C}}_\ell \rangle = \frac{1}{2\ell+1} \sum_{m=-\ell}^{\ell} \sum_{\ell' m'} b_{\ell'}^2 C_{\ell'} |K_{\ell m \ell' m'}|^2 + \langle \hat{\tilde{C}}_\ell^N \rangle, \tag{C.25}$$

which can be written as:

$$\langle \hat{\tilde{C}}_\ell \rangle = \sum_{\ell'} b_{\ell'}^2 C_{\ell'} G_{\ell\ell'} + \langle \hat{\tilde{C}}_\ell^N \rangle, \tag{C.26}$$

where the **mode-coupling kernel** $G_{\ell\ell'}$ is defined as:

$$G_{\ell\ell'} = \frac{1}{2\ell+1} \sum_{m=-\ell}^{\ell} \sum_{m'=-\ell'}^{\ell'} |K_{\ell m \ell' m'}|^2. \tag{C.27}$$

Therefore, in general:

$$\langle \hat{\tilde{C}}_\ell \rangle \neq C_\ell, \tag{C.28}$$

demonstrating that the $\hat{\tilde{C}}_\ell$ estimator is biased.

To obtain an unbiased estimator, the **pseudo-C_ℓ** (PCL) estimator is defined:

$$\hat{C}_\ell^{\mathrm{PCL}} = \frac{1}{b_\ell^2} G_{\ell\ell'}^{-1} \left[\hat{\tilde{C}}_{\ell'} - \langle \hat{\tilde{C}}_{\ell'}^N \rangle \right], \tag{C.29}$$

where summation over repeated indices is implied. This construction directly solves the bias problem. Taking the expectation value:

$$\langle \hat{C}_\ell^{\mathrm{PCL}} \rangle = \frac{1}{b_\ell^2} G_{\ell\ell'}^{-1} \left[\langle \hat{\tilde{C}}_{\ell'} \rangle - \langle \hat{\tilde{C}}_{\ell'}^N \rangle \right], \tag{C.30}$$

and substituting eq. (C.26), using the property $G_{\ell\ell'}^{-1} G_{\ell''\ell'} = \delta_{\ell\ell''}$:

$$\langle \hat{C}_\ell^{\mathrm{PCL}} \rangle = \frac{1}{b_\ell^2} b_\ell^2 C_\ell = C_\ell, \tag{C.31}$$

confirming that $\hat{C}_\ell^{\mathrm{PCL}}$ is an unbiased estimator.

The mode-coupling kernel $G_{\ell'\ell''}$ can also be expressed in terms of the sky mask properties:

$$G_{\ell'\ell''} = \sum_{\ell'''} W_{\ell'''} \frac{(2\ell''+1)(2\ell'''+1)}{4\pi} \begin{pmatrix} \ell' & \ell'' & \ell''' \\ 0 & 0 & 0 \end{pmatrix}^2, \tag{C.32}$$

where the matrix represents the **Wigner 3j symbol**, and $W_{\ell'''}$ is the angular power spectrum of the mask:

$$W_{\ell'''} = \frac{1}{2\ell'''+1} \sum_{m=-\ell'''}^{\ell'''} |w_{\ell''' m}|^2, \tag{C.33}$$

where $w_{\ell''' m}$ are the spherical harmonic coefficients of the mask function:

$$M(\hat{n}) = \sum_{\ell''' m} w_{\ell''' m} Y_{\ell''' m}(\hat{n}). \tag{C.34}$$

Appendix D

Useful Integrals

This section contains the fundamental integrals necessary for manipulating the solutions that appear in the third-order Green's function solution eq. (3.73). The derivation of these integrals relies on systematic application of integration by parts.

$$\int_x^\infty \frac{\mathrm{d}u}{u^2}\, e^{2iu} = \frac{e^{2ix}}{x} + 2i \int_x^\infty \frac{\mathrm{d}u}{u}\, e^{2iu} \tag{D.1a}$$

$$\int_x^\infty \frac{\mathrm{d}u}{u^3}\, e^{2iu} = \left(\frac{1}{2x^2} + \frac{i}{x}\right) e^{2ix} - 2 \int_x^\infty \frac{\mathrm{d}u}{u}\, e^{2iu} \tag{D.1b}$$

$$\int_x^\infty \frac{\mathrm{d}u}{u^4}\, e^{2iu} = \left(\frac{1}{3x^3} + \frac{i}{3x^2} - \frac{2}{3x}\right) e^{2ix} - \frac{4i}{3} \int_x^\infty \frac{\mathrm{d}u}{u}\, e^{2iu} \tag{D.1c}$$

$$\begin{aligned}\int_x^\infty \frac{\mathrm{d}u}{u^2}\, e^{-2iu} \int_u^\infty \frac{\mathrm{d}t}{t}\, e^{2it} = &-\frac{1}{x} + \frac{e^{-2ix}}{x} \int_x^\infty \frac{\mathrm{d}u}{u}\, e^{2iu} \\ &- 2i \int_x^\infty \frac{\mathrm{d}u}{u}\, e^{-2iu} \int_u^\infty \frac{\mathrm{d}t}{t}\, e^{2it}\end{aligned} \tag{D.2a}$$

$$\begin{aligned}\int_x^\infty \frac{\mathrm{d}u}{u^3}\, e^{-2iu} \int_u^\infty \frac{\mathrm{d}t}{t}\, e^{2it} = &-\left(\frac{1}{4x^2} - \frac{i}{x}\right) + \left(\frac{1}{2x^2} - \frac{i}{x}\right) e^{-2ix} \int_x^\infty \frac{\mathrm{d}u}{u}\, e^{2iu} \\ &- 2 \int_x^\infty \frac{\mathrm{d}u}{u}\, e^{-2iu} \int_u^\infty \frac{\mathrm{d}t}{t}\, e^{2it}\end{aligned} \tag{D.2b}$$

$$\begin{aligned}\int_x^\infty \frac{\mathrm{d}u}{u^4}\, e^{-2iu} \int_u^\infty \frac{\mathrm{d}t}{t}\, e^{2it} = &-\left(\frac{1}{9x^3} - \frac{i}{6x^2} - \frac{2}{3x}\right) + \left(\frac{1}{3x^3} - \frac{i}{3x^2} - \frac{2}{3x}\right) e^{-2ix} \int_x^\infty \frac{\mathrm{d}u}{u}\, e^{2iu} \\ &+ \frac{4i}{3} \int_x^\infty \frac{\mathrm{d}u}{u}\, e^{-2iu} \int_u^\infty \frac{\mathrm{d}t}{t}\, e^{2it}\end{aligned} \tag{D.2c}$$

$$\int_x^\infty \frac{\mathrm{d}u}{u^2}\, e^{2iu} \ln u = \frac{e^{2ix}}{x} + \frac{e^{2ix}\ln x}{x} + 2i \int_x^\infty \frac{\mathrm{d}u}{u}\, e^{2iu} + 2i \int_x^\infty \frac{\mathrm{d}u}{u}\, e^{2iu} \ln u \tag{D.3a}$$

$$\begin{aligned}\int_x^\infty \frac{\mathrm{d}u}{u^3}\, e^{2iu} \ln u = {}& \left(\frac{1}{4x^2} + \frac{3i}{2x}\right) e^{2ix} + \left(\frac{1}{2x^2} + \frac{i}{x}\right) e^{2ix} \ln x \\ & - 3 \int_x^\infty \frac{\mathrm{d}u}{u}\, e^{2iu} - 2 \int_x^\infty \frac{\mathrm{d}u}{u}\, e^{2iu} \ln u \end{aligned} \tag{D.3b}$$

$$\begin{aligned}\int_x^\infty \frac{\mathrm{d}u}{u^4}\, e^{2iu} \ln u = {}& \left(\frac{1}{9x^3} + \frac{5i}{18x^2} - \frac{11}{9x}\right) e^{2ix} + \left(\frac{1}{3x^3} + \frac{i}{3x^2} - \frac{2}{3x}\right) e^{2ix} \ln x \\ & - \frac{22i}{9} \int_x^\infty \frac{\mathrm{d}u}{u}\, e^{2iu} - \frac{4i}{3} \int_x^\infty \frac{\mathrm{d}u}{u}\, e^{2iu} \ln u \end{aligned} \tag{D.3c}$$

$$\begin{aligned}\int_x^\infty \frac{\mathrm{d}u}{u^2} \int_u^\infty \frac{\mathrm{d}t}{t}\, e^{-2it} \int_t^\infty \frac{\mathrm{d}s}{s}\, e^{2is} = {}& \frac{1}{x} - \frac{e^{-2ix}}{x} \int_x^\infty \frac{\mathrm{d}u}{u}\, e^{2iu} \\ & + \left(\frac{1}{x} + 2i\right) \int_x^\infty \frac{\mathrm{d}u}{u}\, e^{-2iu} \int_u^\infty \frac{\mathrm{d}t}{t}\, e^{2it} \end{aligned} \tag{D.4a}$$

$$\begin{aligned}\int_x^\infty \frac{\mathrm{d}u}{u^4} \int_u^\infty \frac{\mathrm{d}t}{t}\, e^{-2it} \int_t^\infty \frac{\mathrm{d}s}{s}\, e^{2is} = {}& \left(\frac{1}{27x^3} - \frac{i}{18x^2} - \frac{2}{9x}\right) \\ & - \left(\frac{1}{9x^3} - \frac{i}{9x^2} - \frac{2}{9x}\right) e^{-2ix} \int_x^\infty \frac{\mathrm{d}u}{u}\, e^{2iu} \\ & + \left(\frac{1}{3x^3} - \frac{4i}{9}\right) \int_x^\infty \frac{\mathrm{d}u}{u}\, e^{-2iu} \int_u^\infty \frac{\mathrm{d}t}{t}\, e^{2it} \end{aligned} \tag{D.4b}$$

$$\begin{aligned}\int_x^\infty \frac{\mathrm{d}u}{u^2}\, e^{2iu} \int_u^\infty \frac{\mathrm{d}t}{t}\, e^{-2it} \int_t^\infty \frac{\mathrm{d}s}{s}\, e^{2is} &= \frac{e^{2ix}}{x} - \left(\frac{1}{x} - 2i\right) \int_x^\infty \frac{\mathrm{d}u}{u}\, e^{2iu} \\ &\quad + \frac{e^{2ix}}{x} \int_x^\infty \frac{\mathrm{d}u}{u}\, e^{-2iu} \int_u^\infty \frac{\mathrm{d}t}{t}\, e^{2it} \\ &\quad + 2i \int_x^\infty \frac{\mathrm{d}u}{u}\, e^{2iu} \int_u^\infty \frac{\mathrm{d}t}{t}\, e^{-2it} \int_t^\infty \frac{\mathrm{d}s}{s}\, e^{2is} \end{aligned} \tag{D.5a}$$

$$\begin{aligned}\int_x^\infty \frac{\mathrm{d}u}{u^3}\, e^{2iu} \int_u^\infty \frac{\mathrm{d}t}{t}\, e^{-2it} \int_t^\infty \frac{\mathrm{d}s}{s}\, e^{2is} &= \left(\frac{1}{8x^2} + \frac{5i}{4x}\right) e^{2ix} - \left(\frac{1}{4x^2} + \frac{i}{x} + \frac{5}{2}\right) \int_x^\infty \frac{\mathrm{d}u}{u}\, e^{2iu} \\ &\quad + \left(\frac{1}{2x^2} + \frac{i}{x}\right) e^{2ix} \int_x^\infty \frac{\mathrm{d}u}{u}\, e^{-2iu} \int_u^\infty \frac{\mathrm{d}t}{t}\, e^{2it} \\ &\quad - 2 \int_x^\infty \frac{\mathrm{d}u}{u}\, e^{2iu} \int_u^\infty \frac{\mathrm{d}t}{t}\, e^{-2it} \int_t^\infty \frac{\mathrm{d}s}{s}\, e^{2is} \end{aligned} \tag{D.5b}$$

$$\begin{aligned}\int_x^\infty \frac{\mathrm{d}u}{u^4}\, e^{2iu} \int_u^\infty \frac{\mathrm{d}t}{t}\, e^{-2it} \int_t^\infty \frac{\mathrm{d}s}{s}\, e^{2is} &= \left(\frac{1}{27x^3} + \frac{13i}{108x^2} - \frac{49}{54x}\right) e^{2ix} \\ &\quad - \left(\frac{1}{9x^3} + \frac{i}{6x^2} - \frac{2}{3x} + \frac{49i}{27}\right) \int_x^\infty \frac{\mathrm{d}u}{u}\, e^{2iu} \\ &\quad + \left(\frac{1}{3x^3} + \frac{i}{3x^2} - \frac{2}{3x}\right) e^{2ix} \int_x^\infty \frac{\mathrm{d}u}{u}\, e^{-2iu} \int_u^\infty \frac{\mathrm{d}t}{t}\, e^{2it} \\ &\quad - \frac{4i}{3} \int_x^\infty \frac{\mathrm{d}u}{u}\, e^{2iu} \int_u^\infty \frac{\mathrm{d}t}{t}\, e^{-2it} \int_t^\infty \frac{\mathrm{d}s}{s}\, e^{2is} \end{aligned} \tag{D.5c}$$

$$\begin{aligned}\int_x^\infty \frac{\mathrm{d}u}{u^2}\, e^{-2iu} \int_u^\infty \frac{\mathrm{d}t}{t}\, e^{2it} \ln t &= -\frac{1}{x} - \frac{\ln x}{x} + \frac{e^{-2ix}}{x} \int_x^\infty \frac{\mathrm{d}u}{u}\, e^{2iu} \ln u \\ &\quad - 2i \int_x^\infty \frac{\mathrm{d}u}{u}\, e^{-2iu} \int_u^\infty \frac{\mathrm{d}t}{t}\, e^{2it} \ln t \end{aligned} \tag{D.6a}$$

$$\begin{aligned}\int_x^\infty \frac{\mathrm{d}u}{u^3}\, e^{-2iu} \int_u^\infty \frac{\mathrm{d}t}{t}\, e^{2it} \ln t &= -\left(\frac{1}{8x^2} - \frac{i}{x}\right) - \left(\frac{1}{4x^2} - \frac{i}{x}\right) \ln x \\ &\quad + \left(\frac{1}{2x^2} - \frac{i}{x}\right) e^{-2ix} \int_x^\infty \frac{\mathrm{d}u}{u}\, e^{2iu} \ln u \\ &\quad - 2 \int_x^\infty \frac{\mathrm{d}u}{u}\, e^{-2iu} \int_u^\infty \frac{\mathrm{d}t}{t}\, e^{2it} \ln t \end{aligned} \tag{D.6b}$$

$$\begin{aligned}\int_x^\infty \frac{\mathrm{d}u}{u^4}\, e^{-2iu} \int_u^\infty \frac{\mathrm{d}t}{t}\, e^{2it} \ln t &= -\left(\frac{1}{27x^3} - \frac{i}{12x^2} - \frac{2}{3x}\right) - \left(\frac{1}{9x^3} - \frac{i}{6x^2} - \frac{2}{3x}\right) \ln x \\ &\quad + \left(\frac{1}{3x^3} - \frac{i}{3x^2} - \frac{2}{3x}\right) e^{-2ix} \int_x^\infty \frac{\mathrm{d}u}{u}\, e^{2iu} \ln u \\ &\quad + \frac{4i}{3} \int_x^\infty \frac{\mathrm{d}u}{u}\, e^{-2iu} \int_u^\infty \frac{\mathrm{d}t}{t}\, e^{2it} \ln t \end{aligned} \tag{D.6c}$$

$$\int_x^\infty \frac{\mathrm{d}u}{u^2}\int_u^\infty \frac{\mathrm{d}t}{t}\, e^{2it} = -\frac{e^{2ix}}{x} + \left(\frac{1}{x} - 2i\right)\int_x^\infty \frac{\mathrm{d}u}{u}\, e^{2iu} \tag{D.7a}$$

$$\int_x^\infty \frac{\mathrm{d}u}{u^3}\int_u^\infty \frac{\mathrm{d}t}{t}\, e^{2it} = -\left(\frac{1}{4x^2} + \frac{i}{2x}\right)e^{2ix} + \left(\frac{1}{2x^2} + 1\right)\int_x^\infty \frac{\mathrm{d}u}{u}\, e^{2iu} \tag{D.7b}$$

$$\int_x^\infty \frac{\mathrm{d}u}{u^4}\int_u^\infty \frac{\mathrm{d}t}{t}\, e^{2it} = -\left(\frac{1}{9x^3} + \frac{i}{9x^2} - \frac{2}{9x}\right)e^{2ix} + \left(\frac{1}{3x^3} + \frac{4i}{9}\right)\int_x^\infty \frac{\mathrm{d}u}{u}\, e^{2iu} \tag{D.7c}$$

$$\begin{aligned}\int_x^\infty \frac{\mathrm{d}u}{u^2}\int_u^\infty \frac{\mathrm{d}t}{t}\, e^{2it}\ln t = {}& -\frac{e^{2ix}}{x} - \frac{e^{2ix}\ln x}{x} \\ & - 2i\int_x^\infty \frac{\mathrm{d}u}{u}\, e^{2iu} + \left(\frac{1}{x} - 2i\right)\int_x^\infty \frac{\mathrm{d}u}{u}\, e^{2iu}\ln u\end{aligned} \tag{D.8a}$$

$$\begin{aligned}\int_x^\infty \frac{\mathrm{d}u}{u^4}\int_u^\infty \frac{\mathrm{d}t}{t}\, e^{2it}\ln t = {}& -\left(\frac{1}{27x^3} + \frac{5i}{54x^2} - \frac{11}{27x}\right)e^{2ix} - \left(\frac{1}{9x^3} + \frac{i}{9x^2} - \frac{2}{9x}\right)e^{2ix}\ln x \\ & + \frac{22i}{27}\int_x^\infty \frac{\mathrm{d}u}{u}\, e^{2iu} + \left(\frac{1}{3x^3} + \frac{4i}{9}\right)\int_x^\infty \frac{\mathrm{d}u}{u}\, e^{2iu}\ln u\end{aligned} \tag{D.8b}$$

$$\int_x^\infty \frac{\mathrm{d}u}{u^2}\, e^{-2iu} \ln u \int_u^\infty \frac{\mathrm{d}t}{t}\, e^{2it} = -\frac{2}{x} - \frac{\ln x}{x} + \frac{e^{-2ix}}{x} \int_x^\infty \frac{\mathrm{d}u}{u}\, e^{2iu}$$
$$+ \frac{e^{-2ix} \ln x}{x} \int_x^\infty \frac{\mathrm{d}u}{u}\, e^{2iu} - 2i \int_x^\infty \frac{\mathrm{d}u}{u}\, e^{-2iu} \int_u^\infty \frac{\mathrm{d}t}{t}\, e^{2it}$$
$$- 2i \int_x^\infty \frac{\mathrm{d}u}{u}\, e^{-2iu} \ln u \int_u^\infty \frac{\mathrm{d}t}{t}\, e^{2it} \tag{D.9a}$$

$$\int_x^\infty \frac{\mathrm{d}u}{u^3}\, e^{-2iu} \ln u \int_u^\infty \frac{\mathrm{d}t}{t}\, e^{2it} = -\left(\frac{1}{4x^2} - \frac{5i}{2x}\right) - \left(\frac{1}{4x^2} - \frac{i}{x}\right) \ln x$$
$$+ \left(\frac{1}{4x^2} - \frac{3i}{2x}\right) e^{-2ix} \int_x^\infty \frac{\mathrm{d}u}{u}\, e^{2iu}$$
$$+ \left(\frac{1}{2x^2} - \frac{i}{x}\right) e^{-2ix} \ln x \int_x^\infty \frac{\mathrm{d}u}{u}\, e^{2iu}$$
$$- 3 \int_x^\infty \frac{\mathrm{d}u}{u}\, e^{-2iu} \int_u^\infty \frac{\mathrm{d}t}{t}\, e^{2it}$$
$$- 2 \int_x^\infty \frac{\mathrm{d}u}{u}\, e^{-2iu} \ln u \int_u^\infty \frac{\mathrm{d}t}{t}\, e^{2it} \tag{D.9b}$$

$$\int_x^\infty \frac{\mathrm{d}u}{u^4}\, e^{-2iu} \ln u \int_u^\infty \frac{\mathrm{d}t}{t}\, e^{2it} = -\left(\frac{2}{27x^3} - \frac{2i}{9x^2} - \frac{17}{9x}\right) - \left(\frac{1}{9x^3} - \frac{i}{6x^2} - \frac{2}{3x}\right) \ln x$$
$$+ \left(\frac{1}{9x^3} - \frac{5i}{18x^2} - \frac{11}{9x}\right) e^{-2ix} \int_x^\infty \frac{\mathrm{d}u}{u}\, e^{2iu}$$
$$+ \left(\frac{1}{3x^3} - \frac{i}{3x^2} - \frac{2}{3x}\right) e^{-2ix} \ln x \int_x^\infty \frac{\mathrm{d}u}{u}\, e^{2iu}$$
$$+ \frac{22i}{9} \int_x^\infty \frac{\mathrm{d}u}{u}\, e^{-2iu} \int_u^\infty \frac{\mathrm{d}t}{t}\, e^{2it}$$
$$+ \frac{4i}{3} \int_x^\infty \frac{\mathrm{d}u}{u}\, e^{-2iu} \ln u \int_u^\infty \frac{\mathrm{d}t}{t}\, e^{2it} \tag{D.9c}$$

$$\int_x^\infty \frac{\mathrm{d}u}{u^2}\, \ln u \int_u^\infty \frac{\mathrm{d}t}{t}\, e^{2it} = -\frac{2e^{2ix}}{x} - \frac{e^{2ix} \ln x}{x} + \left(\frac{1}{x} - 4i\right) \int_x^\infty \frac{\mathrm{d}u}{u}\, e^{2iu}$$
$$+ \frac{\ln x}{x} \int_x^\infty \frac{\mathrm{d}u}{u}\, e^{2iu} - 2i \int_x^\infty \frac{\mathrm{d}u}{u}\, e^{2iu} \ln u \tag{D.10a}$$

$$\int_x^\infty \frac{\mathrm{d}u}{u^4}\, \ln u \int_u^\infty \frac{\mathrm{d}t}{t}\, e^{2it} = -\left(\frac{2}{27x^3} + \frac{7i}{54x^2} - \frac{13}{27x}\right) e^{2ix} - \left(\frac{1}{9x^3} - \frac{i}{9x^2} - \frac{2}{9x}\right) e^{2ix} \ln x$$
$$+ \left(\frac{1}{9x^3} + \frac{26i}{27}\right) \int_x^\infty \frac{\mathrm{d}u}{u}\, e^{2iu}$$
$$+ \frac{\ln x}{3x^3} \int_x^\infty \frac{\mathrm{d}u}{u}\, e^{2iu}$$
$$+ \frac{4i}{9} \int_x^\infty \frac{\mathrm{d}u}{u}\, e^{2iu} \ln u \tag{D.10b}$$

$$\begin{aligned}\int_x^\infty \frac{\mathrm{d}u}{u^2}\, e^{2iu} \ln^2 u = {}& \frac{2e^{2ix}}{x} + \frac{2e^{2ix}\ln x}{x} + \frac{e^{2ix}\ln^2 x}{x} \\ &+ 4i \int_x^\infty \frac{\mathrm{d}u}{u}\, e^{2iu} + 4i \int_x^\infty \frac{\mathrm{d}u}{u}\, e^{2iu} \ln u \\ &+ 2i \int_x^\infty \frac{\mathrm{d}u}{u}\, e^{2iu} \ln^2 u \end{aligned} \tag{D.11a}$$

$$\begin{aligned}\int_x^\infty \frac{\mathrm{d}u}{u^3}\, e^{2iu} \ln^2 u = {}& \left(\frac{1}{4x^2} + \frac{7i}{2x}\right) e^{2ix} + \left(\frac{1}{2x^2} + \frac{3i}{x}\right) e^{2ix} \ln x \\ &+ \left(\frac{1}{2x^2} + \frac{i}{x}\right) e^{2ix} \ln^2 x - 7 \int_x^\infty \frac{\mathrm{d}u}{u}\, e^{2iu} \\ &- 6 \int_x^\infty \frac{\mathrm{d}u}{u}\, e^{2iu} \ln u - 2 \int_x^\infty \frac{\mathrm{d}u}{u}\, e^{2iu} \ln^2 u \end{aligned} \tag{D.11b}$$

$$\begin{aligned}\int_x^\infty \frac{\mathrm{d}u}{u^4}\, e^{2iu} \ln^2 u = {}& \left(\frac{2}{27x^3} + \frac{19i}{54x^2} - \frac{85}{27x}\right) e^{2ix} + \left(\frac{2}{9x^3} + \frac{5i}{9x^2} - \frac{22}{9x}\right) e^{2ix} \ln x \\ &+ \left(\frac{1}{3x^3} + \frac{i}{3x^2} - \frac{2}{3x}\right) e^{2ix} \ln^2 x \\ &- \frac{170i}{27} \int_x^\infty \frac{\mathrm{d}u}{u}\, e^{2iu} - \frac{44i}{9} \int_x^\infty \frac{\mathrm{d}u}{u}\, e^{2iu} \ln u \\ &- \frac{4i}{3} \int_x^\infty \frac{\mathrm{d}u}{u}\, e^{2iu} \ln^2 u \end{aligned} \tag{D.11c}$$

Appendix E

Super-Hubble Limits for the Integrals

This appendix presents the evaluation of the integrals appearing in eqs. (3.74) and (3.84) and their asymptotic expressions, computed in the super-Hubble regime, which are essential for determining the PPS of scalar and tensor perturbations.

The analysis begins by recognizing that eq. (3.74) corresponds to the exponential integral

$$\mathrm{Ei}(-2ix) = \int_x^\infty \frac{\mathrm{d}u}{u}\, e^{2iu}\,, \tag{E.1}$$

defined for $x > 0$ with the series representation

$$\mathrm{Ei}(z) \equiv \gamma + \ln(-z) + \sum_{n=1}^{+\infty} \frac{(z)^n}{n!n}\,. \tag{E.2}$$

To evaluate the super-Hubble limit as $x \to 0$, terms up to linear order are retained, yielding

$$\lim_{x\to 0} \int_x^\infty \frac{\mathrm{d}u}{u}\, e^{2iu} = \alpha + \frac{i\pi}{2} - 2 - 2ix - \ln x + \mathcal{O}(x^2)\,, \tag{E.3}$$

where $\alpha = 2 - \gamma - \ln 2$. Similarly, employing the properties of the exponential integral, the following expressions are obtained:

$$\lim_{x\to 0} \int_x^\infty \frac{\mathrm{d}u}{u}\, e^{2iu} \ln u = 2 - i\pi - \frac{\pi^2}{24} + 2ix - 2\alpha + \frac{i\pi\alpha}{2} - 2ix\ln x - \frac{\ln^2 x}{2} + \mathcal{O}(x^2)\,, \tag{E.4}$$

$$\begin{aligned}\lim_{x\to 0} \int_x^\infty \frac{\mathrm{d}u}{u}\, e^{2iu} \ln^2 u = & -\frac{8}{3} + 2i\pi + \frac{\pi^2}{6} + \frac{i\pi^3}{24} - 4ix + 4\alpha - 2i\pi\alpha - \frac{\pi^2\alpha}{12} - 2\alpha^2 \\ & + \frac{i\pi\alpha^2}{2} + \frac{\alpha^3}{3} - \frac{2\zeta(3)}{3} + 4ix\ln x - 2ix\ln^2 x - \frac{\ln^3 x}{3} + \mathcal{O}(x^2)\,,\end{aligned} \tag{E.5}$$

detailed derivations of which can be found in [183, 184].

The double integral appearing in eq. (3.76a) possesses a known analytical solution, as documented in [183]. Retaining the dominant terms in x yields:

$$\begin{aligned}\lim_{x\to 0} \int_x^\infty \frac{\mathrm{d}u}{u}\, e^{-2iu} \int_u^\infty \frac{\mathrm{d}t}{t}\, e^{2it} = & \, 2 - i\pi + \frac{\pi^2}{8} - \pi x - 2\alpha + \frac{i\pi\alpha}{2} + 2ix\alpha + \frac{\alpha^2}{2} \\ & + \left(2 - \frac{i\pi}{2} - 2ix - \alpha\right)\ln x + \frac{\ln^2 x}{2} + \mathcal{O}(x^2)\,.\end{aligned} \tag{E.6}$$

For the double integral in eq. (3.81), the integrand is expanded in the limit $u \to 0$ and subsequently integrated over the interval from x to 1 to ensure convergence of the leading terms.

This approach is valid because for large arguments the exponential function is suppressed by the factor $\ln x/x$. The result is:

$$
\begin{aligned}
\lim_{x\to 0}\int_x^{\infty}\frac{\mathrm{d}u}{u}\,e^{2iu}\ln u\int_u^{\infty}\frac{\mathrm{d}t}{t}\,e^{-2it} \simeq{}& \lim_{x\to 0}\int_x^{1}\mathrm{d}u\,\Big[-2i\ln^2 u+2i\ln u\\
&-\frac{1}{2}i\ln(16)\ln u-\frac{\ln(2u)\ln u}{u}-\gamma\frac{\ln u}{u}\\
&-\frac{i\pi}{2}\frac{\ln u}{u}+\pi\ln u-2i\gamma\ln u\Big]\\
={}&-2i-\pi+2ix+\pi x-2i\alpha+2ix\alpha-(2ix+\pi x+2ix\alpha)\ln x\\
&+\left(1+\frac{i\pi}{4}+2ix-\frac{\alpha}{2}\right)\ln^2 x+\frac{\ln^3 x}{x}+\mathcal{O}(x^2)\,. \qquad \text{(E.7)}
\end{aligned}
$$

This calculation enables the evaluation of the double integral entering eq. (3.79), whose asymptotic behavior is:

$$
\begin{aligned}
\lim_{x\to 0}\int_x^{\infty}\frac{\mathrm{d}u}{u}\,e^{-2iu}\int_u^{\infty}\frac{\mathrm{d}t}{t}\,e^{2it}\ln t ={}&(-4+2i)+(1+i)\pi-\frac{5\pi^2}{12}+\frac{i\pi^3}{48}-2ix+2\pi x-\frac{i\pi^2 x}{12}\\
&+(6+2i)\alpha-i\pi\alpha+\frac{5\pi^2\alpha}{24}-4ix\alpha-\pi x\alpha-3\alpha^2+\frac{i\pi\alpha^2}{4}\\
&+i\alpha^2 x+\frac{\alpha^3}{2}+\left(-2+i\pi+\frac{\pi^2}{24}+4ix+2\alpha-\frac{i\pi\alpha}{2}-\frac{\alpha^2}{2}\right)\ln x\\
&-ix\ln^2 x+\frac{\ln^3 x}{6}+\mathcal{O}(x^2)\,. \qquad \text{(E.8)}
\end{aligned}
$$

In eq. (3.82), the complex conjugate of eq. (E.7) is also required:

$$
\begin{aligned}
\lim_{x\to 0}\int_x^{\infty}\frac{\mathrm{d}u}{u}\,e^{-2iu}\ln u\int_u^{\infty}\frac{\mathrm{d}t}{t}\,e^{2it} ={}&2i-\pi-2ix+\pi x+2i\alpha-2ix\alpha+(2ix-\pi x+2ix\alpha)\ln x\\
&+\left(1-\frac{i\pi}{4}-2ix-\frac{\alpha}{2}\right)\ln^2 x+\frac{\ln^3 x}{x}+\mathcal{O}(x^2)\,. \qquad \text{(E.9)}
\end{aligned}
$$

Finally, to evaluate the triple integral entering eq. (3.79), the limit for $u\to 0$ of the double integral in the integrand, which corresponds to eq. (E.6), is taken and the leading contributions of order $\mathcal{O}(x^0)$, multiplied by e^{2iu}/u, are integrated between x and ∞. This approximation is justified because the integrand exhibits rapid decay to zero for $u>1$, rendering contributions from this region negligible. Expanding in the super-Hubble limit yields:

$$
\begin{aligned}
\lim_{x\to 0}\int_x^{\infty}\frac{\mathrm{d}u}{u}\,e^{2iu}\int_u^{\infty}\frac{\mathrm{d}t}{t}\,e^{-2it}\int_t^{\infty}\frac{\mathrm{d}s}{s}\,e^{2is} ={}&-\frac{4}{3}+i\pi-\frac{\pi^2}{4}+\frac{5i\pi^3}{48}+2\alpha-i\pi\alpha\\
&+\frac{\pi^2\alpha}{8}-\alpha^2+\frac{i\pi\alpha^2}{4}+\frac{\alpha^3}{6}-\frac{\zeta(3)}{3}+\left(-2+i\pi-\frac{\pi^2}{8}+2\alpha-\frac{i\pi\alpha}{2}-\frac{\alpha^2}{2}\right)\ln x\\
&+\left(-1+\frac{i\pi}{4}+\frac{\alpha}{2}\right)\ln^2 x-\frac{\ln^3 x}{6}+\mathcal{O}(x)\,, \qquad \text{(E.10)}
\end{aligned}
$$

where ζ denotes the Riemann zeta function.

An alternative and more rigorous approach involves the following methodology. The integral is decomposed into two parts: one extending from x to 1 and another from 1 to $+\infty$. The contribution from the integral over $[1,+\infty)$ is negligible because the integrand $f(u)$ decreases rapidly for $u\gg 1$. Specifically, the asymptotic behavior of $f(u)$ is such that $f(u)\to 0$ rapidly for large u, making the contribution of the interval $[1,+\infty)$ insignificant compared to that of $[x,1]$. This observation has been verified numerically, confirming the negligible nature of the $[1,+\infty)$ contribution.

Following this approach, the double integral in the integrand can be expanded while retaining contributions of order $\mathcal{O}(x^2)$ and restricting the integral to the interval $[x, 1]$ where the expansion remains valid. This yields:

$$\begin{aligned}
\lim_{x\to 0}\int_x^\infty \frac{\mathrm{d}u}{u}\, e^{2iu}\int_u^\infty \frac{\mathrm{d}t}{t}\, e^{-2it}\int_t^\infty \frac{\mathrm{d}s}{s}\, e^{2is} &= -\frac{25}{4}+\left(-1+\pi+\frac{5i\pi}{2}+5\alpha-2i\alpha\right)\frac{e^{2i}}{4}\\
&-\frac{i\pi}{4}-\frac{3\pi^2}{4}-\frac{i\pi^3}{16}+6\alpha-i\pi\alpha+\frac{3\pi^2\alpha}{8}-3\alpha^2+\frac{i\pi\alpha^2}{4}+\frac{\alpha^3}{2}\\
&+\left(\frac{13}{4}-i\pi+\frac{\pi^2}{8}-2\alpha+\frac{i\pi\alpha}{2}+\frac{\alpha^2}{2}\right)\mathrm{Ei}(2i)\\
&+(-4i-\pi+2i\alpha)\,{}_3F_3(1,1,1;2,2,2;2i)+2i\,{}_4F_4(1,1,1,1;2,2,2,2;2i)\\
&+\left(-2+i\pi-\frac{\pi^2}{8}+2\alpha-\frac{i\pi\alpha}{2}-\frac{\alpha^2}{2}\right)\ln x+\left(-1+\frac{i\pi}{4}+\frac{\alpha}{2}\right)\ln^2 x-\frac{\ln^3 x}{6}+\mathcal{O}(x)\,, \quad \text{(E.11)}
\end{aligned}$$

where ${}_pF_q$ represents the generalized hypergeometric function.

It is noteworthy that eq. (E.10) and eq. (E.11) differ exclusively in their constant terms. Furthermore, the solution presented in [57] also exhibits a different constant term. Given these considerations, the super-Hubble solution of eq. (E.10) is presented as:

$$\begin{aligned}
&= -\frac{4}{3}+i\pi-\frac{\pi^2}{4}+\frac{5i\pi^3}{48}+2\alpha-i\pi\alpha+\frac{\pi^2\alpha}{8}-\alpha^2+\frac{i\pi\alpha^2}{4}+\frac{\alpha^3}{6}-\mathcal{Z}\\
&+\left(-2+i\pi-\frac{\pi^2}{8}+2\alpha-\frac{i\pi\alpha}{2}-\frac{\alpha^2}{2}\right)\ln x\\
&+\left(-1+\frac{i\pi}{4}+\frac{\alpha}{2}\right)\ln^2 x-\frac{\ln^3 x}{6}+\mathcal{O}(x) \qquad \text{(E.12)}
\end{aligned}$$

where $\mathcal{Z}=\zeta(3)/3$ from eq. (E.10), $\mathcal{Z}\sim 2.97353-0.0273557i$ from eq. (E.11), and $\mathcal{Z}=7\zeta(3)/3$ in [57]. Various choices of $\mathcal{Z}$ do not result in numerically significant differences in the final PPS expressions.

In summary, all asymptotic solutions entering the PPS equations and published in [1] demonstrate agreement with the results previously computed in [57], with the exception of one term in eq. (E.10).

Appendix F

Parameterisation of the Power Spectra

The power spectra of scalar and tensor perturbations can be obtained through analytical techniques. A common procedure is to expand the spectra around a reference wavenumber, k_*, and determine the coefficients by means of a slow-roll expansion or another suitable approximation method. Since the analysis must extend across several orders of magnitude in k, it is most convenient to use $\ln k$ as the expansion parameter. In this framework, two different expansions have been proposed in the literature [56]. The first approach, developed up to third order in [57], consists of directly expanding the power spectrum in $\ln k$, leading to

$$\frac{\mathcal{P}_X(k)}{\mathcal{P}_{X0}(k_*)} = a_{X0} + a_{X1} \ln\left(\frac{k}{k_*}\right) + \frac{a_{X2}}{2} \ln^2\left(\frac{k}{k_*}\right) + \frac{a_{X3}}{3!} \ln^3\left(\frac{k}{k_*}\right) , \tag{F.1}$$

where $X = [\zeta, \mathrm{t}]$ and

$$\mathcal{P}_{\zeta 0}(k_*) = \frac{H_*^2}{8\pi^2 M_{\mathrm{Pl}}^2 \epsilon_{1*}} , \qquad \mathcal{P}_{\mathrm{t}0}(k_*) = \frac{2H_*^2}{\pi^2 M_{\mathrm{Pl}}^2} . \tag{F.2}$$

Therefore, the coefficients $a_{\zeta\mathrm{i}}$ and a_{ti} at third order are respectively

$$\begin{aligned}
a_{\zeta 0} =& 1 - 2(1-\alpha)\epsilon_{1*} + \left(-3 - 2\alpha + 2\alpha^2 + \frac{\pi^2}{2}\right)\epsilon_{1*}^2 + \alpha\epsilon_{2*} \\
&+ \left(-6 + \alpha + \alpha^2 + \frac{7\pi^2}{12}\right)\epsilon_{1*}\epsilon_{2*} + \frac{1}{8}\left(-8 + 4\alpha^2 + \pi^2\right)\epsilon_{2*}^2 \\
&+ \frac{1}{24}\left(-12\alpha^2 + \pi^2\right)\epsilon_{2*}\epsilon_{3*} - \frac{1}{24}\left(-16 + 24\alpha - 4\alpha^3 - 3\alpha\pi^2 + 6\mathcal{Z}\right)\left(8\epsilon_{1*}^3 + \epsilon_{2*}^3\right) \\
&+ \frac{1}{12}\left(-72\alpha + 36\alpha^2 + 13\pi^2 + 8\alpha\pi^2 - 36\mathcal{Z}\right)\epsilon_{1*}^2\epsilon_{2*} \\
&- \frac{1}{24}\left(16 + 24\alpha - 12\alpha^2 - 8\alpha^3 - 15\pi^2 - 6\alpha\pi^2 + 84\mathcal{Z}\right)\epsilon_{1*}\epsilon_{2*}^2 \\
&+ \frac{1}{24}\left(16 + 4\alpha^3 - \alpha\pi^2 - 24\mathcal{Z}\right)\left(\epsilon_{2*}\epsilon_{3*}^2 + \epsilon_{2*}\epsilon_{3*}\epsilon_{4*}\right) \\
&+ \frac{1}{24}\left(48\alpha - 12\alpha^3 - 5\alpha\pi^2\right)\epsilon_{2*}^2\epsilon_{3*} \\
&+ \frac{1}{12}\left(-8 + 72\alpha - 12\alpha^2 - 8\alpha^3 + \pi^2 - 6\alpha\pi^2 - 24\mathcal{Z}\right)\epsilon_{1*}\epsilon_{2*}\epsilon_{3*} ,
\end{aligned} \tag{F.3}$$

$$
\begin{aligned}
a_{\zeta 1} =& -2\epsilon_{1*} + 2(-2\alpha+1)\epsilon_{1*}^2 - \epsilon_{2*} - (2\alpha+1)\epsilon_{1*}\epsilon_{2*} - \alpha\epsilon_{2*}^2 + \alpha\epsilon_{2*}\epsilon_{3*} \\
& - \frac{1}{8}\left(-8+4\alpha^2+\pi^2\right)\left(8\epsilon_{1*}^3+\epsilon_{2*}^3\right) - 6\left(-1+\alpha+\frac{\pi^2}{9}\right)\epsilon_{1*}^2\epsilon_{2*} \\
& - \frac{1}{4}\left(-4+4\alpha+4\alpha^2+\pi^2\right)\epsilon_{1*}\epsilon_{2*}^2 + \left(-6+2\alpha+2\alpha^2+\frac{\pi^2}{2}\right)\epsilon_{1*}\epsilon_{2*}\epsilon_{3*} \\
& + \frac{1}{24}\left(-12\alpha^2+\pi^2\right)\left(\epsilon_{2*}\epsilon_{3*}^2+\epsilon_{2*}\epsilon_{3*}\epsilon_{4*}\right) + \frac{1}{24}\left(-48+36\alpha^2+5\pi^2\right)\epsilon_{2*}^2\epsilon_{3*}\,,
\end{aligned}
\tag{F.4}
$$

$$
\begin{aligned}
a_{\zeta 2} =& 4\epsilon_{1*}^2 + 2\epsilon_{1*}\epsilon_{2*} + 6\epsilon_{1*}^2\epsilon_{2*} + \epsilon_{2*}^2 - \epsilon_{2*}\epsilon_{3*} + (1+2\alpha)(\epsilon_{1*}\epsilon_{2*}^2 - 2\epsilon_{1*}\epsilon_{2*}\epsilon_{3*}) \\
& + \alpha(8\epsilon_{1*}^3 + \epsilon_{2*}^3 - 3\epsilon_{2*}^2\epsilon_{3*} + \epsilon_{2*}\epsilon_{3*}^2 + \epsilon_{2*}\epsilon_{3*}\epsilon_{4*})\,,
\end{aligned}
\tag{F.5}
$$

$$
a_{\zeta 3} = -8\epsilon_{1*}^3 - 2\epsilon_{1*}\epsilon_{2*}^2 - \epsilon_{2*}^3 + 4\epsilon_{1*}\epsilon_{2*}\epsilon_{3*} + 3\epsilon_{2*}^2\epsilon_{3*} - \epsilon_{2*}\epsilon_{3*}^2 - \epsilon_{2*}\epsilon_{3*}\epsilon_{4*}\,,
\tag{F.6}
$$

$$
\begin{aligned}
a_{\mathrm{t}0} =& 1 + 2(-1+\alpha)\epsilon_{1*} + \left(-3-2\alpha+2\alpha^2+\frac{\pi^2}{2}\right)\epsilon_{1*}^2 \\
& + \left(-2+2\alpha-\alpha^2+\frac{\pi^2}{12}\right)\epsilon_{1*}\epsilon_{2*} - \frac{1}{3}\left(-16+24\alpha-4\alpha^3-3\alpha\pi^2+6\mathcal{Z}\right)\epsilon_{1*}^3 \\
& + \frac{1}{12}(-96+72\alpha+36\alpha^2-24\alpha^3+13\pi^2-10\alpha\pi^2)\epsilon_{1*}^2\epsilon_{2*} \\
& - \frac{1}{12}\left(8-24\alpha+12\alpha^2-4\alpha^3-\pi^2+\alpha\pi^2+24\mathcal{Z}\right)\left(\epsilon_{1*}\epsilon_{2*}^2+\epsilon_{1*}\epsilon_{2*}\epsilon_{3*}\right),
\end{aligned}
\tag{F.7}
$$

$$
\begin{aligned}
a_{\mathrm{t}1} =& -2\epsilon_{1*} + 2(-2\alpha+1)\epsilon_{1*}^2 + (-2+2\alpha)\epsilon_{1*}\epsilon_{2*} - (-8+4\alpha^2+\pi^2)\epsilon_{1*}^3 \\
& + 6\left(-1-\alpha+\alpha^2+\frac{5\pi^2}{36}\right)\epsilon_{1*}^2\epsilon_{2*} \\
& + \left(-2+2\alpha-\alpha^2+\frac{\pi^2}{12}\right)\left(\epsilon_{1*}\epsilon_{2*}^2+\epsilon_{1*}\epsilon_{2*}\epsilon_{3*}\right),
\end{aligned}
\tag{F.8}
$$

$$
a_{\mathrm{t}2} = 4\epsilon_{1*}^2 + 8\alpha\epsilon_{1*}^3 - 2\epsilon_{1*}\epsilon_{2*} + 2(3-6\alpha)\epsilon_{1*}^2\epsilon_{2*} - 2(1-\alpha)(\epsilon_{1*}\epsilon_{2*}^2 + \epsilon_{1*}\epsilon_{2*}\epsilon_{3*})\,,
\tag{F.9}
$$

$$
a_{\mathrm{t}3} = -8\epsilon_{1*}^3 + 12\epsilon_{1*}^2\epsilon_{2*} - 2\epsilon_{1*}\epsilon_{2*}^2 - 2\epsilon_{1*}\epsilon_{2*}\epsilon_{3*}\,.
\tag{F.10}
$$

Note that $\mathcal{Z}$ enters only the third-order corrections of the LO parts, that are eq. (F.3) and eq. (F.7).

Alternatively, the second kind of expansion consists of expanding the logarithm of the power spectrum in $\ln k$ as

$$
\ln\left[\frac{\mathcal{P}_X(k)}{\mathcal{P}_{X0}(k_*)}\right] = b_{X0} + b_{X1}\ln\left(\frac{k}{k_*}\right) + \frac{b_{X2}}{2}\ln^2\left(\frac{k}{k_*}\right) + \frac{b_{X3}}{3!}\ln^3\left(\frac{k}{k_*}\right)\,.
\tag{F.11}
$$

The coefficients $b_{\zeta\mathrm{i}}$ and b_{ti} up to third-order corrections are respectively

$$\begin{aligned}
b_{\zeta 0} =& -2(1-\alpha)\epsilon_{1*} + \left(-5+2\alpha+\frac{\pi^2}{2}\right)\epsilon_{1*}^2 + \alpha\epsilon_{2*} + \left(-6+3\alpha-\alpha^2+\frac{7\pi^2}{12}\right)\epsilon_{1*}\epsilon_{2*} \\
&+ \frac{1}{24}\left(-12\alpha^2+\pi^2\right)\epsilon_{2*}\epsilon_{3*} - \frac{1}{24}\left(80-48\alpha-24\pi^2+48\mathcal{Z}\right)\epsilon_{1*}^3 + \left(-1+\frac{\pi^2}{8}\right)\epsilon_{2*}^2 \\
&- \frac{1}{12}\left(-8+3\mathcal{Z}\right)\epsilon_{2*}^3 + \left(-12+15\alpha-3\alpha^2+\frac{27\pi^2}{12}-\alpha\pi^2-3\mathcal{Z}\right)\epsilon_{1*}^2\epsilon_{2*} \\
&- \frac{1}{24}\left(64-168\alpha+36\alpha^2-8\alpha^3-21\pi^2+14\alpha\pi^2+84\mathcal{Z}\right)\epsilon_{1*}\epsilon_{2*}^2 \\
&+ \frac{1}{24}\left(16+4\alpha^3-\alpha\pi^2-24\mathcal{Z}\right)\left(\epsilon_{2*}\epsilon_{3*}^2+\epsilon_{2*}\epsilon_{3*}\epsilon_{4*}\right) + \left(2\alpha-\frac{\alpha\pi^2}{4}\right)\epsilon_{2*}^2\epsilon_{3*} \\
&+ \frac{1}{12}\left(-8+72\alpha-24\alpha^2+4\alpha^3+2\pi^2-7\alpha\pi^2-24\mathcal{Z}\right)\epsilon_{1*}\epsilon_{2*}\epsilon_{3*}\,,
\end{aligned} \tag{F.12}$$

$$\begin{aligned}
b_{\zeta 1} =& -2\epsilon_{1*} - 2\epsilon_{1*}^2 - 2\epsilon_{1*}^3 - \epsilon_{2*} - (3-2\alpha)\epsilon_{1*}\epsilon_{2*} + \alpha\epsilon_{2*}\epsilon_{3*} - \frac{2}{3}\left(\frac{45}{2}-9\alpha-\frac{3\pi^2}{2}\right)\epsilon_{1*}^2\epsilon_{2*} \\
&- \left(7-3\alpha+\alpha^2-\frac{7\pi^2}{12}\right)\epsilon_{1*}\epsilon_{2*}^2 + \left(-6+4\alpha-\alpha^2+\frac{7\pi^2}{12}\right)\epsilon_{1*}\epsilon_{2*}\epsilon_{3*} \\
&+ \frac{1}{24}\left(-12\alpha^2+\pi^2\right)\left(\epsilon_{2*}\epsilon_{3*}^2+\epsilon_{2*}\epsilon_{3*}\epsilon_{4*}\right) + \left(-2+\frac{\pi^2}{4}\right)\epsilon_{2*}^2\epsilon_{3*}\,,
\end{aligned} \tag{F.13}$$

$$\begin{aligned}
b_{\zeta 2} =& -2\epsilon_{1*}\epsilon_{2*} - 6\epsilon_{1*}^2\epsilon_{2*} - (3-2\alpha)\epsilon_{1*}\epsilon_{2*}^2 - \epsilon_{2*}\epsilon_{3*} \\
&- 2(2-\alpha)\epsilon_{1*}\epsilon_{2*}\epsilon_{3*} + \alpha\epsilon_{2*}\epsilon_{3*}^2 + \alpha\epsilon_{2*}\epsilon_{3*}\epsilon_{4*}\,,
\end{aligned} \tag{F.14}$$

$$b_{\zeta 3} = -2\epsilon_{1*}\epsilon_{2*}^2 - 2\epsilon_{1*}\epsilon_{2*}\epsilon_{3*} - \epsilon_{2*}\epsilon_{3*}^2 - \epsilon_{2*}\epsilon_{3*}\epsilon_{4*}\,, \tag{F.15}$$

$$\begin{aligned}
b_{\mathrm{t}0} =& -2(1-\alpha)\epsilon_{1*} + \frac{1}{2}(-10+4\alpha+\pi^2)\epsilon_{1*}^2 + \left(-2+2\alpha-\alpha^2+\frac{\pi^2}{12}\right)\epsilon_{1*}\epsilon_{2*} \\
&- \frac{1}{3}\left(10-6\alpha-3\pi^2+6\mathcal{Z}\right)\epsilon_{1*}^3 + \left(-12+14\alpha-3\alpha^2+\frac{15\pi^2}{12}-\alpha\pi^2\right)\epsilon_{1*}^2\epsilon_{2*} \\
&- \frac{1}{12}\left(8-24\alpha+12\alpha^2-4\alpha^3-\pi^2+\alpha\pi^2+24\mathcal{Z}\right)\left(\epsilon_{1*}\epsilon_{2*}^2+\epsilon_{1*}\epsilon_{2*}\epsilon_{3*}\right),
\end{aligned} \tag{F.16}$$

$$\begin{aligned}
b_{\mathrm{t}1} =& -2\epsilon_{1*} - 2\epsilon_{1*}^2 + 2(-1+\alpha)\epsilon_{1*}\epsilon_{2*} - 2\epsilon_{1*}^3 + (-14+6\alpha+\pi^2)\epsilon_{1*}^2\epsilon_{2*} \\
&+ \left(-2+2\alpha-\alpha^2+\frac{\pi^2}{12}\right)\left(\epsilon_{1*}\epsilon_{2*}^2+\epsilon_{1*}\epsilon_{2*}\epsilon_{3*}\right),
\end{aligned} \tag{F.17}$$

$$b_{\mathrm{t}2} = -2\epsilon_{1*}\epsilon_{2*} - 6\epsilon_{1*}^2\epsilon_{2*} - 2(1-\alpha)\epsilon_{1*}\epsilon_{2*}^2 - 2(1-\alpha)\epsilon_{1*}\epsilon_{2*}\epsilon_{3*}\,, \tag{F.18}$$

$$b_{\mathrm{t}3} = -2\epsilon_{1*}\epsilon_{2*}^2 - 2\epsilon_{1*}\epsilon_{2*}\epsilon_{3*}\,. \tag{F.19}$$

Using the latter parameterisation, it is possible to write directly both the scalar and tensor spectral indices, runnings, and runnings of the running with respect to the coefficients b_{Xi} as follows

$$n_{\mathrm{s}} = 1 + b_{\zeta 1} + b_{\zeta 2}\ln\left(\frac{k}{k_*}\right) + \frac{b_{\zeta 3}}{2}\ln^2\left(\frac{k}{k_*}\right)\,, \tag{F.20}$$

$$\alpha_{\mathrm{s}} = b_{\zeta 2} + b_{\zeta 3}\ln\left(\frac{k}{k_*}\right)\,, \tag{F.21}$$

$$\beta_{\mathrm{s}} = b_{\zeta 3} \,, \tag{F.22}$$

$$n_{\mathrm{t}} = b_{\mathrm{t}1} + b_{\mathrm{t}2} \ln\left(\frac{k}{k_*}\right) + \frac{b_{\mathrm{t}3}}{2} \ln^2\left(\frac{k}{k_*}\right) \,, \tag{F.23}$$

$$\alpha_{\mathrm{t}} = b_{\mathrm{t}2} + b_{\mathrm{t}3} \ln\left(\frac{k}{k_*}\right) \,, \tag{F.24}$$

$$\beta_{\mathrm{t}} = b_{\mathrm{t}3} \,. \tag{F.25}$$

Appendix G

Choice of the pivot scale for Isotropic Cosmic Birefringence analysis

The selection of the pivot scale ℓ_{B_0} is assessed by examining three different choices for B_0 across the four component-separation *Planck* datasets. The optimal bin is identified as the one that minimizes the correlation between β_0 and n, remains consistent with the value of β estimated over the complete harmonic range, and yields the smallest possible systematic uncertainty on n arising from $\beta_{\rm res}$.

Numerical results for the four CS datasets and three choices of B_0—corresponding to the third ($\ell \in [202, 281]$), sixth ($\ell \in [442, 521]$), and tenth ($\ell \in [762, 841]$) bins—are reported in tables G.1 and G.2. The corresponding contour plots are displayed in fig. G.1.

The analysis reveals that a common choice of $B_0 = 6$ minimizes both the correlation between the model parameters and the systematic uncertainty on n across all CS methods. This position corresponds to the harmonic region most tightly constrained by the non-parametric reconstruction, as shown in fig. 4.8.

Par.	**Pivot scale**	**Data considered: $\boldsymbol{\beta_B}$**			
		`Commander`	`NILC`	`SEVEM`	`SMICA`
β_0 [deg]	3rd bin	$0.19^{+0.07}_{-0.06}$	0.26 ± 0.07	$0.20^{+0.07}_{-0.06}$	$0.19^{+0.07}_{-0.06}$
	6th bin	0.28 ± 0.05	0.31 ± 0.05	0.30 ± 0.06	0.26 ± 0.05
	10th bin	0.39 ± 0.07	0.36 ± 0.07	0.41 ± 0.08	0.36 ± 0.07
n	3rd bin	$0.53^{+0.33}_{-0.31}$	$0.23^{+0.30}_{-0.29}$	$0.51^{+0.32}_{-0.30}$	$0.44^{+0.35}_{-0.33}$
	6th bin	$0.60^{+0.34}_{-0.31}$	$0.29^{+0.31}_{-0.29}$	$0.57^{+0.33}_{-0.31}$	$0.52^{+0.36}_{-0.34}$
	10th bin	$0.65^{+0.35}_{-0.32}$	$0.34^{+0.32}_{-0.30}$	$0.62^{+0.34}_{-0.31}$	$0.58^{+0.37}_{-0.34}$

Table G.1: Best-fit parameter values with 1σ confidence intervals for (β_0, n) obtained at different pivot scales: 3rd bin ($\ell_{B_0} = 242$), 6th bin ($\ell_{B_0} = 482$), and 10th bin ($\ell_{B_0} = 802$), for the four component-separation methods applied to the measured data β_B.

Par.	**Pivot scale**	**Data considered: $\boldsymbol{\beta}_{\textbf{res}}$**			
		`Commander`	`NILC`	`SEVEM`	`SMICA`
β_0 [deg]	3rd bin	0.019 ± 0.005	0.014 ± 0.005	0.014 ± 0.005	0.017 ± 0.005
	6th bin	0.019 ± 0.003	0.013 ± 0.003	0.013 ± 0.003	0.017 ± 0.003
	10th bin	0.019 ± 0.004	0.014 ± 0.004	$0.014^{+0.005}_{-0.004}$	0.017 ± 0.004
n	3rd bin	$-0.07^{+0.33}_{-0.29}$	$-0.12^{+0.42}_{-0.38}$	$-0.12^{+0.45}_{-0.38}$	$-0.08^{+0.36}_{-0.31}$
	6th bin	$\mathbf{0.00^{+0.35}_{-0.31}}$	$\mathbf{0.00^{+0.45}_{-0.41}}$	$\mathbf{0.00^{+0.49}_{-0.41}}$	$\mathbf{0.00^{+0.38}_{-0.33}}$
	10th bin	$0.05^{+0.36}_{-0.32}$	$0.09^{+0.47}_{-0.42}$	$0.10^{+0.53}_{-0.44}$	$0.06^{+0.39}_{-0.34}$

Table G.2: Best-fit parameter values with 1σ confidence intervals for (β_0, n) at different pivot scales (3rd, 6th, and 10th bins), estimated from the systematic residual term $\beta_{\rm res}$ for the four component-separation methods. The sixth bin row, corresponding to the minimal recovered value for n, is highlighted in boldface.

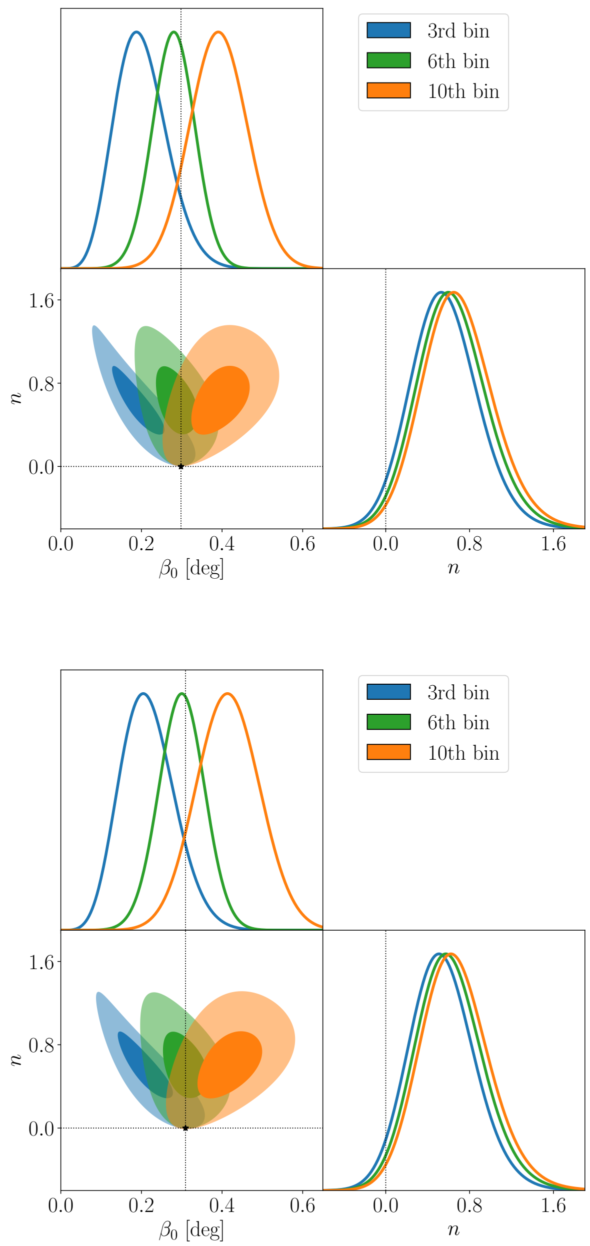

Figure G.1: Triangular contour plots illustrating the power-law analysis results for all four component-separation methods using the D^{EB} estimator with varying pivot bin choices (3rd, 6th, and 10th bins). Upper left panel: `Commander`; upper right panel: `NILC`; lower left panel: `SEVEM`; lower right panel: `SMICA`.

Appendix H

Non-parametric Bayesian reconstruction for $N \neq 4$ nodes

Figure H.1 illustrates the evolution of the reconstructed function as the number of nodes varies compared to the $N = 4$ case examined in section 4.2.4. The shaded regions represent credible intervals derived from posterior samples. These results demonstrate how increasing the number of nodes enhances the reconstruction's capacity to capture fine-scale features in the data, while also revealing diminishing returns as the node count becomes excessive, potentially leading to overfitting. This behavior is further characterized by the deterioration of the Bayes factor with increasing node numbers, as shown in fig. H.2. The reconstruction shows good agreement with the best-fit results obtained using the power-law template presented in table 4.2 and fig. 4.6.

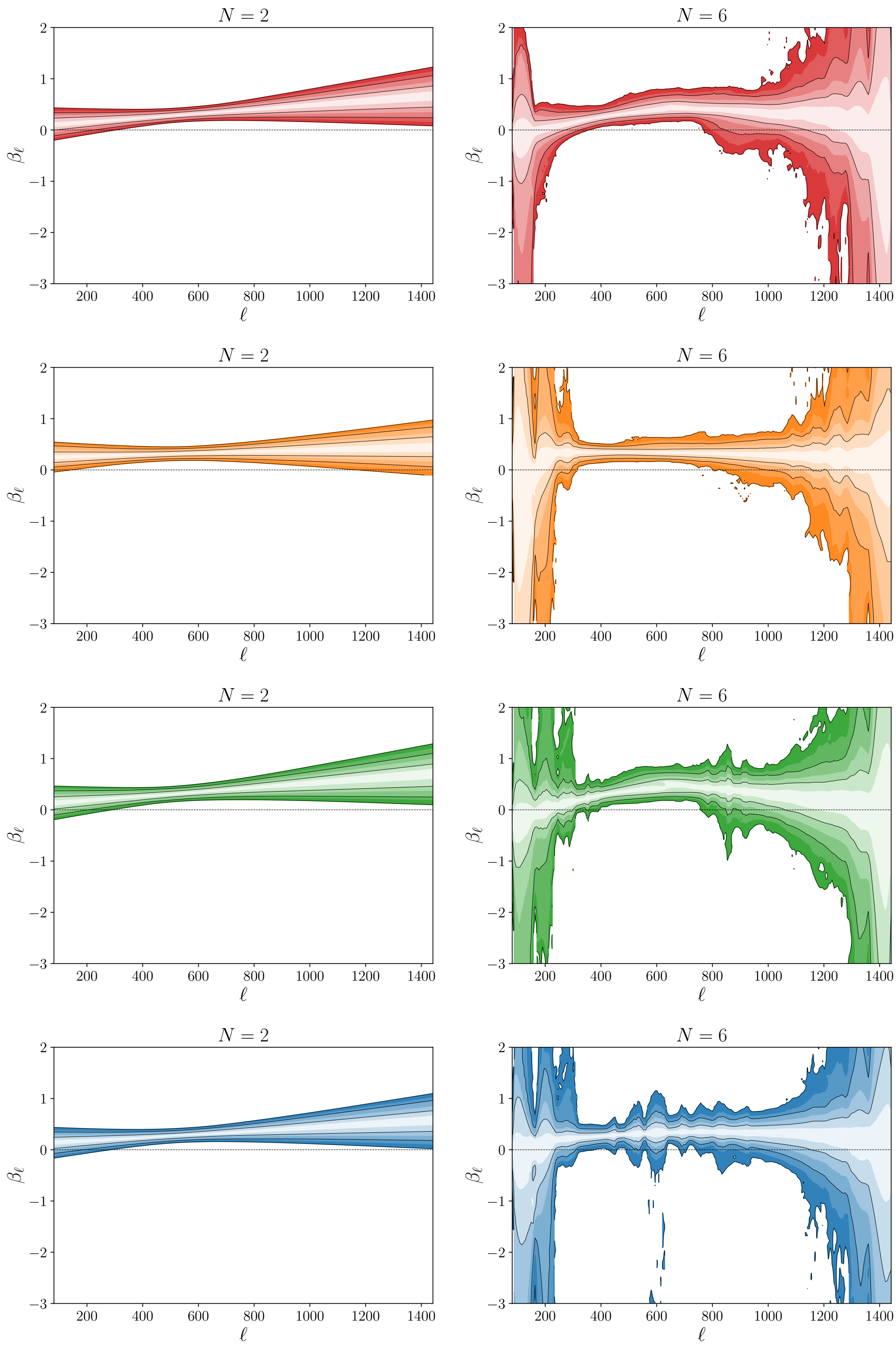

Figure H.1: Reconstruction of the angular isotropic cosmic birefringence angle using iso-probability credibility intervals in the (β_ℓ, ℓ) plane. The interval masses are converted to σ-values via inverse error function transformation, obtained from the EB-based estimator applied to (top to bottom) the `Commander`, `NILC`, `SEVEM` and `SMICA` maps for $N = 2$ (left panels) and $N = 6$ (right panels).

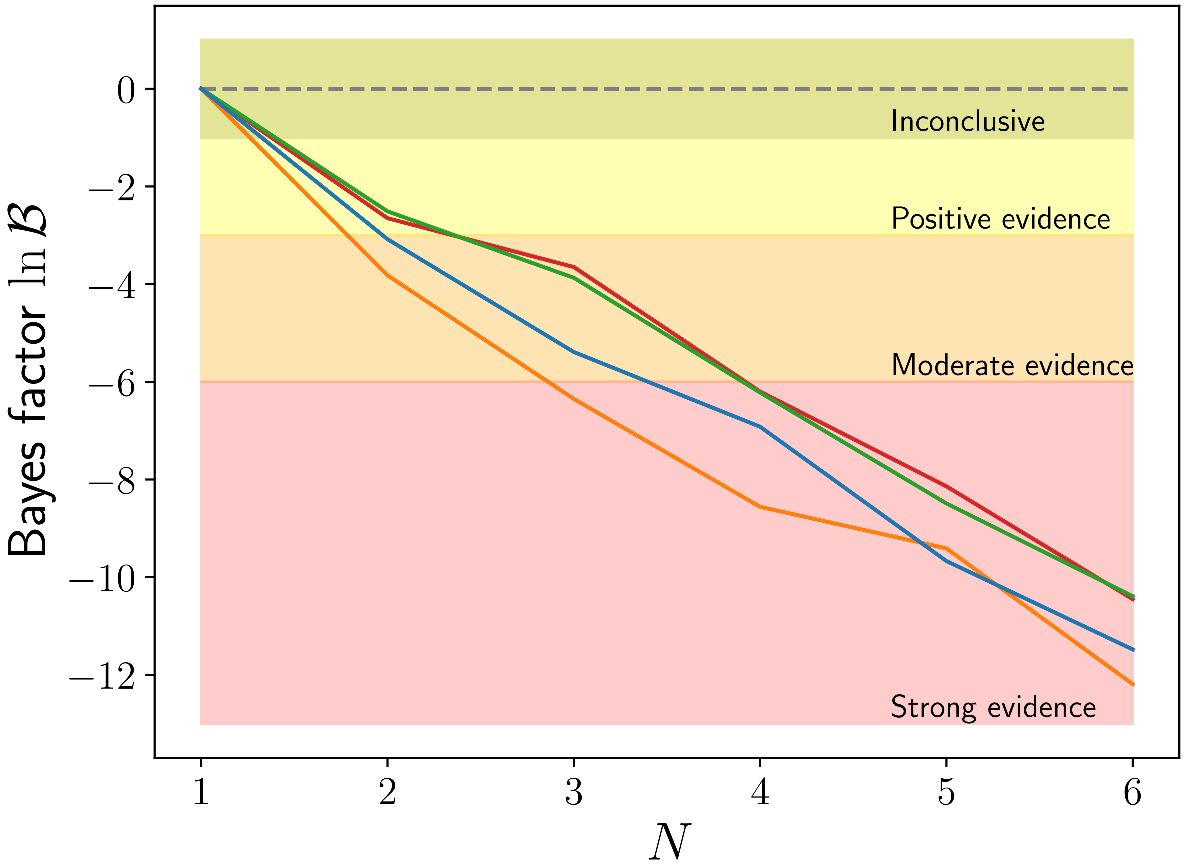

Figure H.2: Bayesian evidence as a function of the number of nodes N for the isotropic cosmic birefringence angle reconstruction. The solid lines follow the standard color scheme: red for `Commander`, orange for `NILC`, green for `SEVEM`, and blue for `SMICA`.

Bibliography

[1] Mario Ballardini, Alessandro Davoli, and Salvatore Samuele Sirletti. Third-order corrections to the slow-roll expansion: Calculation and constraints with Planck, ACT, SPT, and BICEP/Keck. *Phys. Dark Univ.*, 47:101813, 2025. doi: 10.1016/j.dark.2025.101813.

[2] Eleonora Di Valentino et al. The CosmoVerse White Paper: Addressing observational tensions in cosmology with systematics and fundamental physics. *Phys. Dark Univ.*, 49: 101965, 2025. doi: 10.1016/j.dark.2025.101965.

[3] M. Ballardini, A. Gruppuso, S. Paradiso, S. S. Sirletti, and P. Natoli. Planck constraints on the scale dependence of isotropic cosmic birefringence. *JCAP*, 09:075, 2025. doi: 10.1088/1475-7516/2025/09/075.

[4] S. Goldstein, J. C. Hill, and S. S. Sirletti. Multi-resonance photon-axion conversion in galaxy halos: A WKB approach. 2025.

[5] Salvatore Samuele Sirletti, Piero Nicolini, and Mariafelicia De Laurentis. Stellar Objects From Quantum Gravity. 12 2025.

[6] Oliver H. E. Philcox, Kunhao Zhong, and Salvatore Samuele Sirletti. Separating the Inseparable: Constraining Arbitrary Primordial Bispectra with Cosmic Microwave Background Data. 11 2025.

[7] Albert Einstein. Kosmologische Betrachtungen zur allgemeinen Relativitätstheorie. *Sitzungsberichte der Königlich Preussischen Akademie der Wissenschaften*, pages 142–152, January 1917.

[8] Steven Weinberg. *Cosmology*. 2008. ISBN 978-0-19-852682-7.

[9] Albert Einstein. Die Feldgleichungen der Gravitation. *Sitzungsberichte der Königlich Preussischen Akademie der Wissenschaften*, pages 844–847, January 1915.

[10] Edwin Hubble. A Relation between Distance and Radial Velocity among Extra-Galactic Nebulae. *Proceedings of the National Academy of Science*, 15(3):168–173, March 1929. doi: 10.1073/pnas.15.3.168.

[11] H. P. Robertson. Kinematics and World-Structure. 82:284, November 1935. doi: 10.1086/143681.

[12] A. Friedmann. Über die Krümmung des Raumes. *Zeitschrift fur Physik*, 10:377–386, January 1922. doi: 10.1007/BF01332580.

[13] A. G. Walker. On Milne's Theory of World-Structure. *Proc. Lond. Math. Soc. s*, 2-42(1): 90–127, 1937. doi: 10.1112/plms/s2-42.1.90.

[14] Karl Schwarzschild. Über das Gravitationsfeld eines Massenpunktes nach der Einsteinschen Theorie. *Sitzungsberichte der Königlich Preussischen Akademie der Wissenschaften*, pages 189–196, January 1916.

[15] Yaa B. Zeldovich. A hypothesis, unifying the structure and the entropy of the Universe. 160:1P, January 1972. doi: 10.1093/mnras/160.1.1P.

[16] Kevin J. Ludwick. The viability of phantom dark energy: A review. *Mod. Phys. Lett. A*, 32(28):1730025, 2017. doi: 10.1142/S0217732317300257.

[17] Adam G. Riess et al. Observational evidence from supernovae for an accelerating universe and a cosmological constant. *Astron. J.*, 116:1009–1038, 1998. doi: 10.1086/300499.

[18] Planck Collaboration, N. Aghanim, Y. Akrami, M. Ashdown, et al. Planck 2018 results. VI. Cosmological parameters. *Astron. Astrophys.*, 641:A6, 2020. doi: 10.1051/0004-6361/201833910.

[19] L. Balkenhol, D. Dutcher, Spurio Mancini, and SPT-3G Collaboration. Measurement of the CMB temperature power spectrum and constraints on cosmology from the SPT-3G 2018 T T , T E , and E E dataset. *Phys. Rev. D*, 108(2):023510, July 2023. doi: 10.1103/PhysRevD.108.023510.

[20] ACT Collaboration. The Atacama Cosmology Telescope: a measurement of the Cosmic Microwave Background power spectra at 98 and 150 GHz. *J. Cosmology Astropart. Phys.*, 2020(12):045, December 2020. doi: 10.1088/1475-7516/2020/12/045.

[21] Thibaut Louis et al. The Atacama Cosmology Telescope: DR6 Power Spectra, Likelihoods and ΛCDM Parameters. 3 2025.

[22] Planck Collaboration. Planck 2018 results. VI. Cosmological parameters. *A&A*, 641:A6, September 2020. doi: 10.1051/0004-6361/201833910.

[23] Daniel J. Eisenstein et al. Detection of the Baryon Acoustic Peak in the Large-Scale Correlation Function of SDSS Luminous Red Galaxies. *Astrophys. J.*, 633:560–574, 2005. doi: 10.1086/466512.

[24] Kyle S. Dawson et al. The Baryon Oscillation Spectroscopic Survey of SDSS-III. *Astron. J.*, 145:10, 2013. doi: 10.1088/0004-6256/145/1/10.

[25] eBOSS Collaboration. Completed SDSS-IV extended Baryon Oscillation Spectroscopic Survey: Cosmological implications from two decades of spectroscopic surveys at the Apache Point Observatory. *Phys. Rev. D*, 103(8):083533, April 2021. doi: 10.1103/PhysRevD.103.083533.

[26] R. K. Sachs and A. M. Wolfe. Perturbations of a cosmological model and angular variations of the microwave background. *Astrophys. J.*, 147:73–90, 1967. doi: 10.1007/s10714-007-0448-9.

[27] R. A. Sunyaev and Ya. B. Zeldovich. Small scale fluctuations of relic radiation. *Astrophys. Space Sci.*, 7:3–19, 1970.

[28] Duncan Hanson, Anthony Challinor, and Antony Lewis. Weak lensing of the CMB. *Gen. Rel. Grav.*, 42:2197–2218, 2010. doi: 10.1007/s10714-010-1036-y.

[29] Ralph A. Alpher and Robert Herman. Evolution of the Universe. *Nature*, 162(4124):774–775, 1948. doi: 10.1038/162774b0.

[30] A. G. Doroshkevich and I. D. Novikov. Mean Density of Radiation in the Metagalaxy and Certain Problems in Relativistic Cosmology. *Soviet Physics Doklady*, 9:111, August 1964.

[31] Andrei Georgievich Doroshkevich and Igor Dmitriyevich Novikov. Republication of: Mean density of radiation in the Metagalaxy and certain problems in relativistic cosmology. *General Relativity and Gravitation*, 50(11):138, November 2018. doi: 10.1007/s10714-018-2441-x.

[32] A. A. Penzias and R. W. Wilson. A Measurement of Excess Antenna Temperature at 4080 Mc/s. 142:419–421, July 1965. doi: 10.1086/148307.

[33] John C. Mather et al. Measurement of the Cosmic Microwave Background spectrum by the COBE FIRAS instrument. *Astrophys. J.*, 420:439–444, 1994. doi: 10.1086/173574.

[34] George F. Smoot et al. Structure in the COBE differential microwave radiometer first year maps. *Astrophys. J. Lett.*, 396:L1–L5, 1992. doi: 10.1086/186504.

[35] C. L. Bennett et al. Nine-Year Wilkinson Microwave Anisotropy Probe (WMAP) Observations: Final Maps and Results. *Astrophys. J. Suppl.*, 208:20, 2013. doi: 10.1088/0067-0049/208/2/20.

[36] Planck Collaboration. Planck 2013 results. XXII. Constraints on inflation. *A&A*, 571:A22, November 2014. doi: 10.1051/0004-6361/201321569.

[37] Planck Collaboration. Planck 2015 results. XX. Constraints on inflation. *A&A*, 594:A20, September 2016. doi: 10.1051/0004-6361/201525898.

[38] J. Alberto Vázquez, Luis E. Padilla, and Tonatiuh Matos. Inflationary cosmology: from theory to observations. *Rev. Mex. Fis. E*, 17(1):73–91, 2020. doi: 10.31349/RevMexFisE.17.73.

[39] Bicep/Keck Collaboration. Improved Constraints on Primordial Gravitational Waves using Planck, WMAP, and BICEP/Keck Observations through the 2018 Observing Season. *Phys. Rev. Lett.*, 127(15):151301, October 2021. doi: 10.1103/PhysRevLett.127.151301.

[40] BICEP2 Collaboration and Keck Array Collaboration. Constraints on Primordial Gravitational Waves Using Planck, WMAP, and New BICEP2/Keck Observations through the 2015 Season. *Phys. Rev. Lett.*, 121(22):221301, November 2018. doi: 10.1103/PhysRevLett.121.221301.

[41] E. de la Hoz et al. LiteBIRD Science Goals and Forecasts: constraining isotropic cosmic birefringence. 3 2025.

[42] Simons Observatory Collaboration. The Simons Observatory: science goals and forecasts. *J. Cosmology Astropart. Phys.*, 2019(2):056, February 2019. doi: 10.1088/1475-7516/2019/02/056.

[43] M. Abitbol et al. The Simons Observatory: Science Goals and Forecasts for the Enhanced Large Aperture Telescope. 3 2025.

[44] Alan H. Guth. Inflationary universe: A possible solution to the horizon and flatness problems. *Phys. Rev. D*, 23(2):347–356, January 1981. doi: 10.1103/PhysRevD.23.347.

[45] A. A. Starobinsky. A new type of isotropic cosmological models without singularity. *Phys. Lett. B*, 91(1):99–102, March 1980. doi: 10.1016/0370-2693(80)90670-X.

[46] S. W. Hawking, I. G. Moss, and J. M. Stewart. Bubble collisions in the very early universe. *Phys. Rev. D*, 26(10):2681–2693, November 1982. doi: 10.1103/PhysRevD.26.2681.

[47] Planck Collaboration, Y. Akrami, F. Arroja, M. Ashdown, et al. Planck 2018 results. X. Constraints on inflation. *Astron. Astrophys.*, 641:A10, 2020. doi: 10.1051/0004-6361/201833887.

[48] Arthur Kosowsky. Cosmic microwave background polarization. *Annals Phys.*, 246:49–85, 1996. doi: 10.1006/aphy.1996.0020.

[49] Eiichiro Komatsu. New physics from the polarized light of the cosmic microwave background. *Nature Rev. Phys.*, 4(7):452–469, 2022. doi: 10.1038/s42254-022-00452-4.

[50] Sean M. Carroll, George B. Field, and Roman Jackiw. Limits on a Lorentz and Parity Violating Modification of Electrodynamics. *Phys. Rev. D*, 41:1231, 1990. doi: 10.1103/PhysRevD.41.1231.

[51] Jérôme Martin, Christophe Ringeval, and Vincent Vennin. Encyclopædia Inflationaris. *Physics of the Dark Universe*, 5:75–235, December 2014. doi: 10.1016/j.dark.2014.01.003.

[52] V. F. Mukhanov. Gravitational instability of the universe filled with a scalar field. *Soviet Journal of Experimental and Theoretical Physics Letters*, 41:493, May 1985.

[53] Misao Sasaki. Large Scale Quantum Fluctuations in the Inflationary Universe. *Progress of Theoretical Physics*, 76(5):1036–1046, November 1986. doi: 10.1143/PTP.76.1036.

[54] E. D. Stewart and J. O. Gong. The density perturbation power spectrum to second-order corrections in the slow-roll expansion. *Phys. Lett. B*, 510(1-4):1–9, June 2001. doi: 10.1016/S0370-2693(01)00616-5.

[55] D. J. Schwarz, C. A. Terrero-Escalante, and A. A. García. Higher order corrections to primordial spectra from cosmological inflation. *Phys. Lett. B*, 517(3-4):243–249, October 2001. doi: 10.1016/S0370-2693(01)01036-X.

[56] Samuel M. Leach, Andrew R. Liddle, Jérôme Martin, and Dominik J. Schwarz. Cosmological parameter estimation and the inflationary cosmology. *Phys. Rev. D*, 66(2):023515, July 2002. doi: 10.1103/PhysRevD.66.023515.

[57] Pierre Auclair and Christophe Ringeval. Slow-roll inflation at N3LO. *Phys. Rev. D*, 106 (6):063512, September 2022. doi: 10.1103/PhysRevD.106.063512.

[58] Eugenio Bianchi and Mauricio Gamonal. Primordial power spectrum at N3LO in effective theories of inflation. *Phys. Rev. D*, 110(10):104032, November 2024. doi: 10.1103/PhysRevD.110.104032.

[59] LiteBIRD Collaboration. Probing cosmic inflation with the LiteBIRD cosmic microwave background polarization survey. *Progress of Theoretical and Experimental Physics*, 2023 (4):042F01, April 2023. doi: 10.1093/ptep/ptac150.

[60] Euclid Collaboration. Euclid Definition Study Report. *arXiv e-prints*, art. arXiv:1110.3193, October 2011. doi: 10.48550/arXiv.1110.3193.

[61] Luca Amendola, Stephen Appleby, Anastasios Avgoustidis, David Bacon, and et al. Cosmology and fundamental physics with the Euclid satellite. *Living Reviews in Relativity*, 21 (1):2, April 2018. doi: 10.1007/s41114-017-0010-3.

[62] Euclid Collaboration. Euclid preparation. VII. Forecast validation for Euclid cosmological probes. *A&A*, 642:A191, October 2020. doi: 10.1051/0004-6361/202038071.

[63] Euclid Collaboration. Euclid preparation. XV. Forecasting cosmological constraints for the Euclid and CMB joint analysis. *A&A*, 657:A91, January 2022. doi: 10.1051/0004-6361/202141556.

[64] N. Aghanim et al. Planck 2018 results. I. Overview and the cosmological legacy of Planck. *Astron. Astrophys.*, 641:A1, 2020. doi: 10.1051/0004-6361/201833880.

[65] ACT Collaboration. The Atacama Cosmology Telescope: DR4 maps and cosmological parameters. *J. Cosmology Astropart. Phys.*, 2020(12):047, December 2020. doi: 10.1088/1475-7516/2020/12/047.

[66] James M. Bardeen. Gauge Invariant Cosmological Perturbations. *Phys. Rev. D*, 22:1882–1905, 1980. doi: 10.1103/PhysRevD.22.1882.

[67] Jérôme Martin, Christophe Ringeval, and Vincent Vennin. Cosmic Inflation at the crossroads. *J. Cosmology Astropart. Phys.*, 2024(7):087, July 2024. doi: 10.1088/1475-7516/2024/07/087.

[68] Arthur Kosowsky and Michael S. Turner. CBR anisotropy and the running of the scalar spectral index. *Phys. Rev. D*, 52(4):R1739–R1743, August 1995. doi: 10.1103/PhysRevD.52.R1739.

[69] Renata Kallosh, Andrei Linde, and Diederik Roest. Universal Attractor for Inflation at Strong Coupling. *Phys. Rev. Lett.*, 112(1):011303, January 2014. doi: 10.1103/PhysRevLett.112.011303.

[70] Sergio Ferrara, Renata Kallosh, Andrei Linde, and Massimo Porrati. Minimal supergravity models of inflation. *Phys. Rev. D*, 88(8):085038, October 2013. doi: 10.1103/PhysRevD.88.085038.

[71] Renata Kallosh, Andrei Linde, and Diederik Roest. Superconformal inflationary α-attractors. *Journal of High Energy Physics*, 2013:198, November 2013. doi: 10.1007/JHEP11(2013)198.

[72] Renata Kallosh, Andrei Linde, and Diederik Roest. Large field inflation and double α-attractors. *Journal of High Energy Physics*, 2014:52, August 2014. doi: 10.1007/JHEP08(2014)052.

[73] Renata Kallosh, Andrei Linde, and Diederik Roest. The double attractor behavior of induced inflation. *Journal of High Energy Physics*, 2014:62, September 2014. doi: 10.1007/JHEP09(2014)062.

[74] Mario Galante, Renata Kallosh, Andrei Linde, and Diederik Roest. Unity of Cosmological Inflation Attractors. *Phys. Rev. Lett.*, 114(14):141302, April 2015. doi: 10.1103/PhysRevLett.114.141302.

[75] Shamit Kachru, Renata Kallosh, Andrei Linde, and Sandip P. Trivedi. de Sitter vacua in string theory. *Phys. Rev. D*, 68(4):046005, August 2003. doi: 10.1103/PhysRevD.68.046005.

[76] Renata Kallosh and Timm Wrase. dS Supergravity from 10d. *Fortschritte der Physik*, 67 (1-2):1800071, January 2019. doi: 10.1002/prop.201800071.

[77] Johan Blåbäck, Ulf Danielsson, and Giuseppe Dibitetto. A new light on the darkest corner of the landscape. *arXiv e-prints*, art. arXiv:1810.11365, October 2018. doi: 10.48550/arXiv.1810.11365.

[78] Andrew R. Liddle, Paul Parsons, and John D. Barrow. Formalizing the slow-roll approximation in inflation. *Phys. Rev. D*, 50(12):7222–7232, December 1994. doi: 10.1103/PhysRevD.50.7222.

[79] Vincent Vennin. Horizon-flow off-track for inflation. *Phys. Rev. D*, 89(8):083526, April 2014. doi: 10.1103/PhysRevD.89.083526.

[80] Salman Habib, Andreas Heinen, Katrin Heitmann, and Gerard Jungman. Inflationary perturbations and precision cosmology. *Phys. Rev. D*, 71(4):043518, February 2005. doi: 10.1103/PhysRevD.71.043518.

[81] Antony Lewis. Efficient sampling of fast and slow cosmological parameters. *Phys. Rev. D*, 87(10):103529, May 2013. doi: 10.1103/PhysRevD.87.103529.

[82] Antony Lewis, Anthony Challinor, and Anthony Lasenby. Efficient Computation of Cosmic Microwave Background Anisotropies in Closed Friedmann-Robertson-Walker Models. *The Astrophysical Journal (ApJ)*, 538(2):473–476, August 2000. doi: 10.1086/309179.

[83] Cullan Howlett, Antony Lewis, Alex Hall, and Anthony Challinor. CMB power spectrum parameter degeneracies in the era of precision cosmology. *J. Cosmology Astropart. Phys.*, 2012(4):027, April 2012. doi: 10.1088/1475-7516/2012/04/027.

[84] Antony Lewis. GetDist: a Python package for analysing Monte Carlo samples. *arXiv e-prints*, art. arXiv:1910.13970, October 2019. doi: 10.48550/arXiv.1910.13970.

[85] Planck Collaboration. Planck 2018 results. V. CMB power spectra and likelihoods. *A&A*, 641:A5, September 2020. doi: 10.1051/0004-6361/201936386.

[86] D. M. Scolnic, D. O. Jones, A. Rest, Y. C. Pan, and et al. The Complete Light-curve Sample of Spectroscopically Confirmed SNe Ia from Pan-STARRS1 and Cosmological Constraints from the Combined Pantheon Sample. *The Astrophysical Journal (ApJ)*, 859(2):101, June 2018. doi: 10.3847/1538-4357/aab9bb.

[87] Planck Collaboration. Planck 2018 results. VIII. Gravitational lensing. *A&A*, 641:A8, September 2020. doi: 10.1051/0004-6361/201833886.

[88] Silvia Galli, Levon Pogosian, Karsten Jedamzik, and Lennart Balkenhol. Consistency of Planck, ACT, and SPT constraints on magnetically assisted recombination and forecasts for future experiments. *Phys. Rev. D*, 105(2):023513, January 2022. doi: 10.1103/PhysRevD.105.023513.

[89] Tristan L. Smith, Matteo Lucca, Vivian Poulin, Guillermo F. Abellan, Lennart Balkenhol, Karim Benabed, Silvia Galli, and Riccardo Murgia. Hints of early dark energy in Planck, SPT, and ACT data: New physics or systematics? *Phys. Rev. D*, 106(4):043526, August 2022. doi: 10.1103/PhysRevD.106.043526.

[90] Guillermo Franco Abellán, Matteo Braglia, Mario Ballardini, Fabio Finelli, and Vivian Poulin. Probing early modification of gravity with Planck, ACT and SPT. *J. Cosmology Astropart. Phys.*, 2023(12):017, December 2023. doi: 10.1088/1475-7516/2023/12/017.

[91] Akhil Antony, Fabio Finelli, Dhiraj Kumar Hazra, Daniela Paoletti, and Arman Shafieloo. A search for super-imposed oscillations to the primordial power spectrum in Planck and SPT-3G 2018 data. *arXiv e-prints*, art. arXiv:2403.19575, March 2024. doi: 10.48550/arXiv.2403.19575.

[92] Jun-Qian Jiang and Yun-Song Piao. Toward early dark energy and n_s=1 with P l a n c k , ACT, and SPT observations. *Phys. Rev. D*, 105(10):103514, May 2022. doi: 10.1103/PhysRevD.105.103514.

[93] Eleonora Di Valentino, William Giarè, Alessandro Melchiorri, and Joseph Silk. Quantifying the global 'CMB tension' between the Atacama Cosmology Telescope and the Planck satellite in extended models of cosmology. *Monthly Notices of the Royal Astronomical Society*, 520(1):210–215, March 2023. doi: 10.1093/mnras/stad152.

[94] William Giarè, Fabrizio Renzi, Olga Mena, Eleonora Di Valentino, and Alessandro Melchiorri. Is the Harrison-Zel'dovich spectrum coming back? ACT preference for n_s 1 and its discordance with Planck. *Monthly Notices of the Royal Astronomical Society*, 521(2): 2911–2918, May 2023. doi: 10.1093/mnras/stad724.

[95] Jérôme Martin, Christophe Ringeval, and Vincent Vennin. Vanilla inflation predicts negative running. *EPL (Europhysics Letters)*, 148(2):29002, October 2024. doi: 10.1209/0295-5075/ad847c.

[96] J. P. P. Vieira, Christian T. Byrnes, and Antony Lewis. Can power spectrum observations rule out slow-roll inflation? *J. Cosmology Astropart. Phys.*, 2018(1):019, January 2018. doi: 10.1088/1475-7516/2018/01/019.

[97] Lloyd Knox. Determination of inflationary observables by cosmic microwave background anisotropy experiments. *Phys. Rev. D*, 52(8):4307–4318, October 1995. doi: 10.1103/PhysRevD.52.4307.

[98] Samira Hamimeche and Antony Lewis. Likelihood analysis of CMB temperature and polarization power spectra. *Phys. Rev. D*, 77(10):103013, May 2008. doi: 10.1103/PhysRevD.77.103013.

[99] Wayne Hu and Takemi Okamoto. Mass Reconstruction with Cosmic Microwave Background Polarization. *The Astrophysical Journal (ApJ)*, 574(2):566–574, August 2002. doi: 10.1086/341110.

[100] Christopher M. Hirata and Uroš Seljak. Reconstruction of lensing from the cosmic microwave background polarization. *Phys. Rev. D*, 68(8):083002, October 2003. doi: 10.1103/PhysRevD.68.083002.

[101] Kendrick M. Smith, Duncan Hanson, Marilena LoVerde, Christopher M. Hirata, and Oliver Zahn. Delensing CMB polarization with external datasets. *J. Cosmology Astropart. Phys.*, 2012(6):014, June 2012. doi: 10.1088/1475-7516/2012/06/014.

[102] Lloyd Knox and Yong-Seon Song. Limit on the Detectability of the Energy Scale of Inflation. *Phys. Rev. Lett.*, 89(1):011303, July 2002. doi: 10.1103/PhysRevLett.89.011303.

[103] Michael Kesden, Asantha Cooray, and Marc Kamionkowski. Separation of Gravitational-Wave and Cosmic-Shear Contributions to Cosmic Microwave Background Polarization. *Phys. Rev. Lett.*, 89:011304, July 2002. doi: 10.1103/PhysRevLett.89.011304.

[104] Uroš Seljak and Christopher M. Hirata. Gravitational lensing as a contaminant of the gravity wave signal in the CMB. *Phys. Rev. D*, 69(4):043005, February 2004. doi: 10.1103/PhysRevD.69.043005.

[105] F. Finelli, M. Bucher, and et al. Achúcarro. Exploring cosmic origins with CORE: Inflation. *J. Cosmology Astropart. Phys.*, 2018(4):016, April 2018. doi: 10.1088/1475-7516/2018/04/016.

[106] M. Ballardini, F. Finelli, C. Fedeli, and L. Moscardini. Probing primordial features with future galaxy surveys. *J. Cosmology Astropart. Phys.*, 2016(10):041, October 2016. doi: 10.1088/1475-7516/2016/10/041.

[107] Giovanni Cabass, Eleonora Di Valentino, Alessandro Melchiorri, Enrico Pajer, and Joseph Silk. Constraints on the running of the running of the scalar tilt from CMB anisotropies and spectral distortions. *Phys. Rev. D*, 94(2):023523, July 2016. doi: 10.1103/PhysRevD.94.023523.

[108] Julian B. Muñoz, Ely D. Kovetz, Alvise Raccanelli, Marc Kamionkowski, and Joseph Silk. Towards a measurement of the spectral runnings. *J. Cosmology Astropart. Phys.*, 2017(5):032, May 2017. doi: 10.1088/1475-7516/2017/05/032.

[109] Gabriela Sato-Polito, Ely D. Kovetz, and Marc Kamionkowski. Constraints on the primordial curvature power spectrum from primordial black holes. *Phys. Rev. D*, 100(6):063521, September 2019. doi: 10.1103/PhysRevD.100.063521.

[110] Amirhossein Samandar et al. Cosmic topology. Part IIIa. Microwave background parity violation without parity-violating microphysics. *JCAP*, 11:020, 2024. doi: 10.1088/1475-7516/2024/11/020.

[111] Sung Mook Lee, Dong Woo Kang, Jinn-Ouk Gong, Donghui Jeong, Dong-Won Jung, and Seong Chan Park. Cosmic birefringence by dark photon. *JCAP*, 08:037, 2024. doi: 10.1088/1475-7516/2024/08/037.

[112] Arthur Lue, Li-Min Wang, and Marc Kamionkowski. Cosmological signature of new parity violating interactions. *Phys. Rev. Lett.*, 83:1506–1509, 1999. doi: 10.1103/PhysRevLett.83.1506.

[113] Bo Feng, Hong Li, Ming-zhe Li, and Xin-min Zhang. Gravitational leptogenesis and its signatures in CMB. *Phys. Lett. B*, 620:27–32, 2005. doi: 10.1016/j.physletb.2005.06.009.

[114] Guo-Chin Liu, Seokcheon Lee, and Kin-Wang Ng. Effect on cosmic microwave background polarization of coupling of quintessence to pseudoscalar formed from the electromagnetic field and its dual. *Phys. Rev. Lett.*, 97:161303, 2006. doi: 10.1103/PhysRevLett.97.161303.

[115] Hiromasa Nakatsuka, Toshiya Namikawa, and Eiichiro Komatsu. Is cosmic birefringence due to dark energy or dark matter? A tomographic approach. *Phys. Rev. D*, 105(12):123509, 2022. doi: 10.1103/PhysRevD.105.123509.

[116] Alessandro Greco, Nicola Bartolo, and Alessandro Gruppuso. A new solution for the observed isotropic cosmic birefringence angle and its implications for the anisotropic counterpart through a Boltzmann approach. *JCAP*, 10:028, 2024. doi: 10.1088/1475-7516/2024/10/028.

[117] Y. Akrami et al. Planck 2018 results. IV. Diffuse component separation. *Astron. Astrophys.*, 641:A4, 2020. doi: 10.1051/0004-6361/201833881.

[118] Hans Kristian Eriksen et al. CMB component separation by parameter estimation. *Astrophys. J.*, 641:665–682, 2006. doi: 10.1086/500499.

[119] H. K. Eriksen, J. B. Jewell, C. Dickinson, A. J. Banday, K. M. Gorski, and C. R. Lawrence. Joint Bayesian component separation and CMB power spectrum estimation. *Astrophys. J.*, 676:10–32, 2008. doi: 10.1086/525277.

[120] J. Delabrouille, J. F. Cardoso, M. Le Jeune, M. Betoule, G. Fay, and F. Guilloux. A full sky, low foreground, high resolution CMB map from WMAP. *Astron. Astrophys.*, 493:835, 2009. doi: 10.1051/0004-6361:200810514.

[121] E. Martinez-Gonzalez, J. M. Diego, P. Vielva, and J. Silk. CMB power spectrum estimation and map reconstruction with the expectation - Maximization algorithm. *Mon. Not. Roy. Astron. Soc.*, 345:1101, 2003. doi: 10.1046/j.1365-2966.2003.06885.x.

[122] Jacques Delabrouille, J. F. Cardoso, and G. Patanchon. Multi-detector multi-component spectral matching and applications for CMB data analysis. *Mon. Not. Roy. Astron. Soc.*, 346:1089, 2003. doi: 10.1111/j.1365-2966.2003.07069.x.

[123] Jean-Francois Cardoso, Maude Martin, Jacques Delabrouille, Marc Betoule, and Guillaume Patanchon. Component separation with flexible models. Application to the separation of astrophysical emissions. 3 2008.

[124] N. Aghanim et al. Planck intermediate results. XLIX. Parity-violation constraints from polarization data. *Astron. Astrophys.*, 596:A110, 2016. doi: 10.1051/0004-6361/201629018.

[125] Brian G. Keating, Meir Shimon, and Amit P. S. Yadav. Self-Calibration of CMB Polarization Experiments. *Astrophys. J. Lett.*, 762:L23, 2012. doi: 10.1088/2041-8205/762/2/L23.

[126] Yuto Minami, Hiroki Ochi, Kiyotomo Ichiki, Nobuhiko Katayama, Eiichiro Komatsu, and Tomotake Matsumura. Simultaneous determination of the cosmic birefringence and miscalibrated polarization angles from CMB experiments. *PTEP*, 2019(8):083E02, 2019. doi: 10.1093/ptep/ptz079.

[127] Yuto Minami and Eiichiro Komatsu. Simultaneous determination of the cosmic birefringence and miscalibrated polarization angles II: Including cross frequency spectra. *PTEP*, 2020(10):103E02, 2020. doi: 10.1093/ptep/ptaa130.

[128] Yuto Minami and Eiichiro Komatsu. New Extraction of the Cosmic Birefringence from the Planck 2018 Polarization Data. *Phys. Rev. Lett.*, 125(22):221301, 2020. doi: 10.1103/PhysRevLett.125.221301.

[129] P. Diego-Palazuelos et al. Cosmic Birefringence from the Planck Data Release 4. *Phys. Rev. Lett.*, 128(9):091302, 2022. doi: 10.1103/PhysRevLett.128.091302.

[130] P. Diego-Palazuelos, E. Martínez-González, P. Vielva, R.B. Barreiro, M. Tristram, E. de la Hoz, J.R. Eskilt, Y. Minami, R.M. Sullivan, A.J. Banday, K.M. Górski, R. Keskitalo, E. Komatsu, and D. Scott. Robustness of cosmic birefringence measurement against galactic foreground emission and instrumental systematics. *Journal of Cosmology and Astroparticle Physics*, 2023(01):044, January 2023. ISSN 1475-7516. doi: 10.1088/1475-7516/2023/01/044. URL http://dx.doi.org/10.1088/1475-7516/2023/01/044.

[131] P. Diego-Palazuelos and E. Komatsu. Cosmic Birefringence from the Atacama Cosmology Telescope Data Release 6. 9 2025.

[132] J. R. Eskilt. Frequency-dependent constraints on cosmic birefringence from the LFI and HFI Planck Data Release 4. *Astron. Astrophys.*, 662:A10, 2022. doi: 10.1051/0004-6361/202243269.

[133] Tomohiro Fujita, Kai Murai, Hiromasa Nakatsuka, and Shinji Tsujikawa. Detection of isotropic cosmic birefringence and its implications for axionlike particles including dark energy. *Phys. Rev. D*, 103(4):043509, 2021. doi: 10.1103/PhysRevD.103.043509.

[134] Lu Yin, Joby Kochappan, Tuhin Ghosh, and Bum-Hoon Lee. Is cosmic birefringence model-dependent? *JCAP*, 10:007, 2023. doi: 10.1088/1475-7516/2023/10/007.

[135] Joby Kochappan, Lu Yin, Bum-Hoon Lee, and Tuhin Ghosh. Observational evidence for Early Dark Energy as a unified explanation for Cosmic Birefringence and the Hubble tension. 8 2024.

[136] Johannes R. Eskilt, Laura Herold, Eiichiro Komatsu, Kai Murai, Toshiya Namikawa, and Fumihiro Naokawa. Constraints on Early Dark Energy from Isotropic Cosmic Birefringence. *Phys. Rev. Lett.*, 131(12):121001, 2023. doi: 10.1103/PhysRevLett.131.121001.

[137] Toshiya Namikawa, Kai Murai, and Fumihiro Naokawa. Planck Constraints on Axion-Like Particles through Isotropic Cosmic Birefringence. 6 2025.

[138] W. J. Handley, M. P. Hobson, and A. N. Lasenby. PolyChord: nested sampling for cosmology. *Mon. Not. Roy. Astron. Soc.*, 450(1):L61–L65, 2015. doi: 10.1093/mnrasl/slv047.

[139] W. J. Handley, M. P. Hobson, and A. N. Lasenby. polychord: next-generation nested sampling. *Mon. Not. Roy. Astron. Soc.*, 453(4):4385–4399, 2015. doi: 10.1093/mnras/stv1911.

[140] Antonio Raffaelli and Mario Ballardini. Knot reconstruction of the scalar primordial power spectrum with Planck, ACT, and SPT CMB data. *arXiv e-prints*, art. arXiv:2503.10609, March 2025. doi: 10.48550/arXiv.2503.10609.

[141] Marco Bortolami, Matteo Billi, Alessandro Gruppuso, Paolo Natoli, and Luca Pagano. Planck constraints on cross-correlations between anisotropic cosmic birefringence and CMB polarization. *JCAP*, 09:075, 2022. doi: 10.1088/1475-7516/2022/09/075.

[142] Planck Collaboration. Planck pre-launch status: The Planck mission. *AA*, 520:A1, September 2010. doi: 10.1051/0004-6361/200912983.

[143] P. A. R. Ade et al. Planck 2015 results. XII. Full Focal Plane simulations. *Astron. Astrophys.*, 594:A12, 2016. doi: 10.1051/0004-6361/201527103.

[144] N. Aghanim et al. Planck 2018 results. III. High Frequency Instrument data processing and frequency maps. *Astron. Astrophys.*, 641:A3, 2020. doi: 10.1051/0004-6361/201832909.

[145] K. M. Górski, E. Hivon, A. J. Banday, B. D. Wandelt, F. K. Hansen, M. Reinecke, and M. Bartelman. HEALPix - A Framework for high resolution discretization, and fast analysis of data distributed on the sphere. *Astrophys. J.*, 622:759–771, 2005. doi: 10.1086/427976.

[146] David Alonso, Javier Sanchez, and Anže Slosar. A unified pseudo-C_ℓ framework. *Mon. Not. Roy. Astron. Soc.*, 484(3):4127–4151, 2019. doi: 10.1093/mnras/stz093.

[147] E. Hivon, K. M. Gorski, C. B. Netterfield, B. P. Crill, S. Prunet, and F. Hansen. Master of the cosmic microwave background anisotropy power spectrum: a fast method for statistical analysis of large and complex cosmic microwave background data sets. *Astrophys. J.*, 567: 2, 2002. doi: 10.1086/338126.

[148] Gianluca Polenta, D. Marinucci, A. Balbi, P. de Bernardis, E. Hivon, S. Masi, P. Natoli, and N. Vittorio. Unbiased estimation of angular power spectrum. *JCAP*, 11:001, 2005. doi: 10.1088/1475-7516/2005/11/001.

[149] Antony Lewis, Anthony Challinor, and Neil Turok. Analysis of CMB polarization on an incomplete sky. *Phys. Rev. D*, 65:023505, 2002. doi: 10.1103/PhysRevD.65.023505.

[150] Emory F. Bunn, Matias Zaldarriaga, Max Tegmark, and Angelica de Oliveira-Costa. E/B decomposition of finite pixelized CMB maps. *Phys. Rev. D*, 67:023501, 2003. doi: 10.1103/PhysRevD.67.023501.

[151] J. Grain, M. Tristram, and R. Stompor. Polarized CMB spectrum estimation using the pure pseudo cross-spectrum approach. *Phys. Rev. D*, 79:123515, 2009. doi: 10.1103/PhysRevD.79.123515.

[152] E. Y. S. Wu et al. Parity Violation Constraints Using Cosmic Microwave Background Polarization Spectra from 2006 and 2007 Observations by the QUaD Polarimeter. *Phys. Rev. Lett.*, 102:161302, 2009. doi: 10.1103/PhysRevLett.102.161302.

[153] Alessandro Gruppuso, Gianmarco Maggio, Diego Molinari, and Paolo Natoli. A note on the birefringence angle estimation in CMB data analysis. *JCAP*, 05:020, 2016. doi: 10.1088/1475-7516/2016/05/020.

[154] J. Hartlap, Patrick Simon, and P. Schneider. Why your model parameter confidences might be too optimistic: Unbiased estimation of the inverse covariance matrix. *Astron. Astrophys.*, 464:399, 2007. doi: 10.1051/0004-6361:20066170.

[155] Curtis Parvin. An introduction to multivariate statistical analysis, 3rd ed. t.w. anderson. hoboken, nj: John wiley & sons, 2003, 742 pp., 99.95 usd, hardcover. isbn 0-471-36091-0. *Clinical Chemistry*, 50:981–982, 05 2004. doi: 10.1373/clinchem.2003.025684.

[156] Marius Millea and François Bouchet. Cosmic Microwave Background Constraints in Light of Priors Over Reionization Histories. *Astron. Astrophys.*, 617:A96, 2018. doi: 10.1051/0004-6361/201833288.

[157] Will J. Handley, Anthony N. Lasenby, Hiranya V. Peiris, and Michael P. Hobson. Bayesian inflationary reconstructions from Planck 2018 data. *Phys. Rev. D*, 100(10):103511, 2019. doi: 10.1103/PhysRevD.100.103511.

[158] Will Handley. fgivenx: Functional posterior plotter. *The Journal of Open Source Software*, 3(28), Aug 2018. doi: 10.21105/joss.00849. URL http://dx.doi.org/10.21105/joss.00849.

[159] LiteBIRD Collaboration. Probing cosmic inflation with the litebird cosmic microwave background polarization survey. *Progress of Theoretical and Experimental Physics*, 2023 (4):042F01, 11 2022. ISSN 2050-3911. doi: 10.1093/ptep/ptac150. URL https://doi.org/10.1093/ptep/ptac150.

[160] The Simons Observatory collaboration. The simons observatory: science goals and forecasts. *Journal of Cosmology and Astroparticle Physics*, 2019(02):056, feb 2019. doi: 10.1088/1475-7516/2019/02/056. URL https://dx.doi.org/10.1088/1475-7516/2019/02/056.

[161] The CMB-S4 Collaboration. Cmb-s4: Forecasting constraints on primordial gravitational waves. *The Astrophysical Journal*, 926(1):54, feb 2022. doi: 10.3847/1538-4357/ac1596. URL https://dx.doi.org/10.3847/1538-4357/ac1596.

[162] E. Schiappucci, S. Raghunathan, C. To, F. Bianchini, C. L. Reichardt, N. Battaglia, B. Hadzhiyska, S. Kim, J. B. Melin, C. Sifón, and E. M. Vavagiakis. Constraining cosmological parameters using the pairwise kinematic sunyaev-zel'dovich effect with cmb-s4 and future galaxy cluster surveys, 2024. URL https://arxiv.org/abs/2409.18368.

[163] L. Wolfenstein. Neutrino Oscillations in Matter. *Phys. Rev. D*, 17:2369–2374, 1978. doi: 10.1103/PhysRevD.17.2369.

[164] S. P. Mikheyev and A. Yu. Smirnov. Resonance Amplification of Oscillations in Matter and Spectroscopy of Solar Neutrinos. *Sov. J. Nucl. Phys.*, 42:913–917, 1985.

[165] Guido D'Amico and Nemanja Kaloper. Anisotropies in nonthermal distortions of cosmic light from photon-axion conversion. *Phys. Rev. D*, 91(8):085015, 2015. doi: 10.1103/PhysRevD.91.085015.

[166] Suvodip Mukherjee, Rishi Khatri, and Benjamin D. Wandelt. Polarized anisotropic spectral distortions of the CMB: Galactic and extragalactic constraints on photon-axion conversion. *JCAP*, 04:045, 2018. doi: 10.1088/1475-7516/2018/04/045.

[167] Suvodip Mukherjee, David N. Spergel, Rishi Khatri, and Benjamin D. Wandelt. A new probe of Axion-Like Particles: CMB polarization distortions due to cluster magnetic fields. *JCAP*, 02:032, 2020. doi: 10.1088/1475-7516/2020/02/032.

[168] Jens Chluba. The Cosmic Microwave Background: Spectral Distortions. 1 2025.

[169] Cristina Mondino, Dalila Pirvu, Junwu Huang, and C. Johnson. Axion-induced patchy screening of the Cosmic Microwave Background. *JCAP*, 10:107, 2024. doi: 10.1088/1475-7516/2024/10/107.

[170] Samuel Goldstein, Fiona McCarthy, Cristina Mondino, J. Colin Hill, Junwu Huang, and Matthew C. Johnson. Constraints on Axions from Patchy Screening of the Cosmic Microwave Background. *Phys. Rev. Lett.*, 134(8):081001, 2025. doi: 10.1103/PhysRevLett.134.081001.

[171] Dalila Pirvu, Junwu Huang, and Matthew C. Johnson. Patchy screening of the CMB from dark photons. *JCAP*, 01:019, 2024. doi: 10.1088/1475-7516/2024/01/019.

[172] Clarence Zener and Ralph Howard Fowler. Non-adiabatic crossing of energy levels. *Proceedings of the Royal Society of London. Series A, Containing Papers of a Mathematical and Physical Character*, 137(833):696–702, 1932. doi: 10.1098/rspa.1932.0165. URL https://royalsocietypublishing.org/doi/abs/10.1098/rspa.1932.0165.

[173] Pierluca Carenza and M. C. David Marsh. On the applicability of the Landau-Zener formula to axion-photon conversion. *JCAP*, 04:021, 2023. doi: 10.1088/1475-7516/2023/04/021.

[174] Robert J. J. Grand, Facundo A. Gómez, Federico Marinacci, Ruediger Pakmor, Volker Springel, David J. R. Campbell, Carlos S. Frenk, Adrian Jenkins, and Simon D. M. White. The Auriga Project: the properties and formation mechanisms of disc galaxies across cosmic time. *Mon. Not. Roy. Astron. Soc.*, 467(1):179–207, 2017. doi: 10.1093/mnras/stx071.

[175] Dylan Nelson et al. First results from the IllustrisTNG simulations: the galaxy colour bimodality. *Mon. Not. Roy. Astron. Soc.*, 475(1):624–647, 2018. doi: 10.1093/mnras/stx3040.

[176] Steven Weinberg. Lectures on quantum mechanics. *Lectures on Quantum Mechanics, by Steven Weinberg, Cambridge, UK: Cambridge University Press, 2012*, 11 2012. doi: 10.1017/CBO9781139236799.

[177] A. D. Buckingham et al. The cotton-mouton effect of neon and argon: a benchmark study using highly correlated coupled cluster wave functions. *Physical Review A*, 2004. doi: 10.1103/PhysRevA.69.012512. Studio teorico avanzato sull'effetto Cotton-Mouton nei gas neon e argon.

[178] Cedric Deffayet, Diego Harari, Jean-Philippe Uzan, and Matias Zaldarriaga. Dimming of supernovae by photon pseudoscalar conversion and the intergalactic plasma. *Phys. Rev. D*, 66:043517, 2002. doi: 10.1103/PhysRevD.66.043517.

[179] Nirmalya Brahma, Asher Berlin, and Katelin Schutz. Photon-dark photon conversion with multiple level crossings. *Phys. Rev. D*, 108(9):095045, 2023. doi: 10.1103/PhysRevD.108.095045.

[180] Marco Fabbrichesi, Emidio Gabrielli, and Gaia Lanfranchi. The Dark Photon. *SpringerBriefs in Physics*, 2020. doi: 10.1007/978-3-030-62519-1.

[181] Andrea Caputo, Alexander J. Millar, Ciaran A. J. O'Hare, and Edoardo Vitagliano. Dark photon limits: A handbook. *Phys. Rev. D*, 104:095029, 2021. doi: 10.1103/PhysRevD.104.095029.

[182] N. Battaglia, J. R. Bond, C. Pfrommer, and J. L. Sievers. On the Cluster Physics of Sunyaev-Zel'dovich and X-ray Surveys III. Measurement Biases and Cosmological Evolution of Gas and Stellar Mass Fractions. *Astrophys. J.*, 777:123, 2013. doi: 10.1088/0004-637X/777/2/123. [Erratum: Astrophys.J. 780, 189 (2014)].

[183] Murray Geller and Edward W. Ng. A Table of Integrals of the Exponential Integral. *National Institute of Standards and Technology Journal of Research*, 73B:191–210, September 1969. doi: 10.6028/jres.073B.019.

[184] M. Abramowitz and I. A. Stegun. *Handbook of Mathematical Functions.* 1972.